Competing polar and nonpolar distortions and phase transitions in low-dimensional materials

UNIVERSITY OF CAMBRIDGE

Daniel Bennett

Supervisor: Prof. Emilio Artacho

Cavendish Laboratory
Department of Physics

This dissertation is submitted for the degree of
Doctor of Philosophy

St. John's College   November 2021

Declaration

This thesis is the result of my own work and includes nothing which is the outcome of work done in collaboration except as declared in the Preface, Acknowledgements, and as specified in the text. It is not substantially the same as any that I have submitted, or, is being concurrently submitted for a degree or diploma or other qualification at the University of Cambridge or any other university or similar institution except as declared in the Preface and specified in the text. It does not exceed the prescribed word limit for the relevant Degree Committee.

Daniel Bennett

October 2021

Acknowledgements

I would first like to thank my supervisor, Emilio Artacho, for invaluable help and guidance throughout my PhD. I would also like to thank Nicholas Bristowe, a close collaborator for most of my PhD. I would like to thank Michael Rutter and Philip Blakely for their continuous technical support. I am extremely grateful to have undertaken my PhD in TCM. It is an inspiring research group to work in, and I have made many lifelong collaborators and friends. Finally, I would like to thank my family, Liam, Trish, Hollie, James, Phyllis and Mairéad, and friends, Alex, Fabio and Kyle, for their constant love and support.

Abstract

Knowledge of different phases and phase transitions in low-dimensional systems is essential for the understanding and control of nanoscale devices. Theoretical models aided by first-principles calculations have proven invaluable in this respect. However, observed behaviour often differs from what is predicted theoretically. One common reason for this is that in many systems several different phase transitions are possible, and the phases typically compete, or even coexist.

The aim of this thesis is to provide a theoretical and computational study of competing phases and phase transitions in several interesting nanoscale systems. The first is polar-nonpolar interfaces such as $LaAlO_3$/$SrTiO_3$, where an insulator–metal transition occurs at the interface via the formation of a two-dimensional electron gas (2DEG) which screens the polar discontinuity there. In spite of the interest, tunability, and very special properties of the 2DEG, important uncertainties remain about the character of the metal–insulator transition induced by film thickness and/or perpendicular electric field. We show that a rich variety of scenarios is possible for the apearance of free carriers in such systems due to the coupling of the dielectric response of the film with common structural distortions of the perovskite systems employed, namely the rotations of oxygen octahedra (tilts). We show that continuous or discontinuous, and simultaneous or separate appearances of tilts and carriers can occur, depending very sensitively on the energetics of the tilts, carriers, the biquadratic coupling between them, and the correlation length of the tilts in the polar film.

The second is ferroelectric thin films, which tend to fall victim to depolarization effects, limiting their use in practical applications. It is well-known that depolarization can be mitigated by the formation of complex domain structures, but recently it has been proposed theoretically and signalled experimentally that the formation of a 2DEG at the surfaces of the films may make it possible to sustain a polarization without domains. Previous theoretical studies have suggested that the effects compete, and that either domains or a 2DEG will form in the thin and thick limits, respectively. However, recent experimental observations

suggest they can coexist. We propose a model of ferroelectric interfaces in which the polar discontinuities can be screened both by domains and a 2DEG. We find that the polydomain and monodomain phases are separated by a region of coexistence in which both phenomena are simultaneously observed.

The final example comes from twistronics, an emerging field in which the properties of layered systems are tuned by introducing a relative twist or lattice mismatch between the layers (moiré superlattice). Recently, ferroelectricity was observed in a typically non-polar system, facilitated by twisting, although the phenomenon has not yet been understood theoretically. It is well-known that stacking domains form in moiré superlattices due to the competition between the interlayer van der Waals forces and intralayer elastic forces, which can be recognized as polar domains due to the local spontaneous polarization in bilayers without centrosymmetry. We propose a theoretical model which captures the effect of an applied electric field on the domain structure. The coupling between the spontaneous polarization and field leads to uneven relaxation of the domains, and a net polarization in the superlattice at nonzero fields, which is sensitive to the moiré period. We show that the dielectric response to the field reduces the stacking energy and leads to softer domains in all bilayers.

Table of contents

Chapter 1

Introduction

The study of phase transitions has driven the advancement of technology and our understanding of the world around us for centuries. For example, thermodynamics was developed in order to better understand the transition between water and steam, with the aim of increasing the efficiency of the steam engine. The ability to switch the orientation of the magnetization of a ferromagnet with an applied field, was used as one of the first mechanisms for random-access memory (RAM) in the early days of computers.
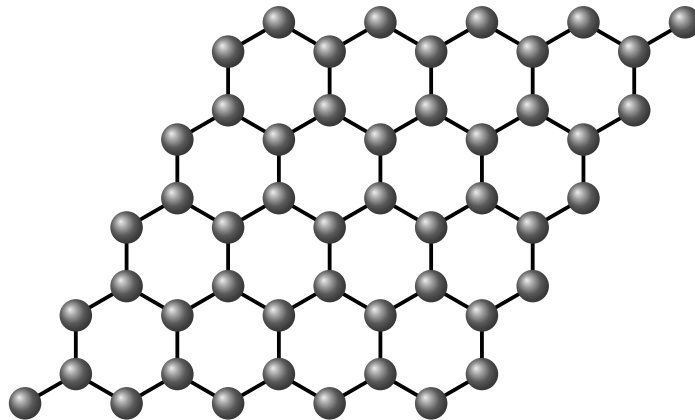
Fig. 1.1 Atomic structure of a layer of graphene.

With advancements in nanotechnology, it is possible to fabricate and control devices comprised of a small number of atoms in one or more dimensions, the properties of which vary considerably from their bulk counterparts. Graphene, a one atom thick layer of carbon atoms (see Fig. 1.1), is of huge interest to the scientific community due to its high tensile strength and electrical conductivity, and has become a household name in the last decade [1]. Owing

to experimental techniques such as liquid exfoliation [2], it is possible to synthesize a wide variety of two-dimensional materials (2D) from van der Waals materials in a way which is relatively inexpensive and provides a high yield. Besides graphene, one of the most popular classes of 2D materials is the transition metal dichalcogenides (TMDs) MX_2, where M is a transition metal and X is a chalcogen, such as MoS_2 and WSe_2. Unlike graphene, TMD monolayers have a direct band gap, and have applications in electronics as transistors, and in optics as emitters and detectors [3]. Their in-plane crystal structure is the same as graphene, but TMD monolayers are three atoms thick.

Using other techniques such as pulsed laser deposition (PLD), it is possible to grow thin films of oxide materials, which are a few unit cells in thickness [4]. Perovskites, the class of materials with the same crystal structure as calcium titanate (CaTiO3), have become widely known in many areas of science due to the huge number of interesting properties observed across many different materials. Halide perovskites have achieved record solar cell efficiencies in recent years [5]. Oxide perovskites such as lead titanate ($PbTiO_3$, PTO) and barium titanate ($BaTiO_3$, BTO) are some of the most well-known examples of ferroelectric materials [6, 7]. Bismuth ferrite ($BiFeO_3$ BFO) is one of the most promising multiferroic materials [8], being both ferroelectric and ferromagnetic. Strontium titanate ($SrTiO_3$, STO) should be ferroelectric, but remains paraelectric down to very low temperatures, making it a quantum paraelectric material [9, 10].

Most of these interesting properties are governed by various types of phase transitions. In order to understand the behavior of these materials, and utilize them for future applications in nanotechnology, a good understanding of the phases they exhibit and the phase transitions they can undergo is essential. Theoretical and computational condensed matter physics have proven invaluable in this respect. Concepts such as universality, criticality and renormalization [11, 12], have shaped our understanding of modern theoretical physics. These concepts, as well as complex many-body models are essential to a deeper understanding of the physical mechanisms underpinning phenomena such as superconductivity, quantum phase transitions and the insulator–metal transition. The insulator–metal transition is one of the most widely studied problems in condensed matter physics [13, 14], particularly in oxide materials [15–18]. It is simple to model and understand the behavior of good insulators, such as silicon and germanium, or good metals, such as silver or gold. But developing a theory which can describe both, and the transition from one to the other, is a very difficult problem. The two limits, a good metal and a good insulator, have different elementary excitations. For metals, the excitations are fermionic quasiparticles, corresponding to electrons above the

Fermi sea. For insulators, the excitations are bosonic, such as phonons, like the polar mode for ferroelectrics, or spin waves for ferromagnets. In the intermediate region, both types of excitations coexist, and it is difficult to write down an order parameter which describes the transition between a metallic and insulating phases. Insulator-metal transitions in 2D have attracted additional interest [19, 20], in particular, the one occurring at polar-nonpolar perovskite interfaces, first observed for thin films of lanthanum aluminate ($LaAlO_3$, LAO) grown on STO [21, 22].

However there are some phenomena, such as ferroelectricity and ferromagnetism, for which an understanding of their behavior in nanoscale systems can be obtained from a qualitative, phenomenological description. We can describe these systems using Landau theory, a simple but powerful method for theoretically describing and understanding phase transitions in crystals [23, 24]. It was originally conceived as a thermodynamic description of continuous transitions between liquid and crystal phases, facilitated by a discontinuous change in the symmetry of the system. The theory revolves around the construction of a Landau free energy, which describes a phase transition from a high symmetry phase to a lower symmetry phase via some symmetry breaking. The symmetry breaking is described by some internal order parameters, and the Landau free energy is written as an expansion of these order parameters, using symmetries such as locality, rotational and translational invariance to reduce the number of terms in the expansion. Then, for a given set of external parameters, the stable phase of the system is described by the set of order parameters which minimize the free energy.

We can illustrate many concepts in Landau theory using the example of a ferroelectric perovskite, e.g. PTO or BTO. The zero polarization phase is the one corresponding to the ideal perovskite structure, where the Ti atom lies at the center of the O_6 octahedron. A polar phase can be adopted via the off-centering of the Ti atoms with respect to the oxygen octahedra, driven by the hybridization of the O 2p and the Ti 3d orbitals [6, 7]. In three dimensions, the stable equilibrium state is sixfold degenerate, but we can write a one-dimensional version of the Landau free energy as

$$\mathcal{F} = \frac{1}{2}X_P^{-1}\left(\frac{1}{4}\left(\frac{P_\eta}{P_s}\right)^4 - \frac{1}{2}\left(1 - \frac{T}{T_C}\right)\left(\frac{P_\eta}{P_s}\right)^2\right), \qquad (1.1)$$

where P_η is the average polarization associated to a polar mode η and $\pm P_s$ is the spontaneous polarization, i.e. the polarizations at which $\mathcal{F}$ is minimized, which is only twofold degenerate
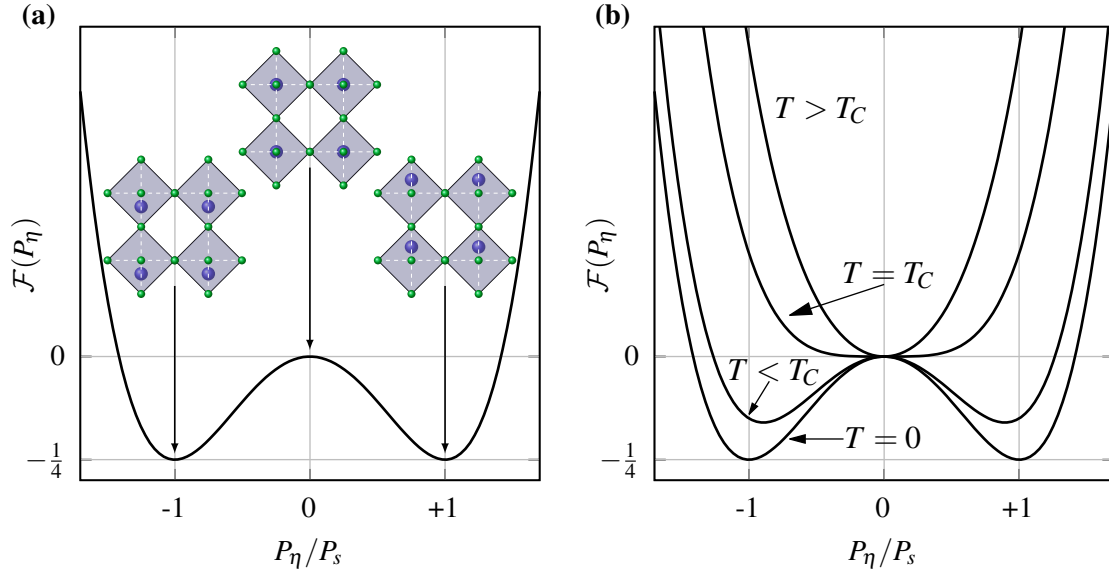
Fig. 1.2 **(a)**: Landau free energy of a ferroelectric perovskite as a function of polarization P_η, in units of $\frac{1}{2}X_P^{-1}$. Sketches of the perovskite at $P_\eta = 0, \pm P_s$ are shown above the curve. **(b)**: Landau free energy curves at several different temperatures.

in one dimension. X_P describes the curvature of the free energy about the minima, and $\frac{1}{2}X_P^{-1}$ has units of energy per unit volume, which sets the energy scale (the depth of the wells is an appropriate alternative). The double well is shown in Fig. 1.2 (a), with sketches of the perovskite at $P_\eta = 0, \pm P_s$ above. At zero temperature, the system can undergo a displacive transition from $P_\eta = 0$ to $P_\eta = \pm P_s$, facilitated by Ti off-centering. At a nonzero temperature, each Ti atom will experience thermal fluctuations about $\pm P_s$, and the average polarization of the system decreases. At smaller temperatures, there is still a net polarization, so the Landau free energy still has the shape of a double well, but with a reduced width and depth. Eventually, the fluctuations will be large enough that the polarization averages to zero. We call the temperature at which this occurs T_C, the Curie temperature. At and above T_C, the Landau free energy becomes a single well, see Fig. 1.2 (b).

Landau theory can provide a physically intuitive thermodynamic description of second order phase transitions in periodic crystals in terms of a homogeneous order parameter, but is not appropriate for semi-periodic systems, such as a semi-infinite slab or a thin film, where the order parameter cannot be homogeneous due to the presence of free surfaces. These types of systems can be described using Ginzburg-Landau theory, a generalization of Landau theory in which the order parameters vary in space, and the free energy is also expanded in powers of the gradients of the order parameters. While Ginzburg-Landau theory is perhaps most

well-known in the context of superconductivity [25], it has been successful in describing phase transitions in e.g. ferromagnetic [26] and ferroelectric [27–29] thin films, in which the magnetization or polarization in the out of plane direction can increase or decrease towards the free surfaces, and complex domain structures can form in the plane.

We can write down the Ginzburg-Landau free energy of a ferroelectric thin film by generalizing Eq. (1.1) [28, 29]:

$$\mathcal{F} = \frac{1}{2} X_P^{-1} \frac{1}{V} \int \left(\lambda^2 \left(\nabla \left(\frac{P_\eta}{P_s} \right) \right)^2 + \frac{1}{4} \left(\frac{P_\eta}{P_s} \right)^4 - \frac{1}{2} \left(\frac{P_\eta}{P_s} \right)^2 \right) \mathrm{d}V , \qquad (1.2)$$

where $\lambda > 0$ is the correlation length and V is the volume of the thin film. We set $T = 0$ in this example, but the correlation length is temperature dependent. The gradient term is essentially an energy penalty for having spatial variations in polarization, and in the absence of any free surfaces, the energy is minimized by a homogeneous polarization. Eq. (1.2) could be used to describe spatial variations in a thin film in the out-of-plane direction due to the difference in the energy at the surfaces and in the interior of the thin film. This will cause the polarization to either turn up or down towards the surfaces. The amount by which the polarization changes towards the surfaces is determined by the competition between the surface energy and the energy penalty for having gradients in the polarization. Eq. (1.2) could also be used to describe spatial variations of the polarization in the plane. The presence of free surfaces leads to a depolarizing electric field in ferroelectric thin films, which can reduce or completely suppress the polarization in the absence of any charge compensation. Depolarization effects can be mitigated by the formation of ferroelectric domains with polarizations of alternating sign, causing the depolarizing field to bend around the surfaces and domain walls [30, 31]. Domain structures in ferroelectric films tend to be much sharper than in ferromagnetic films, and a typical approximation made is that the walls are infinitely thin, i.e. the spontaneous polarization takes the form of a square wave. While this is a rather large approximation, especially for ultra thin films (only a few unit cells thick), it has historically been successful in providing insight into the behavior of domain structures in ferroelectric systems [32, 33].

Many materials have several energetically stable phases available to them, and can undergo several phase transitions. Typically, there is competition between the phases. A well-known example of this is is the competition between polarization and the rotations of oxygen octahedra (tilts, see Fig. 1.3 (a)) in oxide perovskites [34–37]. The antiferrodistortive (AFD) phase transition from an untilted phase to a tilted phase is another example of a displacive

(a)

(b)
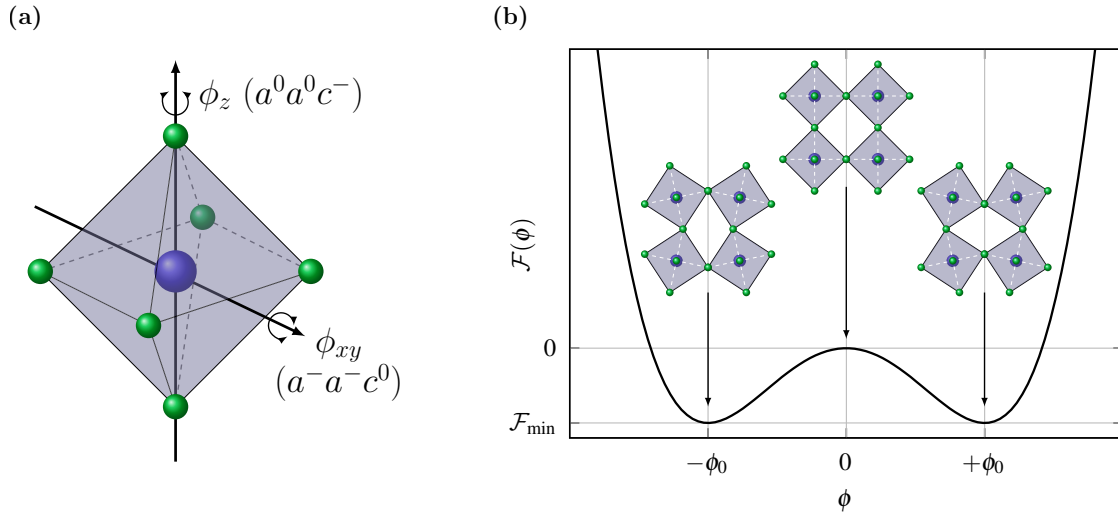
Fig. 1.3 **(a)**: Sketch of a single oxygen octahedron of a perovskite material. Two different tilting modes, ϕ_z and ϕ_{xy}, and their principle axes of rotation, are shown. **(b)**: Landau free energy of a tilted perovskite as a function of the tilt angle ϕ. Sketches of the untilted and tilted phases are shown above the curve.

phase transition which can occur in oxide perovskites. Tilts were originally classified by Glazer using group theory [38], but can also be described thermodynamically using a double well for the Landau free energy, similarly to ferroelectrics, see Fig. 1.3 (b). Many perovskite materials possess ferroelectric instabilities at zero temperature, but are not observed to be ferroelectric. This is because they also possess AFD instabilities, and it may be more energetically favorable for some materials to adopt a nonpolar tilted phase rather than a ferroelectric one. This is a result of the competition between the two phases. Empirically, this competition has been rationalized in terms of the Goldschmidt tolerance factor of an ABO_3 perovskite [39]:

$$t = \frac{1}{\sqrt{2}} \frac{R_{A-O}}{R_{B-O}} \tag{1.3}$$

where R_{A-O} and R_{B-O} are the $A-O$ and $B-O$ bond lengths, respectively. When $t < 1$, the ferroelectricity is suppressed and the material becomes tilted. When $t \sim 1$, in PTO and BTO for example, the ferroelectricity suppresses the tilts.

Competition between order parameters can also affect phase transitions, leading to a very different picture than the one obtained when considering the separate phases in isolation. At the Landau level, the competition can be considered by constructing a Landau free energy as

an expansion of both order parameters, including coupling terms. The coupling terms are subject to the same symmetry constraints as the isolated free energies [40, 37]. The most common type of coupling is biquadratic, i.e. quadratic in both order parameters, which is allowed if both free energies have quadratic terms. A bilinear coupling is also allowed if both order parameters have the exact same symmetries, e.g. for tilts and ferroelectricity. The coupling can lead to simultaneous or separate transitions, and even change the order of a phase transition [40, 37].

The aim of this thesis is to provide a theoretical and computational study of competing phases and phase transitions for several interesting nanoscale systems. The first is polar-nonpolar perovskite interfaces, where two-dimensional electron gas (2DEG) formation has been observed at the interface between two insulating materials. The second is ferroelectric thin films, where similar 2DEG formation has been theorized and recently observed, and competes with the formation of ferroelectric domains. The third comes from twistronics, a newly established field in condensed matter physics, in which the properties of layered systems are tuned by introducing a twist or lattice mismatch. Recently, ferroelectricity has been observed, facilitated by the twist angle, although the underlying physical mechanisms are not yet well-understood theoretically. A brief introduction to each of the three topics is provided in the next three sections.

1.1   Polar-nonpolar perovskite interfaces

The discovery of an insulator–metal transition at the interface between two insulating perovskites was of huge interest to the scientific community [21, 22]. When thin films of LAO were grown on substrates of STO, a 2DEG was found to appear at the interface in order to screen the polar discontinuity there. This 2DEG has been found to be associated with interesting phenomena such as enhanced capacitance [41], superconductivity [42] and magnetism [43], even at the same time [44, 45]. It also has potential for applications in field effect transistors (FET) [46–48], sensors [49], photodetection [50], thermoelectrics [51, 52] and solar cells [53, 54].

The physical origin and character of this insulator–metal transition have been debated for many years, and discussed in several reviews [55–66]. Two of the most popular theories for the physical origin are indirectly supported by experimental evidence: the first is electronic reconstruction, where the 2DEG forms via a transfer of electrons from the valence band at
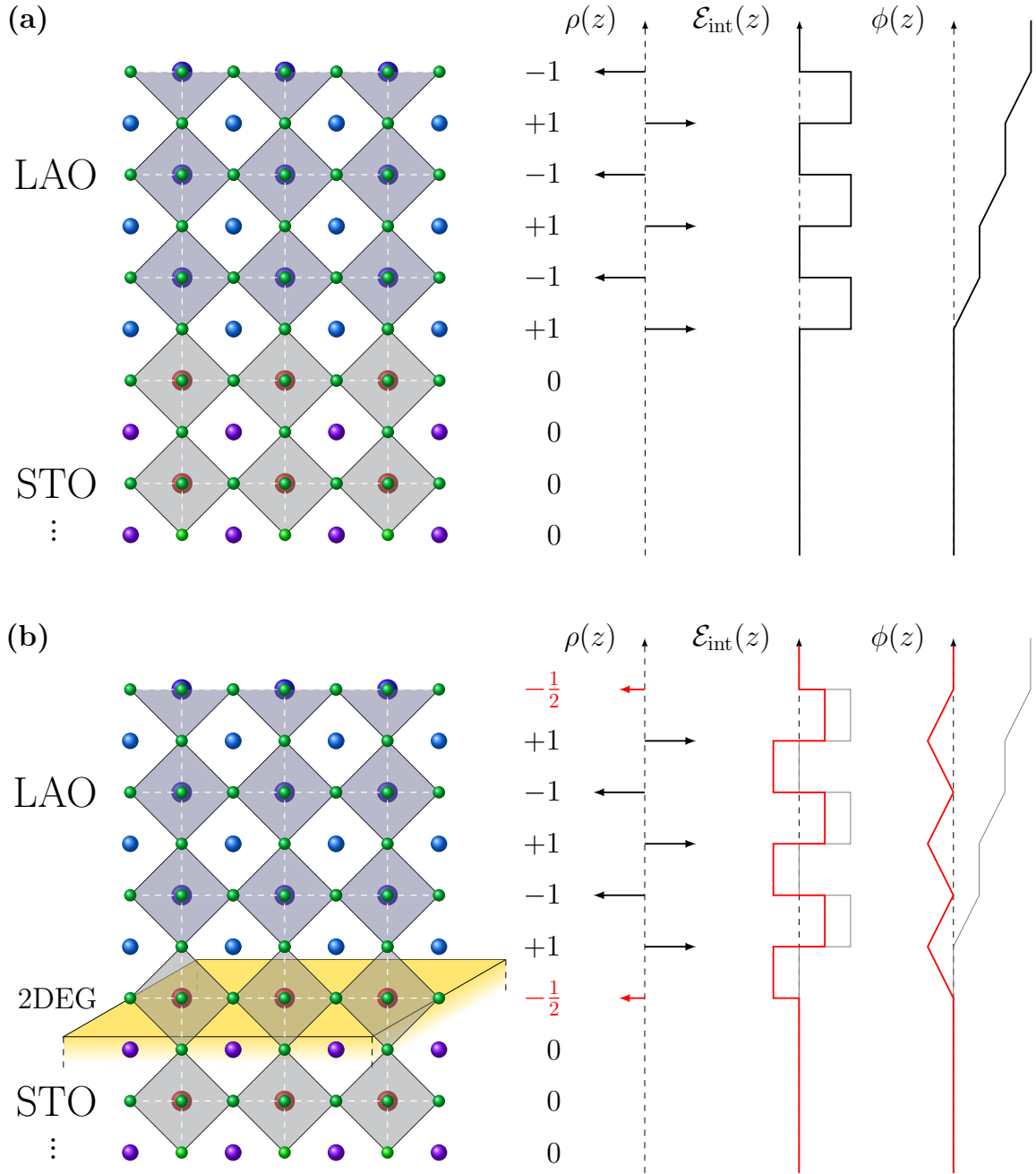
Fig. 1.4 Illustration of the **(a)**: polar catastrophe and **(b)**: 2DEG formation for a polar-nonpolar perovskite interface such as LAO/STO. On the left is a sketch of a thin film of LAO grown on top of a semi-infinite substrate of STO. The formal polarizations of each half layer are shown to the right of the sketch. The charge density, internal field and electrostatic potential are shown on the right. In **(a)** we see that the electrostatic potential diverges in the LAO film. This is known as the polar catastrophe. In **(b)**, a 2DEG forms at the interface in order to screen the polar discontinuity there and prevent the polar catastrophe.
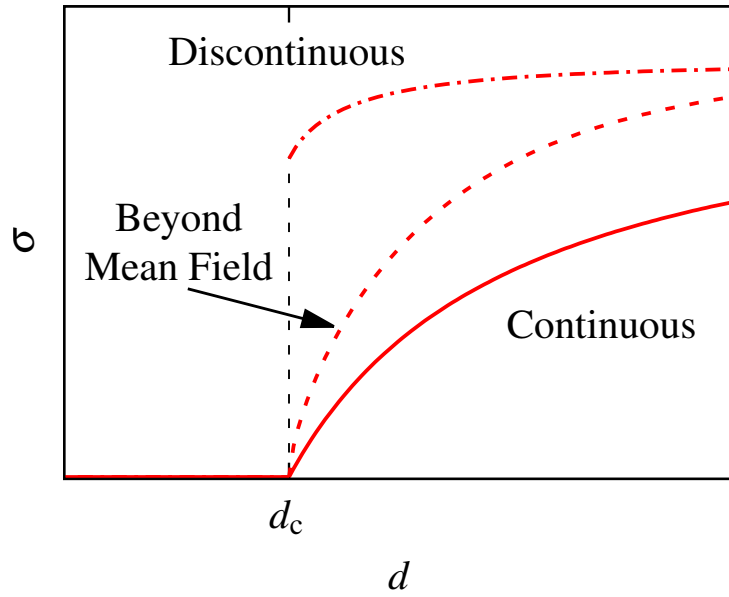
Fig. 1.5 Sketch of the various predictions for the carrier concentration σ as a function of LAO film thickness. The solid curve shows the prediction from the phenomenological theory in Ref. [66]. The dashed curve shows the beyond mean-field correction to this theory. The dot-dash curve shows a discontinuous transition, which has been experimentally observed and predicted in other theoretical studies.

the surface of the thin film to the conduction band at the interface in order to screen the polar discontinuity [67–69]. The second is redox screening, where oxygen vacancies or hydrogen adatoms, for example, form at the surface, creating charge carriers that can move to the interface [70–76]. In Ref. [77] it was predicted that both mechanisms are possible, depending on the experimental conditions such as the oxygen pressure and the growth temperature [76, 78].

The character of the transition with film thickness, i.e. whether the carriers appear continuously or discontinuously after a critical thickness, is still debated. It has been observed in experimental studies [22] and suggested in theoretical studies [66, 79] based on redox effects that a discontinuous transition occurs at a critical thickness d_c between 3 and 4 unit cells of LAO. However, film thickness is not a good parameter with which to make any conclusions about the order of the transition, since it is fixed for each sample and is changed discretely by a number of unit cells. Thus, it is impossible to conclude whether the transition is continuous or discontinuous, and the problem is only of theoretical interest. A more realistic approach to investigate this would be to apply an electric field, using top and back gates [80], to a sample which is close to the critical thickness. An electric field can be used to switch the 2DEG on

[81] and off [82] in a single sample, which is a desirable feature in practical applications. It can also enhance the properties of the 2DEG such as the superconductivity [83–85] magneto-transport [86] and optical behavior [87]. An electric field could be tuned with more precision and thus would be more suitable for studying the character of the insulator–metal transition experimentally.

A phenomenological theory at the mean-field level, which treats the carriers as a homogeneous charge distribution σ, predicts that the onset of carriers with thickness is continuous, with a critical exponent for σ of 1 [66]. When thinking about the redox defects proposed in Ref. [66], an assumption of non-interacting defects suggests a drastically discontinuous transition, switching on directly to $\sigma \sim P_s$ [79], P_s being the polar discontinuity, half an electron per primitive unit cell surface area for LAO/STO; when it becomes favorable for one vacancy-carrier pair to form, it is favorable for all of them to form, giving the mentioned discontinuity at d_c. One can go beyond the mean-field level by considering the interactions between the traps [88]. The vacancy at the surface and carrier at the interface act like a dipole, and thus there would be dipole-dipole interactions between the vacancies. This predicts a transition which is still continuous, but with a critical exponent of $\frac{2}{3}$. The different predictions for the behavior of σ with film thickness are illustrated in Fig. 1.5.

Something that has to our knowledge not yet been considered is the influence of other phase transitions, such as tilting, which both LAO and STO can exhibit. As mentioned previously, tilts compete with the polar mode, so it is reasonable to expect that they may indirectly interact with the carriers, which appear to screen the polar discontinuity. The competition between tilts and the polar mode in LAO/STO has been considered in a previous study [89], although not in the context of the appearance of carriers.

1.2 Ferroelectric Thin Films and Superlattices

1.2.1 Electrostatics

The formation of ferromagnetic [32, 90–92] and ferroelectric [33, 30] domain structures in thin films is a well-known phenomenon. Polydomain structures appear in ferroelectric thin films in order to screen the electric depolarizing field arising at the interfaces between the surfaces of the thin film and its environment, such as vacuum or a non-metallic substrate
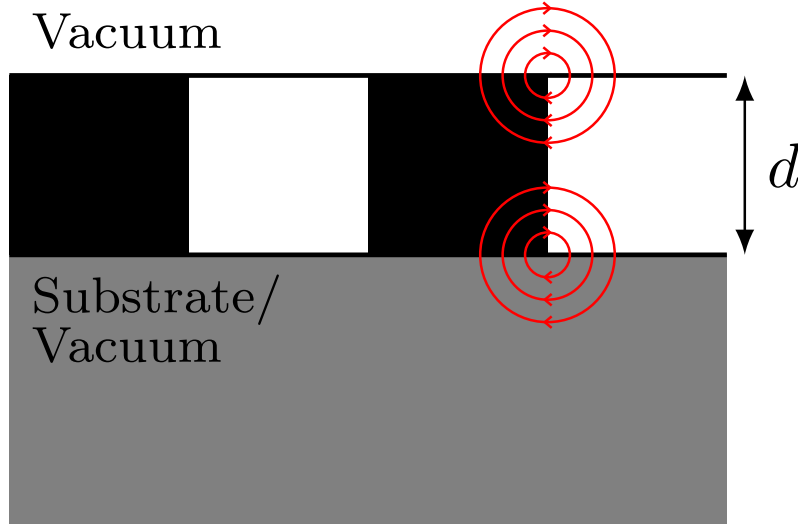
Fig. 1.6 Sketch of a ferroelectric thin film of thickness d with a 180° stripe domain structure. The red lines represent the electrostatic depolarizing field, which bend around the interfaces and domain walls.

(see Fig. 1.6). The electrostatic description of an isolated ferroelectric thin film in an infinite vacuum has been studied in detail [30, 31]. The equilibrium domain width w follows Kittel's law: $w \propto \sqrt{d}$ when $w \ll d$, d being the film thickness. Within the same model but making no approximations on the electrostatics arising from an ideal, regular polydomain structure, for $w \gtrsim d$, w reaches a minimum and grows again with decreasing d, until the monodomain phase is reached [30, 31]. A similar effect was first predicted and observed in ferromagnetic thin films [93–96]. This description of an isolated thin film, however, does not describe the effect that the surrounding environment has on the electrostatics of the thin film and hence the domain structure.

It is now possible to fabricate ferromagnetic and ferroelectric samples by growing alternating layers of different thin films, just a few unit cells in thickness, in a periodic array (superlattice) [97–99]. Alternating between ferroelectric and paraelectric layers (FE/PE superlattice, see Fig. 1.7), a great deal of control over the superlattice's properties can be achieved by changing the relative thicknesses of the layers [100–103]. This has generated interest in the study of FE/PE superlattices from the theoretical [104, 105] and computational [106] perspectives.

The dependence of the domain structure on superlattice geometry cannot be described using the theory of a thin film in an infinite vacuum, however. Some generalizations have appeared in the literature which include the effects of surrounding materials [107, 107–113, 104]. For a free-standing thin film on a substrate, it was claimed that the electrostatic description is the same as for a thin film of half the width sandwiched between two paraelectric media
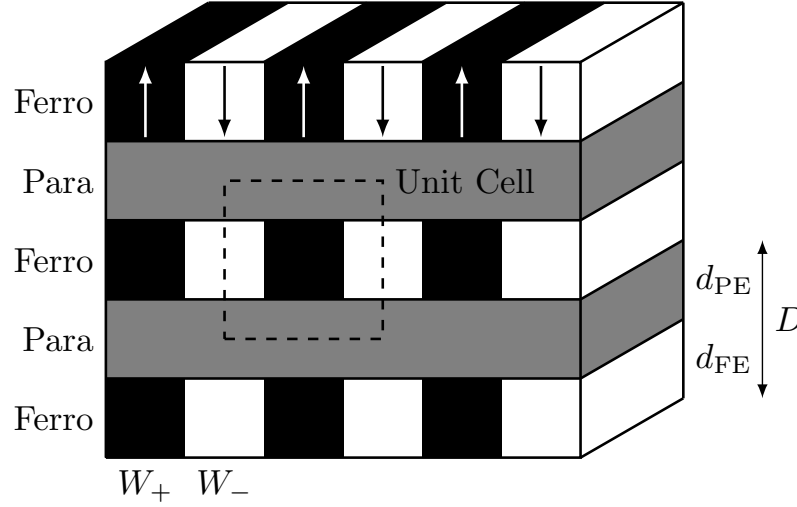
Fig. 1.7 Geometry of a FE/PE periodic superlattice. The unit cell is indicated by the dashed square. The thicknesses of the layers are indicated on the right and W_+ and W_- are the widths of the positive and negative polarization domains. In polydomain limit, these widths are equal: $W_+ = W_- = w$. The ferroelectric and paraelectric layers have thicknesses d_{FE} and d_{PE}, respectively, and the thickness of the unit cell is $D = d_{FE} + d_{PE}$.

[107]. This has been used to fit measurements of ferroelectric domains [114, 115], but a free-standing film on a substrate was never studied explicitly.

By placing a ferroelectric thin film together with a paraelectric layer between two short circuited capacitor plates, it was found that the domain structure could be controlled by tuning the properties of the paraelectric layer, and the stability of the ferroelectric film could be improved [108–113]. This system is to some extent equivalent to a FE/PE superlattice since the capacitor plates impose periodic electrostatic boundary conditions.

Although ferroelectric thin films have been frequently simulated from first principles in different settings and environments [116–121], ferroelectric domains are quite demanding to simulate from first principles, as they require much larger supercells. Recent developments in effective model building from first-principles calculations (second-principles methods) make it possible to study very large systems, including large domain structures in ferroelectric materials [122–130] and observe interesting related effects such as negative capacitance [131] and polar skyrmions [132]. These scientific advances, both experimental and computational, have motivated us to revisit the electrostatic description of ferroelectric domains.

The continuum electrostatic description of a monodomain ferroelectric thin film is essentially unaffected by a dielectric environment of the film. This is because there is zero field outside

the thin film and hence these regions make no contributions to the electrostatic energy. For a polydomain ferroelectric thin film, the domain structure introduces stray electric fields into the regions outside the film, see Fig. 1.6. We expect different behavior if we replaced the vacuum regions with a dielectric medium. Understanding the effect of more general geometries on the electrostatic description of ferroelectric thin films not only gives an insight into how the surrounding dielectric media contribute to the screening of the depolarizing field, but also allows us to understand the behavior of the domain structure of the film in different environments, bringing us closer to a realistic description of a thin film.

1.2.2 Appearance of carriers at ferroelectric interfaces

As mentioned in the previous section, interesting effects can occur at interfaces between different materials such as the formation of a 2DEG at polar-nonpolar interfaces. It is thought that the 2DEG appears to screen the polar discontinuity at the LAO/STO interface [66], and similarly, it has recently been proposed as a mechanism to screen the depolarizing field at FE/PE interfaces [133, 116]. This has proven difficult to directly observe experimentally, and indirect evidence for 2DEG formation at FE/PE interfaces has only very recently been found [134–136].

The difficulty in experimentally observing 2DEG formation at ferroelectric-insulator interfaces is most likely due to competition with ferroelectric domains. In LAO/STO, the polar discontinuity arises due to the different formal polarization lattices of the two materials. If the polar material is replaced with a ferroelectric one, the polar discontinuity is caused by the spontaneous polarization of the film. This is a well-known problem, and as already discussed, ferroelectric materials can form polydomain structures in order to mitigate depolarization effects. If ferroelectric systems can already screen polar discontinuities by the formation of domains, it is unclear when, or if at all, it would be more favorable to screen via the formation of a 2DEG instead.

In Ref. [133], a model of a monodomain ferroelectric film sustained by a 2DEG generated via oxygen vacancies was compared against a polydomain film with no 2DEG, following Kittel's law. It was found that for thinner films, the polydomain phase with no 2DEG was more energetically favorable. However, above a crossover thickness (4.6 nm for PTO), the monodomain phase sustained by a 2DEG became energetically favorable. This suggests that, with increasing film thickness, the domain width follows Kittel's law until a crossover

thickness where a 2DEG appears. With the polar discontinuity screened by the carriers, there is no need for a polydomain structure, and the film abruptly adopts a monodomain phase. This suggests that experimental measurements of domain widths in ferroelectric materials may serve as a signal for 2DEG formation: if a deviation from Kittel's law is observed, it may indicate that interfacial carriers have formed and are screening the polar discontinuity.

The competition-based comparison between monodomain (with a 2DEG) and polydomain phases suggests that an abrupt transition between the two should occur at a critical thickness. However, this does not agree with experimental observations. In fact, evidence for 2DEG formation has been observed in thin films of $BiFeO_3$ grown on TbScO3, coexisting with a $109°$ ferroelectric domain structure [134]. In addition, recent measurements of domain widths in PTO/STO superlattices have shown a continuous deviation from Kittel's law above a critical thickness[1]. Both of these observations indicate that the crossover between monodomain and polydomain phases may actually be continuous, with both effects coexisting and simultaneously screening the polar discontinuity. Of course, by comparing the free energies of the polydomain and monodomain phases separately, we can only predict that either one or the other will more energetically favorable. In order to describe the aforementioned experimental observations, a more general model in which it is possible for both effects to coexist is needed.

1.3   Polarization in 2D materials

1.3.1   Flexoelectricity in nanotubes

The polar response to an inhomogeneous strain, known as flexoelectricity, is a property of all insulators and was predicted in the late 1950s [137, 138], with theoretical descriptions following shortly afterwards [139–142]. The components of the polar response P to the gradient of a strain σ are

$$P_i = \mu_{ijkl}\partial_l\sigma_{jk} \tag{1.4}$$

where $\partial_l \equiv \frac{\partial}{\partial x_l}$ and

---

[1]Matthew Dawber, private communication

$$\mu_{ijkl} = \frac{\partial P_i}{\partial(\partial_l \sigma_{jk})} \tag{1.5}$$

is the flexoelectric tensor. Unlike the more well-known piezoelectricity, the polar response to an homogeneous strain, flexoelectricity can be observed in materials that are centrosymmetric, because a strain gradient will always locally break centrosymmetry. This is illustrated in Fig. 1.8. Understanding the electromechanical properties of solids such as piezoelectric and flexoelectric responses is important for their practical application in technology.
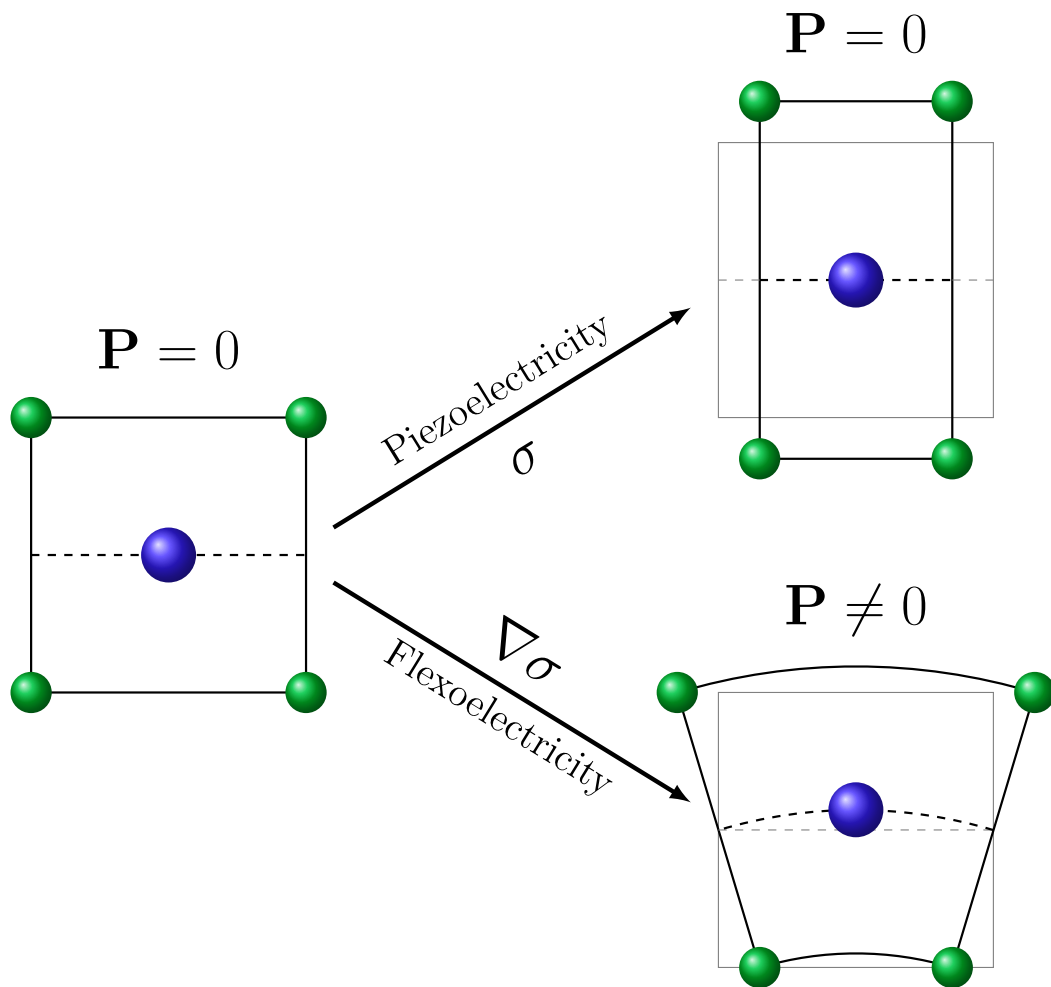
Fig. 1.8 Sketch of applying a strain and strain gradient to a centrosymmetric material. When a strain is applied, the centrosymmetry is preserved, so no polarization is induced. An additional symmetry breaking is required for a piezoelectric response. When a strain gradient is applied, the centrosymmetry is always broken, leading to a flexoelectric response.

Flexoelectricity is not as widely-known or applied as piezoelectricity, likely for two reasons. Firstly, it is a more complex phenomenon than piezoelectricity. Significant progress on the de-

velopment of theoretical descriptions of flexoelectricity has been made in the last few decades, however [143–151]. Significant progress has also been made on first-principles descriptions of flexoelectricity, including density functional theory [152], effective modeling [153], and, perhaps most successfully, density functional perturbation theory [147–151]. Some aspects were not well understood, such as the distinction between surface and bulk effects [144, 154]. The components of the flexoelectric tensor, i.e. the flexoelectric coefficients, are also difficult to calculate, and consistent results remained elusive [155, 143, 152] until recently [154, 150, 151]. The second reason is that flexoelectricity is a size dependent effect, which scales as e/a, where e is the electron charge and a is the system size [141, 142, 156–158]. In bulk-like systems it is typically negligible in comparison to piezoelectricity.

While the second reason seems to suggest that it may not a very significant or useful effect, it actually implies that flexoelectricity would be most prominent and have the greatest potential for applications in nanoscale systems, such as thin films and 2D materials [159–163, 155]; it has been suggested that flexoelectricity could be utilized in electromechanical devices [164], as well as for energy and information technology [165–167]. It has also been found that flexoelectricity plays a role in the bending and vibration of piezoelectric nanobeams [168, 169]. In addition to solid devices, the study of flexoelectricity in liquid and biological systems is an active field of research, and plays a significant role in liquid crystals and biological membranes, for example [170–176]. There are many comprehensive reviews in the literature, both general [177–181] and more focused on 2D and biological systems [182–185, 171, 170].

While flexoelectricity is a property of all insulators, calculations are typically restricted to cubic crystals such as STO, since the number of independent flexoelectric coefficients reduces to 3. This is unfortunate, because as mentioned above flexoelectricity has the most potential in low-dimensional systems, not bulk. Flexoelectric effects have been studied and observed in graphene and graphene based nanostructures [186–191], as well as in TMD monolayers [192–195].

The effects of flexoelectricity in 1D structures i.e. nanotubes (NTs) is not as well known, however. In addition to carbon nanotubes (CNTs), it is also possible to fabricate transition metal dichalcogenide nanotubes (TMD NTs) from monolayers such as WS_2 [196], MoS_2 [197], etc. Although not as widely studied and used as CNTs, structural and electronic properties of TMD NTs have been investigated using first-principles calculations [198–201, 201]. To our knowledge, the role of flexoelectricity in TMD NTs has not been investigated.

$$\vec{P}_R = P_{\text{flex}}\hat{r}$$
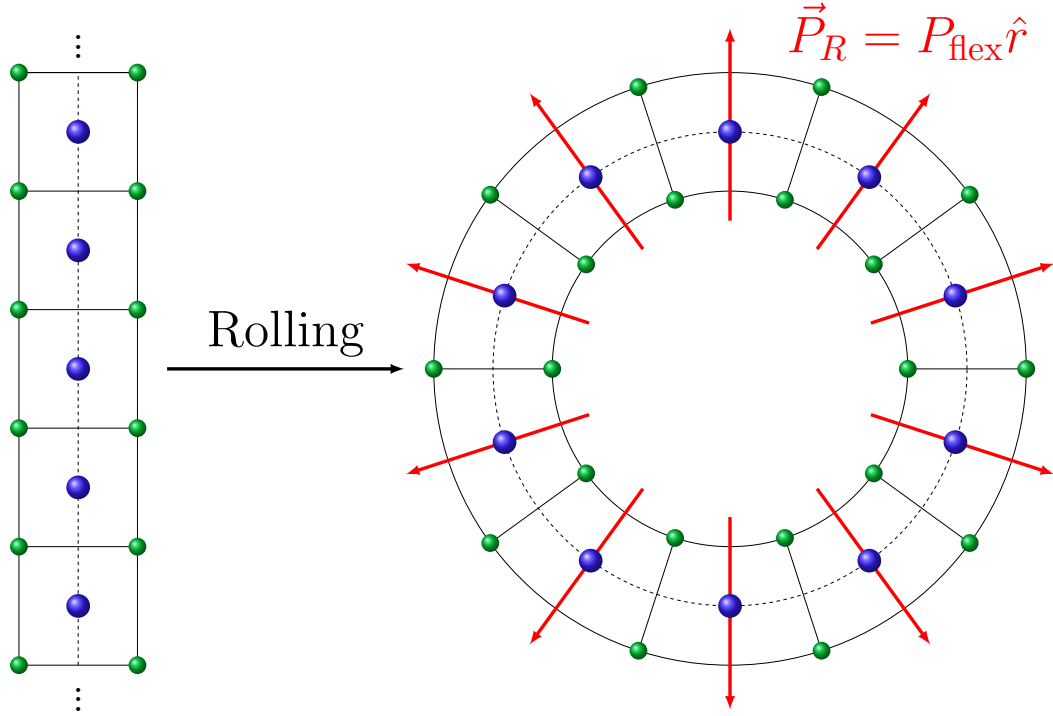
Fig. 1.9 Illustration of the polarization induced by rolling a 2D monolayer into a NT. There is a strain gradient in each unit cell around the wall of the NT with respect to the geometry of the monolayer, and hence a radial polarization P_{flex} via flexoelectricity.

The effect of flexoelectricity on electronic and optical properties of single- and double-wall CNTs has been investigated very recently, however [202].

If a NT is formed by rolling a 2D layer of finite thickness, there would be a difference in strain between the inside and outside of the wall. Hence we would expect the wall of the NT to have a finite polarization around the wall in the radial direction in response to this difference in strain, see Fig. 1.9. We would naturally expect this effect to occur in TMD NTs since the walls are three atoms thick. In fact, we would still expect this to occur in CNTs, but it would be a purely electronic effect in this case and may be much weaker.

1.3.2 Twistronics

Perhaps the most exciting advancement in the study of 2D materials in recent years is the establishment of the field of twistronics [203], the study of layered systems where a relative twist angle or lattice mismatch between the layers is introduced. This leads to an interference

$$\theta = 0° \qquad \theta = 5°$$

$$\theta = 9° \qquad \theta = 13°$$
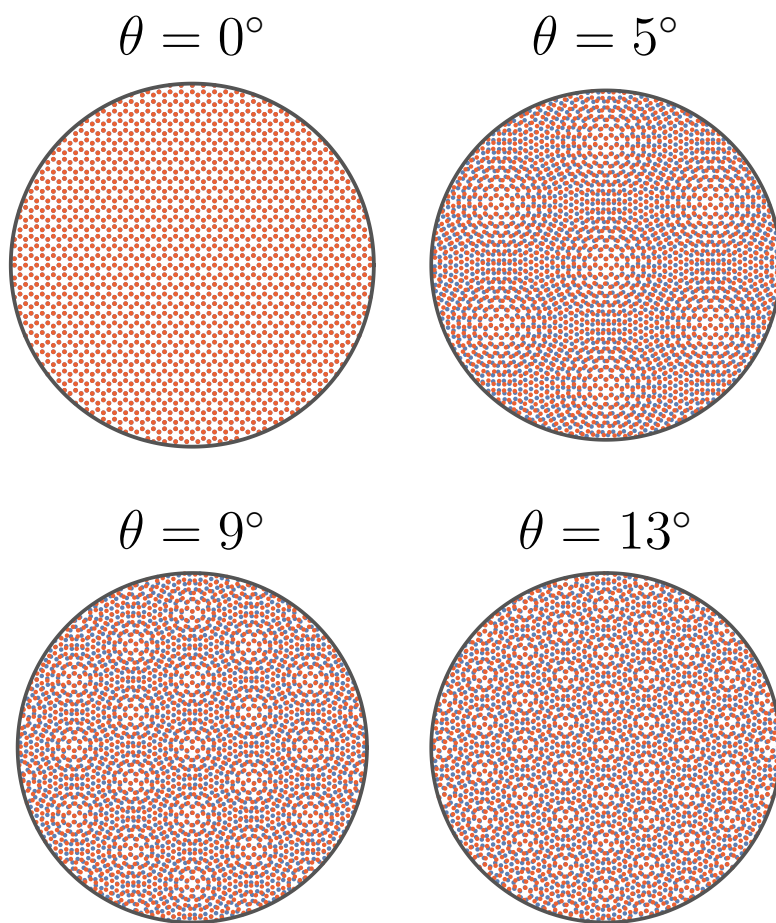
Fig. 1.10 Atomic structure of a 2D bilayer system at various twist angles. The first panel shows a twist angle of $0°$, i.e. the two layers (red and blue) are perfectly aligned. The next three panels show different non-zero twist angles. We can see that an interference pattern (moiré superlattice) forms, the period of which is sensitive to the magnitude of the twist angle.

pattern known as a moiré superlattice (see Fig. 1.10), which changes the properties of the system and is sensitive to the twist angle and degree of lattice mismatch.

It was predicted about a decade ago that introducing a small relative twist in a layered system such as bilayer graphene could lead to flat electronic bands, and strongly correlated behavior [204, 205]. Moiré superlattices have since been shown to exhibit superconductivity [206, 207], metal-insulator transitions [208], as well as magnetic [209], topological [210–213] and excitonic [214, 215] behavior, facilitated by the tuning of the twist angle or lattice mismatch. Recently, ferroelectricity was observed in bilayer graphene [216] and hexagonal boron nitride (hBN) [217], which is highly unusual, because the constituent materials are non-polar, and bilayer graphene is normally metallic. The ferroelectricity was found to be
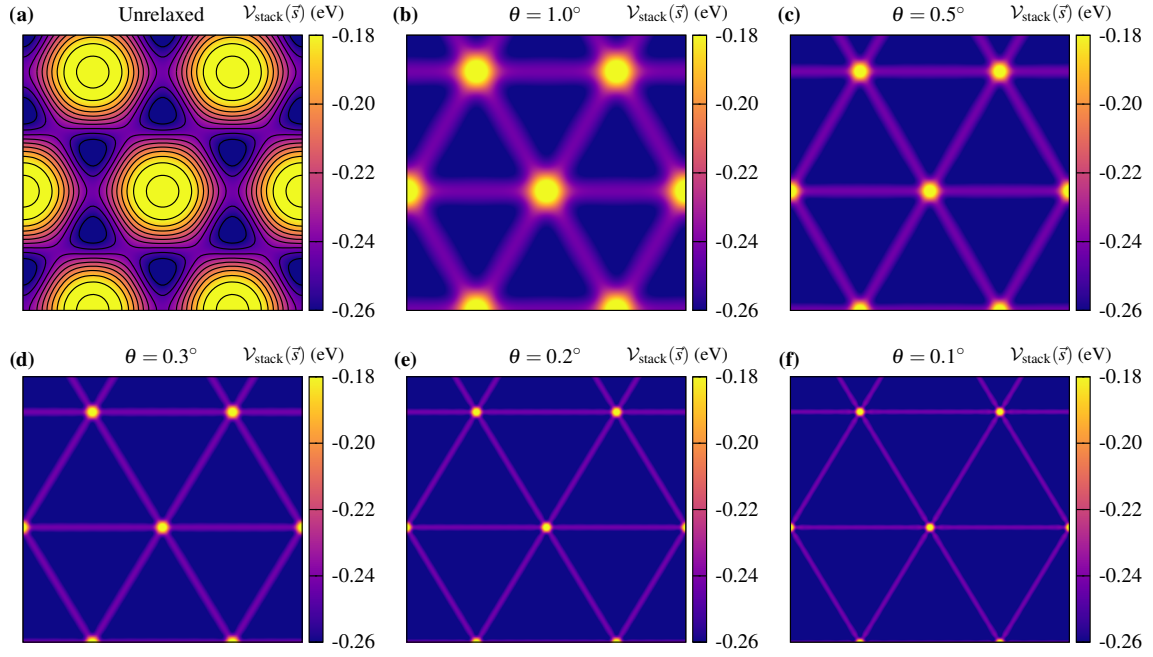
Fig. 1.11 Illustration of lattice relaxation as a function of twist angle. **(a)**: stacking energy of bilayer MoS$_2$ in configuration space without lattice relaxation. **(b)-(f)**: stacking energy after lattice relaxation for decreasing twist angles.

sensitive to the twist angle and lattice mismatch, with some samples exhibiting no hysteresis and some exhibiting strong hysteresis. The ferroelectricity is clearly very unconventional, and the physical mechanism is currently not well understood.

Structural phenomena in moiré superlattices are generally well understood. It is known that the interlayer separation ripples in space due to the local misalignment of the atoms, which can influence physical properties [218, 219]. Additionally, lattice relaxation occurs due to the competition between the in-plane strains and out-of-plane van der Waals interactions, leading to the formation of stacking domains [220–226], see Fig. 1.11. The elastic energy depends on the twist angle and lattice mismatch quadratically [223], meaning the domains can be tuned. The domain structures have been shown to have a large influence on the properties of the system [227–229, 220, 221, 203, 222], leading to the opening of band gaps and enhanced Fermi velocity, for example. Polar effects have been given less consideration because the typical materials use to fabricate moiré superlattices, graphene, hBN and TMDs such as MoS$_2$, are non-polar.

There are two main mechanisms by which polar phenomena could manifest in moiré systems. The first is a local spontaneous out-of-plane polarization [230], which occurs in bilayers

without centrosymmetry and averages to zero over the moiré period. The second is the couplings between strain and polarization mentioned previously, namely piezoelectricity [231–233] and flexoelectricity [231]. The strain gradient is largest across the domain walls, and via flexoelectricity, they have an inherent polarization. The flexoelectric response in 2D materials can be estimated by measuring the potential drop across the wall of a nanotube in the large radius limit [154, 231, 202, 234], and it has been estimated that the flexoelectric coefficients in bilayer graphene is similar in magnitude to the clamped-ion flexoelectric response in oxide perovskites [231, 154, 149]. The flexoelectric polarization is localized within the relatively narrow domain walls, however.

If we identify the stacking domains as polar domains via the two aforementioned mechanisms, then the stacking domains may serve as the basis for understanding polar phenomena in moiré materials. Thus, in order to understand the observed ferroelectricity, it is essential to understand how the stacking domains respond to an electric field. It is known that the domain structures in moiré materials can lead to interesting effects such as the opening of band gaps and topologically protected states or channels when an electric field is applied [235, 210–212, 236]. To our knowledge, the influence of an applied electric field on the domains themselves has not been considered. It is known that an electric field can modify the interlayer separation and lead to a breakdown of TMD bilayers, for example [237, 238]. The stacking domains are a result of lattice relaxation, which describes the delicate competition between the interlayer interactions and the intralayer elasticity. Since the interlayer interactions are sensitive to an applied field, it is reasonable to expect that the field would change the delicate balance and affect the resulting domain structure.

1.4 Summary

A brief summary of the layout of this thesis is given below.

In Chapter 2, we provide a brief overview density functional theory, and the main approximations used in typical first-principles calculations, the main computational method to supplement the theoretical models developed in this thesis.

In Chapter 3 we generalize the phenomenological model of carrier formation at polar-nonpolar perovskite interfaces to account for coupling with tilts in the thin film. We show that, upon coupling to homogeneous tilts, four new distinct types of transitions are possible,

depending only on the energetics of the tilts, polar discontinuity and the coupling between them, regardless of whether the transition occurs with film thickness or an applied electric field. These include continuous and discontinuous transitions of the carriers, facilitated by the tilts, and both simultaneous and distinct transitions of tilts and carriers. Using first principles calculations, we can make predictions about the type of transition which occurs at the LAO/STO interface.

In Chapter 4, we generalize the model developed in Chapter 3 to allow for inhomogeneous tilts in the polar thin film, using Ginzburg-Landau theory. The inhomogeneity of the tilts is determined by the correlation length in the film and the extrapolation lengths, which describe the relative energy differences between the tilts in the interior and at the surfaces. We show that two of the transitions predicted in Chapter 3 are unaffected by the inhomogeneity of the tilts, other than the values at which the transitions occur being renormalized. For the other two transitions, their character can be changed by decreasing the correlation length, leading to two entirely new types of transitions which are not possible for homogeneous tilts. Motivated by experimental [89] and first-principles measurements of tilts in LAO/STO, we also consider additional types of couplings beyond the biquadratic coupling with the polar mode, namely the direct bilinear coupling between oxygen vacancies and the tilt at the surface. We show that this coupling implies that the appearance of carriers will always result in a surface tilt, which can propagate into the thin film and possibly the substrate. Including this direct coupling, we predict that very thin films, down to 3 unit cells, exhibit a small tilt in the presence of carriers, where an untilted phase is predicted when only considering the biquadratic coupling, rationalizing results from first-principles calculations.

In Chapter 5, we first review the continuum model of an isolated ferroelectric thin film in a vacuum (IF) with the full treatment of the electrostatics and a domain wall term. We then generalize the theory for three different systems: a thin film on an infinite substrate (overlayer, OL), a thin film sandwiched between two infinite dielectric media (SW), and a FE/PE superlattice (SL). We keep the prevalent nomenclature in the literature of referring to a spacer material such as STO as paraelectric, but the description will be exclusively that of a dielectric material with a given isotropic dielectric permittivity. All of these systems except the OL have appeared in the literature in various contexts and with different levels of detail. We compare the different cases, first in the Kittel limit ($w \ll d$), for which analytic expressions are obtained for $w(d)$, and also in the general situation. Previous studies of periodic superlattices have assumed ferroelectric and paraelectric layers of equal width. Here

we provide a more general study of domain structures as a function of superlattice geometry. We also present a detailed derivation of the electrostatic energies.

In Chapter 6, we introduce a model which addresses and explains the observed coexistence between ferroelectric domains and 2DEG formation at ferroelectric-insulator interfaces. After reviewing the competition-based theory between a monodomain ferroelectric film with a 2DEG and a polydomain film with no 2DEG, we introduce a model which allows for the possibility of both domains and a 2DEG. The thin and thick film limits agree with the previous competition-based study [133], in which the polydomain and monodomain phases are realized respectively, but we show that the two regimes are separated by a region of coexistence where both effects are observed simultaneously.

In Chapter 7 we demonstrate using first-principles calculations that the walls of CNTs and TMD NTs are polarized in the radial direction, the strength of the polarization increasing as the size of the NT decreases. This is reminiscent of a flexoelectric response in bulk insulators, the strain gradient being achieved by bending the 2D monolayers into NTs. For CNTs and TMD NTs with chiral indices (n, m), the radial polarization of the walls P_R diverges below $C(n, m)/a = \sqrt{n^2 + nm + m^2} \sim 10$, where $C(n, m)$ is the circumference and a is the monolayer lattice constant. For CNTs, P_R drops to zero above this value but for TMD NTs there is a non-zero polarization, which is ionic rather than electronic. The size dependence of P_R in the TMD NTs is interesting: it increases gradually and reaches a maximum of $P_R \sim 100$ C/cm^2 at $C(n, m)/a \sim 15$, then decreases until $C(n, m)/a \sim 10$ where it starts to diverge. Measurements of the radial strain on the bonds with respect to the monolayers shows that this polarization is the result of a larger strain on the outer bonds than the inner bonds, but did not explain the peculiar size dependence. These results suggest that while the walls of smaller CNTs and TMD NTs are polarized, the walls of larger TMD NTs are also polarized due to a difference in strain on the inner and outer bonds.

In Chapter 8, we propose a theoretical model which captures the effect of an applied electric field on the domain structure in moiré superlattices. The coupling between the spontaneous polarization and field leads to uneven relaxation of the domains, and a net polarization in the superlattice at nonzero fields, which is sensitive to the moiré period. We also show that the dielectric response to the field reduces the stacking energy and leads to softer domains in all bilayers. Finally, we discuss the recent observations of ferroelectricity in the context of our model.

Chapter 2

Density functional theory

Density functional theory (DFT) [239, 240] is probably the most widely used and successful method for describing the physical properties of solids. In order to obtain a quantum mechanical description of a system of electrons and nuclei, the total energy must be obtained and minimized with respect to the electronic and nuclear coordinates. This requires the treatment of a complex quantum many-body system of interacting electrons and nuclei which cannot be done analytically, and for realistic systems is too computationally demanding to be done numerically. Fortunately, we can make use of some invaluable theorems from DFT and other useful approximations to make quantum mechanical total energy calculations feasible.

There are large specialized communities dedicated to developing and improving the methods which make DFT calculations efficient and accurate. The broader communities of condensed matter physicists, solid-state chemists and materials scientists are not exclusively dedicated to this purpose, but rather using DFT calculations to supplement their theoretical or experimental research by helping them understand the properties of a wide range of systems. The work presented in this thesis falls under this category: we mainly used DFT calculations as a tool to parameterize the theoretical models we developed, and also verify that they give sensible results. Thus, in this chapter we provide a general overview of DFT and the approximations used in a realistic DFT calculation, with no aim to be exhaustive. For that purpose, there already exists many excellent reviews [241–244].

The Hamiltonian for a system of interacting electrons and nuclei in atomic mass units ($m_e = \hbar = e = 1$) is

$$\hat{H} = -\frac{1}{2}\sum_{\mu}\frac{1}{M_{\mu}}\nabla_{\mu}^2 - \frac{1}{2}\sum_i \nabla_i^2 - \sum_{i,\mu}\frac{Z_{\mu}}{r_{i\mu}} + \frac{1}{2}\sum_{i \neq j}\frac{1}{r_{ij}} + \frac{1}{2}\sum_{\nu \neq \mu}\frac{Z_{\nu}Z_{\mu}}{R_{\nu\mu}} , \tag{2.1}$$

where μ, ν are used for nuclei and i, j are used for electrons. The first two sums contain the kinetic energy operators of the nuclei and electrons, respectively, where M is the mass of the nuclei. The third sum describes the Coulomb interactions between the electrons and nuclei, where Z_{μ} is the atomic number of the nuclei, and $r_{i\mu} = |\mathbf{r}_i - \mathbf{R}_{\mu}|$ is the distance between an electron at $\mathbf{r}_i$ and a nucleus at $\mathbf{R}_{\mu}$. The last two sums describe the Coulomb repulsion between the electrons and nuclei respectively, both of which have a factor of $\frac{1}{2}$ to avoid double counting.

The many-body wavefunction of an electronic system with n_e electrons and N nuclei is

$$\psi(\mathbf{r}_1,\ldots,\mathbf{r}_{n_e},\mathbf{R}_1,\ldots,\mathbf{R}_N) , \tag{2.2}$$

which is obtained by solving the Schrödinger equation: $\hat{H}\psi = E\psi$. The probability of finding the system in a given configuration is

$$P = |\psi|^2 = \psi^*\psi , \tag{2.3}$$

and the probability of finding the first electron at position r is

$$P(\mathbf{r}_1 = \mathbf{r}) = \int |\psi(\mathbf{r},\mathbf{r}_2,\ldots,\mathbf{R}_N)|^2 \, d\mathbf{r}_2 \ldots d\mathbf{R}_N . \tag{2.4}$$

Thus, the probability of finding any electron at position r is

$$n(\mathbf{r}) = \sum_i P(\mathbf{r}_i = \mathbf{r}) = \int |\psi(\mathbf{r},\mathbf{r}_2,\ldots,\mathbf{R}_N)|^2 \, d\mathbf{r}_2 \ldots \ldots d\mathbf{R}_N , \tag{2.5}$$

which is normalizable,

$$\int n(\mathbf{r}) \, d\mathbf{r} = n_e , \tag{2.6}$$

i.e. if we look everywhere, we should find all of the electrons. Of course, solving the Schrödinger equation and obtaining an $n_e + N$ dimensional wavefunction is difficult even for small n_e and N, and practically impossible when they are very large. If we are to have any chance of obtaining a quantum mechanical description of a realistic system, we will need to make a few approximations.

2.0.1 Born-Oppenheimer Approximation

Because of the large difference in mass between the electrons and nuclei ($M \sim 1836m_e$), it is reasonable to assume that the nuclei are fixed with respect to the electrons. This is known as the clamped nuclei approximation. Under this approximation, the kinetic energy of the nuclei is zero, and the Coulomb energy is constant. Thus, we can write the electronic Hamiltonian with respect to a set of fixed nuclear coordinates $\{\mathbf{R}_\mu\}$:

$$\hat{H}^{\text{el}}_{\mathbf{R}_\mu} = -\frac{1}{2}\sum_i \nabla^2_i + \frac{1}{2}\sum_{i \neq j}\frac{1}{r_{ij}} + V^{\text{ext}}_{\mathbf{R}_\mu}(\{\mathbf{r}_i\}) \ , \tag{2.7}$$

where $V^{\text{ext}}_{\mathbf{R}_\mu}(\{\mathbf{r}_i\})$ is effectively the external potential felt by the electrons due to the nuclei. We then proceed to solve the Schrödinger equation for the electronic Hamiltonian of each configuration. For the nuclear problem, we replace the electronic terms in Eq. (2.1) with the resulting electronic ground state energy:

$$\hat{H}^{\text{n}} = -\frac{1}{2}\sum_\mu \frac{1}{M_\mu}\nabla^2_\mu + E^{\text{el}}_0\left(\{\mathbf{R}_\mu\}\right) \ , \tag{2.8}$$

which can be thought of as the effective potential felt by the nuclei due to the electrons.

Thus, we have obtained a separation of the electronic and nuclear Hamiltonians, and hence wavefunctions, reducing the complexity of the problem by a great deal, starting from the simple fact that the nuclei are much heavier than the electrons. This is known as the Born-Oppenheimer approximation [245].

2.0.2 Hartree and Hartree-Fock equations

Even after having simplified the problem with the Born-Oppenheimer approximation, the many-body problem is still difficult because of the electron-electron interactions. In an attempt to simplify things, we can write the total electronic Hamiltonian as a sum of single-electron Hamiltonians plus the electron-electron interactions:

$$
\begin{aligned}
\hat{H}^{\text{el}} &= \sum_i \hat{h}_i + \frac{1}{2} \sum_{j \neq i} \frac{1}{r_{ij}} \\
\hat{h}_i &= -\frac{1}{2} \nabla_i^2 + V^{\text{ext}}(\mathbf{r}_i)
\end{aligned}
\tag{2.9}
$$

If we ignore the electron-electron interactions, we obtain a set of single electron Schrödinger equations which can be solved independently:

$$
\hat{h}_i \phi_{in} = \varepsilon_{in} \phi_{in} ,
\tag{2.10}
$$

where n is the energy level. Having solved the single-electron equations, we can build a many-body wavefunction from the single-electron wavefunctions:

$$
\psi_n = \prod_i \phi_{in}(\mathbf{r}_i) .
\tag{2.11}
$$

Thus,

$$
\begin{aligned}
\hat{H} \psi_n &= E_n \psi_n \\
E_n &= \sum_i \varepsilon_{in}
\end{aligned}
\tag{2.12}
$$

This is a very crude approximation because it violates the Pauli exclusion principle and ignores electron-electron interactions.

Since electrons are fermions, the electronic wavefunction must be skew-symmetric under particle exchange. This is known as the Pauli exclusion principle. A system of indistinguishable particles is invariant under any relabeling:

$$P(\sigma\{\mathbf{r}_i\}) = P(\{\mathbf{r}_i\})$$
$$\implies \psi(\sigma\{\mathbf{r}_i\}) = s\psi(\{\mathbf{r}_i\}) \tag{2.13}$$

where σ is some permutation, and $|s|^2 = 1$. An obvious choice is $s = \pm 1$, where $s = +1$ is for bosons and $s = -1$ is for fermions. Clearly, the independent electron wavefunction is not skew-symmetric, but we can use single electron wavefunctions to build one that is. When $n_e = 2$, for example,

$$\psi(\mathbf{r}_1, \mathbf{r}_2) = \frac{1}{\sqrt{2}}(\phi_1(\mathbf{r}_1)\phi_2(\mathbf{r}_2) - \phi_2(\mathbf{r}_1)\phi_1(\mathbf{r}_2)) = \frac{1}{\sqrt{2}}\begin{bmatrix} \phi_1(\mathbf{r}_1) & \phi_1(\mathbf{r}_2) \\ \phi_2(\mathbf{r}_1) & \phi_2(\mathbf{r}_2) \end{bmatrix} \tag{2.14}$$

satisfies the Pauli exclusion principle. In general, this is known as a Slater determinant,

$$\psi(\{\mathbf{r}_i\}) \equiv \frac{1}{\sqrt{n_e!}}||\phi_1 \ldots \phi_{n_e}|| = \frac{1}{\sqrt{n_e!}}\begin{bmatrix} \phi_1(\mathbf{r}_1) & \cdots & \phi_{n_e}(\mathbf{r}_1) \\ \vdots & \ddots & \vdots \\ \phi_1(\mathbf{r}_{n_e}) & \cdots & \phi_{n_e}(\mathbf{r}_{n_e}) \end{bmatrix}, \tag{2.15}$$

which is skew-symmetric under the exchange of any pair of electrons.

Perhaps the simplest way to reintroduce the electron-electron interactions is using mean-field theory, i.e. every electron feels the average electronic Coulomb potential. This is known as the Hartree method. From Poisson's equation, the electronic charge distribution generates a potential, which we call the Hartree potential, V^H:

$$\nabla^2 V^H(\mathbf{r}) = -4\pi n(\mathbf{r})$$
$$\implies V^H(\mathbf{r}) = \int d\mathbf{r}' \frac{n(\mathbf{r})}{|\mathbf{r} - \mathbf{r}'|} . \tag{2.16}$$

Next we add the average Hartree potential to each single-electron hamiltonian:

$$\hat{h}_i = -\frac{1}{2}\nabla_i^2 + V_{\mathbf{R}_\mu}^{\text{ext}}(\mathbf{r}_i) + V^{\text{H}}(\mathbf{r}_i) \, , \qquad (2.17)$$

and the system is described by the solutions to a set of self-consistent equations:

$$\begin{aligned} \hat{h}_i\phi_i &= \varepsilon_i\phi_i \\ n(\mathbf{r}) &= \sum_j |\psi_j(\mathbf{r})|^2 \\ \nabla^2 V^{\text{H}}(\mathbf{r}) &= -4\pi n(r) \end{aligned} \qquad (2.18)$$

We can account for exchange by using a Slater determinant for the many-body wavefunction. Then we obtain the Hartree-Fock equations:

$$\begin{aligned} \hat{h}_i\phi_i + \int V^{\text{x}}(\mathbf{r},\mathbf{r}')\phi_i(\mathbf{r}')\,\mathrm{d}\mathbf{r}' &= \varepsilon_i\phi_i \\ n(\mathbf{r}) &= \sum_j |\psi_j(\mathbf{r})|^2 \\ \nabla^2 V^{\text{H}}(\mathbf{r}) &= -4\pi n(\mathbf{r}) \end{aligned} \qquad , \qquad (2.19)$$

where

$$V^{\text{x}}(\mathbf{r},\mathbf{r}') = -\sum_j \frac{\phi_j^*(\mathbf{r}')\phi_j(\mathbf{r})}{|\mathbf{r}-\mathbf{r}'|} \qquad (2.20)$$

is the exchange potential, which arises from the Pauli exclusion principle and prevents self-interactions. The Hartree-Fock equations are an improvement on the Hartree equations, but the exchange potential is non-local, which makes them more difficult to solve.

2.0.3   Density Functional Theory

Hohenberg and Kohn proved that the total energy of an electron gas is a unique functional of the electronic charge density [239]. This means that the instead of trying to obtain the complex many-body wavefunction of a given system, we can consider the electron density as

the fundamental quantity of a system. The minimum value of the total energy functional is the exact ground state energy:

$$E[n(\mathbf{r})] \geq E^{\text{GS}}$$
$$E\left[n^{\text{GS}}(\mathbf{r})\right] = E^{\text{GS}} \,. \tag{2.21}$$

Writing the Hamiltonian as

$$\hat{H} = \underbrace{\hat{T} + V^{\text{e-e}}}_{\hat{F}=F[n]} + \sum_i V^{\text{ext}}(\mathbf{r}_i) \,, \tag{2.22}$$

and the external potential in terms of the density,

$$\sum_i V^{\text{ext}}(\mathbf{r}_i) = \sum_i \langle \psi | V^{\text{ext}}(\mathbf{r}_i) | \psi \rangle = \int \left(V^{\text{ext}}(\mathbf{r}) \sum_i \psi_i^* \psi_i \right) d\mathbf{r} = \int V^{\text{ext}}(\mathbf{r}) n(\mathbf{r}) \, d\mathbf{r} \,, \quad (2.23)$$

the energy functional is of the form

$$E[n(\mathbf{r})] = \int \left(V_{\text{ext}}(\mathbf{r}) n(\mathbf{r}) + F[n] \right) d\mathbf{r} \,. \tag{2.24}$$

The Hohenberg-Kohn theorem can be illustrated using Levy's construction [246]. We construct the functional F as

$$F[n] = \min_{|\psi\rangle \to n(\mathbf{r})} \langle \psi | \hat{F} | \psi \rangle \,, \tag{2.25}$$

i.e. it takes the minimal value with respect to all states ψ that give the density $n(\mathbf{r})$. For a system with external potential $V^{\text{ext}}(\mathbf{r})$, ground state $|\psi_0\rangle$ and energy E_0, consider a state $|\psi_{[n]}\rangle$ which gives the $n(r)$ that minimizes $F[n]$. Let

$$E^V[n] = F[n] + \int V^{\text{ext}}(\mathbf{r}) n(\mathbf{r}) \, d\mathbf{r} = \langle \psi_{[n]} | \hat{F} + V^{\text{ext}} | \psi_{[n]} \rangle \,. \tag{2.26}$$

Since $\hat{H} = \hat{F} + V_{\text{ext}}$, the variational principle gives

$$E^V[n] \geq E_0 \tag{2.27}$$

where the equality is true if and only if $|\psi_0\rangle = |\psi_{[n]}\rangle$. From the definition of of $F[n]$, we must have

$$F[n_0] \leq \langle \psi_0 | F | \psi_0 \rangle \tag{2.28}$$

because $F[n_0]$ will take the minimum with respect to all states that generate n_0. ψ_0 may give n_0, but it may not be the state that minimizes F. Adding V^{ext} to both sides, we get

$$E^V[n_0] \leq E_0 \tag{2.29}$$

Combining Eqs. (2.27) and (2.29), we must have

$$E^V[n_0] = E_0 \tag{2.30}$$

i.e. the ground state density gives the exact ground state energy. This almost seems trivial, but it illustrates that DFT is an exact theory, in theory.

The Hohenberg-Kohn theorem proves the existence of the energy as a functional of electronic density, but does not provide its explicit form. Kohn and Sham showed that it is possible to map the many-body problem onto another system of non-interacting particles moving in an external potential with the same ground state density [240]:

$$E[n] = \int V^{\text{ext}}(\mathbf{r})n(\mathbf{r})\,\mathrm{d}\mathbf{r} - \sum_i \int \phi_i^* \left(\frac{1}{2}\nabla_i^2\right) \phi_i\,\mathrm{d}\mathbf{r} \\ + \frac{1}{2} \int \int \frac{n(\mathbf{r})n(\mathbf{r}')}{|\mathbf{r} - \mathbf{r}'|}\,\mathrm{d}\mathbf{r}\,\mathrm{d}\mathbf{r}' + E^{\text{XC}}[n] \tag{2.31}$$

The first term is the external potential, the second is the kinetic energy of the electrons, the third is the Hartree potential and the last term contains the exchange and correlation energy functionals. The ground state density, $n_0(r)$ is the one that minimizes the total energy via the variational principle:

$$\left. \frac{\delta E[n]}{\delta n} \right|_{n_0} = 0 \, . \tag{2.32}$$

For orthonormal wavefunctions, this gives the Kohn-Sham equations,

$$\left(-\frac{1}{2} \nabla_i^2 + V^{\text{ext}} + V^{\text{H}} + V^{\text{XC}} \right) \phi_i(\mathbf{r}) = \varepsilon_i \phi_i(\mathbf{r})$$
$$V^{\text{XC}} = \frac{\delta E^{\text{XC}}}{\delta n} \tag{2.33}$$

The explicit form of the exchange-correlation potential remains unknown, but it can be efficiently approximated.

2.0.4 Approximate Exchange Correlation Functionals

The exchange-correlation energy is expected to be a universal functional of the density. However, the Hohenberg-Kohn theorem provides motivation for using approximations. The first and historically most widely used approximation is the local density approximation (LDA) [240]. It assumes i) that E^{XC} per particle at each point $\mathbf{r}$ only depends on the density and ii) that it is equal to the exchange-correlation energy per particle of a homogeneous electron gas of density $n(\mathbf{r})$ in a neutralizing background:

$$E_{\text{LDA}}^{\text{XC}} = \int \varepsilon_{\text{LDA}}^{\text{XC}}(\mathbf{r}) n(\mathbf{r}) \, d\mathbf{r}$$
$$\varepsilon_{\text{LDA}}^{\text{XC}}(\mathbf{r}) = \varepsilon_{\text{hom}}^{\text{XC}}[n(\mathbf{r})] \tag{2.34}$$

The form of $\varepsilon_{\text{hom}}^{\text{XC}}[n(\mathbf{r})]$ can be obtained from various sources. The exchange part can be obtained analytically from Hartree-Fock theory, where it can be shown that it scales like

$$\varepsilon_{\text{hom}}^{\text{XC}}[n(\mathbf{r})] \sim \frac{3}{4\pi} \left(3\pi^2 \right)^{1/3} n^{1/3} \, . \tag{2.35}$$

For the correlation part, Ceperly and Alder made approximations using Monte Carlo simulations of a homogeneous electron gas [247], and there are many other viable alternatives [248, 240, 249–251].

The LDA is probably the most crude approximation we could make, but it has the advantage of simplicity. It describes structural and dynamical properties of systems with surprising accuracy: calculated bond lengths and angles are usually within a few % of experiment, and phonon frequencies are usually within 5-10% [243, 252]. However, the LDA typically gives poor results for cohesive energies and dielectric susceptibilities.

There are many sophisticated techniques to go beyond LDA. A first alternative is to use a semi-local functional which also depends on the gradient of the density. Different forms have been proposed, which are known as generalized gradient approximations (GGA). They are based on a functional of the form [253, 254]

$$E_{\text{GGA}}^{\text{XC}}[n] = \int \varepsilon_{\text{GGA}}^{\text{XC}}[n(\mathbf{r}), \nabla n(\mathbf{r}), \ldots] n(\mathbf{r}) \, d\mathbf{r} \, . \tag{2.36}$$

This kind of approximation improves approximations to the cohesive energy with respect to LDA. It can also improve the description of bond lengths and lattice parameters, but overestimates compared to experiment [255, 256]. It also gives a rather limited improvement to the dielectric susceptibility.

2.0.5 Bloch's Theorem

Theoretical descriptions of periodic solids are described by a basic unit cell, repeated in one to three spatial directions to form a crystal lattice. The atomic position $\mathbf{R}_{i,a}$ of atom i in unit cell a is given by

$$\mathbf{R}_{i,a} = \mathbf{R}_a + \mathbf{r}_i \, , \tag{2.37}$$

where $\mathbf{R}_a$ is a lattice vector and $\mathbf{r}_i$ is the atom's position in the unit cell.

By imposing periodic boundary conditions on the unit cell, the wavefunctions can be written as a product of a plane wave and a function $u(\mathbf{r})$ which has the same periodicity as the lattice,

$$\psi_{n,\mathbf{k}}(\mathbf{r}) = \frac{1}{\sqrt{N\Omega_0}} e^{i\mathbf{k}\cdot\mathbf{r}} u_{n,\mathbf{k}}(\mathbf{r}) \ , \tag{2.38}$$

where $\mathbf{k}$ is a reciprocal lattice vector, N is the number of unit cells and Ω_0 is the unit cell volume. $\psi_{n,\mathbf{k}}(\mathbf{r})$ are known as Bloch functions.

Bloch's theorem reduces the problem of calculating an infinite number of electronic wavefunctions in real space to a finite number in reciprocal space, but over an infinite number of $\mathbf{k}$ vectors. The periodicity of real space leads to the periodicity of reciprocal space, so we only need to consider the $\mathbf{k}$ vectors in the first Brillouin zone (BZ).

The electron density in terms of the cell Bloch functions is

$$n(\mathbf{r}) = \frac{N\Omega_0}{(2\pi)^3} \int_{\mathrm{BZ}} \mathrm{d}\mathbf{k} \sum_{m}^{\mathrm{occ}} s\psi_{m,\mathbf{k}}^{*}(\mathbf{r}) \psi_{m,\mathbf{k}}(\mathbf{r}) \ , \tag{2.39}$$

where s is the occupation number (2 for spin-degenerate systems).

2.0.6 Pseudopotentials

The pseudopotential approximation is essential to nearly all modern total energy calculations [257–259, 252]. Because the core electrons are chemically inert, and in most materials, the physical and chemical properties typically only depend on valence electrons, we can apply the frozen core approximation, in which the core electrons are treated as they would be for an isolated atom. If the core is frozen, there is no need to solve for the Kohn-Sham wavefunctions of the core electrons. However, removing the core electrons is not trivial, since the valence electron wavefunctions oscillate and have nodes near the nucleus in order to be orthogonal to the core wavefunctions.

We can replace the 'all-electron' wavefunctions with pseudowavefunctions, which are equal to the all-electron wavefunctions outside of the core region, but don't have nodes inside the core region. Below some radial cutoff r_c, the oscillating part is replaced with a smooth, nodeless part. The values of the wavefunctions and their derivatives must be matched at r_c in order to ensure smooth continuity [260, 261]. We must also ensure that the total charge in

the core region is correct,

$$\int_0^{r_c} |\psi(r)|^2 r^2 \, \mathrm{d}r = \int_0^{r_c} |\psi^{\mathrm{PS}}(r)|^2 r^2 \, \mathrm{d}r \,. \tag{2.40}$$

We get pseudowavefunctions by solving the Kohn-Sham equations with a pseudopotential. Above r_c, it coincides with the regular potential. Below r_c, the solution of the Kohn-Sham equations give the pseudowavefunction.

2.0.7 Basis Sets

The final essential ingredient in a total energy calculation is a suitable basis set. Using a finite basis, $\{\phi_i(\mathbf{r})\}$, a general state can be expanded

$$\psi_n(\mathbf{r}) = \sum_i c_{n,i} \phi_i(\mathbf{r}) \,. \tag{2.41}$$

Inserting this into the Schrödinger equation gives

$$\sum_i c_{n,i} \hat{h} \phi_i = \varepsilon_n \sum_i c_{n,i} \phi_i \,. \tag{2.42}$$

Multiplying by ϕ_j^* and integrating:

$$\begin{aligned}
\sum_i \left(\int \phi_j^* \hat{h} \phi_i \, \mathrm{d}\mathbf{r} \right) c_{n,i} &= \varepsilon_n \sum_i \left(\int \phi_j^* \phi_i \, \mathrm{d}\mathbf{r} \right) c_{n,i} \\
\sum_i \langle \phi_j | \hat{h} | \phi_i \rangle c_{n,i} &= \varepsilon_n \sum_i \langle \phi_j | \phi_i \rangle c_{n,i} \\
\sum_i h_{ij} c_{n,i} &= \varepsilon_n \sum_i S_{ij} c_{n,i}
\end{aligned} \qquad . \tag{2.43}$$

h_{ij} are the Hamiltonian matrix elements and S_{ij} the overlap matrix elements. For orthonormal basis sets, S is simply the identity matrix. In a basis of atomic orbitals, the density functional is given by

$$\rho(r) = \sum_n^{\text{occ}} |\psi_n(\mathbf{r})|^2 = \sum_{i,j} \sum_n^{\text{occ}} c_{n,i}^* c_{n,j} \phi_i^* \phi_j$$

$$= \sum_{i,j} \phi_i^* \phi_j \sum_n^{\text{occ}} c_{n,i}^* c_{n,j} \,, \tag{2.44}$$

$$= \sum_{i,j} \phi_i^* \phi_j \rho_{ij}$$

where

$$\rho_{ij} = \sum_n^{\text{occ}} c_{n,i}^* c_{n,j} \tag{2.45}$$

is the density matrix.

From Bloch's theorem, we know that the electronic wavefunction can be represented using a discrete plane-wave basis in the **k**-points in the BZ [244]:

$$\psi_{n,\mathbf{k}}(\mathbf{r}) = \frac{1}{\sqrt{N\Omega_0}} \sum_{\mathbf{g}} c_{n,\mathbf{g}} e^{i(\mathbf{k}+\mathbf{g}) \cdot \mathbf{r}} \,, \tag{2.46}$$

where the sum is performed over reciprocal lattice vectors **g**. Of course, we can't include an infinite number of reciprocal lattice vectors, so we must choose a suitable cutoff. This can be done using a kinetic energy cutoff: Let $\mathbf{g}_{\text{max}}$ be the largest vectors such that

$$E_{\text{cut}} = \frac{1}{2} |\mathbf{g}_{\text{max}}|^2 \,. \tag{2.47}$$

In Eq. (2.46) we include all **g** that satisfy

$$\frac{1}{2} |\mathbf{g}|^2 \leq E_{\text{cut}} \,. \tag{2.48}$$

The Kohn-Sham equations are then solved for the coefficients. Plane-wave basis sets are used in DFT codes such as CASTEP [262, 263] and ABINIT [264–268]. They are conceptually

simple and can be systematically converged for a given system with very little human input: only a kinetic energy cutoff needs to be specified.

Another option is to expand the wavefunctions using a basis of atomic orbitals [269–271]:

$$
\begin{aligned}
\psi_i(\mathbf{r}) &= \sum_{i,nlm} c_{i,nlm} \phi_{i,nlm}(\mathbf{r} - \mathbf{R}_i) \\
\phi_{i,nlm}(\mathbf{r}) &= R_{i,nl}(r) Y_{i,lm}(\hat{r})
\end{aligned}
\tag{2.49}
$$

R is the radial part of the atomic wavefunction and Y are spherical harmonics. Atomic orbitals are used in SIESTA [272]. They have the advantage of being very quick, efficient and accurate, as well has having a straightforward physical interpretation. However, the basis cannot be systematically converged. For a given system, a basis set must be constructed and tested by hand. Also, the basis depends on the atomic positions, which can lead to additional complications in time-dependent calculations, for example [273].

Chapter 3

Coupling between homogeneous tilts and 2DEG formation

In this chapter we generalize the phenomenological model of carrier formation at polar-nonpolar interfaces to account for coupling with homogeneous tilts in the polar film. We show that, upon coupling to homogeneous tilts, four new distinct types of transitions are possible, depending only on the energetics of the tilts, polar discontinuity and the coupling between them, regardless of whether the transition occurs with film thickness or an applied electric field. These include continuous and discontinuous transitions of the carriers, facilitated by the tilts, and both simultaneous and distinct transitions of tilts and carriers. Using first principles calculations, we make predictions about the type of transition which occurs at the LAO/STO interface.

3.1   Phenomenological theory of 2DEG formation

First, we review the phenomenological model of carrier formation at polar-nonpolar perovskite interfaces [66]. A sketch of the system is shown in Fig. 3.1. We have a polar thin film of thickness d on top of a non-polar substrate, with a vacuum region above. An external electric field, which can be thought of as the total electric field in the substrate, is applied across the entire system with an electrode / tip at the surface of the film and a back gate the bottom of the substrate [274, 48, 82], following a similar treatment in Ref. [133]. In order
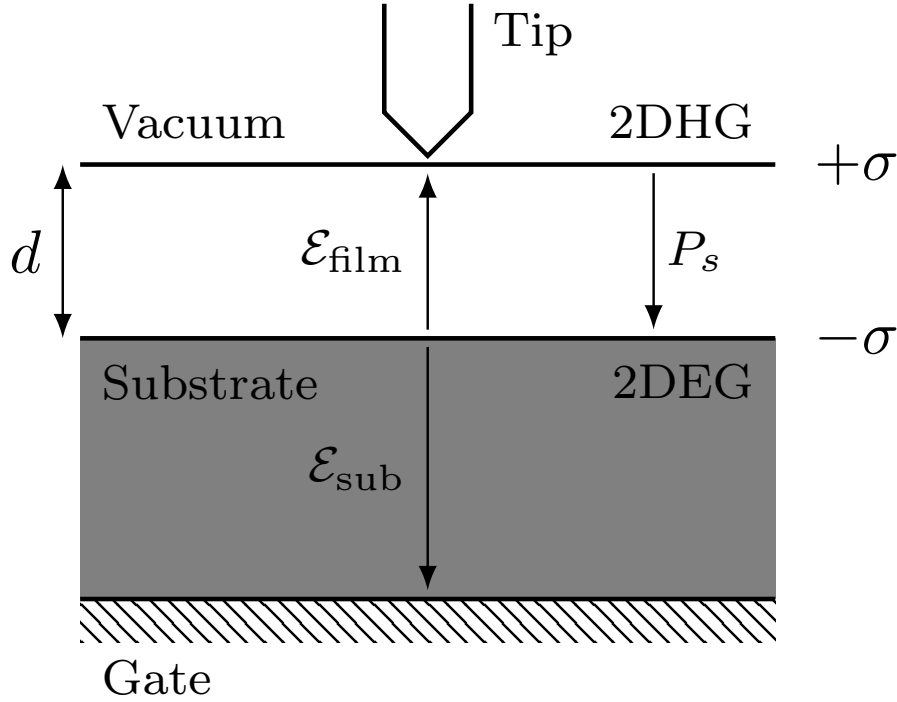
Fig. 3.1 Sketch of the electrostatics of a polar-nonpolar interface. A thin film of thickness d is placed on top of a semi-infinite substrate. An electric field is applied using a back gate under the substrate and a biased tip at the surface of the film. A 2DEG forms at the interface and a corresponding 2DHG forms at the surface of the thin film. The vectors in the film represent the total electric field $\mathcal{E}_{\text{film}}$ and polar discontinuity P_s. The vector in the substrate represents the total electric field $\mathcal{E}_{\text{sub}}$.

to screen this discontinuity, a 2DEG of carrier concentration σ forms between the film and substrate, and a corresponding two-dimensional hole gas (2DHG) forms at the surface.

We assume that the film and substrate are linear dielectrics, so the displacement fields are $D_{\text{film}} = \varepsilon_{\text{film}}\mathcal{E}_{\text{film}} + P_s$ and $D_{\text{sub.}} = \varepsilon_{\text{sub}}\mathcal{E}_{\text{sub}}$, respectively, where $\varepsilon_{\text{film}}$ and $\varepsilon_{\text{film}}$ are the dielectric permittivities. All vectors are normal to the plane of the interface, so the vector notation is omitted. Then from Maxwell's equations, the boundary condition at interface relates the displacement fields in the film and the substrate to the 2DEG carrier concentration σ:

$$(D_{\text{sub}} - D_{\text{film}}) \cdot \hat{n} = -\sigma$$
$$\varepsilon_{\text{sub}}\mathcal{E}_{\text{sub}} - \varepsilon_{\text{film}}\mathcal{E}_{\text{film}} - P_s = -\sigma \qquad (3.1)$$
$$\implies \mathcal{E}_{\text{film}} = \frac{\varepsilon_{\text{sub}}}{\varepsilon_{\text{film}}}\mathcal{E}_{\text{sub}} - \frac{1}{\varepsilon_{\text{film}}}(P_s - \sigma)$$

where $\hat{n}$ points outwards from the film. Using Eq. (3.1) we can write the electrostatic energy in terms of $\mathcal{E}_{\text{sub}}$, P_s and σ:

$$
\begin{aligned}
\mathcal{F}_{\text{elec}} &= \frac{1}{2}\varepsilon_{\text{film}}\mathcal{E}_{\text{film}}^2 \\
&= \frac{1}{2}\frac{\varepsilon_{\text{sub}}^2}{\varepsilon_{\text{film}}}\mathcal{E}_{\text{sub}}^2 - \frac{\varepsilon_{\text{sub}}}{\varepsilon_{\text{film}}}\mathcal{E}_{\text{sub}} \cdot (P_s - \sigma) + \frac{1}{2\varepsilon_{\text{film}}}(P_s - \sigma)^2
\end{aligned}
\tag{3.2}
$$

The first term corresponds to the energy of the applied field in the film, which does not depend affect the carrier concentration and can be neglected. The second term represents the coupling between the applied field and the polar mode and the third term is the electrostatic energy of the polar discontinuity. Writing Eq. (3.2) in terms of reduced variables $\sigma' = \frac{\sigma}{P_s}$ and $\mathcal{E}' = \frac{\mathcal{E}_{\text{sub}}}{(P_s/\varepsilon_{\text{sub}})}$, we get

$$
\mathcal{F}_{\text{elec}}(\sigma', \mathcal{E}') = \frac{P_s^2}{2\varepsilon}(1 - \sigma')^2 - \frac{P_s^2}{\varepsilon}\mathcal{E}' \cdot (1 - \sigma') ,
\tag{3.3}
$$

where we drop the subscript of the permittivity of the film, $\varepsilon_{\text{film}} \to \varepsilon$, since the permittivity of the substrate has been absorbed into the scale for the applied field and no longer appears in the free energy. The first term is the electrostatic energy of the polar discontinuity, and the second term is the linear coupling between the polarization and the applied field. For $\mathcal{E}' = 0$, the energy is minimized when $\sigma' = 1$, i.e. the polar discontinuity is fully screened by the carriers. For LAO/STO, this corresponds to a carrier concentration of exactly half an electron per unit cell surface area. However, we have neglected the formation energy of the carriers which appear the interface. Including the cost of generating an electron-hole pair across a gap Δ, the free energy is

$$
\mathcal{F}_{\sigma}(\sigma', \mathcal{E}') = \frac{P_s^2}{\varepsilon}\left(\frac{d_c}{d}\sigma' + \frac{1}{2}(1 - \sigma')^2 - \mathcal{E}' \cdot (1 - \sigma')\right) ,
\tag{3.4}
$$

where $d_c = \frac{\varepsilon_0 \Delta}{P_s}$ is the critical thickness, above which it is favorable for carriers to appear. Minimizing with respect to σ' gives:

$$
\sigma'(d, \mathcal{E}) = 1 - \left(\frac{d_c}{d} + \mathcal{E}'\right) ,
\tag{3.5}
$$

which implies that the carrier concentration increases with the thickness of the film, and can be tuned, and even switched on/off with an electric field. When an electric field is applied, the critical thickness for carriers to appear is

$$d_c(\mathcal{E}') = \frac{d_c}{1 - \mathcal{E}'} \,, \tag{3.6}$$

which can be reduced or increased, depending on the sign of $\mathcal{E}'$. In Fig. 3.2 (a) we show the carrier concentration as a function of thickness at zero field, and at positive and negative values of $\mathcal{E}'$. When $\mathcal{E}' = 0$, the appearance of carriers is as described in Ref. [66]: σ' switches on at d_c and approaches 1 asymptotically from below. When a negative field is applied, the polar discontinuity is enhanced, and the carrier transition occurs at a reduced thickness. In this case there is a second critical thickness where σ' reaches 1 and saturates:

$$d_{c,2}(\mathcal{E}') = -\frac{d_c}{\mathcal{E}'} \,. \tag{3.7}$$

When $\mathcal{E}' = -1$, the critical thicknesses are $d_c(-1) = \frac{d_c}{2}$ and $d_{c,2}(-1) = d_c$, i.e. the carriers appear at half the original critical thickness and saturate at the original critical thickness. When a positive field is applied, the polar discontinuity is partially screened, and the critical thickness increases.

The other (more realistic) possibility is to fix the thickness and induce the carriers with an applied field. From Eq. (3.6), at a fixed thickness there is a critical field value for which the carriers appear:

$$\mathcal{E}'_c(d) = 1 - \frac{d_c}{d} \,. \tag{3.8}$$

If $d < d_c$, the film is sub-critical and $\mathcal{E}'_c(d) < 0$. If $d \geq d_c$, the carriers will already be present at zero field. Applying a positive field partially screens the polar discontinuity, reducing the need for carriers. There is a second critical field value at which the carrier concentration saturates:

$$\mathcal{E}'_{c,2}(d) = -\frac{d_c}{d} \,, \tag{3.9}$$
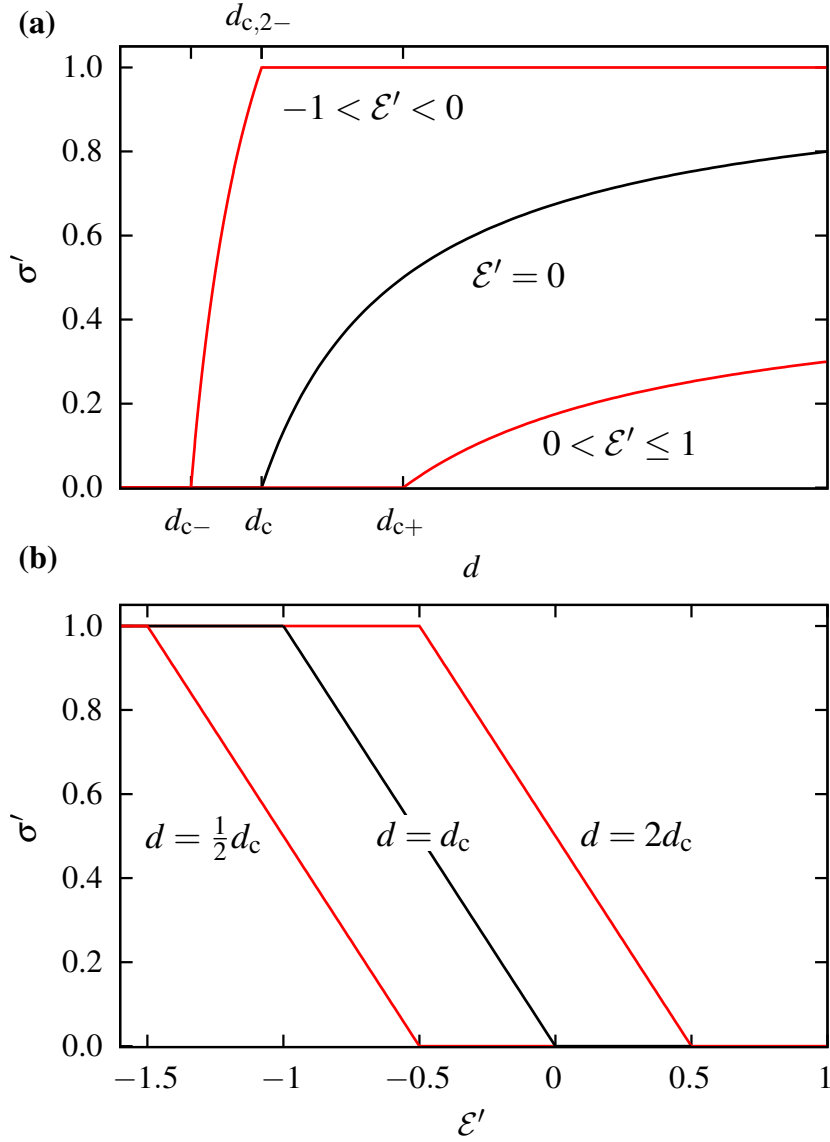
Fig. 3.2 **(a)**: Carrier concentration as a function of thickness for zero (black), positive and negative (red) values of reduced electric field $\mathcal{E}'$. When $\mathcal{E}'$ is positive, d_c increases to d_{c+}. When $\mathcal{E}'$ is negative, d_c is reduced to d_{c-}, and σ' saturates to 1 at a second critical thickness. **(a)**: Reduced carrier concentration with applied field at different thicknesses. The critical thickness $d = d_c$ is shown in black, and the sub- and super-critical thicknesses, $d = \frac{1}{2}d_c$ and $d = 2d_c$, respectively, are shown in red.

which is always negative for finite d. We have the relation between the two critical field values:

$$\mathcal{E}'_c(d) - \mathcal{E}'_{c,2}(d) = 1 \ . \tag{3.10}$$

The different scenarios for inducing or suppressing carriers with an applied field are summarized in Fig. 3.2 (b).

3.2   Coupling to homogeneous tilts

In this section we consider the effect of coupling to homogeneous tilts on the formation of carriers. The simplest way to consider this is to add the independent free energies of the tilts and carriers plus a coupling term: $\mathcal{F} = \mathcal{F}_\sigma + \mathcal{F}_\phi + \mathcal{F}_{\sigma\phi}$.

For simplicity we assume that the thin film undergoes a simple displacive transition from untilted to tilted below some temperature T_C. Thus, the free energy of tilts can be described by a double well:

$$\mathcal{F}_\phi(\phi,T) = \frac{1}{2\chi_\phi} \left(\frac{1}{4}\frac{\phi^4}{\phi_0^2} - \frac{1}{2}\left(1 - \frac{T}{T_C}\right)\phi^2 \right) , \qquad (3.11)$$

where ϕ is the tilt angle, ϕ_0 is the bulk equilibrium tilt angle and χ_ϕ is the curvature about the minima of the double well.

Bulk LAO undergoes a transition from cubic to rhombohedral at $T_C \sim 541°C$ [276]. The tilt pattern observed is, in Glazer notation [38], $a^- a^- a^-$. For a thin film of LAO, the tilt pattern changes to $a^- a^- c^0$ due to the tensile biaxial imposed by clamping to the STO substrate [277, 278]. If a compressive biaxial strain were applied by using a substrate with a smaller lattice constant than LAO, the observed tilt pattern changes to $a^0 a^0 c^-$ [277].

The simplest coupling we can introduce is a biquadratic coupling between the tilts and the polar mode [34, 37, 89]:

$$\mathcal{F}_{\sigma\phi}(\sigma,\phi) = \frac{1}{2}\alpha\phi^2(P_s - \sigma)^2 . \qquad (3.12)$$

Combining Eqs. (3.4), (3.11) and (3.12), and introducing a reduced variable for the tilt, $\phi' = \frac{\phi}{\phi_0}$, the total free energy is

$$\mathcal{F}_{\text{tot}} = \mathcal{F}_\sigma + \mathcal{F}_\phi + \mathcal{F}_{\sigma\phi}$$

$$
\begin{aligned}
\mathcal{F}_\sigma &= \frac{P_s^2}{\varepsilon}\left(\frac{d_{\text{c}}}{d}\sigma' + \frac{1}{2}\left(1-\sigma'\right)^2 - \mathcal{E}'\cdot\left(1-\sigma'\right)\right) \\
\mathcal{F}_\phi &= \frac{1}{2}X_\phi^{-1}\left(\frac{1}{4}\phi'^4 - \frac{1}{2}\left(1-\frac{T}{T_C}\right)\phi'^2\right) \\
\mathcal{F}_{\sigma\phi} &= \frac{1}{2}A\phi'^2(1-\sigma')^2
\end{aligned}
\tag{3.13}
$$

where

$$
\begin{aligned}
X_\phi^{-1} &= \phi_0^2\chi_\phi^{-1} \\
A &= \phi_0^2 P_s^2 \alpha
\end{aligned}
\tag{3.14}
$$

which both have units of energy per unit volume. They define the energy scales associated with the tilts and the biquadratic coupling, respectively. The energy scale associated with the carriers, i.e. the polar discontinuity, is $\frac{P_s^2}{\varepsilon}$.

Setting $T = 0$ and minimizing Eq. (3.13) with respect to σ' and ϕ', we get

$$
\begin{aligned}
\phi' &= \sqrt{1 - 2AX_\phi(1-\sigma')^2} \\
\sigma' &= 1 - \frac{1}{1+\frac{A}{(P_s^2/\varepsilon)}\phi'^2}\left(\frac{d_{\text{c}}}{d}+\mathcal{E}'\right)
\end{aligned}
\tag{3.15}
$$

Note that when we set $A = 0$, we recover the solutions of the uncoupled order parameters: Eq. (3.5) for σ' and $\phi' = 1$. Eq. (3.15) is a pair of self-consistent equations which does not have analytic solutions. However, we can use physical constraints to understand the behavior of σ' and ϕ' upon coupling. Firstly, the square of the tilts cannot be negative:

$$
\begin{aligned}
& 1 - 2AX_\phi(1-\sigma')^2 \geq 0 \\
\implies & 1 - \frac{1}{\sqrt{2AX_\phi}} \leq \sigma' \leq 1 + \frac{1}{\sqrt{2AX_\phi}}
\end{aligned}
\tag{3.16}
$$

The right-hand side of the inequality is always satisfied since σ' saturates at 1. The left-hand side can lead to situations where $\sigma < 0$, which is not physical. This leads to a condition which determines whether or not it is favorable for tilts to appear:

$$A = \frac{1}{2}X_\phi^{-1} \; . \tag{3.17}$$

Above this line, for $\sigma' = 0$ we would have $\phi^2 < 0$, so the tilts must be zero in the absence of carriers. Thus, the carriers will appear at d_c as in the uncoupled model, and the tilts will appear at a new critical thickness, d_ϕ, which is greater than d_c. Below the line, the tilts can be finite in the absence of carriers: $\phi' = \sqrt{1 - 2AX_\phi}$. In this case, carriers appear earlier at $d_\phi < d_c$, facilitated by a change in the tilts.

To summarize, above the straight line in Eq. (3.17), there are two separate transitions, the uncoupled carrier transition at d_c and a second one facilitated by tilts at $d_\phi > d_c$. Below the line, both transitions occur simultaneously at $d_\phi < d_c$, i.e. there is one critical thickness which is reduced by tilting. It is interesting to note that Eq. (3.17) is obtained independently of whether the carriers are induced via thickness or electric field.

While the uncoupled carrier transition at d_c is always continuous, we can investigate whether the transition at d_ϕ is continuous or discontinuous. If we insert the solution for ϕ' into σ' in Eq. (3.15), we obtain a cubic equation,

$$\begin{aligned} f(\sigma') = 2AX_\phi(1-\sigma')^3 &- \left(1 + \frac{P_s^2/\varepsilon}{A}\right)(1-\sigma') \\ &+ \left(\frac{P_s^2/\varepsilon}{A}\right)\left(\frac{d_c}{d} + \mathcal{E}'\right) = 0 \end{aligned} \tag{3.18}$$

the roots of which determine the value of σ'. We cannot obtain the roots analytically, but we can plot $f(\sigma')$ at different thicknesses and field strengths to get some insight about the transition, see Fig. 3.3.

Since d and $\mathcal{E}$ only appear in the constant term, the curve is shifted up or down by changing thickness or electric field, and the positions of the extrema are unaffected. The maximum and minimum are uniquely determined by the energy densities X_ϕ^{-1}, A and $\frac{P_s^2}{\varepsilon}$,
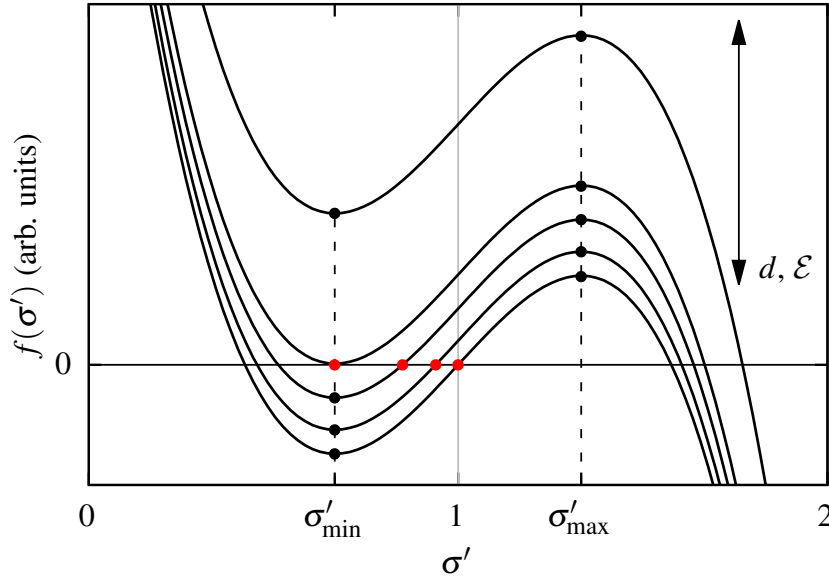
Fig. 3.3 Plots of the cubic polynomial $f(\sigma')$ for different values of thickness or electric field. The polynomial has extrema $\sigma'_{\text{min/max}}$ indicated by the black dots on each curve, where $\sigma'_{\text{min}} \leq 1$ and $\sigma'_{\text{max}} \geq 1$. The curve is shifted up and down by changing thickness or electric field. A non-zero carrier concentration is obtained when the polynomial has a root between 0 and 1, indicated by the red dots. For the highest curve, there is no root between 0 and 1, so the carrier concentration is zero. As we increase thickness (say), the curve is lowered. When σ'_{min} crosses the zero axis, carriers appear. Since $\sigma'_{\text{min}} > 0$, the carrier concentration jumps from zero to a finite value, and the transition is discontinuous. As the curve is shifted further downwards, the root moves to the right until it reaches 1, i.e. σ' increases until it reaches 1, where it saturates.

$$\sigma'_{\text{min/max}} = 1 \pm \sqrt{\frac{1}{6AX_\phi}\left(1 + \frac{P_s^2/\varepsilon}{A}\right)}\,. \tag{3.19}$$

σ'_{max} is always greater than 1, which is not physical, but σ'_{min} is bounded from above by 1. This provides a clear picture of how the carrier transition occurs: the curve in Eq. (3.18) is shifted by changing d or $\mathcal{E}$, and carriers appear when there is a root between 0 and 1. If $\sigma'_{\text{min}} < 0$, they appear continuously and if $0 < \sigma'_{\text{min}} < 1$ they appear discontinuously. Thus, $\sigma'_{\text{min}} = 0$ defines a boundary between first and second order transitions:

$$6A^2 - X_\phi^{-1}\left(A + \frac{P_s^2}{\varepsilon}\right) = 0\,, \tag{3.20}$$

which is quadratic in A and has one positive solution:

$$A = \frac{1}{12} X_\phi^{-1} \left(1 + \sqrt{1 + 24 \frac{(P_s^2/\varepsilon)}{X_\phi^{-1}}} \right) . \tag{3.21}$$

Above this curve, the transition at d_ϕ is discontinuous and below it is continuous. Once again, Eq. (3.21) was derived independently of whether the transition occurs via thickness or electric field. Combining Eqs. (3.17) and (3.21) results in four different possible sequences of transitions, depending only on the energy densities X_ϕ^{-1}, A and $\frac{P_s^2}{\varepsilon}$. These transitions are summarized in Fig. 3.4. The lines intersect at a tetra-critical point (A^*, X_ϕ^{-1*}), where

$$\begin{aligned} A^* &= \frac{P_s^2}{2\varepsilon} \\ X_\phi^{-1*} &= \frac{P_s^2}{\varepsilon} \end{aligned} . \tag{3.22}$$

In Figs. 3.5 and 3.6 we plot the order parameters as a function of thickness and electric field respectively, as well as contours of the total free energy as a function of σ' for several thicknesses and electric field strengths.
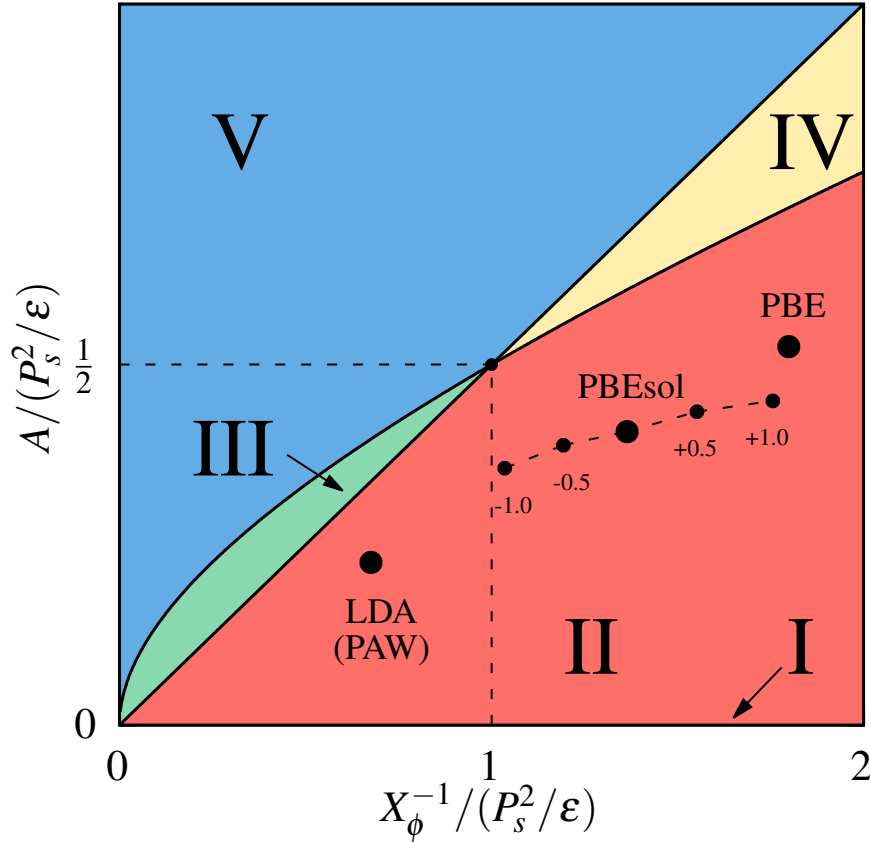
Fig. 3.4 Diagram summarizing the coupled transitions of carriers and tilts. Region I, the line $A = 0$, describes the uncoupled order parameters. The straight line has slope $\frac{1}{2}$. Above this line, the tilts switch on after the 2DEG at $d_\phi > d_c$ and are zero beforehand. When the tilts switch on, there is a continuous (region III) or discontinuous (region V) change in the 2DEG, separate to the uncoupled carrier transition at d_c. Below the straight line, there is a kink in the tilts at $d_\phi < d_c$, accompanied by a kink in the carrier concentration which can be continuous (region II) or discontinuous (region IV). First-principles calculations using LDA (PAW), PBE and PBEsol functionals, summarized in Table 3.1, were used to place the LAO/STO interface on the diagram, indicated by the large black dots. The smaller dots show the effect of applying a small amount of compressive or tensile strain on the in-plane lattice parameter a_{STO}, using the PBEsol functional.
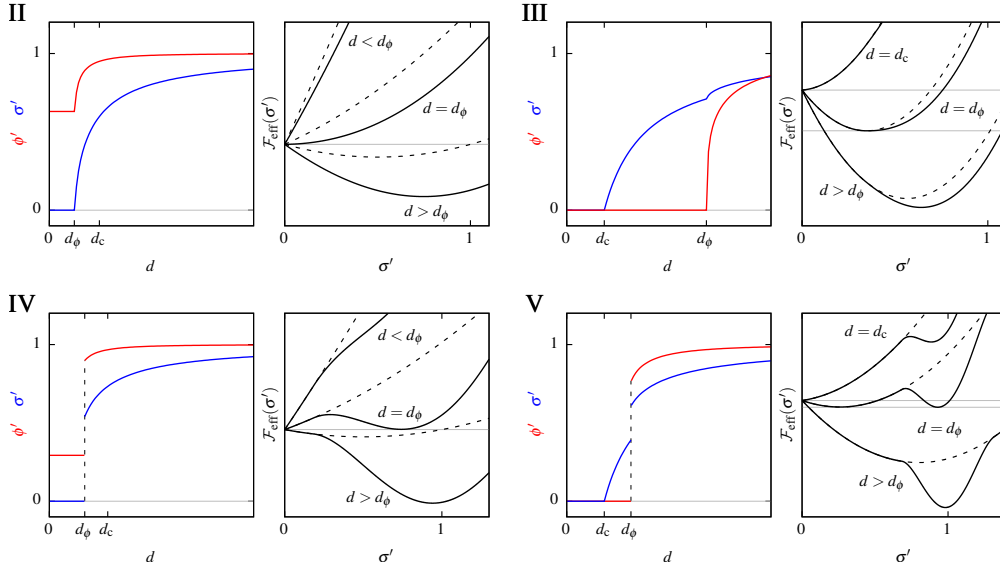
Fig. 3.5 Summary of the carrier transitions with film thickness for the four coupled regions in Fig. 3.4. The left panel for each region is an order parameter plot of ϕ' and σ' with thickness. The critical thickness from the uncoupled theory is d_c, and the additional critical thickness at which the tilts switch on/jump is d_ϕ. The right panel shows an effective theory, $\mathcal{F}_{\text{eff}}(\sigma')$, obtained by using Eq. (3.15) to write Eq. (3.13) solely in terms of σ'. Several energy curves are shown for different thicknesses in each panel, and the dashed line shows a continuation of the uncoupled theory. The value of σ' at each value of d is given by the horizontal position of the minimum on each curve.
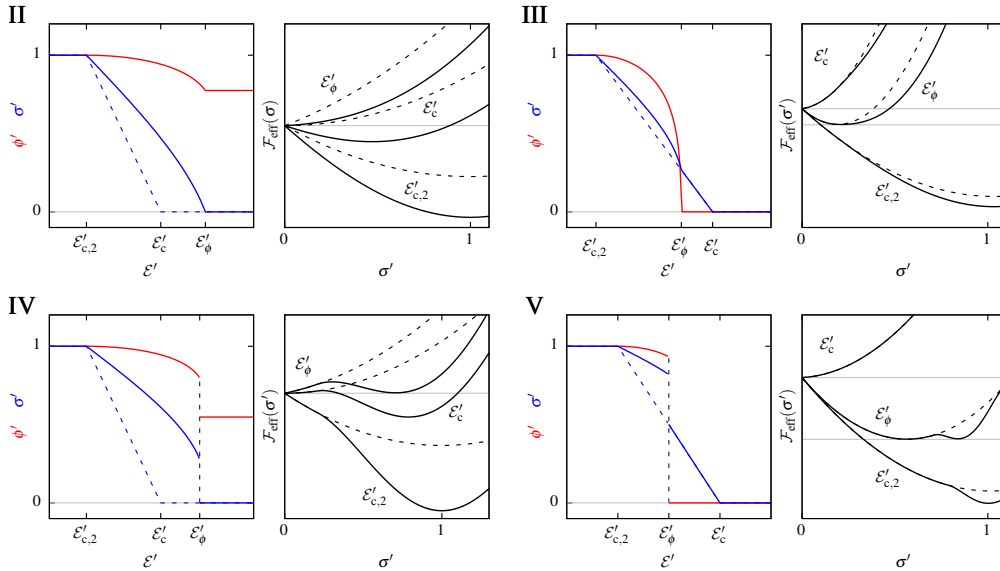
Fig. 3.6 Summary of the carrier transitions with applied electric field for the four coupled regions in Fig. 3.4. The critical field values at which the carriers appear and saturate in the uncoupled theory are given by $\mathcal{E}'_c$ and $\mathcal{E}'_{c,2}$, respectively, and the additional critical field value at which the tilts switch on/jump is given by $\mathcal{E}'_\phi$. The right panels are as described in Fig. 3.5. The dashed blue line shows the value of σ' without coupling to tilts.

3.3   Estimating the order of the carrier transition from first-principles

We can approximate X_ϕ^{-1}, A and $\frac{P_s^2}{\varepsilon}$ for LAO/STO by performing first-principles calculations using bulk LAO, biaxially strained to the lattice parameter of cubic STO. We follow the methodology in Ref. [89], where similar calculations were performed.

First-principles density functional theory (DFT) calculations were performed using the ABINIT code [264–268]. We used both Perdew-Burke-Edwards (PBE) [279] and PBEsol [280, 281] exchange-correlation functionals within the generalized gradient approximation (GGA) using PSML [282] norm-conserving [283] pseudopotentials, obtained from pseudo-dojo [284]. We also performed calculations using the Perdew-Wang (PW92) [285] exchange-correlation functional within the local density approximation (LDA), using the projector augmented-wave method [286, 287] (PAW) in order to compare to Ref. [89]. For the electronic configurations, we included 11 valence electrons for La ($5s^2 5p^6 5d^1 6s^2$), 11 for Al ($2s^2 2p^6 3s^2 3p^1$) and 6 for O ($2s^2 2p^4$), explicitly including the semicore $2s^2 2p^6$ states in the valence configuration of Al. When the semicore electrons were included for Al, a cutoff of 2500 eV was required to adequately converge the total energy of the 5-atom unit cell. A Monkhorst-Pack k-point grid [288] of $6 \times 6 \times 6$ was used for the 5-atom calculations and a grid of $4 \times 4 \times 3$ was used for the 20-atom calculations.

We first optimized the geometry of cubic STO in order to obtain the lattice parameter, a_{STO}. The in-plane lattice parameters of LAO were then fixed to a_{STO}, and the out-of-plane lattice parameter c was allowed to relax. It was found that the lattice parameter was not affected significantly more by the tilt or the electric fields applied, so it was fixed to the value obtained in the untilted case in the more time-consuming calculations. The untilted calculations were performed using the 5-atom primitive cell. To allow for tilts, we used a $\sqrt{2} \times \sqrt{2} \times 2$ supercell containing 20 atoms, which is the smallest cell required to allow for the $a^- a^- c^0$ tilt pattern which appears in LAO when biaxially strained to a_{STO} [277]. The depth of the tilt double well, E_0, is the energy difference per 5 atom unit cell between the tilted and untilted systems. Using $\mathcal{F}_\phi(\phi' = \pm 1) = E_0$, we get

$$X_\phi^{-1} = -8E_0 \,. \tag{3.23}$$

E_0 and X_ϕ^{-1} are given in Table I for all of the functionals used, in units of meV/Ω_5, where Ω_5 is the volume of the 5-atom unit cell. The LDA results are close to those obtained in Ref. [89], but the results obtained using PBE and PBEsol differ by a factor of ~ 2.
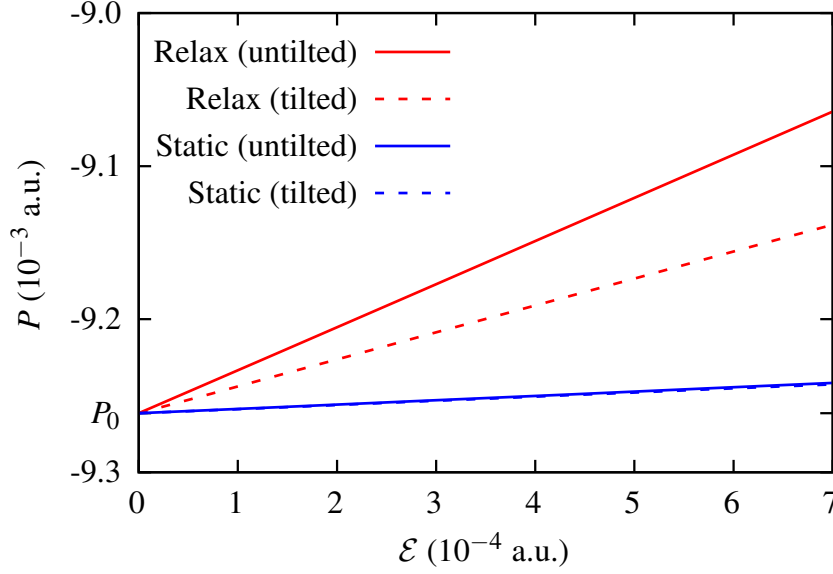
Fig. 3.7 Polarization as a function of applied electric field, from the PBEsol calculations. The solid lines are results obtained from the untilted system and the dashed lines are results obtained for the tilted system. The blue lines indicate the static case, where the ions were fixed and the red lines indicate the relaxed case, where a geometry relaxation was performed at each value of $\mathcal{E}$.

A and $\frac{P_s^2}{\mathcal{E}}$ were obtained by calculating the dielectric constants in the untilted and tilted systems. This was done by performing a set of bulk calculations using a finite electric field parallel to the c-axis [289–293]. In Ref. [89] a finite displacement field was used [275], but either type of field can be used to calculate A. The polarization, calculated using Berry phases [294, 295], was measured in the presence of a small applied field $\mathcal{E}$, with the ions both fixed and allowed to relax. Plots of polarization as a function of applied field are shown in Fig. 3.7. In Gaussian units, the relation between polarization and electric field, and dielectric constant is

$$P_i = \chi_{ij}\mathcal{E}_j + \mathcal{O}(\mathcal{E}^2)$$
$$\varepsilon_{ij} = 1 + 4\pi\chi_{ij} \qquad (3.24)$$

The slope of $P(\mathcal{E})$ is reduced in the tilted case, because the tilts compete with the polar mode. For the static calculations, the tilted and untilted systems gave identical results. When the tilts are allowed to relax, the relation between P and $\mathcal{E}$ is

$$P(\mathcal{E}, \phi(\mathcal{E})) = \left(\frac{1}{\varepsilon_5} + \frac{A}{P_s^2} \phi'(\mathcal{E})^2 \right)^{-1} \mathcal{E} , \qquad (3.25)$$

where ε_5 is the dielectric constant of the untilted system. The dielectric constant of the tilted system, ε_{20}, is obtained in the limit $\mathcal{E} \to 0$:

$$\frac{1}{\varepsilon_{20}} = \frac{1}{\varepsilon_5} + \frac{A}{P_s^2} , \qquad (3.26)$$

where we used $\phi'(\mathcal{E} \to 0) = 1$. Rearranging Eq. (3.26) gives

$$\frac{\varepsilon_{20}^{-1} - \varepsilon_5^{-1}}{\varepsilon_5^{-1}} = \frac{A}{(P_s^2/\varepsilon_5)} , \qquad (3.27)$$

which is exactly the vertical axis of the phase transition diagram in Fig. 3.4. Values of ε_5, ε_{20}, A and $\frac{P_s^2}{\varepsilon_5}$ are given in Table 3.1 for all of the functionals used. For the LDA (PAW) calculations, the electric field calculations for the tilted system failed to converge, so we used the value of A from Ref. [89] in Fig. 3.4.

Functional	a_{LAO}	a_{STO}	c	E_0	X_ϕ^{-1}	ε_5	ε_{20}	$\frac{P_s^2}{\varepsilon_5}$	A
PAW LDA [89]	3.75	3.85	3.68	27.7	221.6	-	-	-	96.1
PAW LDA	3.75	3.86	3.67	35.9	287.8	26.1	-	425.7	-
PBE	3.81	3.93	3.72	60.5	483.9	40.4	26.5	268.9	141.2
PBEsol	3.77	3.89	3.69	54.2	433.8	34.6	24.6	317.9	129.4

Table 3.1 Summary of results from first-principles calculations. The lattice constants are in units of Å, the energies are in units of meV/Ω_5, and the dielectric constants are dimensionless.

The results in Table 3.1 were used to place the LAO/STO interface on the phase transition diagram in Fig. 3.4. Although there is a relatively large distance between the three points,

each exchange-correlation functional predicts that the LAO/STO interface is in region II, i.e. a single second order transition at a reduced critical thickness d_ϕ. The difference in LDA can be attributed to the shallower tilt double well. The difference between PBE and PBEsol appears to arise from the difference in the untilted dielectric constants.

We also performed calculations to investigate the effect of strain on the carrier transition, using the PBEsol exchange-correlation functional. Calculations were repeated but with small amounts of compressive and tensile strain applied to a_{STO}, up to $\pm 1\%$. The results are included in Fig. 3.4, indicated by the smaller dots. We found that a compressive strain moved the point towards the origin and a tensile strain moved the point up and to the right, although it appears that a significantly larger amount of strain than the ones investigated here would be required to change the order of the carrier transition. It may be possible to change the character of the transitions using biaxial strain for a system with a point which lies closer to a boundary between regions, however.

3.4 Coupled Transitions with temperature

In this section we investigate the possibility of inducing a carrier transition with temperature. When the order parameters are uncoupled, at a nonzero temperature we have

$$
\begin{aligned}
\sigma'(d) &= 1 - \frac{d_{\text{c}}}{d} \\
\phi'(T) &= \sqrt{1 - \frac{T}{T_C}}
\end{aligned}, \tag{3.28}
$$

where we set $\mathcal{E}' = 0$ for simplicity. For nonzero A, minimizing Eq. (3.13) gives

$$
\begin{aligned}
\phi' &= \sqrt{\left(1 - \frac{T}{T_C}\right) - 2AX_\phi(1-\sigma')^2} \\
\sigma' &= 1 - \frac{1}{1 + \frac{A}{(P_s^2/\varepsilon)}\phi'^2}\frac{d_{\text{c}}}{d}
\end{aligned}. \tag{3.29}
$$

If we require that $\phi^2 \geq 0$ as before, we get

$$1 - \frac{1}{\sqrt{2AX_\phi(T)}} \leq \sigma' \leq 1 + \frac{1}{\sqrt{2AX_\phi(T)}} \ , \tag{3.30}$$

where $X_\phi(T) = \left(1 - \frac{T}{T_C}\right)^{-1} X_\phi$. As in Eq. (3.16), the inequality on the left hand side can lead to situations where $\phi^2 < 0$. This implies that there is an additional critical temperature, T_C':

$$T_C' \equiv T_C \left(1 - 2AX_\phi\right) \ . \tag{3.31}$$

This is the reduced critical temperature of the thin film, a phenomenon which is typically seen in phase transitions when going from bulk to thin films [26, 27, 25, 28]. Interestingly, we have $T_C' = 0$ when

$$A > \frac{1}{2}X_\phi^{-1} \ , \tag{3.32}$$

i.e. there is no tilt transition at all. This is the same straight line obtained for transitions with thickness and electric field at zero temperature. However, it has a different meaning for transitions with temperature: below the line there is a tilt transition at a reduced critical temperature T_C', and above the line there is no tilt transition. There is a second transition temperature, T_C'', below which the carriers appear. Inserting ϕ' into σ' in Eq. (3.29) and letting $\sigma'(T_C'') = 0$, we get

$$T_C'' \equiv T_C' - T_C \left(\frac{P_s^2/\varepsilon}{A}\right)\left(\frac{d_c}{d} - 1\right) \tag{3.33}$$

We can see that $T_C'' < T_C'$ for sub-critical films, and $T_C'' = T_C'$ when $d = d_c$. Thus, two transitions are possible by decreasing temperature in sub-critical films and only one transition is possible otherwise. Additionally, it is possible for the transition at T_C'' to be first or second order. Inserting ϕ' into σ' as before, we obtain another cubic equation in σ':

$$f_T(\sigma') = \underbrace{2AX_\phi}_{\Lambda}(1-\sigma')^3 - \underbrace{\left(1 - \frac{T}{T_C} + \frac{P_s^2/\varepsilon}{A}\right)}_{\Gamma(T)}(1-\sigma')$$
$$+ \left(\frac{P_s^2/\varepsilon}{A}\right)\frac{d_c}{d} = 0 \tag{3.34}$$

with extrema

$$\sigma'_{\text{max/min}}(T) = 1 \pm \sqrt{\frac{\Gamma(T)}{3\Lambda}} . \tag{3.35}$$

In the previous section, the positions of the extrema were not dependent on the quantity that induced the transitions. Assuming the transition occurs at some temperature T^*, we can determine the character of the transition by requiring that $f_T(\sigma_{\text{min}}(T^*)) = 0$,

$$-\Lambda\left(\sqrt{\frac{\Gamma(T^*)}{3\Lambda}}\right)^3 + \Gamma(T^*)\left(\sqrt{\frac{\Gamma(T^*)}{3\Lambda}}\right)\left(\frac{P_s^2/\varepsilon}{A}\right)\frac{d_c}{d} = 0$$
$$\implies \Gamma(T^*) = \sqrt[3]{\frac{27}{4}\left(\left(\frac{P_s^2/\varepsilon}{A}\right)\frac{d_c}{d}\right)^2\Lambda} \tag{3.36}$$

and also requiring that $\sigma_{\text{min}}(T^*) > 0$,

$$\frac{1}{4}\left(\frac{P_s^2/\varepsilon}{A}\right)\frac{d_c}{d} < \Lambda . \tag{3.37}$$

Thus, we get

$$A > \sqrt{\frac{1}{4}\frac{d_c}{d}\left(\frac{P_s^2}{\varepsilon}\right)X_\phi^{-1}} \tag{3.38}$$

The lines in Eqs. (3.32) and (3.38) form a diagram for transitions with temperature, shown in Fig. 3.8. There are only two distinct regions (II and III), but the number of transitions in each

is determined by the ratio $\frac{d}{d_c}$, so four different types of carrier transitions are possible. Plots of the order parameters for the four different scenarios are shown in Fig. 3.9.
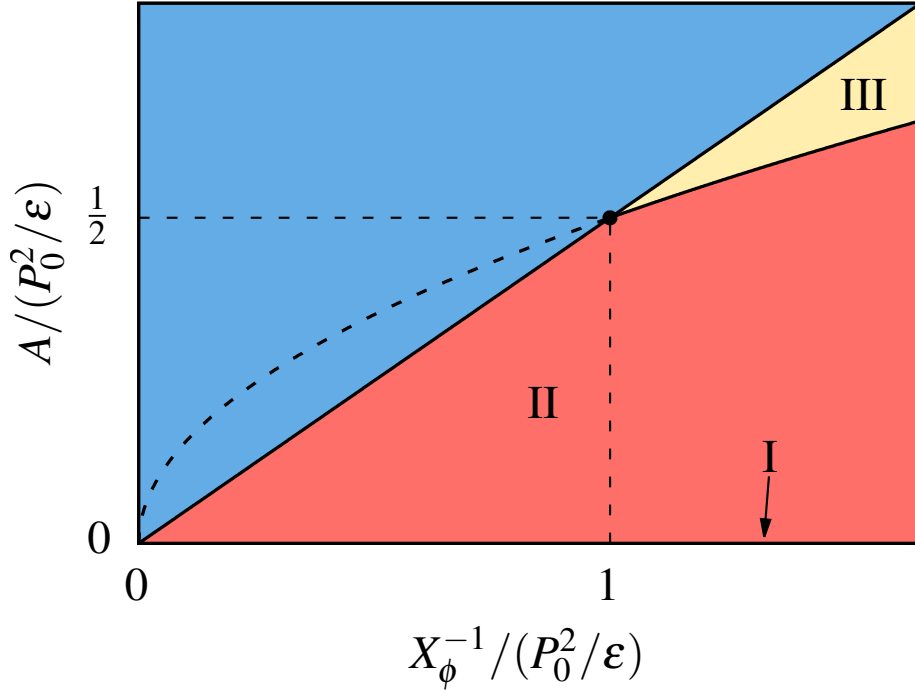
Fig. 3.8 Phase transition diagram for transitions driven by temperature. The line $A = 0$ describes the uncoupled order parameters (region I). The straight line is the same as in Fig. 3.4. Above this line, no tilt transitions with temperature are possible: $T_C' = 0$. The curved line is given by Eq. (3.38) and determines whether the carrier transition is continuous (below) or discontinuous (above). The number of transitions, i.e. whether or not T_C' and T_C'' are different is determined by the ratio $\frac{d}{d_c}$ only: if $\frac{d}{d_c} < 1$ there are two transitions and if $\frac{d}{d_c} \geq 1$ there is only one transition.
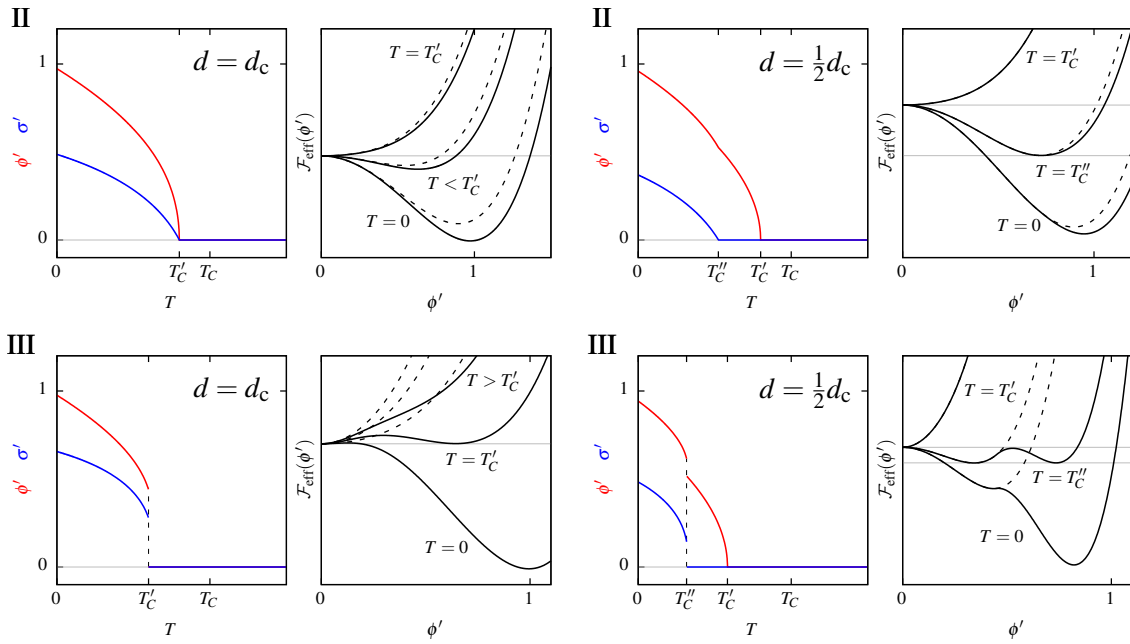
Fig. 3.9 Summary of the carrier transitions with temperature for the two coupled regions in Fig. 3.8. The left hand side shows transitions for thin films at the uncoupled critical thickness ($d = d_c$) and the right hand side shows transitions for sub-critical thin films ($d = \frac{1}{2}d_c$). The right panels shows energy contours for different temperatures and are as described in Fig. 3.5, but an effective theory in ϕ' instead of σ' is used.

Chapter 4

Coupling between inhomogeneous tilts and 2DEG formation

In this chapter we generalize the model developed in the previous chapter to consider coupling between carriers and inhomogeneous tilts at polar-nonpolar perovskite interfaces. In thicker films, the tilts will deviate from the bulk equilibrium value at the boundaries due to surface effects, but will be close to the bulk value sufficiently far away from the boundaries. In thinner films, the behavior of the tilts may be dominated by surface effects, and thus very different from a bulk crystal. Additionally, it is also possible to have tilts in the substrate, which can couple to the tilts in the film across the interface: STO is tetragonal below room temperature, facilitated by an $a^0 a^0 c^-$ tilt. The behavior of coupled carriers and homogeneous tilts uncovered in the previous chapter is very rich and interesting, but it is a very ideal scenario. While it may be appropriate for thicker films, it is already known experimentally that the tilts in LAO/STO are very inhomogeneous for thinner films of LAO close to the critical thickness for carrier formation [89]. Thus, in order to provide a more realistic description of the coupling between tilts and carriers, we must allow for inhomogeneous tilting: $\phi' = \phi'(\mathbf{r})$.

4.1 Ginzburg-Landau theory of inhomogeneous tilts

We can allow for inhomogeneous tilts by generalizing from a Landau theory to a Ginzburg-Landau theory, i.e. the free energy is expanded in powers of both the order parameter and its
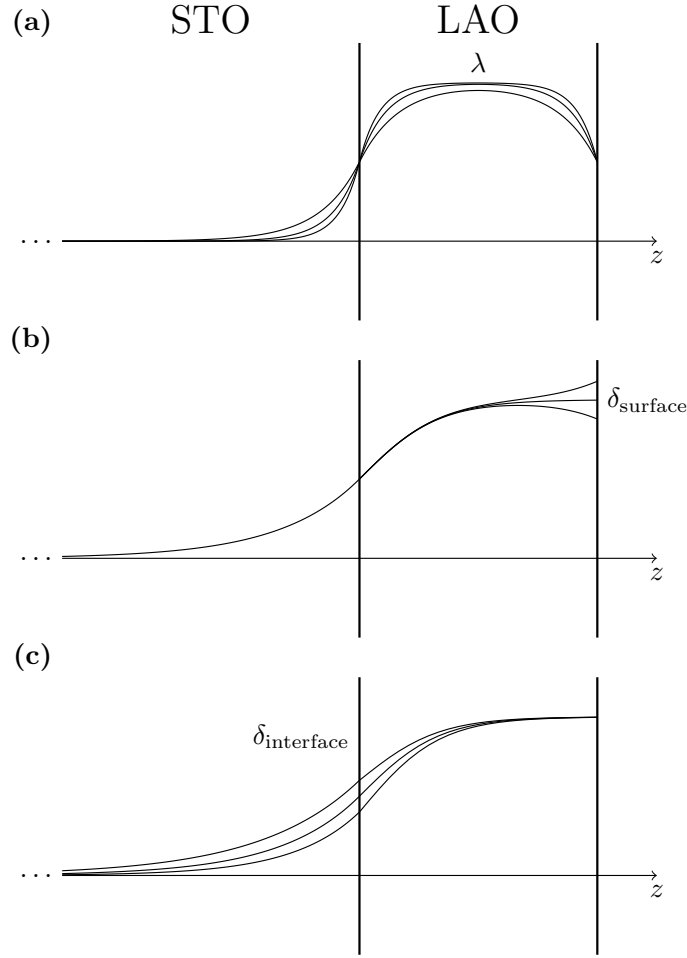
Fig. 4.1 Sketch of inhomogeneous tilts in a thin film grown on a substrate, e.g. LAO/STO, and the effect of **(a)**: λ, the correlation length of the tilts in the LAO film **(b)**: δ_{surface}, the relative difference in the energy of the tilts at the surface with respect to the bulk and **(c)**: $\delta_{\text{interface}}$, the relative difference in the energy of the tilts at the interface with respect to the bulk. The effect of the energetics of the tilts in the substrate may be absorbed into $\delta_{\text{interface}}$.

gradient. We do this following the methodology which has been used to describe semi-infinite ferromagnetic [26], ferroelectric [27–29] and superconducting [25] systems in which the order parameter is inhomogeneous due to the presence of a free surface. Considering only the tilts in the thin film, Eq. (3.11) becomes an integral over the volume of the film:

$$\mathcal{F}'^{\text{GL}}_{\phi} = \frac{1}{V} \int_V \left[\lambda^2 \left(\nabla \phi'(\boldsymbol{r}) \right)^2 + \frac{1}{4} \phi'(\boldsymbol{r})^4 - \frac{1}{2} \phi'(\boldsymbol{r})^2 \right] dV \,, \qquad (4.1)$$

where $\mathcal{F}' \equiv \mathcal{F}/\frac{1}{2} X_{\phi}^{-1}$ and $\lambda > 0$ is the correlation length of the tilts, which sets the length scale for the variations of the tilts, see Fig. 4.1 (a). The correlation length depends on the

temperature of the system, but we assume a fixed temperature for simplicity. Eq. (4.1) is written so that each term in the integrand is dimensionless, and the free energy is in units of $\frac{1}{2}X_\phi^{-1}$, the energy scale of the homogeneous tilts.

Next, we reintroduce the carriers. We take the order parameter to be the carrier concentration averaged over an in-plane unit cell: $\sigma' \equiv \langle \sigma' \rangle = \frac{1}{A}\int \sigma'(x,y)\,dA$. If we assume that the in-plane variance in σ' is small, so that $\langle(1-\sigma')\rangle^2 \approx (1-\langle\sigma'\rangle)^2$, then $\mathcal{F}'^{\text{GL}}_\sigma = \mathcal{F}'_\sigma$. It should be noted that this is a significant assumption, especially in the low carrier regime.

For inhomogeneous tilts, the biquadratic coupling term becomes

$$\mathcal{F}'^{\text{GL}}_{\sigma\phi} = \frac{1}{V}\int \frac{1}{2}(2AX_\phi)\phi'(\mathbf{r})^2(1-\sigma')^2\,dV \, , \tag{4.2}$$

which, since we assume the in-plane variance in σ' is small, reduces to

$$\mathcal{F}'^{\text{GL}}_{\sigma\phi} = \frac{1}{2}(2AX_\phi)(1-\sigma')^2\left\langle\phi'^2\right\rangle \, , \tag{4.3}$$

where

$$\left\langle\phi'^2\right\rangle = \frac{1}{V}\int \phi'(\mathbf{r})^2\,dV \tag{4.4}$$

is the mean of the square of the tilt throughout the film.

Under these assumptions, the free energy can be minimized with respect to σ' as in the homogeneous case, yielding

$$\sigma' = 1 - \frac{1}{1 + \frac{A}{P_0^2/\varepsilon}\left\langle\phi'^2\right\rangle}\left(\frac{d_c}{d} + \mathcal{E}'\right) \, , \tag{4.5}$$

which is the same as the second line of Eq. (3.15), but with $\phi'^2 \to \left\langle\phi'^2\right\rangle$. We only consider transitions with thickness for illustrative purposes, although it would be simple enough to include an applied electric field as we did in the previous chapter.

For the tilts, we have

$$\mathcal{F}'^{\mathrm{GL}}_{\phi} + \mathcal{F}'^{\mathrm{GL}}_{\sigma\phi} = \frac{1}{V} \int_V \left[\lambda^2 \left(\nabla\phi' \right)^2 + \frac{1}{4}\phi'^4 \right. \tag{4.6}$$
$$\left. - \frac{1}{2} \left(1 - 2AX_\phi(1-\sigma')^2 \right) \phi'^2 \right] \mathrm{d}V$$

Following a similar treatment of ferroelectric thin films with inhomogeneous polarization [28], we split the free energy into interior and surface contributions: $\mathcal{F}^{\mathrm{GL}} = \mathcal{F}^{\mathrm{GL}}_{\mathrm{interior}} + \mathcal{F}^{\mathrm{GL}}_{\mathrm{boundary}}$, where $\mathcal{F}^{\mathrm{GL}}_{\phi,\mathrm{boundary}}$ is given in terms of an expansion of a local order parameter at the boundaries. First, we use the reverse product rule to rewrite the gradient term:

$$(\nabla\phi')^2 = \nabla \cdot (\phi'\nabla\phi') - \phi'\nabla^2\phi' , \tag{4.7}$$

then we use Stokes' theorem on the first term in Eq. (4.1):

$$\int (\nabla\phi')^2 \, \mathrm{d}V = \int \left[\nabla \cdot (\phi'\nabla\phi') - \phi'\nabla^2\phi' \right] \mathrm{d}V$$
$$= \int \phi'\nabla\phi' \, \mathrm{d}S - \int \phi'\nabla^2\phi' \, \mathrm{d}V \tag{4.8}$$

where for a thin film on a substrate the surface integral has two terms: one at the free surface and one at the interface with the substrate:

$$\mathcal{F}'^{\mathrm{GL}} = \frac{1}{V} \int_V \left[\frac{1}{4}\phi'^4 - \frac{1}{2} \left(1 - 2AX_\phi(1-\sigma')^2 \right) \phi'^2 - \lambda^2\phi'\nabla^2\phi' \right] \mathrm{d}V$$
$$+ \frac{1}{V} \int_{\mathrm{s}} \left[\lambda^2 \left(\hat{n} \cdot \nabla\phi' \right) \phi' \right] \mathrm{d}S \tag{4.9}$$
$$+ \frac{1}{V} \int_{\mathrm{i}} \left[\lambda^2 \left(\hat{n} \cdot \nabla\phi' \right) \phi' \right] \mathrm{d}S$$

where s and i refer to the surface and interface, respectively. Note that the surface free energies are also in units of $\frac{1}{2}X_\phi^{-1}$, and the surface integrals are dimensionless.

Next we claim that there must be a difference in the energies at the boundaries compared to the interior of the film [26, 25, 28], which can described using an expansion of the local order parameters at the boundaries:

$$\mathcal{F}'^{\text{GL}}_{\phi,\text{boundary}} = \frac{1}{V} \int_{\text{s}} \left[\lambda^2 \left(\hat{n} \cdot \nabla \phi' \right) \phi' + \frac{1}{2} \delta_{\text{s}} \phi'^2 \right] \mathrm{d}S$$
$$+ \frac{1}{V} \int_{\text{i}} \left[\lambda^2 \left(\hat{n} \cdot \nabla \phi' \right) \phi' + \frac{1}{2} \delta_{\text{i}} \phi'^2 \right] \mathrm{d}S \tag{4.10}$$

The quadratic coefficient of the surface order parameter describes the relative difference between the energy of the tilts at the surface and the energy per unit volume of the tilts in the bulk, and therefore must have units of length. We call this the extrapolation length, δ. δ_{s} and δ_{i} are the surface and interface extrapolation lengths, respectively, which describe the difference in energy at the surface and interface with respect to the bulk, see Figs. 4.1 (b) and (c). In general, higher order terms could be included in this expansion, but we assume that the leading term is the quadratic one [28]. Also, the boundaries may have a temperature dependence which differs from the bulk, which could lead to a change in sign of the extrapolation lengths.

Minimizing the total free energy in the bulk and at both boundaries, we get

$$\phi'^3 - \left(1 - 2AX_\phi (1 - \sigma')^2 \right) \phi' - \lambda^2 \nabla^2 \phi' = 0$$
$$\left(\hat{n} \cdot (\nabla \phi') \right) + \frac{\delta_{\text{i}}}{\lambda^2} \phi' = 0, \qquad z = 0$$
$$\left(\hat{n} \cdot (\nabla \phi') \right) + \frac{\delta_{\text{s}}}{\lambda^2} \phi' = 0, \qquad z = d \tag{4.11}$$
$$\sigma' = 1 - \frac{1}{1 + \frac{A}{P_0^2/\varepsilon} \langle \phi'^2 \rangle} \left(\frac{d_{\text{c}}}{d} + \mathcal{E}' \right)$$

This is the generalization of Eq. (3.15) but with inhomogeneous tilts. The expression for σ' is almost identical, but with the square of the tilt replaced with the mean of the square of the tilt throughout the film. ϕ' is described by a second order differential equation plus two boundary conditions, one for the free surface and one for the interface. These boundary conditions are referred to as Robin boundary conditions, i.e. a linear combination of the tilt and its gradient at each boundary. The equations for ϕ' and σ' are again self-consistent, making them difficult to solve. In the previous chapter we used physical constraints to determine the character of the carrier and tilt transitions under various conditions, summarized in Fig. 3.4, but this would be difficult or impossible for Eq. (4.11). Thus, our only option is obtaining numerical solutions, solving for σ' and ϕ' iteratively until both are converged below a suitable tolerance.

This approach was used in the previous chapter to obtain the order parameter plots shown in Figs. 3.5, 3.6 and 3.9. With Eq. (4.11) however, each step requires the solution of a nonlinear second order differential equation with Robin boundary conditions, which is not trivial. Before examining solutions to Eq. (4.11), we briefly describe the methods used to solve the differential equations.

4.1.1 Solutions to nonlinear ODEs with Robin boundary conditions

Consider a one-dimensional nonlinear ordinary differential equation (ODE):

$$\phi''(z) + f(\phi(z)) = 0 .$$

(4.12)

We discretize the equation using finite difference methods by discretizing real space with an evenly spaced grid: $z_n = z_0 + nh$, and using central differences to approximate the second derivative:

$$\phi''(z_n) = \frac{\phi(z_{n+1}) - 2\phi(z_n) + \phi(z_{n-1})}{h^2} .$$

(4.13)

Thus, Eq. (4.12) becomes

$$\phi(z_{n+1}) - 2\phi(z_n) + \phi(z_{n-1}) + h^2 f_n = 0, \quad n = 1, \dots, N-1$$

(4.14)

Consider a situation where the values at the boundaries are fixed:

$$\begin{aligned} \phi(z_0) &= \alpha \\ \phi(z_n) &= \beta \end{aligned} .$$

(4.15)

We can write Eq. (4.14) as a nonlinear system of the form

$$\mathbf{G}(\boldsymbol{\phi}) = \begin{bmatrix} (\alpha - 2\phi_1 + \phi_2) + h^2 f_1 \\ (\phi_1 - 2\phi_2 + \phi_3) + h^2 f_2 \\ \vdots \\ (\phi_{N-3} - 2\phi_{N-2} + \phi_{N-1}) + h^2 f_{N-2} \\ (\phi_{N-2} - 2\phi_{N-1} + \beta) + h^2 f_{N-1} \end{bmatrix} = 0, \tag{4.16}$$

where $\boldsymbol{\phi} = \{\phi_1, \dots, \phi_{N-1}\}$, and $\phi_n \equiv \phi(z_n)$, etc.

Eq. (4.16) can be solved iteratively using Newton's method. Starting with an initial guess $\boldsymbol{\phi}^0$, the kth iteration is obtained by Taylor expanding Eq. (4.16):

$$G(\phi^{k+1}) = G(\phi^k) + G'(\phi^k)(\phi^{k+1} - \phi^k), \tag{4.17}$$

where we drop the vector notation. If ϕ^{k+1} is the solution then $G(\phi^{k+1}) = 0$, and rearranging gives

$$\phi^{k+1} = \phi^k - J^{-1}(\phi^k)G(\phi^k), \tag{4.18}$$

where J is the Jacobian matrix:

$$J_{ij} = \partial_j G_i. \tag{4.19}$$

Fortunately, we can write down the Jacobian analytically:

$$J = \begin{bmatrix} -2 + h^2 f_1' & 1 & 0 & \cdots & & 0 \\ 1 & -2 + h^2 f_2' & 1 & & & \\ 0 & \ddots & \ddots & \ddots & & \\ \vdots & & 1 & -2 + h^2 f_{N-2}' & 1 \\ 0 & \cdots & & 1 & -2 + h^2 f_{N-1}' \end{bmatrix}, \tag{4.20}$$

which greatly reduces the computational effort required to calculate Eq. (4.18).

Eq. (4.16) assumes fixed values at the boundaries (Dirichlet boundary conditions). However, the ODE in Eq. (4.11) has Robin boundary conditions, a linear combination of the function and its derivative at each boundary:

$$\begin{aligned} \alpha_0 \partial_z \phi_0 + \beta_0 \phi_0 = \gamma_0 \\ \alpha_N \partial_z \phi_N + \beta_N \phi_N = \gamma_N \end{aligned}. \tag{4.21}$$

These can be treated using the 'ghost point method', where we include fictitious points z_{-1} and z_{N+1} to write the derivatives at the boundary using central differences:

$$\begin{aligned} \partial_z \phi_0 = \frac{\phi_1 - \phi_{-1}}{2h} \\ \partial_z \phi_N = \frac{\phi_{N+1} - \phi_{N-1}}{2h} \end{aligned} \tag{4.22}$$

Discretizing the derivatives in Eq. (4.21), we get

$$\begin{aligned} \alpha_0 \left(\frac{\phi_1 - \phi_{-1}}{2h} \right) + \beta_0 \phi_0 = \gamma_0 \\ \implies \phi_{-1} = \phi_1 + 2h \frac{\beta_0}{\alpha_0} \phi_0 - 2h \frac{\gamma_0}{\alpha_0} \\ \phi_{N+1} = \phi_{N-1} - 2h \frac{\beta_N}{\alpha_N} \phi_N + 2h \frac{\gamma_N}{\alpha_N} \end{aligned}. \tag{4.23}$$

Discretizing the ODE, Eq. (4.12) becomes

$$\phi_{n+1} - 2\phi_n + \phi_{n-1} + h^2 f_n = 0, \quad n = 0, \ldots, N \tag{4.24}$$

which is identical to Eq. (4.14), but the range has been extended to include the ghost points. The vector G then becomes

$$G(\phi) = \begin{bmatrix} (\phi_{-1} - 2\phi_0 + \phi_1) + h^2 f_0 \\ (\phi_0 - 2\phi_1 + \phi_2) + h^2 f_1 \\ \vdots \\ (\phi_{N-2} - 2\phi_{N-1} + \phi_N) + h^2 f_{N-1} \\ (\phi_{N-1} - 2\phi_N + \phi_{N+1}) + h^2 f_N \end{bmatrix} = 0 . \tag{4.25}$$

Using Eq. (4.23) to write the values of ϕ at the ghost points, we get

$$\phi_{-1} - 2\phi_0 + \phi_1 + h^2 f_0 = 0$$
$$\implies -2\left(1 - h\frac{\beta_0}{\alpha_0}\right)\phi_0 - 2h\frac{\gamma_0}{\alpha_0} + 2\phi_1 + h^2 f_0 = 0 , \tag{4.26}$$
$$\implies -\left(1 - h\frac{\beta_0}{\alpha_0}\right)\phi_0 + \phi_1 + \frac{h^2}{2}f_0 - h\frac{\gamma_0}{\alpha_0} = 0$$

for ϕ_{-1}, and similarly for ϕ_{N+1}. Thus, the vector G becomes

$$G(\phi) = \begin{bmatrix} -\left(1 - h\frac{\beta_0}{\alpha_0}\right)\phi_0 + \phi_1 + \frac{h^2}{2}f_0 - h\frac{\gamma_0}{\alpha_0} \\ (\phi_0 - 2\phi_1 + \phi_2) + h^2 f_1 \\ (\phi_1 - 2\phi_2 + \phi_3) + h^2 f_2 \\ \vdots \\ (\phi_{N-3} - 2\phi_{N-2} + \phi_{N-1}) + h^2 f_{N-2} \\ (\phi_{N-2} - 2\phi_{N-1} + \phi_N) + h^2 f_{N-1} \\ x_{N-1} - \left(1 - h\frac{\beta_N}{\alpha_N}\right)\phi_N + \frac{h^2}{2}f_N - h\frac{\gamma_N}{\alpha_N} \end{bmatrix} = 0 . \tag{4.27}$$

In this case, the Jacobian is

$$J = \begin{bmatrix} \left(-1+h\frac{\beta_0}{\alpha_0}\right)+\frac{h^2}{2}f_0' & 1 & 0 & \cdots & \cdots & \cdots & 0 \\ 1 & -2+h^2f_1' & 1 & 0 & \cdots & \cdots & \vdots \\ 0 & 1 & -2+h^2f_2' & 1 & 0 & \cdots & \vdots \\ \vdots & \cdots & \ddots & \ddots & \ddots & \cdots & \vdots \\ \vdots & \cdots & 0 & 1 & -2+h^2f_{n-2}' & 1 & 0 \\ \vdots & \cdots & \cdots & 0 & 1 & -2+h^2f_{n-1}' & 1 \\ 0 & \cdots & \cdots & \cdots & 0 & 1 & \left(-1+h\frac{\beta_n}{\alpha_n}\right)+\frac{h^2}{2}f_n' \end{bmatrix}. \quad (4.28)$$

4.1.2   Coupling between carriers and inhomogeneous tilts

Eq. (4.11) is solved as follows: the tilt profile inside the film is obtained by solving the first three lines using finite difference methods. The mean of the tilt squared in the film is then used to calculate the carrier concentration, which is re-inserted into the ODE. The two are solved self-consistently until their relative changes between successive iterations are below a suitable tolerance.

For a given set of system parameters, we can obtain order parameter plots as a function of thickness or applied field, similar to Figs. 3.5 and 3.6. The main difference with the inhomogeneous tilts is that λ, δ_s and δ_i need to be specified, in addition to X_ϕ^{-1}, A and d_c. Thus, for inhomogeneous tilts, Fig. 3.4 becomes five dimensional, and systemically navigating such a diagram would be impractical.

It is also difficult to estimate λ, δ_s and δ_i. Previous studies have fixed λ to a small number of unit cells [27]. In Ref. [89], λ is estimated to be around 1-2 unit cells in bulk LAO from calculations of the dispersion of the phonon branch corresponding to the $a^-a^-c^0$ tilt. To our knowledge, it is not possible to directly measure the extrapolation lengths. In principle, one could fit measurements of tilts in a thin film, either from experiment or first-principles calculations, to Eq. (4.11), but the tilts at the boundaries are strongly affected by both the correlation length and the extrapolation length, which would lead to overfitting.

It is helpful to note that, since we only consider indirect coupling, the carrier concentration depends only on the mean of the square of the tilts, and not on the specific shape of the tilts. Thus, we can understand the influence of the inhomogeneity of the tilts by fixing the extrapolation lengths and allowing the correlation length to change.
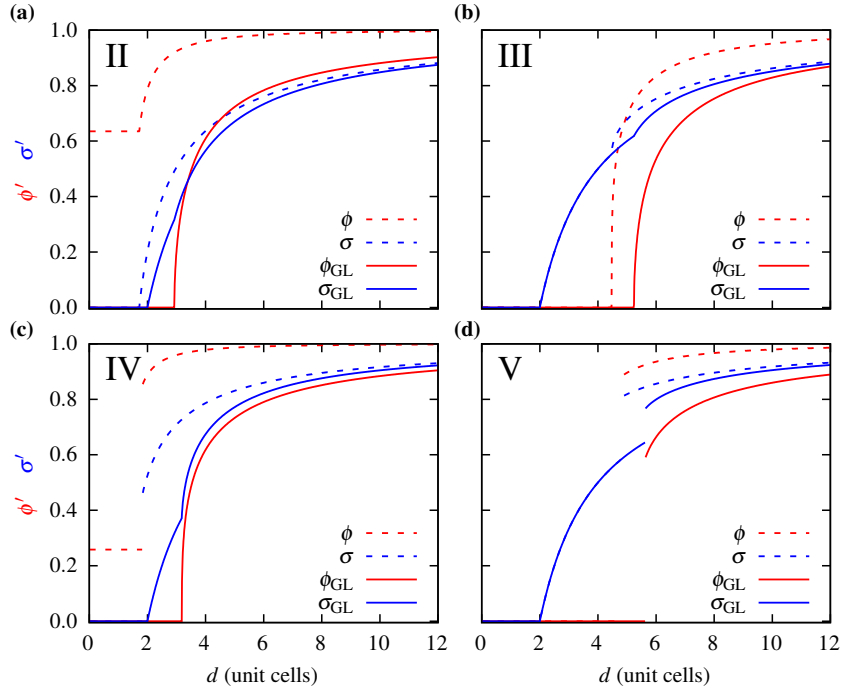
Fig. 4.2 Order parameter plots in the four coupled regions in Fig. 3.4, for both homogeneous (dashed lines) and inhomogeneous (solid lines) tilts. **(a)**: Region II (red): $X_\phi^{-1} = 1.36454$, $A = 0.407$. **(b)**: Region III (green): $X_\phi^{-1} = 0.2$, $A = 0.5$. σ and σ_{GL} are identical between d_c and d_ϕ. **(c)**: Region IV (yellow): $X_\phi^{-1} = 3$, $A = 1.4$. **(d)**: Region V (blue): $X_\phi^{-1} = 0.5$, $A = 1.5$. σ and σ_{GL} are identical between d_c and d_ϕ. In all regions, $d_c = 2$ unit cells.

First, we examine the behavior of the order parameters in the different regions in Fig. 3.4 and compare them to results obtained for homogeneous tilting. For each region, we set $\lambda = 2$ unit cells, $d_c = 2$ unit cells, the thickness at which a density of trapped Ti $3d$-like states has been observed in LAO/STO [296–299], $\delta_i = 5$ unit cells and $\delta_s = 0$. The order parameter plots are shown in 4.2 (solid lines), alongside the corresponding result from the homogeneous theory (dashed lines). We see that, for this choice of parameters, all of the points except the one in region V shift to region III when the tilts become inhomogeneous. In all cases, the carriers appear continuously at d_c, and d_ϕ increases with respect to the corresponding scenario from the homogeneous theory. This makes sense, since at smaller thicknesses there would be a large gradient in the tilts and hence a large energy penalty. Thus, the tilts can only appear at larger thicknesses, where the magnitude is roughly constant inside the bulk of the film and only changes in a small region near both boundaries.

Next, we examine the effect of changing λ. We found that for regions III and V, the transitions remain in regions III and V, but the value of d_ϕ is sensitive to λ. For regions II and IV, the
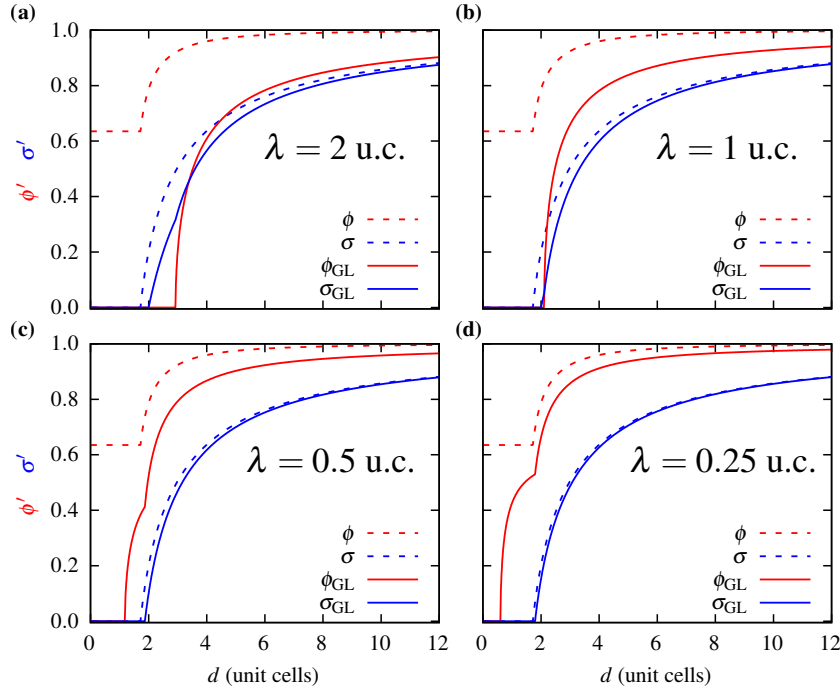
Fig. 4.3 Order parameter plots in region II for several values of λ, for both homogeneous (dashed lines) and inhomogeneous (solid lines) tilts. **(a)**: $\lambda = 2$ unit cells, **(b)**: $\lambda = 1$ unit cell, **(c)**: $\lambda = 0.5$ unit cells, and **(d)**: $\lambda = 0.5$ unit cells.

points move through different regions as λ decreases, shown in Figs. 4.3 and 4.4, respectively. As λ decreases, and there is less of a penalty for the inhomogeneity of the tilts, d_ϕ decreases, and eventually the order of the transitions reverse, which occurs continuously in region II (Figs. 4.3 (c) and (d)) and discontinuously in region IV (Fig. 4.4 (d)). These types of transitions do not correspond to any of the regions in Fig. 3.4, so we label them regions VI and VII. In region VI, tilts first appear continuously at d_ϕ, and then carriers at a critical thickness between d_ϕ and d_c. In region VII, the order of the transitions with thickness is the same, but the carriers appear discontinuously.

In Fig. 4.5 we summarize the transitions observed in the inhomogeneous theory. Regions III and V remain unchanged, with the exception that d_ϕ is renormalized by λ. For regions II and IV, the type of transition can change, depending on the value of λ (and the other parameters). The different transitions that can occur by changing λ but fixing the rest of the parameters are shown. For $\lambda \to \infty$, the homogeneous case is realized. As λ decreases, the character of the transition changes. For sufficiently small λ, two entirely new types of transitions occur, which we label region VI (Figs. 4.3 (c) and (d)) and region VII (Fig. 4.4 (d)).
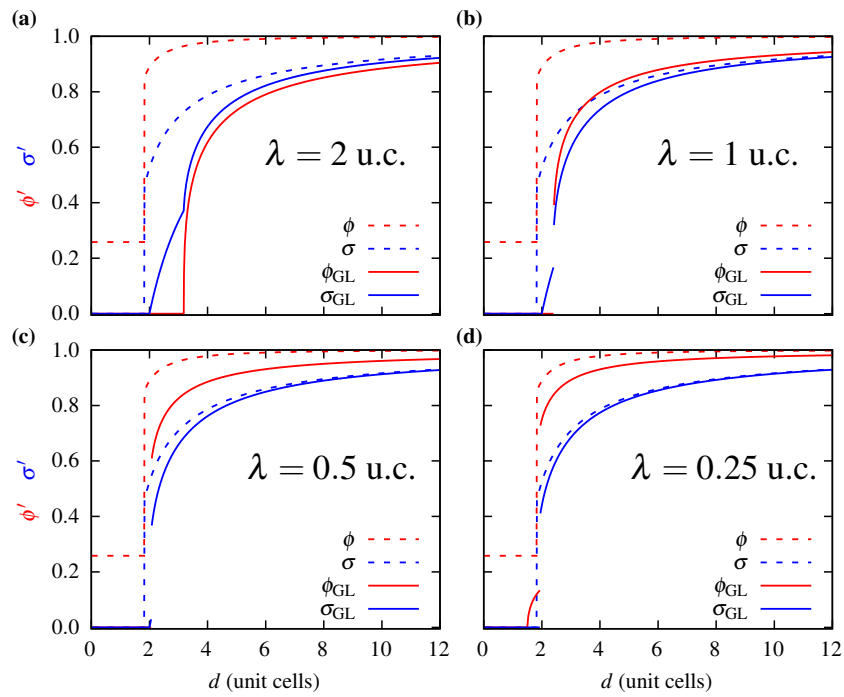
Fig. 4.4 Order parameter plots in region IV for several values of λ, for both homogeneous (dashed lines) and inhomogeneous (solid lines) tilts. (a): $\lambda = 2$ unit cells, (b): $\lambda = 1$ unit cell, (c): $\lambda = 0.5$ unit cells, and (d): $\lambda = 0.5$ unit cells.

Fig. 4.5 Summary of the additional carrier and tilt transitions which can occur when the tilts are inhomogeneous. The sequence of transitions which can occur in regions II and IV by changing λ (fixing the rest of the parameters) are shown below and above the diagram, respectively.

4.2 Direct coupling between tilts and oxygen vacancies

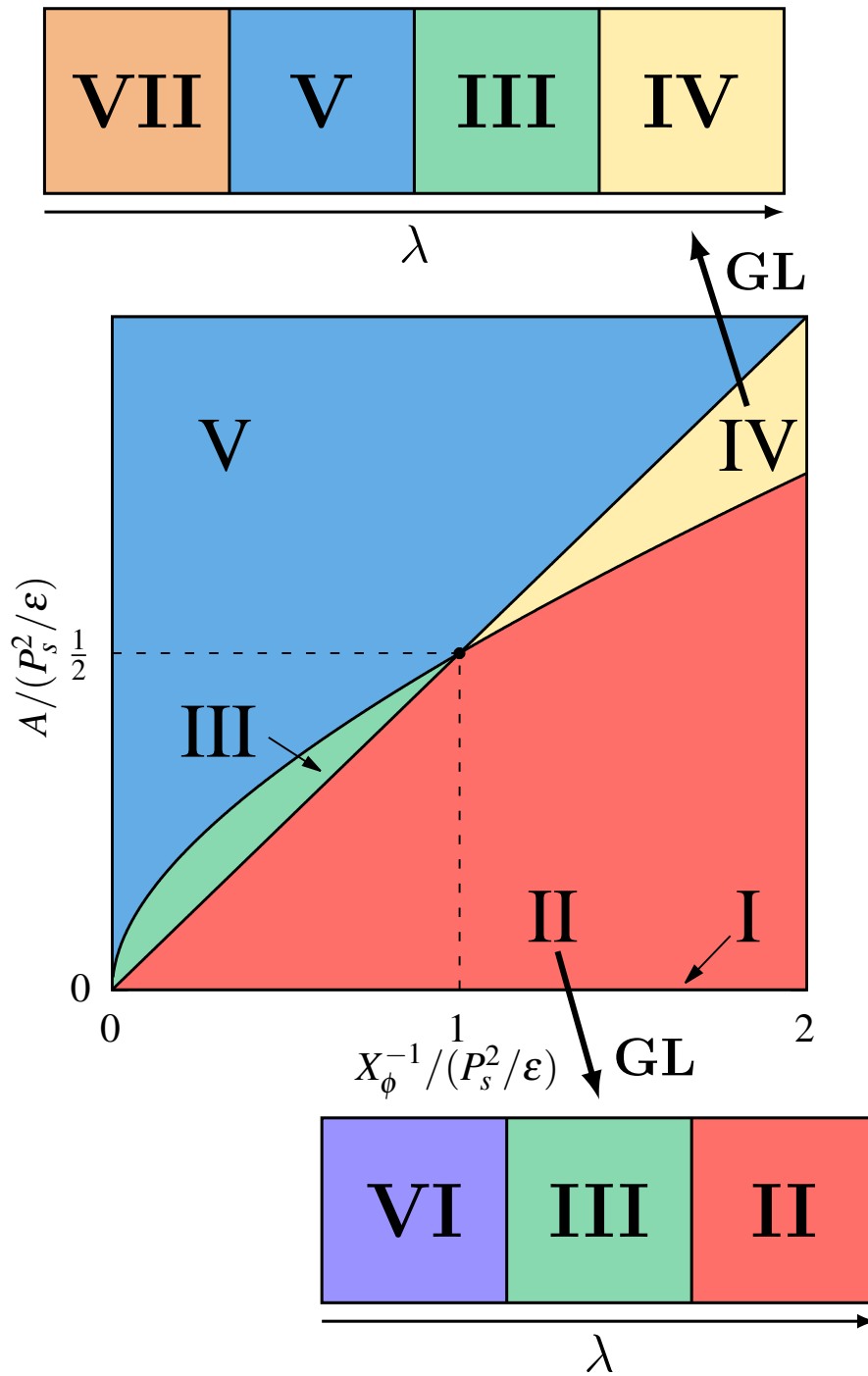So far, we have only considered the indirect biquadratic coupling between the carriers and the tilts through the polar mode. However, other types of interactions between tilts and carriers may be possible. For example, if carriers at the interface are generated by oxygen vacancies at the free surface of the film, there would be a direct coupling at the surface, since removing an oxygen vacancy may break an oxygen octahedron. This coupling may have a large influence on the tilts at the surface which could propagate into the film, and even the substrate for very thin films.

In this section we show results from first principles calculations of the LAO/STO interface[1], where carriers are induced at the interface both via oxygen vacancies at the surface and fictitiously via the use of virtual atoms with fractional charge. We found that the behavior of the tilts is very different in both cases, motivating the study of the direct coupling between oxygen vacancies and the tilts at the surface.

4.2.1 First-principles calculations of the LAO/STO interface

First-principles calculations were performed using the SIESTA code [272], which employs a basis of localized numerical atomic orbitals (NAOs) [270]. Real space integrations were performed on a uniform real space grid with an equivalent plane wave cutoff of 800 Ry, and a Monkhorst-Pack sampling [288] equivalent to $12 \times 12 \times 12$ in a five atom perovskite unit cell was used for BZ integrations. Calculations were carried out within the LDA. For geometry optimizations, the in-plane lattice parameter was fixed to the theoretical value for bulk STO ($a = 3.896$ Å), and a threshold of 0.001 eV/Åwas used for the forces. All atomic positions were allowed to relax, except for the layer at the bottom of the STO substrate, whose internal coordinates were fixed to the bulk structure in order to mimic the presence of a semi-infinite substrate.

A Hubbard U term [300] was added to the Ti $3d$ orbitals of STO in order to obtain a better approximation to the band gap and avoid underestimating the layer breakdown in LAO with film thickness. A value of $U = 8.5$ eV was found to produce a band gap of 2.95 eV, close to the experimental value of 3.2 eV [301, 302]. Such a large value greatly underestimates the relative permittivity and polarizabilitiy of STO, which is important for the tail of the 2DEG

---

[1]calculations performed by Pablo Aguado-Puente.

deep in the substrate, where the displacement field decreases and the dielectric constant massively increases [303]. However, the tail of the 2DEG is truncated in our calculations due to the finite thickness of the STO slab.

The calculations were performed on vacuum-terminated $(SrTiO_3)_n/(LaAlO_3)_m$ slabs, where $n = 8, 15$ unit cells, and $m = 3$ unit cells. Three different mechanical boundary conditions were used, corresponding to different rotation patterns at the bottom of the substrate. At room temperature (RT), STO has an ideal undistorted perovskite structure. Below 105 K, AFD rotations of oxygen octahedra emerge and the material evolves into a tegragonal phase, facilitated by a $a^0 a^0 c^-$ rotation, in Glazer notation [38]. This gives rise to two possible orientations of the tetragonal axis with respect to the interface: the tetragonal axis perpendicular (Z-domain) or parallel (X-domain) to the interface.

The electrical boundary conditions for the LAO film are determined by the presence of free charge at the free surface and interface with STO, coming from (i) an intrinsic breakdown due to the electric field resulting from the polar discontinuity from STO and LAO [304] or (ii) the oxygen vacancies on the free the surface. The vacancies can be introduced by removing one of the oxygen atoms from the AlO_2 surface; removing one oxygen atom from a 2×2 in-plane supercell is equivalent to imposing a displacement field of $D = 0.5$ electrons per unit cell surface area in LAO. In order to distinguish between the effect an oxygen vacancy has on just the electrostatic boundary conditions, and overall, i.e. also on the tilts, we used the virtual crystal approximation (VCA) to include 'virtual atoms' with fractional atomic numbers to gradually modify the electrostatic boundary conditions of the slab [305]. In this case, substituting the oxygen atom at the surface with $O_{1-x}F_x$ can be used to mimic the presence of charged defects at different concentrations.

The tilt profiles for the Z domain are shown in Fig. 4.6, for a LAO film which is 3 unit cells thick. The hollow points represent calculations with no 2DEG, and the filled points represent calculations where the 2DEG was induced using the VCA and explicitly via oxygen vacancies at the surface in Figs. 4.6 (a) and (b), respectively. Note that ϕ corresponds to the $a^- a^- c^0$ tilt, which is the one observed in LAO under biaxial strain, and θ is the tilt $a^0 a^0 c^-$ axis, which does not couple as strongly with the polar mode. We can see for the Z domain calculations, the ϕ tilt is zero, both in LAO and STO. We can see that in the oxygen vacancy calculations a very large tilt is induced at the interface, which decays into the thin film and into STO. This effect is completely absent in the VCA calculations however, indicating that there is a significant coupling between carriers / vacancies and tilts, beyond the indirect

biqaudratic coupling through the polar mode, which has not yet been considered in our model.
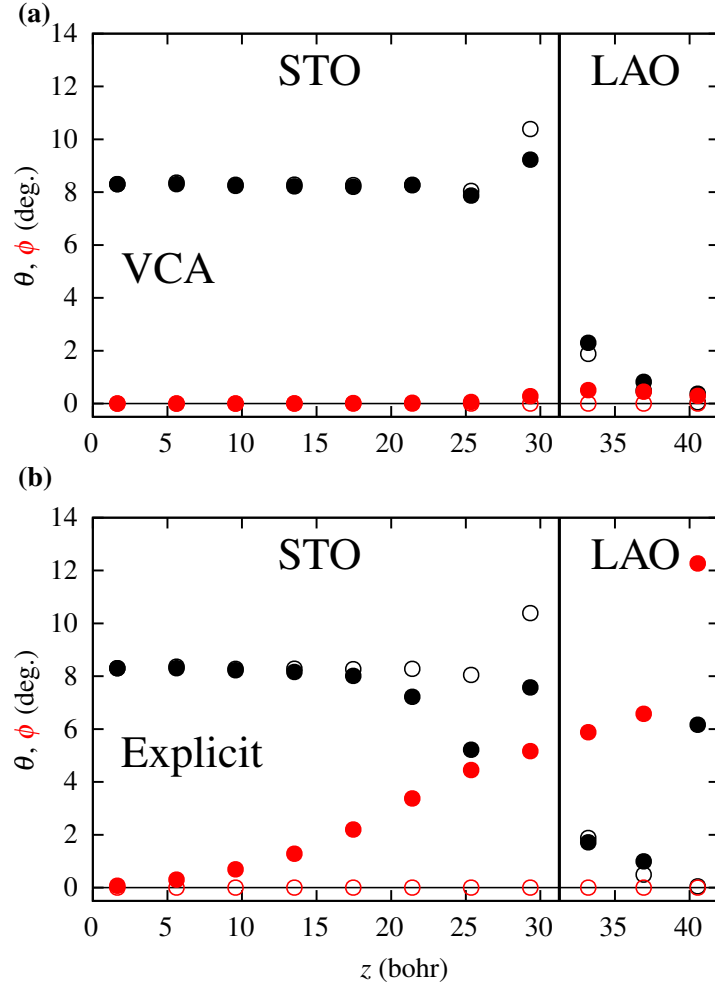
Fig. 4.6 Tilt profiles in LAO/STO from first-principles calculations for **(a)**: VCA **(b)**: explicit oxygen vacancies. The hollow points show results with no 2DEG, and the filled points show results with a fully saturated 2DEG.

4.2.2   Direct coupling between tilts and vacancies

Starting with the phenomenological theory proposed in the previous section which describes the formation of carriers, including coupling to inhomogeneous tilts, we propose a direct coupling between the oxygen vacancies and the tilts at the surface ϕ'_s:

$$\mathcal{F}'^{\text{direct}} = \frac{1}{d}\beta_1 \sigma' \left|\phi'_s\right| + \frac{1}{d}\beta_2 \sigma' \phi'^2_s \,, \tag{4.29}$$

We also include the a term which is quadratic in the surface tilt. β_i have units of length, and represent of the energy per unit area of the direct couplings with respect to the energy per unit volume of the bulk tilt, similar to the extrapolation lengths introduced in the previous section. When $\beta_i < 0$ it becomes favorable for a tilt to appear at the surface when carriers appear via oxygen vacancies. The Ginzburg-Landau free energy developed in the previous section is now given by

$$
\begin{aligned}
\mathcal{F}'^{\text{GL}} = {} & 2X_\phi \frac{P_s^2}{\varepsilon}\left(\frac{d_{\text{c}}}{d}\sigma' + \frac{1}{2}\left(1-\sigma'\right)^2\right) \\
& + \frac{1}{V}\int_V \left[\frac{1}{4}\phi'^4 - \frac{1}{2}\left(1-2AX_\phi\left(1-\sigma'\right)^2\right)\phi'^2 - \lambda^2\phi'\nabla^2\phi'\right]dV \\
& + \frac{1}{V}\int_s \left[\lambda^2\left(\hat{n}\cdot\nabla\phi'_s\right)\phi'_s + \frac{1}{2}\delta_s\phi'^2_s + \beta_1\sigma'\left|\phi'_s\right| + \beta_2\phi'^2_s\right]dS \\
& + \frac{1}{V}\int_i \left[\lambda^2\left(\hat{n}\cdot\nabla\phi'_s\right)\phi'_s + \frac{1}{2}\delta_i\phi'^2_s\right]dS
\end{aligned}
\tag{4.30}
$$

The last two lines describe the boundary conditions of the tilts at the free surface, which includes the direct coupling between the surface tilt and oxygen vacancy, and the interface with the substrate. Minimizing Eq. (4.30) with respect to σ', we get

$$\sigma' = 1 - \frac{1}{1+\frac{A}{P_0^2/\varepsilon}\langle\phi'^2\rangle}\left(\frac{d_{\text{c}}}{d} + \frac{\frac{1}{2}X_\phi^{-1}}{P_s^2/\varepsilon}\frac{1}{d}\left(\beta_1\left|\phi'_s\right| + \beta_2\phi'^2_s\right)\right) \,, \tag{4.31}$$

where we take the surface tilt to be averaged in-plane. The surface tilt is determined by the following boundary condition:

$$\hat{n}\cdot\left(\nabla\left|\phi'_s\right|\right) + \frac{1}{\lambda^2}\left(\delta_s + \beta_2\sigma'\right)\left|\phi'_s\right| + \frac{1}{\lambda^2}\beta_1\sigma' = 0 \,, \tag{4.32}$$

The general solution to Eq. (4.32) is

$$\left| \phi'_s \right| = c_1 e^{-\frac{1}{\lambda^2}(\delta_1 + \beta_2)(z-d)} - \frac{\beta_1 \sigma'}{\delta_1 + \beta_2 \sigma'} \tag{4.33}$$

(a)

(b)

Fig. 4.7 Solutions to Eq. (4.34) at several values of β_1, in units of $|\beta_1^*|$, with $\beta_2 = 0$, $\delta_s = d_c$, and $\frac{P_s^2}{\varepsilon} = \frac{1}{2}X_\phi^{-1}$.

We could proceed to minimize the Eq. (4.30) numerically for σ' and ϕ' as we did in the previous chapter. First, it is instructive to examine the effect of the direct coupling in isolation. In order to do this, we neglect the direct coupling between tilts and carriers by setting $A = 0$ in Eq. (4.31). Also, we assume that in the absence of oxygen vacancies there are no tilts in the film, as observed in Fig. 4.6. This can be achieved by setting $c_1 = 0$ in Eq. (4.33). Then, σ' and ϕ' are obtained by self-consistently solving
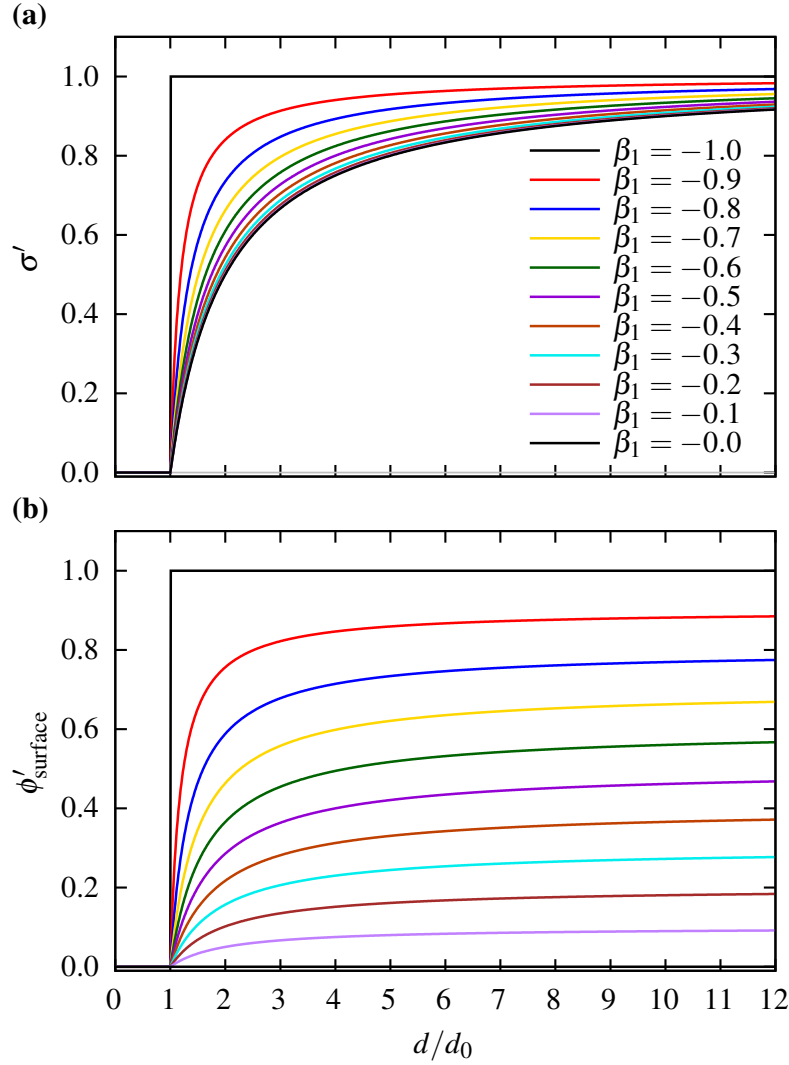
(a)

(b)
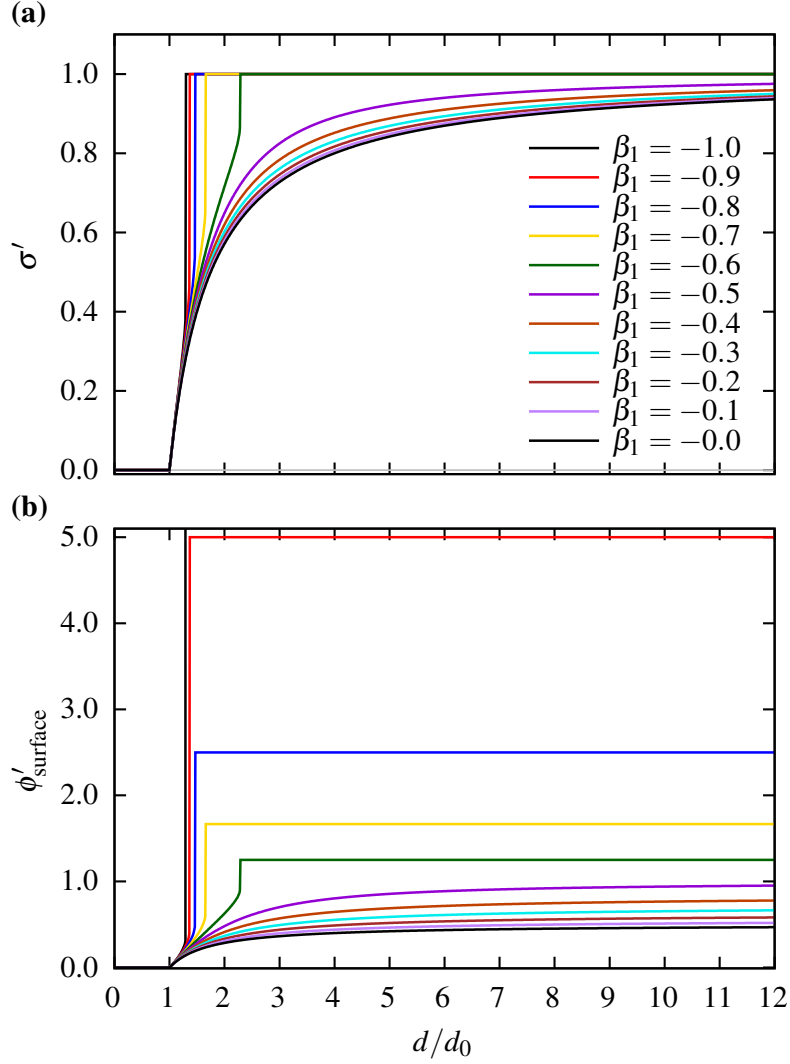
Fig. 4.8 Solutions to Eq. (4.34) at several values of β_1, in units of $|\beta_1^*|$, with $\beta_2 = -0.5$, $\delta_s = d_c$, and $\frac{P_s^2}{\varepsilon} = \frac{1}{2}X_\phi^{-1}$.

$$\phi_s' = -\frac{\beta_1 \sigma'}{\delta_s + \beta_2 \sigma'}$$
$$\sigma' = 1 - \left(\frac{d_c}{d} + \frac{\frac{1}{2}X_\phi^{-1}}{P_s^2/\varepsilon} \frac{1}{d} \left(\beta_1 |\phi_s'| + \beta_2 \phi_s'^2 \right) \right) \tag{4.34}$$

For $\beta_2 = 0$ and $\beta_1 < 0$, σ' switches on at d_c and increase more rapidly as $|\beta_1|$ increases. The appearance of carriers is always accompanied by the appearance of a surface tilt at d_c, i.e. the

oxygen vacancies always result in a surface tilt. σ' and ϕ'_s are plotted for several values of β_1 in Fig. 4.7. σ' and ϕ'_s both jump to 1 at d_c for a critic value of β_1:

$$\beta_1^* = -\sqrt{\left(\frac{P_s^2/\varepsilon}{\frac{1}{2}X_\phi^{-1}}\right)\delta_s d_c} \ . \tag{4.35}$$

If we switch on β_2, the surface tilt and carrier concentration are slightly enhanced at smaller values, but at larger values a discontinuous jump occurs, where σ' saturates to 1 and ϕ'_s saturates at a value larger than 1. Results for $\beta_2 \neq 0$ are shown in Fig. 4.8.
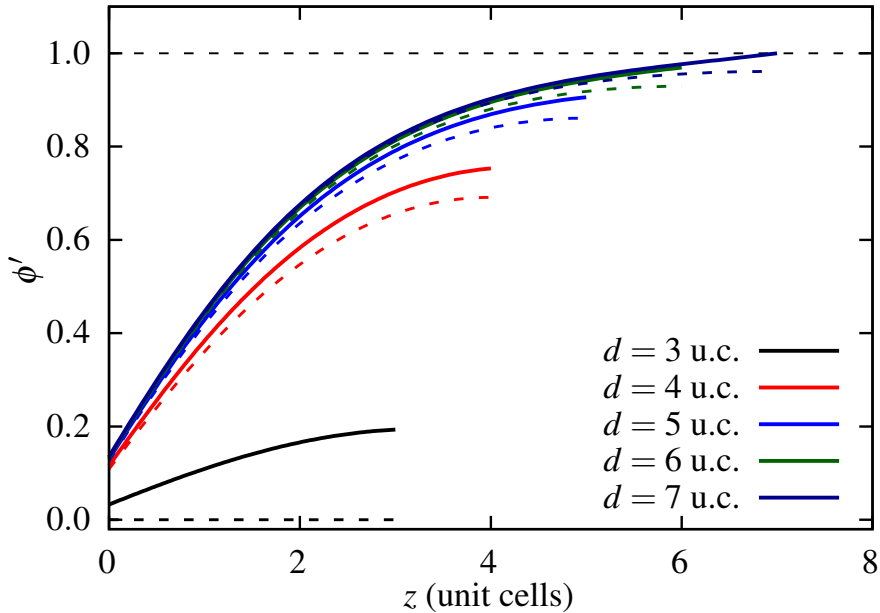

Fig. 4.9 Tilt profile for films of several thicknesses, with (solid lines) and without (dashed lines) direct coupling between tilts and oxygen vacancies. The values of the parameters used are: $X_\phi^{-1} = 1.36454$ and $A = 0.407$ obtained from PBEsol calculations, $\lambda = 2$ u.c., $\delta_i = 10$ u.c., $\delta_s = 0$ u.c., $d_c = 2$ u.c. and $\beta_1 = -0.125$.

Next, we proceed to minimize Eq. (4.30) and solve the resulting equations self-consistently, including the direct coupling at the surface. In Fig. 4.9 we plot the tilt profile $\phi'(z)$ in films of several thicknesses, both with and without direct coupling. We see that for $d = 3$ u.c., the film is predicted to be untilted without direct coupling, but with the direct coupling included, a tilt appears at the surface which decays into the film. A surface tilt occurs for any $\beta_1 < 0$ in films where $d > d_c$. As d increases, the contribution from direct coupling becomes negligible, and the bulk tilting in the interior of the film become dominant.

In Fig. 4.10 we plot σ' and $\phi'_{RMS} \equiv \sqrt{\langle\phi'^2\rangle}$ for several values of β_1. We can see that when $\beta_1 < 0$, the appearance of carriers at $d = d_c$ is always accompanied by a tilt at the surface. For stronger direct coupling, both carrier and tilts saturate more quickly. For sufficiently strong direct coupling, the carriers switch on discontinuously at d_c and are fully saturated.
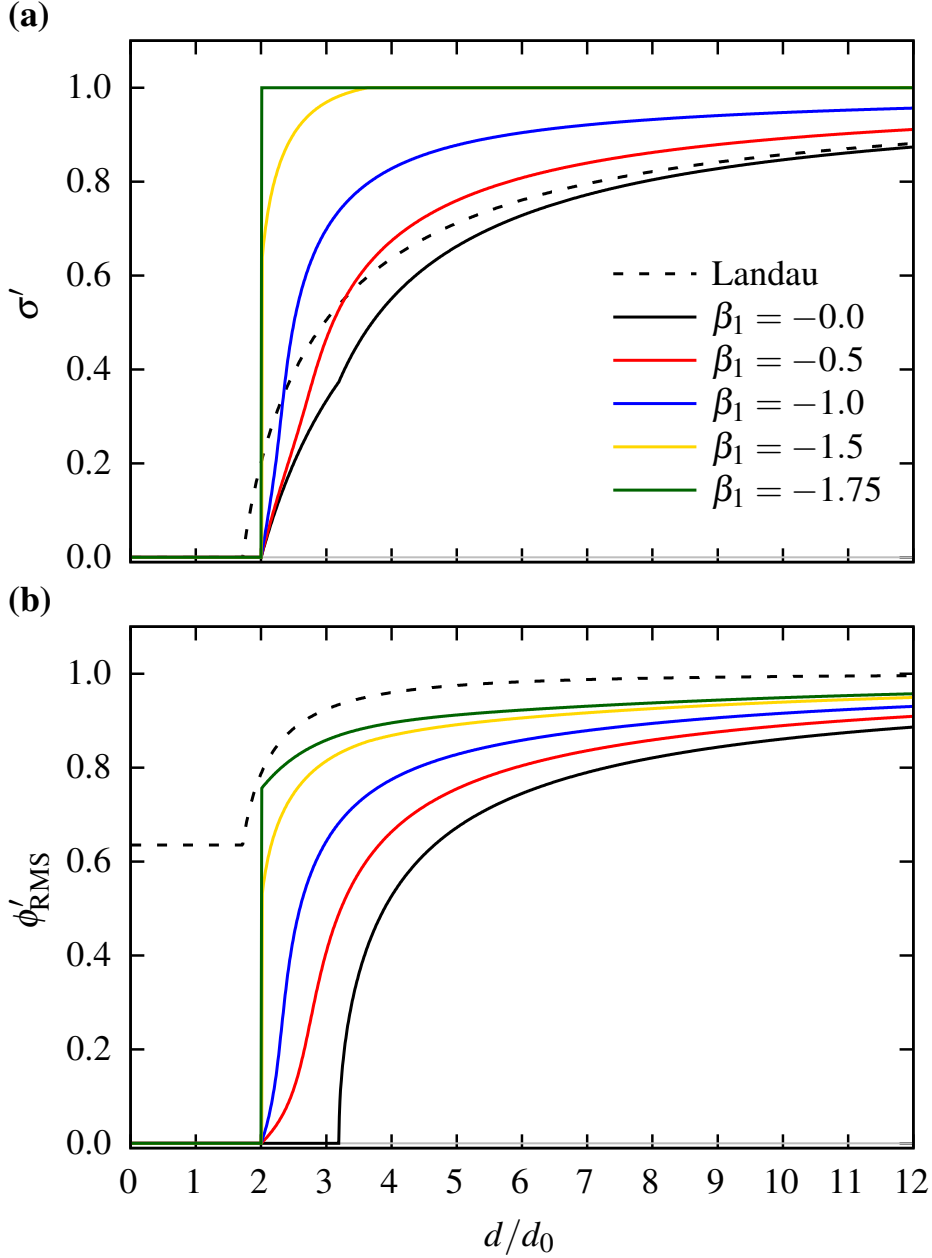

Fig. 4.10 Numerical solutions to Eq. (4.30) as a function of d for several values of β_1, with $\beta_2 = 0$. The dashed lines show similar results obtained for homogeneous tilting. The values of the parameters used are: $X_\phi^{-1} = 1.36454$ and $A = 0.407$ obtained from PBEsol calculations, $\lambda = 2$ u.c., $\delta_i = 10$ u.c., $\delta_s = 0$ u.c. and $d_c = 2$ u.c.

Chapter 5

Electrostatics and domains in ferroelectric superlattices

In this chapter we present a detailed study of the electrostatics of ferroelectric thin films and superlattices. As mentioned in the introduction, a ferroelectric film with a $180°$ stripe domain structure is a well-studied system. However, some details, and generalizations from a thin film in a vacuum to other geometries remain scattered in the literature. The purpose of this chapter is to provide a detailed review of the electrostatics of an isolated polydomain thin film in a vacuum (IF), and introduce the generalizations to a thin film on top of a substrate (overlayer, OL), a thin film sandwiched between two infinite dielectric media (SW), and a periodic ferroelectric/paraelectric superlattice (SL).

5.1   Review of electrostatics of a thin film in vacuum

The fundamental model used in this chapter is based on the following free energy per unit volume of a ferroelectric thin film in a vacuum with a $180°$ stripe domain structure [32, 33] (e.g. Fig. 1.6),

$$\mathcal{F} = \mathcal{F}_0(P) + \frac{\Sigma}{w} + \mathcal{F}_{\text{elec}}(w, d) , \qquad (5.1)$$

where $\mathcal{F}_0(P)$, defined as

$$\mathcal{F}_0(P) = \frac{1}{2\varepsilon_0 \kappa_c} \left(\frac{1}{4} \frac{P^4}{P_s^2} - \frac{1}{2} P^2 \right), \tag{5.2}$$

is the bulk ferroelectric energy with spontaneous polarization P_s and dielectric permittivity κ_c, which describes the curvature about $P = P_s$. Σ is the energy cost per unit area of creating a domain wall, $\mathcal{F}_{\mathrm{elec}}$ is the electrostatic energy associated with the depolarizing field, and w and d are the width of one domain and thickness of the film, respectively.

In the Kittel model, instead of solving for P in Eq. (5.2), the total polarization field $\mathbf{P}(\mathbf{r})$ is taken to deviate from the spontaneous polarization $\pm P_s$ in linear response to the electric depolarizing field, according to the dielectric susceptibilities normal and parallel to the film, κ_c and κ_a, respectively. This model makes significant approximations about the form of $\mathbf{P}(\mathbf{r})$, such as neglecting domain-wall width and surface/interface effects. Ferroelectric domain walls tend to be much thinner than ferromagnetic domain walls, typically of order 1 nm. Realistic descriptions of nanometric films should rather resort to theories with proper consideration of those effects, such as explicit first-principles calculations or Ginzburg-Landau (see for example Refs. [104, 105, 29]). There are situations, however, for which this model is relevant (in our case, this work was prompted by situations as described in Ref. [133]), and, more generally, a clear account for the behavior of this simple model in the electrostatic settings considered represents a valuable paradigmatic reference.

Since we will be interested in the electrostatic effects due to a finite polarization, we will consider the polarization to be P_s, except for its modification in linear response to the depolarizing field implicit when using a dielectric permittivity for the material normal to the field, κ_c. This assumption is equivalent to replacing the form of $\mathcal{F}_0(P)$ in Eq. 5.2 by

$$\mathcal{F}_0(P) = \frac{1}{2\varepsilon_0 \kappa_c} (P - P_s)^2. \tag{5.3}$$

The equilibrium domain structure for this system for a given thickness is obtained by minimizing the energy: $\partial_w \mathcal{F} = 0$.

As mentioned above, we consider an ideal domain structure made by regular straight stripes of width w. For an isolated film, the electrostatic energy for such a structure is given by [30]

$$\mathcal{F}_{\text{elec}} = \frac{8P_s^2}{\varepsilon_0\pi^3}\frac{w}{d}\sum_{n\text{ odd}}\frac{1}{n^3}\frac{1}{1+\chi\kappa_c\coth\left(\frac{n\pi}{2}\chi\frac{d}{w}\right)}\ , \tag{5.4}$$

where κ_a, κ_c are the dielectric permittivities in the directions parallel and normal to the film and $\chi = \sqrt{\kappa_a/\kappa_c}$ is the dielectric anisotropy of the film. In the Kittel limit [32, 33], $\frac{w}{d} \ll 1$, Eq. (5.4) reduces to

$$\mathcal{F}_{\text{elec}}^{\text{Kittel}} = \frac{P_s^2}{2\varepsilon_0}\beta\frac{w}{d}\ , \tag{5.5}$$

where

$$\beta = \frac{14\zeta(3)}{\pi^3}\frac{1}{1+\chi\kappa_c}\ , \tag{5.6}$$

and $\zeta(n)$ is the Riemann zeta function. An analytic expression is obtained for the equilibrium domain width:

$$w(d) = \sqrt{l_k d}\ , \tag{5.7}$$

where

$$l_k = \frac{2\varepsilon_0\Sigma}{P_s^2\beta} \tag{5.8}$$

is the Kittel length, which defines a characteristic length scale of the system. Eq. (5.7) is known as Kittel's law [32].

Beyond the Kittel regime, we can obtain the equilibrium domain width from the numerical solution to Eq. (5.1) for the full electrostatic expression in Eq. (5.4). In Fig. 5.1, we plot the domain width as a function of thickness both from the Kittel law and Eq. 5.4 with numerical solutions, truncated at $n = 100$ terms. We use PTO and STO as examples of ferroelectric and paraelectric materials, respectively, using suitable parameters. PTO and STO are some of the the most widely studied ferroelectric and paraelectric materials respectively, both experimentally and theoretically, particularly in the context of FE/PE superlattices. The
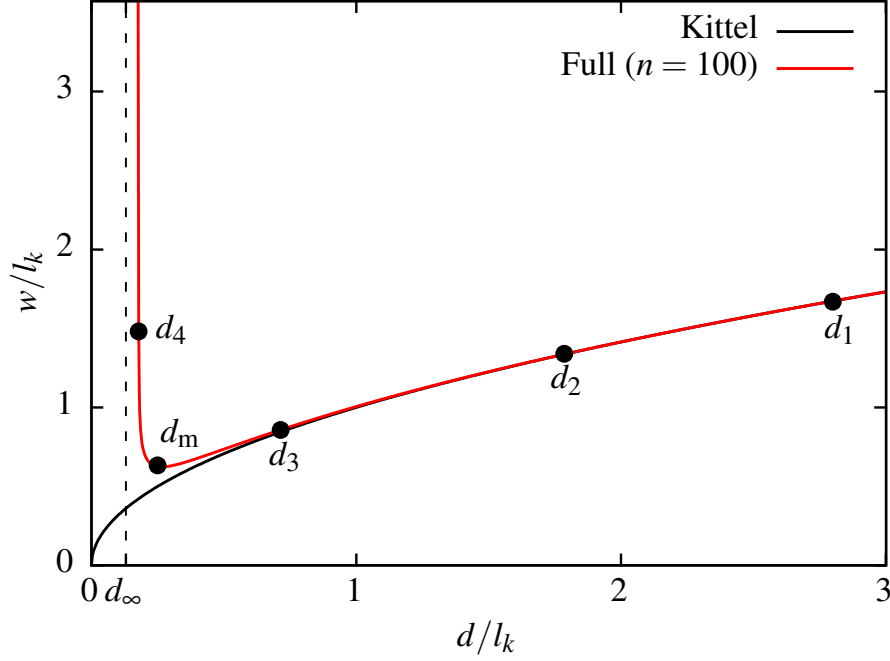
Fig. 5.1 Equilibrium domain width as a function of thickness for an isolated thin film. The red curve shows the numerical solution using the full expression for the electrostatic energy, truncated at $n = 100$ terms. The solid black curve is the Kittel curve, scaled by the Kittel length: $w(d)/l_k = \sqrt{d/l_k}$. A number points are marked with black dots, which are referred to in Fig. 5.2 in order to show the evolution of domain width with thickness (scaled by the Kittel length). In particular, d_{m} is the thickness at which the domain width is minimal and d_{∞} is the thickness at which the domain width diverges. The following values of d were used: $d_1 = 2$ nm, $d_2 = 1$ nm, $d_3 = 0.4$ nm, $d_4 = 0.105$ nm, $d_5 = 0.1$ nm, $d_6 = 0.99$ nm, $d_6 = 0.9$ nm. The values of the parameters used are: $P_s = 0.78$ C/m^2, $\Sigma = 0.13$ J/m^2, $\chi_{\eta} = 26$, $\kappa_a = 185$, $\kappa_c = 34$, $\kappa_s = 300$.

predictions of the model should be reliable in the Kittel regime, but other materials will better conform to the approximations of this model for single sub-Kittel thin films. The model is suitable, however, for strongly coupled PTO/STO superlattices, as for the situations described in Ref. [133].

In Fig. 5.1 we see that the domain width follows Kittel's law at large values of d, but, for decreasing d, w reaches a minimum at d_{m} and then diverges at d_{∞}. We can understand this behavior by studying the shape of the energy curves as a function of domain width and thickness, which is done in Fig. 5.2. The energy per unit volume associated with creating the domain walls, shown in red, is unaffected by the thickness of the film. The dashed lines show the electrostatic energy Eq. (5.4) at different thicknesses. We can see in each case that for small w, the energy is approximately linear in w, following Kittel's law. As w increases,
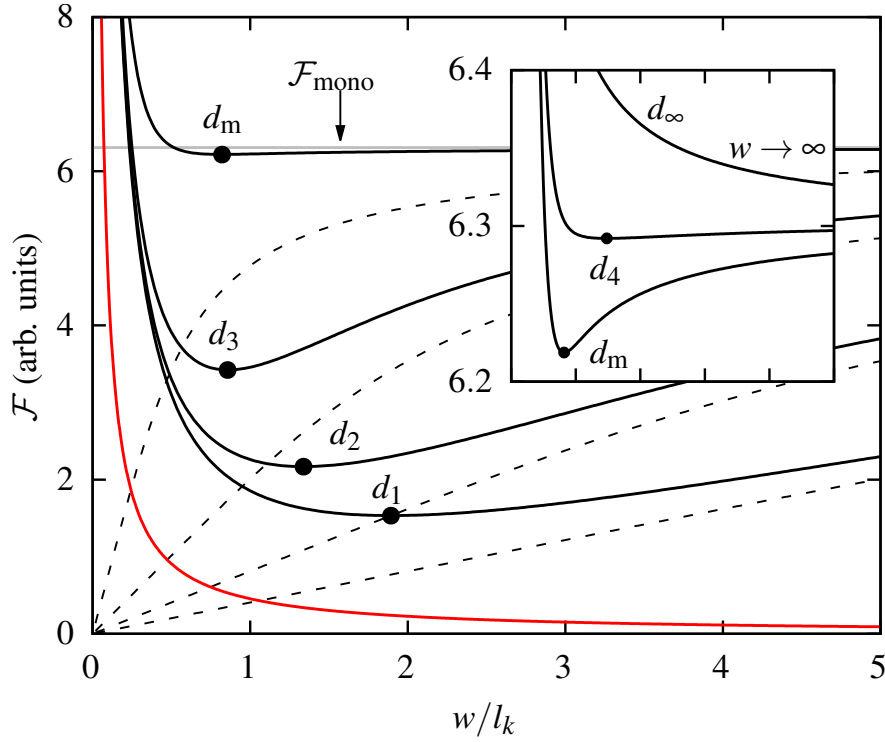
Fig. 5.2 Energy as a function of domain width (scaled by the Kittel length) for the various values of d introduced in Fig. 5.1 The red curve is the domain wall term. The black curves are the total energies for different values of d, and the dashed curves immediately beneath are the respective electrostatic energies at the same thicknesses (truncated at $n = 100$ terms). The minimum with respect to w is indicated with a black dot. The inset shows the energy curves near where the equilibrium domain width diverges.

Kittel's law breaks down, and the curves begin to saturate to the monodomain electrostatic energy:

$$\mathcal{F}_{\text{mono}} = \frac{P_s^2}{2\varepsilon_0 \kappa_c} . \tag{5.9}$$

As d decreases, the saturation of the electrostatic energy is realized earlier, and the minimum in total energy becomes shallower, eventually disappearing, the equilibrium domain width thereby diverging. We can visualize this by looking at the minima of the total energy curves as d is decreased. The minima are marked with black dots on Fig. 5.2 and are also shown on the plot of $w(d)$ in Fig. 5.1.

The described deviation from Kittel's law is sensitive to the system's parameters. In Ref. [31], an expression for d_{m} was reported of the form
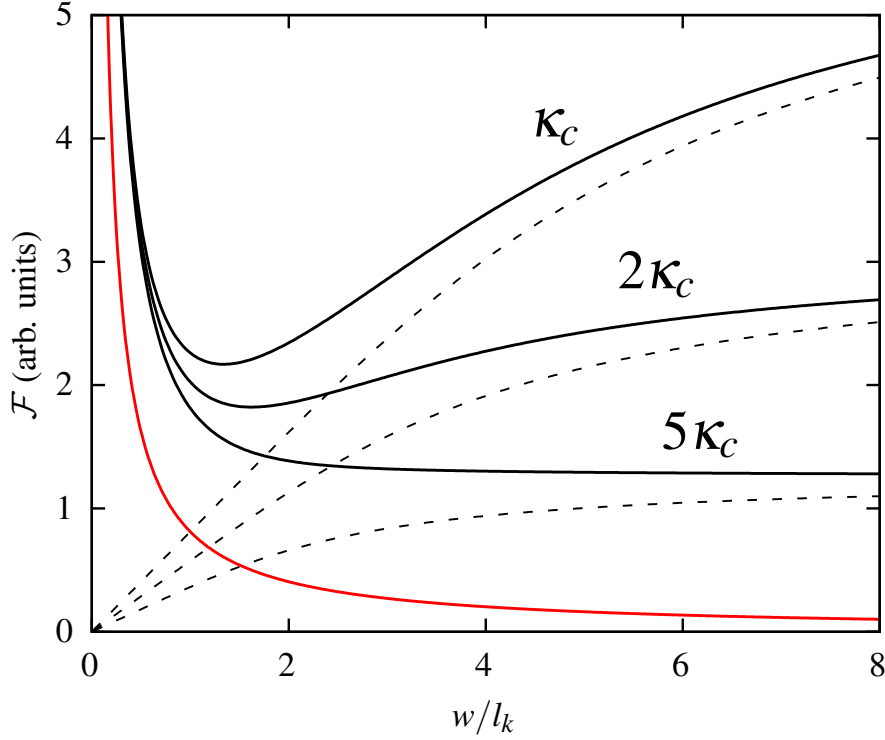
Fig. 5.3 Energy as a function of domain width (scaled by the Kittel length) for a fixed value of d and various multiples of $\kappa_c = 34$. The red curve is the energy cost of creating a domain structure. The black curves are the total energies for different values of κ_c, and the dashed grey curves immediately beneath are the respective electrostatic energies at the same thicknesses (truncated at $n = 100$ terms).

$$d_{\mathrm{m}} = 5\pi\Sigma\varepsilon_0 \frac{\kappa_c}{\chi} \frac{1}{P_s^2} \, , \tag{5.10}$$

although details on how this was obtained were not provided.

In Fig. 5.3 we show the effect of changing κ_c. Increasing κ_c decreases the curvature of the electrostatic energy and also decreases the monodomain energy (the asymptotic energy for large w). By increasing κ_c for a fixed value of d, the total energy minimum again becomes shallower and then disappears.

Although analytic solutions for the equilibrium domain width can not be obtained using Eq. (5.4), we can obtain approximate solutions, following the method in Ref. [108]. For the IF system, the total energy is approximately

$$\mathcal{F} \cong \frac{\Sigma}{w} + \frac{8P_s^2}{\varepsilon_0 \kappa_c \pi^2} \frac{1}{\zeta} \sum_{n=0}^{\infty} \frac{1}{(2n+1)^3} \tanh\left(\frac{(2n+1)}{2}\zeta\right), \tag{5.11}$$

when $\zeta = \pi\chi\frac{d}{w} \ll 1$. Using

$$\tanh\left(\frac{(2n+1)}{2}\zeta\right) = \int_0^1 \partial_\lambda \left(\tanh\left(\frac{(2n+1)}{2}\zeta\lambda\right)\right) d\lambda \tag{5.12}$$

we get

$$\begin{aligned}
\mathcal{F} &\cong \frac{\Sigma}{w} + \frac{4P_s^2}{\varepsilon_0 \kappa_c \pi^2} \int_0^1 d\lambda \sum_{n=0}^{\infty} \frac{1}{(2n+1)^2} \frac{1}{\cosh^2\left(\frac{(2n+1)}{2}\zeta\lambda\right)} \\
&\approx \frac{\Sigma}{w} + \frac{16P_s^2}{\varepsilon_0 \kappa_c \pi^2} \int_0^1 d\lambda \sum_{n=0}^{\infty} \frac{e^{-(2n+1)\zeta\lambda}}{(2n+1)^2}
\end{aligned} \tag{5.13}$$

From Ref. [108]:

$$\int_0^1 d\lambda \sum_{n=0}^{\infty} \frac{e^{-(2n+1)\zeta\lambda}}{(2n+1)^2} = \frac{\pi^2}{8} - \frac{\zeta}{4}\ln\left(\frac{e^p}{\zeta}\right) + \mathcal{O}(\zeta^3), \tag{5.14}$$

where $p = \frac{1}{2}(3 + \ln(4))$. Thus, the approximation to the energy becomes

$$\mathcal{F} \cong \frac{\Sigma}{w} + \frac{P_s^2}{2\varepsilon_0 \kappa_c} + \frac{P_s^2}{2\varepsilon_0 \kappa_c}\left(3 - \frac{8}{\pi}\chi\frac{d}{w}\ln\left(\Lambda\frac{w}{d}\right)\right), \tag{5.15}$$

where

$$\Lambda = \frac{e^p}{\pi\chi}. \tag{5.16}$$

The first two terms are the energy of creating a domain wall and monodomain electrostatic energy, and the third term is an asymptotic correction. Minimizing with respect to w, we get

$$w(d) = \frac{\pi\chi}{2\sqrt{e}} d \exp\left(\frac{\pi^2}{8}\frac{\kappa_c}{\chi}\beta\frac{l_k}{d}\right) . \qquad (5.17)$$

The corresponding minimum width is

$$d_{\mathrm{m}} = \frac{\pi^2}{8}\frac{\kappa_c}{\chi}\beta l_k . \qquad (5.18)$$

Close to d_{m}, below which the width begins to diverge, we have

$$\begin{aligned} w(d) &\cong \frac{\pi\chi}{2\sqrt{e}} d \exp\left(\frac{\pi^2}{8}\frac{\kappa_c}{\chi}\beta\frac{l_k}{d}\right) \\ d_{\mathrm{m}} &\cong \frac{\pi^2}{8}\frac{\kappa_c}{\chi}\beta l_k = \frac{\pi^2}{4}\Sigma\varepsilon_0\frac{\kappa_c}{\chi}\frac{1}{P_s^2} \end{aligned} . \qquad (5.19)$$

In this approximation d_{m} has the same dependence on the systems parameters as Eq. (5.10), but the constant prefactor is different.

We can also obtain an analytic approximation to the domain width at all thicknesses by replacing Eq. (5.4) with a simpler expression which reproduces the monodomain and Kittel energies in the appropriate limits. For the IF system, we could use:

$$\mathcal{F}^*_{\mathrm{elec}} = \underbrace{\frac{P_s^2}{2\varepsilon_0\kappa_c}}_{\mathcal{F}_{\mathrm{mono}}}\frac{1}{1+\frac{1}{\kappa_c\beta}\frac{d}{w}} . \qquad (5.20)$$

When w/d is very large, the second term in the denominator goes to zero and we get $\mathcal{F}^*_{\mathrm{elec}} = \mathcal{F}_{\mathrm{mono}}$. When w/d is very small, the second term in the denominator dominates and we get $\mathcal{F}^*_{\mathrm{elec}} = \frac{P^2}{2\varepsilon_0}\beta\frac{w}{d} = \mathcal{F}_{\mathrm{Kittel}}$. This approximation can also be used for the OL and SW systems, since as we will see later, the generalization to these systems is simply achieved via $\beta = \beta_{\mathrm{IF}} \to \beta_{\mathrm{OL/SW/SL}}$.

Minimizing Eq. (5.20), we get

$$w(d) = \frac{\sqrt{l_k d}}{1 - \kappa_c \beta \sqrt{\frac{l_k}{d}}} \ . \tag{5.21}$$

The width diverges at

$$d_\infty = \kappa_c^2 \beta^2 l_k \ , \tag{5.22}$$

and has a minimum at

$$d_\mathrm{m} = 4 d_\infty = 4 \kappa_c^2 \beta^2 l_k = 8 \varepsilon_0 \kappa_c^2 \beta \Sigma \frac{1}{P_s^2} \ . \tag{5.23}$$

Interestingly, the relation $d_\mathrm{m} = 4 d_\infty$ is independent of system-specific parameters.

This approximation is of the same form as Eq. (5.10) but again with a different numerical prefactor. Eq. (5.21) gives a good approximation to d_m, but overestimates the domain width near d_m. This is because, while Eq. (5.20) has the correct behavior in the monodomain and polydomain limits, it underestimates the curvature of the energy in the intermediate region. In spite of this, the approximation predicts the correct dependence on the system's parameters.

Having understood the behavior of the equilibrium domain width with thickness and the system's parameters, we proceed to investigate the effect of changing the surrounding environment of the thin film. For that purpose more general expressions for the electrostatic energy, similar to Eq. (5.4) are needed.

5.2 Generalized electrostatics

In this section we obtain the electrostatic energies for the OL, SW and SL systems. Some of the predictions of the model have been discussed previously in the literature [107, 107–113, 104] . The results for all systems are presented and compared here. To our knowledge, some of the SL results and all of the OL results are new.

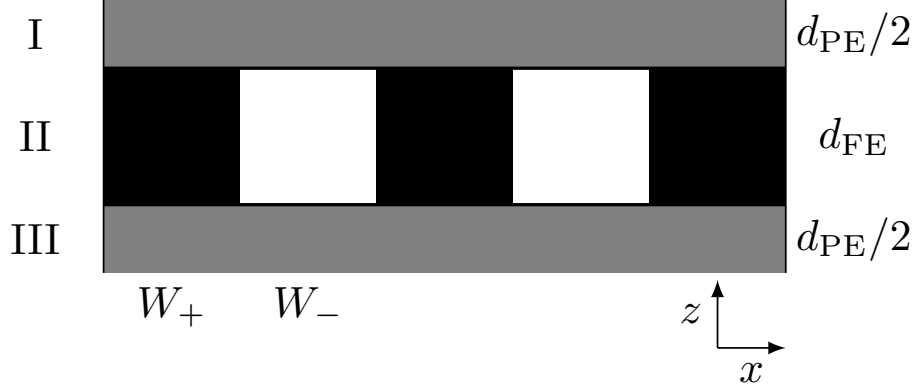## 5.2.1   Electrostatics of a ferroelectric/paraelectric superlattice

Fig. 5.4 The geometry of a FE/PE superlattice. Regions I and III correspond to half of a paraelectric layer each and region II is the ferroelectric layer. The thicknesses of the layers are indicated on the right and W_+ and W_- are the widths of the different domain orientations. The black squares are positive domains, with polarization $+P$ and the white squares are negative domains with polarization $-P$. The system is periodic in the horizontal and vertical directions, with periods $W = W_+ + W_-$ and $D = d_{FE} + d_{PE}$, respectively.

We present the derivation for the SL system, but the method also applies to the OL and SW systems, the only difference being that the boundary conditions change from periodic to infinite.

Consider a periodic array of ferroelectric and paraelectric layers as shown in Fig. 5.4. The spontaneous polarization of the ferroelectric layer has a 180° stripe domain structure with magnitude $\pm P_s$ and widths $W_\pm$. The unit cell of such a system is formed by one positive and one negative polarization domain in the x-direction, with period $W = W_+ + W_-$, and one ferroelectric and one paraelectric layer in the z-direction, with period $D = d_{FE} + d_{PE}$. As mentioned previously, we assume that the domain walls are infinitely thin. Thus, we write the spontaneous polarization as a Fourier series:

$$P_s(x) = AP_s + \sum_{n=1}^{\infty} \frac{4P_s}{n\pi} \sin\left(\frac{n\pi}{2}(A+1)\right) \cos(nkx), \qquad (5.24)$$

where $A = \frac{W_+ - W_-}{W}$ is the mismatch between the domains and $k = \frac{2\pi}{W}$. We can see that the spontaneous polarization is split into a monodomain term, the average polarization AP_s, and polydomain terms in the infinite series. The polydomain limit is obtained when $A \to 0$, i.e. the domain widths are equal. The monodomain limit is obtained when $A \to \pm 1$, i.e. one

of the domain widths tends to zero. To obtain the electric fields in the SL, we must first determine the electrostatic potentials. They satisfy the following Laplace equations:

$$\kappa_{ij}\partial_i\partial_j\phi_{\text{II}} = 0$$
$$\kappa_s\nabla^2\phi_{\text{I}} = \kappa_s\nabla^2\phi_{\text{III}} = 0 \quad, \tag{5.25}$$

where regions I, II and III are the different parts of the unit cell as shown in Fig. 5.4, and $\kappa = \begin{bmatrix} \kappa_a & 0 \\ 0 & \kappa_c \end{bmatrix}$. Since the terms in (5.24) are linearly independent, we can treat the monodomain and polydomain cases separately. Clearly the potentials must be even and periodic in x, so the general solutions to (5.25) are of the form

$$\phi_{\text{I}}(x,z) = c_0^1(z) + \sum_{n=1}^{\infty} \cos(nkx)\left(c_n^1 e^{nkz} + d_n^1 e^{-nkz}\right)$$

$$\phi_{\text{II}}(x,z) = c_0^2(z) + \sum_{n=1}^{\infty} \cos(nkx)\left(c_n^2 e^{nk\sqrt{\frac{\kappa_a}{\kappa_c}}z} + d_n^2 e^{-nk\sqrt{\frac{\kappa_a}{\kappa_c}}z}\right). \tag{5.26}$$

$$\phi_{\text{III}}(x,z) = c_0^3(z) + \sum_{n=1}^{\infty} \cos(nkx)\left(c_n^3 e^{nkz} + d_n^3 e^{-nkz}\right)$$

In order to obtain the potentials, we use the symmetries and boundary conditions of the system to determine the coefficients:

$$\phi_{\text{I}}(d_{\text{FE}}/2) = \phi_{\text{II}}(d_{\text{FE}}/2)$$
$$\phi_{\text{III}}(-d_{\text{FE}}/2) = \phi_{\text{II}}(-d_{\text{FE}}/2)$$
$$\phi_{\text{I}}(D/2) = \phi_{\text{III}}(-D/2)$$
$$(D_{\text{I}} - D_{\text{II}})\cdot\hat{n} = 0 \tag{5.27}$$
$$(D_{\text{III}} - D_{\text{II}})\cdot\hat{n} = 0$$
$$\phi_{\text{I}}(z) = -\phi_{\text{III}}(-z)$$

The first two conditions are obtained by matching the potentials at the interfaces. The third comes from imposing periodic boundary conditions on the unit cell. The fourth and fifth are obtained by matching the normal components of the displacement fields,

$$
\begin{aligned}
D_{\mathrm{I}} &= \varepsilon_0 \kappa_s \mathcal{E}_{\mathrm{I}} \\
D_{\mathrm{II}} &= \varepsilon_0 \kappa \mathcal{E}_{\mathrm{II}} + P_s \ , \\
D_{\mathrm{III}} &= \varepsilon_0 \kappa_s \mathcal{E}_{\mathrm{III}}
\end{aligned}
\tag{5.28}
$$

at the interfaces, and the final condition is obtained from the symmetry of the system under $z \to -z$.

After some algebra, we find that the potentials are given by

$$
\begin{aligned}
\phi_{\mathrm{I}}(z) &= -\frac{AP_s}{\varepsilon_0 \left[\frac{\kappa_c}{d_{\mathrm{FE}}} + \frac{\kappa_s}{d_{\mathrm{PE}}}\right] d_{\mathrm{PE}}}(z - D/2) - \sum_{n=1}^{\infty} \alpha_n \beta_n \frac{\cos(nkx)\sinh(nk(z-D/2))}{\chi\kappa_c\cosh\left(nk\chi\frac{d_{\mathrm{FE}}}{2}\right) + \kappa_s\coth\left(nk\frac{d_{\mathrm{PE}}}{2}\right)\sinh\left(nk\chi\frac{d_{\mathrm{FE}}}{2}\right)} \\
\phi_{\mathrm{II}}(z) &= \frac{AP_s}{\varepsilon_0 \left[\frac{\kappa_c}{d_{\mathrm{FE}}} + \frac{\kappa_s}{d_{\mathrm{PE}}}\right] d_{\mathrm{FE}}}z + \sum_{n=1}^{\infty} \alpha_n \frac{\cos(nkx)\sinh(nk\chi z)}{\chi\kappa_c\cosh\left(nk\chi\frac{d_{\mathrm{FE}}}{2}\right) + \kappa_s\coth\left(nk\frac{d_{\mathrm{PE}}}{2}\right)\sinh\left(nk\chi\frac{d_{\mathrm{FE}}}{2}\right)} \\
\phi_{\mathrm{III}}(z) &= -\frac{AP_s}{\varepsilon_0 \left[\frac{\kappa_c}{d_{\mathrm{FE}}} + \frac{\kappa_s}{d_{\mathrm{PE}}}\right] d_{\mathrm{PE}}}(z + D/2) - \sum_{n=1}^{\infty} \alpha_n \beta_n \frac{\cos(nkx)\sinh(nk(z+D/2))}{\chi\kappa_c\cosh\left(nk\chi\frac{d_{\mathrm{FE}}}{2}\right) + \kappa_s\coth\left(nk\frac{d_{\mathrm{PE}}}{2}\right)\sinh\left(nk\chi\frac{d_{\mathrm{FE}}}{2}\right)}
\end{aligned}
\tag{5.29}
$$

where

$$
\begin{aligned}
\alpha_n &= \frac{4P_s}{\varepsilon_0 n^2 \pi k} \sin\left(\frac{n\pi}{2}(A+1)\right) \\
\beta_n &= \frac{\sinh\left(nk\chi\frac{d_{\mathrm{FE}}}{2}\right)}{\sinh\left(nk\frac{d_{\mathrm{PE}}}{2}\right)}
\end{aligned}
\tag{5.30}
$$

The monodomain part of the potential has a zig-zag shape which is sensitive to the ratio of layer thicknesses and permittivities, as expected. The electrostatic energy of the system is obtained from

$$\mathcal{F}_{\text{elec}} = \frac{1}{2} \int \kappa_{ij} \mathcal{E}_i \mathcal{E}_j \, dx \, dz \,, \tag{5.31}$$

where the fields are the gradients of the potentials: $\mathcal{E} = -\nabla \phi$. We integrate over the domain period in the x-direction and over both layers in the z-direction. Finally, the total electrostatic energy of the SL system is given by

$$\mathcal{F}_{\text{elec}}^{\text{SL}} = \frac{1}{(1+\alpha)} \frac{P_s^2}{2\varepsilon_0 \kappa_c} \left(\frac{\kappa_c}{\kappa_c + \alpha^{-1} \kappa_s} A^2 + \frac{16\kappa_c}{\pi^3} \frac{w}{d} \sum_{n=1}^{\infty} \frac{\sin^2\left(\frac{n\pi}{2}(A+1)\right)}{n^3} \frac{1}{\chi \kappa_c \coth\left(\frac{n\pi}{2} \chi \frac{d}{w}\right) + \kappa_s \coth\left(\frac{n\pi}{2} \alpha \frac{d}{w}\right)} \right), \tag{5.32}$$

where

$$d = d_{\text{FE}}$$
$$\alpha = \frac{d_{\text{PE}}}{d_{\text{FE}}} \,, \tag{5.33}$$

so that

$$d_{\text{PE}} = \alpha d$$
$$D = (1+\alpha)d \,. \tag{5.34}$$

The energy of the SW system is

$$\mathcal{F}_{\text{elec}}^{\text{SW}} = \frac{P_s^2}{2\varepsilon_0 \kappa_c} \left(A^2 + \frac{16\kappa_c}{\pi^3} \frac{w}{d} \sum_{n=1}^{\infty} \frac{\sin^2\left(\frac{n\pi}{2}(A+1)\right)}{n^3} \frac{1}{\kappa_s + \chi \kappa_c \coth\left(\frac{n\pi}{2} \chi \frac{d}{w}\right)} \right), \tag{5.35}$$

and the energy of the OL system is

$$\mathcal{F}_{\text{elec}}^{\text{OL}} = \frac{P_s^2}{2\varepsilon_0 \kappa_c} \left(A^2 + \frac{8\kappa_c}{\pi^3} \frac{w}{d} \sum_{n=1}^{\infty} \frac{\sin^2\left(\frac{n\pi}{2}(A+1)\right)}{n^3} \gamma_n^{-2} \Gamma_n \right), \tag{5.36}$$

where

$$\gamma_n = (\chi^2 \kappa_c^2 + \kappa_s) \sinh\left(n\pi\chi\frac{d}{w}\right) + \chi\kappa_c(1+\kappa_s)\cosh\left(n\pi\chi\frac{d}{w}\right)$$

$$\Gamma_n = (\chi^2\kappa_c^2 - \kappa_s)(1+\kappa_s) - 4\chi^2\kappa_c^2(1+\kappa_s)\cosh\left(n\pi\chi\frac{d}{w}\right)$$

$$+ (1+\kappa_s)(3\chi^2\kappa_c^2 + \kappa_s)\cosh\left(2n\pi\chi\frac{d}{w}\right)$$

$$- 4\chi\kappa_c(\chi^2\kappa_c^2 + \kappa_s)\sinh\left(n\pi\chi\frac{d}{w}\right)$$

$$+ \chi\kappa_c(1 + 2\chi^2\kappa_c^2 + \kappa_s(4+\kappa_s))\sinh\left(2n\pi\chi\frac{d}{w}\right)$$

(5.37)

In all cases the energy is split into monodomain and polydomain parts. We can see that the monodomain parts for the OL and SW cases are identical to that of a thin film in a vacuum, as expected. We can also see that the polydomain part vanishes when $A \to \pm 1$, and the polydomain limit is obtained when $A \to 0$.

It is important to check that the polydomain part of the energy reproduces the monodomain and Kittel energies in the appropriate limits. Letting $A = 0$, we have

$$\mathcal{F}_{\text{elec}}^{\text{SL}} = \frac{P_s^2}{2\varepsilon_0 \kappa_c}\left(\frac{16\kappa_c}{\pi^3}\frac{w}{d}\sum_{n \text{ odd}}\frac{1}{n^3}\frac{1}{\chi\kappa_c\coth\left(\frac{n\pi}{2}\chi\frac{d}{w}\right) + \kappa_s\coth\left(\frac{n\pi}{2}\alpha\frac{d}{w}\right)}\right),$$

(5.38)

ignoring the prefactor of $(1+\alpha)^{-1}$. The monodomain limit is realized when $w \to \infty$. Using the expansion $\coth(ax) \sim \frac{1}{ax}$ about $x = 0$, we get

$$\mathcal{F}_{\text{elec}}^{\text{SL}} \to \frac{P_s^2}{2\varepsilon_0(\kappa_c + \alpha^{-1}\kappa_s)}\frac{8}{\pi^2}\sum_{n \text{ odd}}\frac{1}{n^2},$$

$$= \frac{P_s^2}{2\varepsilon_0(\kappa_c + \alpha^{-1}\kappa_s)}$$

(5.39)

since $\sum_{n \text{ odd}}\frac{1}{n^2} = \frac{\pi^2}{8}$. For the Kittel limit, $\frac{d}{w} \gg 1$, using $\coth(x) \to 1$ for large x, we get

$$\mathcal{F}_{\text{elec}}^{\text{SL}} \to \frac{P_s^2}{2\varepsilon_0} \frac{14\zeta(3)}{\pi^3} \frac{1}{\kappa_s + \chi\kappa_c} \frac{w}{d} \, , \tag{5.40}$$

where we used $\sum_{n \text{ odd}} \frac{1}{n^3} = \frac{7\zeta(3)}{8}$.

5.2.2 Generalized Kittel law
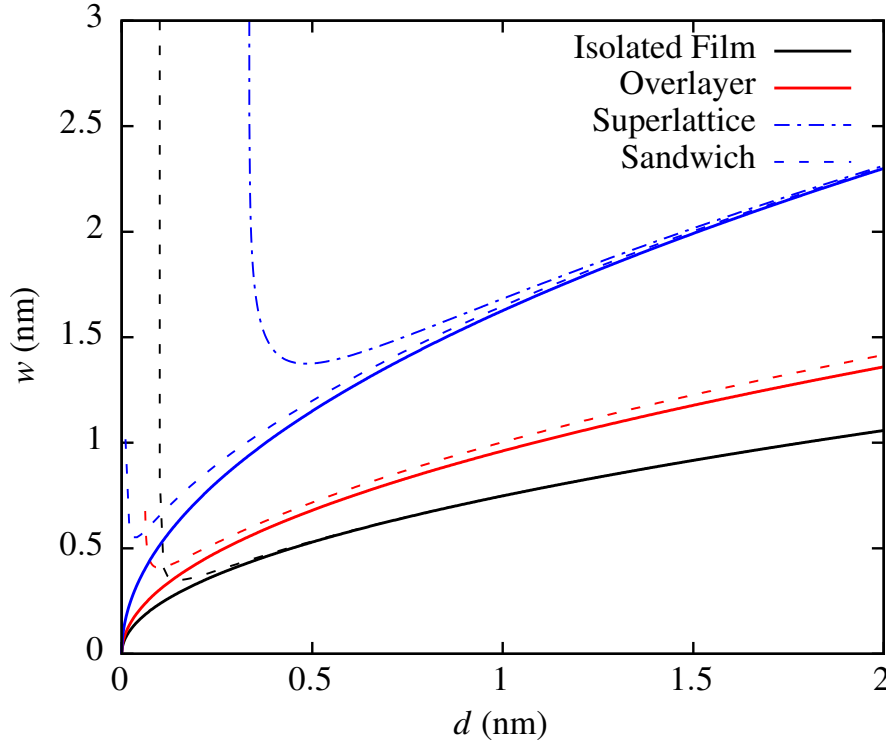
Fig. 5.5 $w(d)$ for the IF system (black), the OL system (red), the SW and the SL system with $\alpha = 3$ (blue). The solid lines show the analytic solutions from the generalized Kittel's law and the dashed lines show numerical results obtained by minimizing the full electrostatic energies. The SL and SW systems have identical square root curves in the Kittel limit.

Taking the Kittel limit for the energies in Eqs. (5.32), (5.35) and (5.36), we obtain a generalization of Kittel's law:

$$\begin{aligned} w(d) &= \sqrt{l_k(\kappa_s)d} \\ l_k(\kappa_s) &= \frac{2\varepsilon_0\Sigma}{P_s^2\beta(\kappa_s)} \end{aligned} \tag{5.41}$$

The generalization is introduced through the factor β:

$$\beta_{\text{SL}}(\kappa_s, \alpha) = \frac{1}{1+\alpha} \frac{14\zeta(3)}{\pi^3} \frac{1}{\kappa_s + \chi\kappa_c}$$
$$\beta_{\text{SW}}(\kappa_s) = \frac{14\zeta(3)}{\pi^3} \frac{1}{\kappa_s + \chi\kappa_c} \qquad . \qquad (5.42)$$
$$\beta_{\text{OL}}(\kappa_s) = \frac{7\zeta(3)}{\pi^3} \left(\frac{1 + \kappa_s + 2\chi\kappa_c}{(1 + \chi\kappa_c)(\kappa_s + \chi\kappa_c)} \right)$$

The SL system has an additional dependence on $\alpha \equiv d_{\text{PE}}/d_{\text{FE}}$, the ratio of thicknesses of the paraelectric and ferroelectric layers. However, the energy cost of creating a domain wall is also renormalized by this prefactor, and thus, in the Kittel limit, the ratio α affects the energy scale but does not influence the behavior of the domains. For each case in Eq. (5.42), Eq. (5.6) is recovered in the limit $\kappa_s \to 1$.

The domain widths for the four different systems are plotted in Fig. 5.5. We can see that including the environment has the effect of shifting the curve upwards, but the square root behavior is unaffected. This makes sense physically: the paraelectric medium contributes to the screening of the depolarizing field. For higher dielectric constants, this contribution grows, meaning less screening is required by the domains, so there are fewer domains, and hence the width increases.

The SL and SW cases have the exact same behavior in the Kittel limit. This is expected, since in the Kittel limit, the electric field in the superlattice loops in the paraelectric layers but does not penetrate through to neighboring ferroelectric layers. In this regime, the coupling between the ferroelectric layers is weak, and the ferroelectric layers are essentially isolated from each other, tending to the SW case.

In Ref. [107], it was claimed that there should be a factor of two between the length scales of the OL and SW systems. From Eq. (5.42) we have:

$$\frac{l_{k,\text{OL}}(\kappa_s)}{l_{k,\text{SW}}(\kappa_s)} = \frac{\beta_{\text{SW}}(\kappa_s)}{\beta_{\text{OL}}(\kappa_s)} = \frac{1 + \chi\kappa_c}{1 + \kappa_s + 2\chi\kappa_c} \, . \qquad (5.43)$$

When $\kappa_s \approx 1$, this is indeed true. However, when κ_s is comparable to or larger than $\chi\kappa_c$, the approximation is not valid. For example, for PTO and STO, $\chi\kappa_c \sim 79$ and $\kappa_s = 300$ and

can be as large as 10^4 at low temperatures, and the difference in the Kittel lengths becomes significantly larger than a factor of two.

5.2.3 Beyond Kittel: thin films
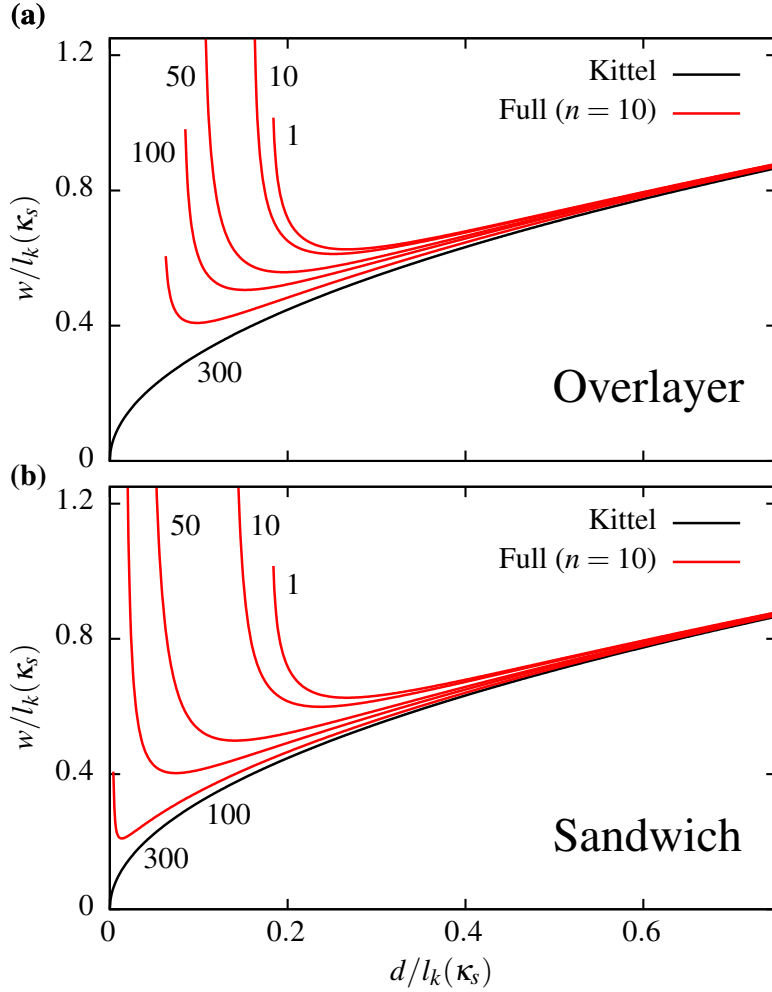
Fig. 5.6 Domain widths as a function of thickness for various values of κ_s for **(a)** the OL system and **(b)** the SW system. The domain width and film thickness are normalized by the Kittel length for that value of κ_s.

Although the square root curve is simply shifted upwards when generalizing to different geometries, the behavior for thinner films is quite different. In Fig. 5.5 we can see that the thickness at which the domain width diverges is very sensitive to the dielectric environment. In Fig. 5.6, we plot the domain widths for various values of the permittivity of the dielectric

material, κ_s for the OL and SW systems, each curve scaled by the relevant Kittel length, $l_k(\kappa_s)$. We see that d_m decreases with increasing κ_s. In Fig. 5.7 we plot the critical thickness as a function of κ_s to illustrate this effect. For the SW system, d_m decreases more dramatically. This is expected, as there is screening on both sides of the thin film in the SW system.
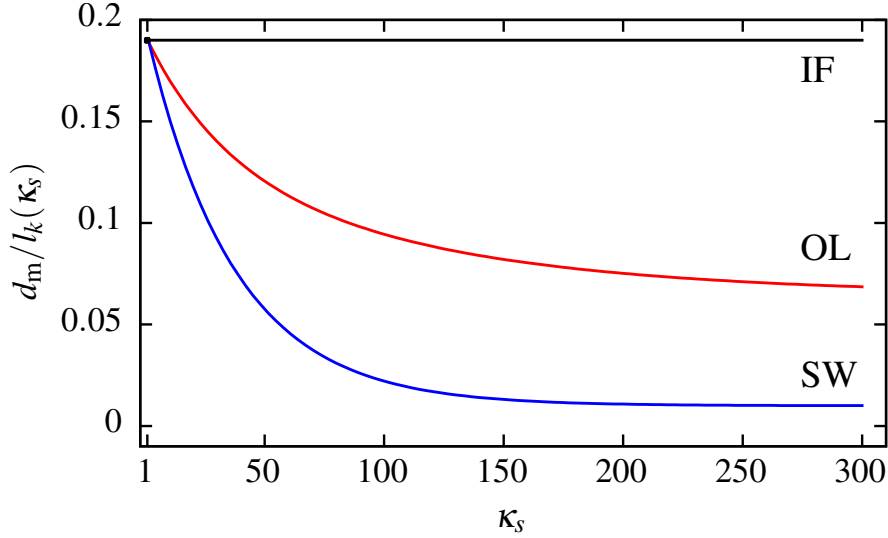

Fig. 5.7 d_m relative to the corresponding Kittel length as a function of dielectric permittivity of the substrate material for the IF (black), OL (red) and SW (blue) systems.

We can understand the effect the permittivity has on d_m by examining the form of the electrostatic energy. For example, for the SW system:

$$\mathcal{F}_{\mathrm{elec}}^{\mathrm{SW}} = \frac{1}{\kappa_s} \frac{8P_s^2}{\varepsilon_0 \pi^3} \frac{w}{d} \sum_{n \text{ odd}} \frac{1}{n^3} \frac{1}{1 + \chi \frac{\kappa_c}{\kappa_s} \coth\left(\frac{n\pi}{2} \chi \frac{d}{w}\right)} . \tag{5.44}$$

This is equivalent to the the electrostatic energy of the IF system, but with the overall energy and κ_c both scaled by κ_s. As we know from Eqs. (5.10), (5.19) and (5.23), $d_m \propto \kappa_c^{3/2}$, and it is clear that d_m should decrease with increasing κ_s.

5.2.4   Beyond Kittel: superlattices

For the SL system with with $\alpha = d_{\mathrm{PE}}/d_{\mathrm{FE}} = 1$, we find that d_m actually increases with the permittivity of the paraelectric layers, as shown in Fig. 5.8 (a), contrary to the behavior observed in the OL and SW systems. For small values of α, the periodic boundary conditions of the superlattice make the electrostatic description very different from the OL and SW

systems. When the paraelectric layers are thin, the depolarizing field penetrates through them and there is strong coupling between the ferroelectric layers. The superlattice acts as an effectively uniform ferroelectric material. The average polarization decreases with the permittivity of the paraelectric layers, and according to Eqs. (5.10), (5.19) and (5.23), d_m increases.

For large spacings between the ferroelectric layers ($\alpha \gg 1$), the coupling between them becomes weak, the SW system being realized for $\alpha \to \infty$. This is illustrated in Fig. 5.8 (c), which is identical to Fig. 5.6 (b).

Interestingly, when $\alpha = \alpha_c \equiv \chi = \sqrt{\kappa_a/\kappa_c}$, $d_m/l_k(\kappa_s)$ is independent of κ_s. At this ratio, the permittivity of the paraelectric layers has no influence on the equilibrium domain structure, relative to the length scale given by $l_k(\kappa_s)$. This is shown in Fig. 5.8 (b). In Fig. 5.9 we plot d_m as a function of κ_s for different values of α. We see that when $\alpha > \alpha_c$, d_m increases with κ_s, while it decreases for $\alpha < \alpha_c$, and remains constant when $\alpha = \alpha_c$. Thus, α_c represents a natural boundary between the strong and weak coupling regimes of FE/PE superlattices.

The critical ratio α_c can be predicted from both the asymptotic and analytic approximations, Eqs. (5.19) and (5.23), respectively. We can illustrate this by generalizing Eq. (5.23) to the SL system. In this case, the monodomain energy is

$$\mathcal{F}_{\text{mono}}^{\text{SL}} = \frac{1}{(1+\alpha)} \frac{P_s^2}{2\varepsilon_0(\kappa_c + \alpha^{-1}\kappa_s)} \ . \tag{5.45}$$

The prefactor $(1+\alpha)^{-1}$ scales the energy with the ratio of the layer thicknesses. The energy cost of creating a domain structure is scaled by this prefactor. Thus, the equilibrium domain width will be unaffected by this prefactor, and we can neglect it. Now, the monodomain energy for a SL is similar to the case of a thin film, but with renormalized permittivity: $\kappa_c \to \kappa_c + \alpha^{-1}\kappa_s$.

The total energy for the SL system is

$$\mathcal{F} = \frac{\Sigma}{w} + \frac{\mathcal{F}_{\text{mono}}^{\text{SL}}}{1 + \frac{x}{w}} \ , \tag{5.46}$$
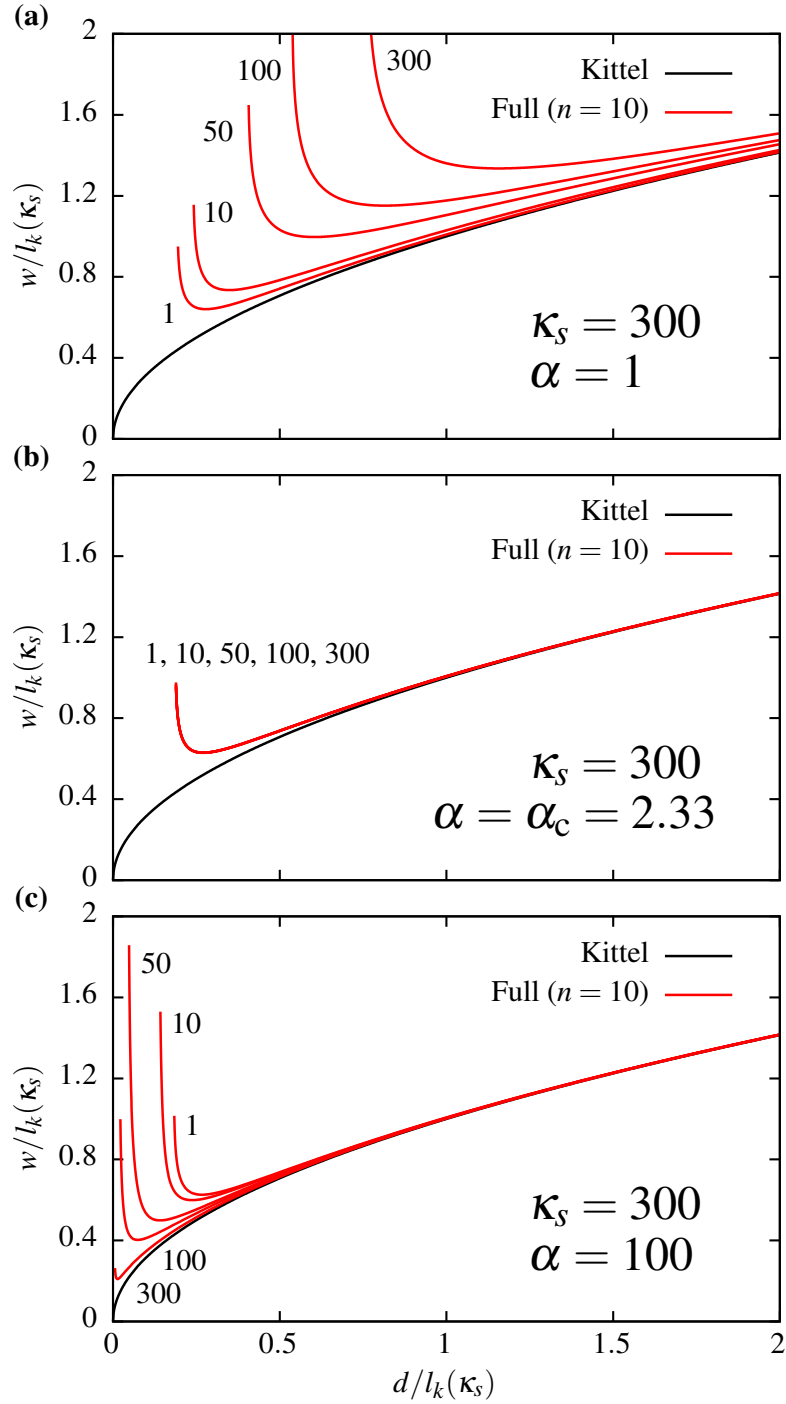
where

Fig. 5.8 Domain width as a function of thickness for the SL system with (a) $\alpha = 1$, (b) $\alpha = \alpha_c$ (= 2.33 for PTO/STO), and (c) $\alpha = 100$. Each domain width and film thickness is normalized by the Kittel length for that value of κ_s.
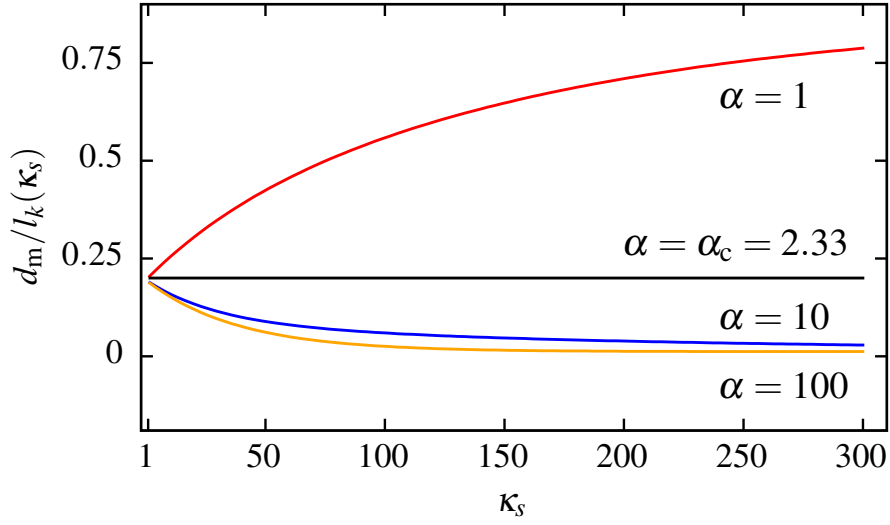
Fig. 5.9 Critical thickness of the SL system as a function of κ_s for several values of α. Each value of d is scaled by the appropriate Kittel length.

$$x = \frac{d}{(\kappa_c + \alpha^{-1}\kappa_s)\beta(\kappa_s)} \; . \tag{5.47}$$

Minimizing Eq. (5.46), we get

$$w(d) = \frac{\sqrt{l_k(\kappa_s)d}}{1 - (\kappa_c + \alpha^{-1}\kappa_s)\beta(\kappa_s)\sqrt{\frac{l_k(\kappa_s)}{d}}} \; . \tag{5.48}$$

Eq. (5.48) has square root behavior for large d (Kittel) and diverges for small d (monodomain). The width diverges at

$$d_\infty = (\kappa_c + \alpha^{-1}\kappa_s)^2\beta(\kappa_s)^2 l_k(\kappa_s) \, , \tag{5.49}$$

and has a minimum at

$$\begin{aligned} d_m &= 4(\kappa_c + \alpha^{-1}\kappa_s)^2\beta(\kappa_s)^2 l_k(\kappa_s) = 4d_\infty \\ &= 8\varepsilon_0(\kappa_c + \alpha^{-1}\kappa_s)^2\beta(\kappa_s)\Sigma\frac{1}{P_s^2} \end{aligned} \tag{5.50}$$

Again, the relation $d_\mathrm{m} = 4d_\infty$ is independent of system-specific parameters. Dividing by the Kittel length, we get

$$\frac{d_\mathrm{m}}{l_k(\kappa_s)} = 4(\kappa_c + \alpha^{-1}\kappa_s)^2 \beta(\kappa_s)^2$$
$$\propto \frac{\kappa_c}{\kappa_a} \frac{(1 + \frac{\kappa_s}{\alpha\kappa_c})^2}{(1 + \frac{\kappa_s}{\chi\kappa_c})^2} \frac{1}{P_s^2} \qquad . \qquad (5.51)$$

From this we can see that when $\alpha = \alpha_\mathrm{c} = \chi$, the dependence on κ_s vanishes.

Chapter 6

2DEG formation in polydomain ferroelectrics

In this chapter, we introduce a model which allows for the possibility of both domains and a 2DEG in a ferroelectric system, building on the model which considered the competition between a polydomain phase and a monodomain phase sustained by a 2DEG [133].

6.1   2DEG formation in monodomain ferroelectrics

First, we review the theory of 2DEG formation for a monodomain ferroelectric thin film. Consider an isolated ferroelectric thin film of thickness d and polarization P in a vacuum. In the absence of any charge compensation, a depolarizing field will reduce or suppress the polarization. As discussed in the previous chapter, ferroelectric thin films can form polydomain structures in order to screen the depolarizing field. However, it has recently been proposed that the depolarizing field could be screened in a monodomain film by the formation of a 2DEG/2DHG at the interfaces, similar to the those observed in LAO/STO [133]. Starting with the phenomenological model of 2DEG formation at polar-nonpolar interfaces used in Chapters 3 and 4, we can generalize to a ferroelectric thin film:

$$\mathcal{F} = \mathcal{F}_0(P) + \frac{\Delta}{d}\sigma + \frac{1}{2gd}\sigma^2 + \frac{1}{2\varepsilon_0\kappa_c}(P - \sigma)^2 \,, \qquad (6.1)$$

where σ is the carrier concentration of the 2DEG, Δ is the band gap, g is the density of states (DOS) and κ_c is the dielectric permittivity in the direction normal to the thin film. The key difference between Eq. (6.1) is the source of the polar discontinuity, and the fact that the polarization is described by a double well potential $\mathcal{F}_0(P)$ with spontaneous polarization P_s, i.e. Eq. (5.2). The second term is the energy cost of creating an electron-hole pair across the gap Δ, and the the third term is the cost of filling the energy bands with a finite DOS g. As in Chapters 3 and 4, these terms could be repurposed to describe the formation of carriers via surface vacancies. The last term is the electrostatic energy of the depolarizing field. A 2DEG will appear when the energy saved by screening the depolarizing field is greater than the energy cost of creating creating the electron-hole pairs and filling the bands. If we minimize (6.1) with respect to P and σ, we find that there is a critical thickness d_c at which the carriers appear discontinuously. Assuming the DOS to be infinite ($g \to \infty$), this leads to a jump in polarization,

$$P_{\text{crit}} = \frac{1}{\sqrt{3}} P_s \, , \qquad (6.2)$$

which is independent of the material properties. After this, the polarization approaches the bulk spontaneous polarization with increasing thickness. A finite DOS has the effect of slightly shifting the critical thickness and changing the size of the polarization jump, but the transition remains discontinuous [133]. For an isolated film of PTO, d_c was predicted to be around 1.6 nm, or 4 unit cells, assuming that the carriers are generated by oxygen vacancies at the surface of the film [133]. Below d_c, it is not energetically favorable for carriers to form, the depolarizing field will suppress the spontaneous polarization, and the system will adopt a paraelectric phase. In reality, a polydomain structure may form at lower thicknesses [117, 118]. If we compare the free energy from Eq. (6.1) against the free energy of a polydomain ferroelectric film, e.g. Eq. (5.1), we find that, with increasing film thickness, the energetically stable phase changes discontinuously from the polydomain phase to the monodomain phase, sustained by a 2DEG. In PTO for example, the crossover between polydomain and monodomain phases was predicted to occur at around 4.6 nm [133]. Of course, if we only consider the two phases in isolation, our model cannot predict the observed coexistence between the two.

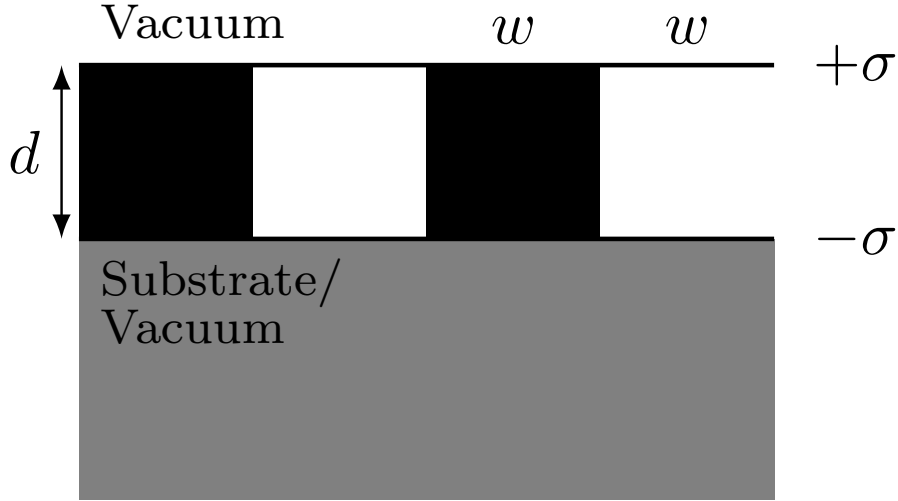# 6.2 Coexistence model of ferroelectric domains and 2DEG formation

Fig. 6.1 Geometry of a ferroelectric thin film of thickness d with a 180° stripe domain structure in a vacuum or on a substrate. The positive and negative domains are both of width w and polarization $\pm P$, and the walls between domains are infinitely thin. $\pm\sigma$ show the orientation of the 2DEG/2DHG at the interfaces with the vacuum and/or substrate.

Using the model of polydomain ferroelectric films discussed in the previous chapter, we generalize Eq. (6.1) to allow for the formation of a polydomain structure as well as a 2DEG, see Fig. 6.1. The free energy is modified as follows:

$$\mathcal{F} = \mathcal{F}_0(P) + \mathcal{F}_{2\text{DEG}} + \frac{\Sigma}{w} + \mathcal{F}_{\text{dep}}(P - \sigma, w) , \tag{6.3}$$

where we have included the energy cost of creating a domain wall, with w being the width of a single domain and Σ the surface energy associated with creating a domain wall. The depolarizing energy is also replaced by the polydomain equivalent, Eq. (5.4). For the monodomain phase, the depolarizing field is constant and contained entirely within the film, assuming it extends infinitely in the plane. A domain structure will cause the depolarizing field to bend and loop around the interfaces and domain walls [30, 31]. In the Kittel limit, $w \ll d$, the depolarizing energy of is given by

$$\mathcal{F}_{\text{dep}}(P, w) = \frac{1}{2\varepsilon_0} \beta \frac{w}{d} P^2 , \tag{6.4}$$

where from the previous chapter

$$\beta = \frac{7\zeta(3)}{\pi^3} \frac{1}{1 + \sqrt{\kappa_a \kappa_c}} \ . \tag{6.5}$$

Putting all of this together, Eq. (6.1) becomes

$$\mathcal{F} = \mathcal{F}_0(P) + \frac{\Sigma}{w} + \frac{\Delta}{d}\sigma + \frac{1}{2gd}\sigma^2 + \frac{1}{2\varepsilon_0}\beta\frac{w}{d}(P-\sigma)^2 \ . \tag{6.6}$$

We can see that the depolarizing field is being screened by both the 2DEG and the domain structure, i.e. for larger σ or smaller w (more domains), the depolarization energy is reduced.

The equilibrium values of the polarization, domain width and carrier concentration can be determined by minimizing the free energy: $\partial_P\mathcal{F} = \partial_\sigma\mathcal{F} = \partial_w\mathcal{F} = 0$. For the polarization, we find that the behavior is the same as in the monodomain theory, i.e. Eq. (6.2). Fixing the polarization to the spontaneous polarization of the material, $P = P_s$, say, we can obtain analytic expressions for σ and w with thickness:

$$\begin{aligned} \sigma(d) &= g\Delta\left(\sqrt{\frac{d}{d_1}} - 1\right) \\ w(d) &= \frac{\sqrt{l_k d}}{1 - \frac{g\Delta}{P_s}\left(\sqrt{\frac{d}{d_1}} - 1\right)} \end{aligned} \ , \tag{6.7}$$

where

$$d_1 = \frac{\varepsilon_0\Delta^2}{2\Sigma\beta} \ , \tag{6.8}$$

is the critical thickness, below which $\sigma = 0$ and the domains follow the Kittel law:

$$\begin{aligned} w(d) &= \sqrt{l_k d} \\ l_k &= \frac{2\varepsilon_0\Sigma}{P_s^2\beta} \end{aligned} \ . \tag{6.9}$$

Δ (eV/e)	d (nm)	IF	OL	SL/SW
3.6	d_1	65.3	107.8	308.4
	d_2	272.1	449.1	1285.1
1	d_1	5.0	8.3	23.8
	d_2	113.6	187.5	536.7

Table 6.1 Summary of critical thicknesses of the coexistence model for different band gaps and geometries. The SL and SW systems give identical results in the Kittel limit.

There is a second critical thickness,

$$d_2 = d_1 \left(1 + \frac{P_s}{g\Delta} \right)^2 , \qquad (6.10)$$

at which σ saturates and the domain width diverges.

To summarize, below d_1, there is no 2DEG and the domains follow the Kittel law. Above d_1, carriers begin to appear at the interface and contribute the to screening of the depolarizing field. This means that fewer domains are required to screen the field, so the width increases and deviates from the Kittel law. At $d = d_2$, the carrier concentration completely screens the depolarizing field and saturates, meaning no domains are required, and the width of the domains diverges. This behavior is summarized in Fig. 6.2.

The most notable difference between this and the previous model is the continuous transition between polydomain and monodomain phases in the region of coexistence between d_1 and d_2. The onset of this region is quadratically dependent on the gap, and the range of this region is sensitive to the gap and the DOS. Interestingly, the value of d_1 does not depend on the DOS, unlike the monodomain theory, and the range of the coexistence region is crucially dependent on a finite DOS: if $g \to \infty$, then $d_2 \to d_1$. In Table 6.1 we compare the different values of d_1 and d_2 obtained using values for the gap: $\Delta = 3.6$ eV is the experimental band gap of bulk PTO and $\Delta = 1$ eV is the approximate energy required to create an oxygen vacancy [133].

As in the previous chapter, one of the largest approximations of this model is that the ferroelectric thin film is isolated in an infinite vacuum. As we have seen, the surrounding media, such as the substrate on which the thin film is grown, can have a big influence on the
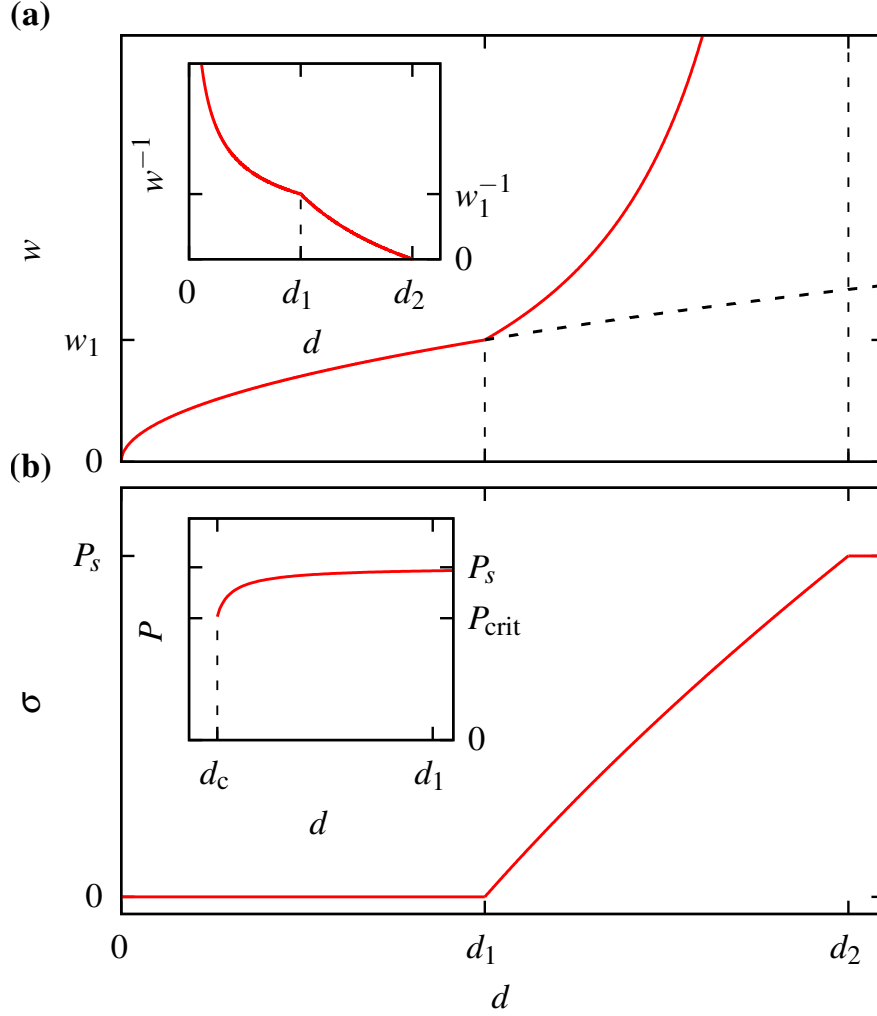
(a)

(b)

Fig. 6.2 Plots of **(a)**: domain width w and **(b)**: 2DEG carrier concentration σ from Eq. (6.7), for an isolated thin film of PTO. In **(a)**, the dashed line shows the continuation of the square root behavior of the Kittel law beyond the width $w_1 = w(d_1)$. The inset shows the inverse domain width, which has a kink at d_1 and tends to zero at d_2, illustrating the divergence of domain width. In **(b)**, σ switches on at d_1 and saturates at d_2. The inset shows the polarization as a function of thickness ($g \to \infty$). The discontinuous jump at d_c is much smaller than d_1 and d_2.

properties of the film. We can generalize our model to SL, SW and OL systems by changing the value of β using Eq. (5.42). Changing the geometry of the system changes d_1 and d_2:

$$\frac{d_i^{\text{OL/SL/SW}}}{d_i^{\text{IF}}} = \frac{\beta_{\text{IF}}}{\beta_{\text{OL/SL/SW}}(\kappa_s)}, \qquad i = 1, 2 . \tag{6.11}$$

This implies that a substrate or paraelectric layer with a large permittivity can shift the onset and extend the range of the coexistence region. To illustrate the effect of the geometry, we compare the 2DEG carrier concentration and domain width for the IF, OL and SL systems in Fig. 6.3, using PTO and STO as the ferroelectric and paraelectric materials, using the same parameters as in the previous chapter. We see that d_1 and d_2 have a significant dependence on the permittivity of STO. A comparison of d_1 and d_2 for the three different geometries is given in Table 6.1.

Another difference between the SL and IF systems is the behavior of the domains at the interfaces. It is possible for the domains to induce a weak domain structure in the paraelectric layers [104, 306, 106], i.e. when there is strong coupling between the ferroelectric and paraelectric layers. In this scenario, the energy cost of creating a domain wall becomes

$$\Sigma = \Sigma_{\mathrm{FE}} + \frac{1}{\alpha}\Sigma_{\mathrm{PE}} \ . \tag{6.12}$$

We consider this contribution to be negligible except when $d_{\mathrm{PE}} \to 0$ i.e. for very small values of α. Thus, we neglect it in our model.

Perhaps the largest approximation of our model is that the electrostatics takes the simple form of the Kittel expression screened by the 2DEG, which is valid for thicker films but not for very thin films.

Using Eqs. (5.4), (5.36) and (5.32), truncating the infinite series at $n = 100$ terms, the free energies were minimized numerically for the IF, OL and SL systems. The results were found to be in agreement with the analytic solutions except near d_2, where the domain widths diverge, and near $d = 0$, where the domain width also diverges. The behavior of the domains near d_2 is summarized in Fig. 6.4 for the three different systems. In the ultrathin limit, $\sigma = 0$ and the typical behavior of polydomain ferroelectrics was observed: the widths obey the Kittel law until a critical thickness, below which the widths increase again and eventually diverge. In the intermediate region, the theoretical and analytic results are in agreement. Thus, the Kittel approximation is suitable for describing the coexistence between domains and the 2DEG.

(a)

(b)
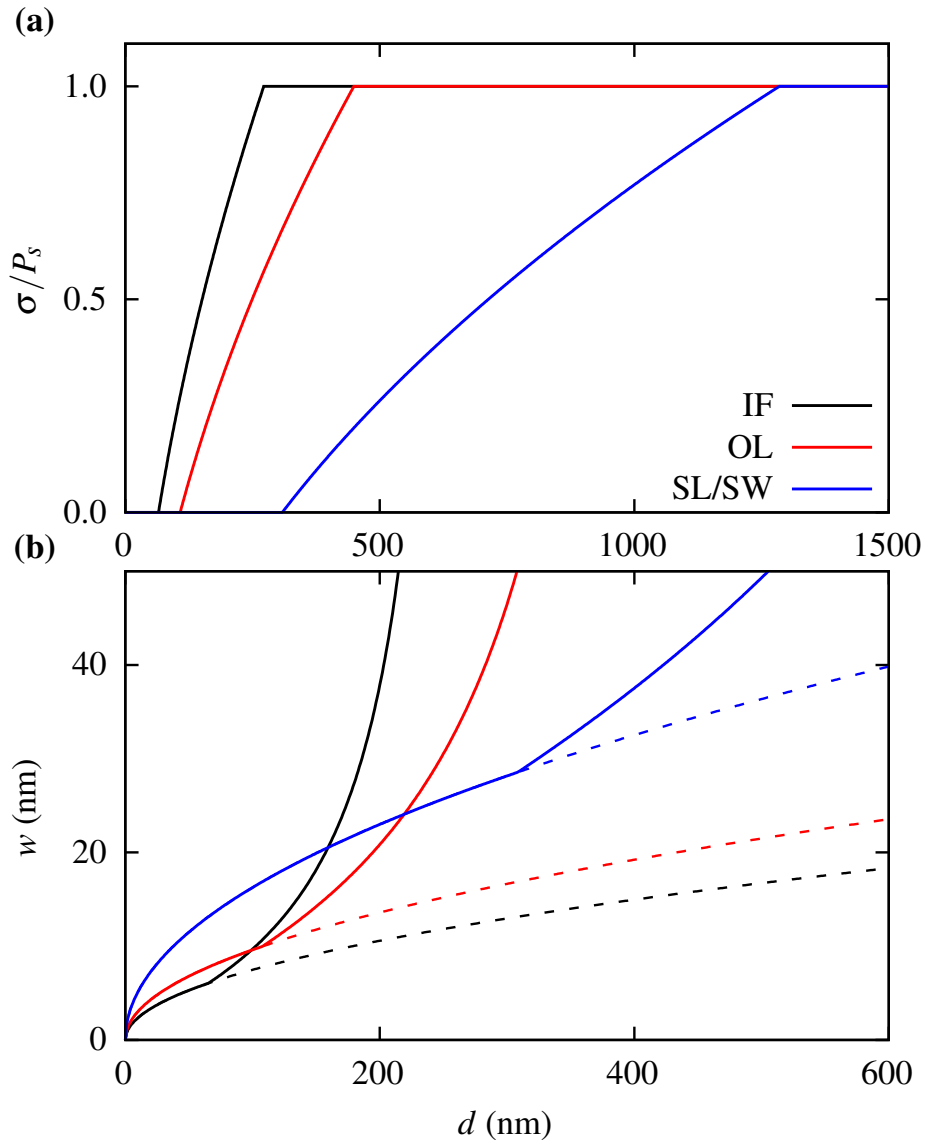
Fig. 6.3 **(a)**: 2DEG carrier concentration as a function of thickness for IF (black), OL (red) and SL with $\alpha = 1$ (blue) systems, using the theoretical values of the parameters for PTO and STO. For the superlattice, the thickness of the ferroelectric layer is used. **(b)**: domain width as a function of thickness for the same three systems. For each plot, the dashed line shows the continuation of the square root curve from the generalized Kittel law.

Fig. 6.4 Comparison of inverse domain width given by analytic solutions and numerical solutions using the full electrostatic energies, truncated at $n = 100$ terms for IF (black), OL (red) and SL with $\alpha = 1$ (blue) systems.

Chapter 7

Flexoelectric polarization of single-walled nanotubes

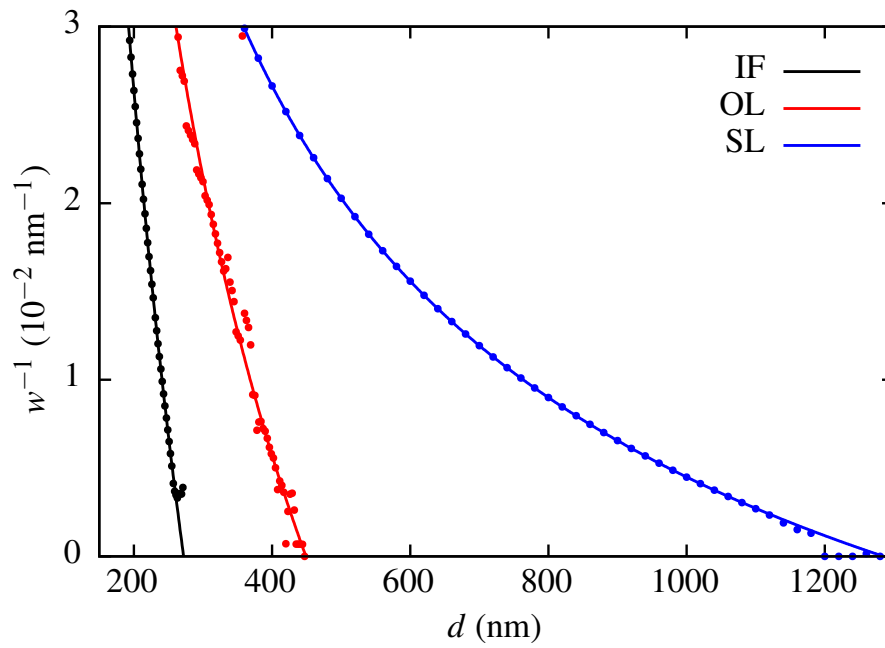In this chapter we illustrate, using first-principles DFT calculations, that the walls of both carbon nanotubes (CNTs) and TMD nanotubes (NTs) in general have a radial polarization. It is difficult to measure polarization of low-dimensional structures using DFT calculations, since Berry phase techniques cannot be used. Instead, we estimate polarizations from the electrostatic potentials, using the method of macroscopic averaging [307–309], which has been used successfully to measure polarization in slab-like systems. The electrostatic potential is obtained in the direction normal to the slab or interface, averaging in the other directions. The rapid oscillations caused by the ions are filtered out to obtain a smooth potential, and the polarization can be estimated by measuring the electric field or voltage drop across the thin film or interface. Since the number of atoms in the walls of NTs is small (≤ 3), it is not possible to smooth out the oscillations, nor is it possible to define the exact width of the wall. However, a potential drop between the inside and the outside of the wall would indicate that there is a finite electric field in the wall, and hence a polarization.

First-principles DFT calculations were performed using the SIESTA code [272] using PSML [282] norm-conserving [283] pseudopotentials, obtained from pseudo-dojo [284]. DZP orbitals were used for all calculations. The basis sets were optimized by hand, following the methodology in Ref. [310]. Calculations were performed using both Perdew-Wang (PW92) [285] LDA and PBE [279] functionals. A mesh cutoff of 800 Ry was used for the real space grid in all calculations. A Monkhorst-Pack k-point grid [288] of $12 \times 12 \times 1$ was used for the 2D monolayers and a grid of $1 \times 1 \times 12$ was used for the NTs.

Calculations were first performed for monolayers of graphene, and the TMDs MoS_2, $MoSe_2$, WS_2 and WSe_2 to be used as reference geometries for the NTs. A dipole correction [311–314] was used in the vacuum region to prevent long-range interactions between periodic images. To perform the geometry relaxations, the size of the in-plane lattice vectors a was relaxed while preserving the angle between them and the in-plane atomic positions. For the TMDs, the out-of-plane atomic coordinates were also relaxed in order to obtained the thickness t of the monolayers. The results were found to be in agreement to similar calculations in the literature [315] and are summarized in Table 7.1.

Material	LDA		PBE	
	a (Å)	t (Å)	a (Å)	t (Å)
Graphene	2.468	-	2.475	-
MoS_2	3.141	3.137	3.207	3.155
$MoSe_2$	3.282	3.367	3.356	3.393
WS_2	3.151	3.140	3.217	3.163
WSe_2	3.286	3.377	3.358	3.407

Table 7.1 Lattice constants a and thicknesses t of the 2D monolayers obtained using both LDA and PBE functionals.

NT structures were generated from the relaxed monolayers using the C2X utility [316]. Geometry relaxation calculations were then performed, relaxing the atomic coordinates in the plane of the circumference of the NTs, and the c lattice vector, but fixing the atomic coordinates along the c lattice vector.

A number of quantities obtained from the DFT calculations can be used to measure strain effects and estimate the polarization in the NTs. The strain energy per atom is a typical quantity used to measure such strain effects:

$$E_{strain} = \frac{E_{tot} - n_{cells}E_{2D}}{n_{tot}} , \qquad (7.1)$$

where E_{tot} is the total energy of the NT, E_{2D} is the energy of the monolayer, n_{tot} is the number of atoms in the NT and $n_{cells} = \frac{n_{tot}}{n_{2D}}$ is the number of unit cells of the monolayer required to form the NT. It is well-known that $E_{strain} \sim R^{-2}$ in general, where R is the radius of the NT.
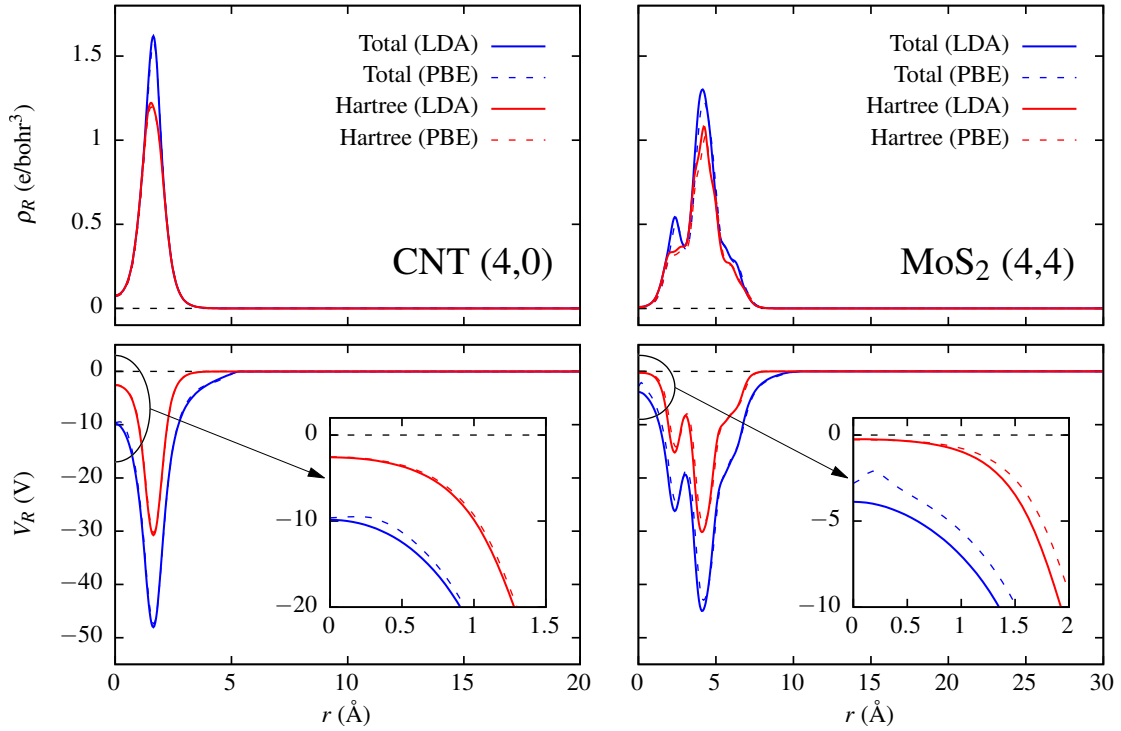
Fig. 7.1 Radial electrostatic densities (top) and potentials (bottom) for a (4,0) CNT (left) and a (4,4) MoS_2 NT (right). The red lines show the Hartree density and potential, which do not include exchange-correlation contributions, and the blue lines show the total density and potential, which do. The solid lines show results obtained using the PW92 functional and the dashed lines show results obtained using the PBE functional. The insets in the bottom plots show a close up of the potentials close to the center of the NT.

The electrostatic potentials and densities obtained from SIESTA, both with (total) and without (Hartree) exchange-correlation contributions, were converted to radial potentials using the C2X:

$$
\begin{aligned}
V_R(r) &= \frac{1}{2\pi c} \int V(\mathbf{r})\, dz\, d\theta \\
\rho_R(r) &= \frac{1}{2\pi c} \int \rho(\mathbf{r})\, dz\, d\theta
\end{aligned}
,
\tag{7.2}
$$

where r is the distance from the center of the NT. Examples of these potentials are plotted in Fig. 7.1 for a (4,0) CNT and a (4,4) MoS_2 NT. The electric field in the wall, and hence the polarization, is proportional to the potential drop ΔV_R across the wall:

$$\Delta V_R = V_R(L/2) - V_R(0) \, , \tag{7.3}$$

where $L \times L$ is the area of the unit cell in the plane of the circumference of the NT. Measuring the radii of the TMD NTs is a subtle problem. For CNTs, The standard formula

$$R(n,m) = \frac{C(n,m)}{2\pi} \equiv \frac{a}{2\pi} \sqrt{n^2 + nm + m^2} \tag{7.4}$$

is normally used, where (n,m) are the chiral indices, $C(n,m)$ is the circumference and a is the length of the in-plane lattice vectors of graphene (see Table 7.1). This is exactly the same as the radius obtained from the relaxed geometry obtained from DFT calculations, except when the radius is very small. The radii are also sensitive to DFT parameters such as the exchange-correlation functional, for example.

For TMD NTs, there are three atoms in the wall, and hence three radii: $R_{S,inner}$, R_{Mo} and $R_{S,outer}$, and Eq. (7.4) does not correspond to any of them. In order to estimate the polarization of the walls of the TMD NTs we also require the thickness of the wall. As with the monolayers, we will take this to be the distance between the chalcogen atoms, $R_{S,outer} - R_{S,inner}$, however as we can see from the density plots in Fig. 7.1 the wall extends slightly beyond the chalcogen atoms and hence this will be a lower bound on the thickness of the wall. In order to avoid confusion and for consistency across different NTs and exchange-correlation functionals we use $C(n,m)/a = \sqrt{n^2 + nm + m^2}$ as a measure of the size of the NTs, as it only depends on the chiral indices. We can estimate the polarization across the wall of a TMD NT using

$$P_R \approx \varepsilon_0 \mathcal{E}_R = \frac{\varepsilon_0 \Delta V_R}{R_{S,outer} - R_{S,inner}} \, , \tag{7.5}$$

where $\mathcal{E}_R$ is the electric field across the wall. However this will be an upper bound for the reasons mentioned above. We can calculate the radial strain on the bonds with respect to the monolayer:

$$e_{in/out} = \frac{\Delta R_{in/out} - t/2}{t/2} \, , \tag{7.6}$$

where

$$\Delta R_{\text{in}} = |R_{\text{S,inner}} - R_{\text{Mo}}|$$
$$\Delta R_{\text{out}} = |R_{\text{S,outer}} - R_{\text{Mo}}| \, , \tag{7.7}$$

and t is the thickness of the monolayer, as in Table 7.1.

7.0.1 Carbon nanotubes

Geometries of zigzag $(n,0)$ CNTs were created from the graphene monolayers using C2X. The chiral index n ranged from 6-20. Geometry relaxations were performed using both PW92 and PBE functionals until the total force on each atoms was less than 1 meV/Å. The electrostatic potentials and densities were then converted into radial potentials and densities using c2x. The strain energy per atom and the potential drop are plotted as a function of $C(n,m)/a$ for both functionals in Fig. 7.2. We can see that the strain energy per atom is inversely proportional to radii of the NTs, as expected.

The results for the potential drop are more interesting. The potential drop is zero until $C(n,m)/a \sim 10$, below which it begins to diverge. By plotting the drop for both Hartree and total potentials, we can see that this effect mainly comes from the exchange-correlation part of the potential. Both LDA and PBE results are in good agreement.

7.0.2 TMD nanotubes

Similar calculations were performed for MoS_2, $MoSe_2$, WS_2 and WSe_2 NTs, both zigzag $(n,0)$ and armchair (n,n) with chiral indices n ranging from 6-20 and 4-20, respectively. The strain energy per atom was found to have similar size dependence as the CNTs in all cases. The potential drops for the TMD NTs are shown in Fig. 7.3

The potential drops of the TMD NTs also diverged below $C(n,m)/a \sim 10$, as in the case of the CNTs. With the TMD NTs however, the potential is non-zero above this value. The potential drop increases gradually as $C(n,m)/a$ decreases. There is a maximum at $C(n,m)/a \sim 15$, below which it starts to decrease, before eventually diverging at $C(n,m)/a \sim 10$. This behavior is not observed in the CNTs, and thus we can conclude that it arises from a difference in strain on the bonds in the walls of the TMD NTs. We can use Eq. (7.5) to
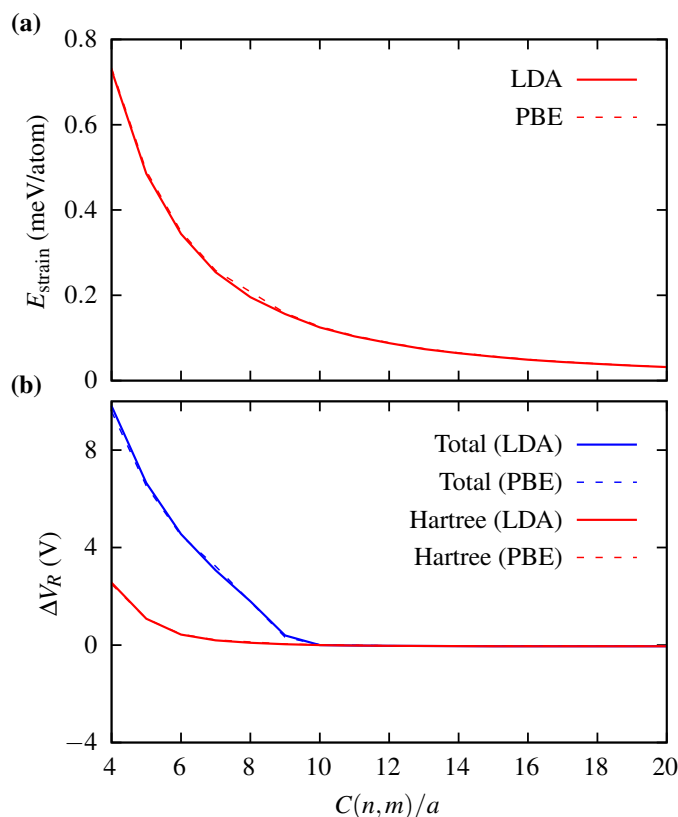
Fig. 7.2 Strain energy per atom (top) and potential drop (bottom) as a function of $C(n,m)/a$ for the zigzag CNTs. The red lines show the Hartree density and potential, which does not include exchange-correlation contributions and the blue lines show the total density and potential, which does. The solid lines show results obtained using the PW92 functional and the dashed lines show results obtained using the PBE functional.

estimate the polarization across the wall from the potential drops in Fig. 7.3. In Fig. 7.4 we plot the polarization in the walls, P_R, of the TMD NTs. First we note that, even before the potential drop diverges, the polarization across the walls is of the order of 100 C/cm^2. The maximum at $C(n,m)/a \sim 15$ is interesting and unexpected behavior. Typically we expect strain effects to decrease monotonically with NT size, such as the strain energy per atom in Fig. 7.2.

In Fig. 7.5 we plot the radial strain on the inner and outer bonds, obtained using Eq. (7.6), for the MoS_2 NTs. From this we can see that the strain on the bonds increases monotonically as $C(n,m)/a$ decreases, which does not explain the maximum of the polarization. It does however illustrate that the polarization is a result of an inhomogeneous compression of the inner and outer bonds, the compression of the outer bond being much larger.
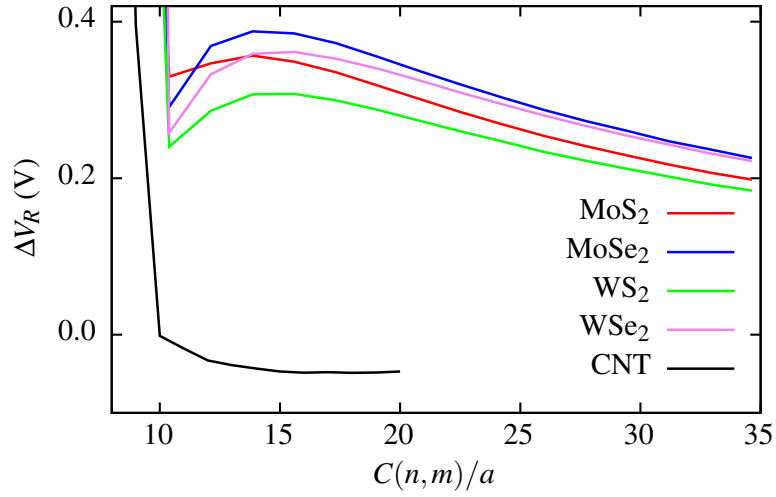
Fig. 7.3 Potential drops for the TMD NTs as a function of $C(n,m)/a$, obtained from the LDA calculations. The potential drop for the CNTs is also plotted in black for comparison.

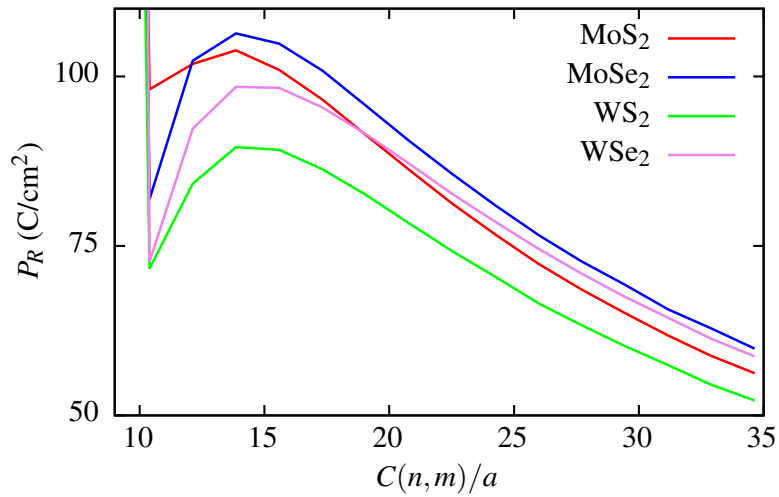Fig. 7.4 Estimation of the radial polarization P_R in the walls of the TMD NTs as a function of $C(n,m)/a$, obtained from the LDA calculations using Eq. (7.5).
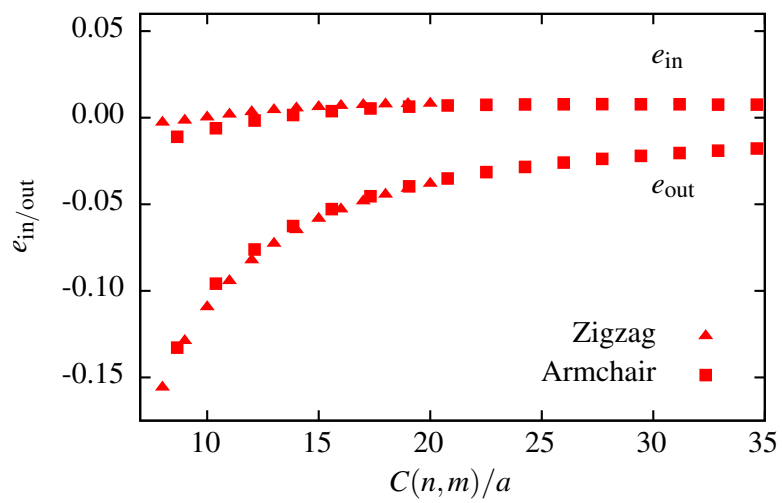
Fig. 7.5 Radial strain on the inner and outer bounds as a function of $C(n,m)/a$ for the MoS_2 NTs, obtained using the LDA calculations.

Chapter 8

Ferroelectricity in moiré superlattices

Twisted bilayer systems are the subject or intense study at present. In this chapter we introduce a model of lattice relaxation in a moiré superlattice which includes the effect of an applied field on the bilayer. The total energy is an integral of the energy density over a moiré supercell

$$V_{\text{tot}} = \frac{1}{A_{\text{sc}}} \int_{A_{\text{sc}}} \mathcal{V}_{\text{tot}}(\mathbf{r}) \, d\mathbf{r} \, , \tag{8.1}$$

where A_{sc} is the area of the supercell. For a bilayer system Eq. (8.1) is a discrete sum over atomic sites, but generalizes to a continuum field theory when the moiré period is much larger than the lattice constants of the monolayers.

We can model moiré superlattices at different levels of theory depending on the contributions we include in Eq. (8.1). The stacking energy $\mathcal{V}_{\text{stack}}$ captures the weak van der Waals interactions between the layers in terms of the layer separation d. The elastic energy $\mathcal{V}_{\text{elastic}}$ allows for in-plane displacements of the atoms in the layers. Together, the stacking and elastic energies provide a good description of the atomic structure in moiré superlattices, namely lattice relaxation and the formation of stacking domains. Having obtained a realistic description of the structure, we could proceed to obtain the electronic bands from tight-binding theory.

In order to consider the effect of an electric field on the atomic structure, we also include the electrostatic energy induced by an electric field $\mathcal{E}$ perpendicular to the bilayer, see Fig. 8.1 (d). The total energy density is
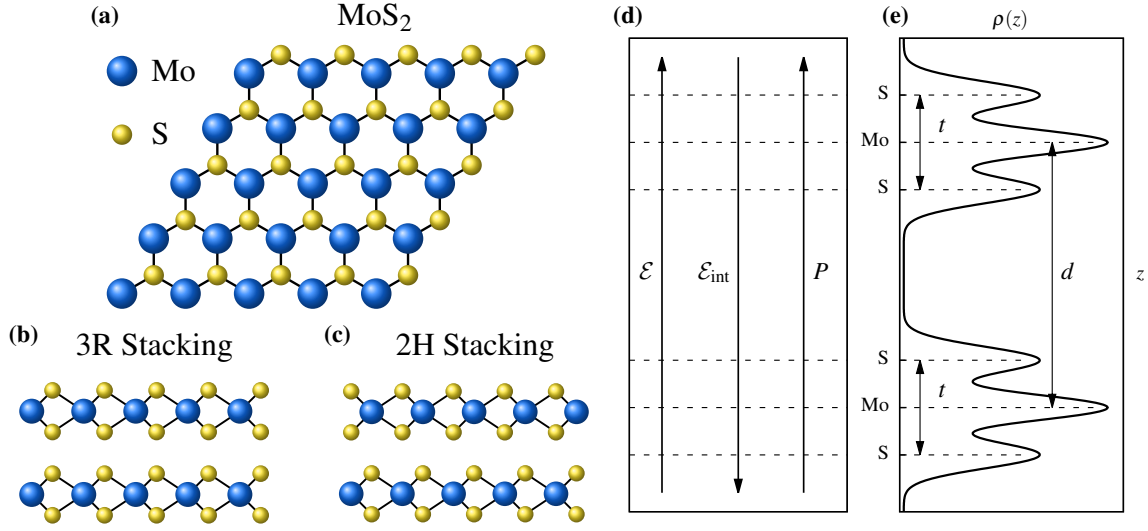
Fig. 8.1 **(a)**: Atomic structure of a MoS_2 monolayer. The two stacking configurations are shown below: **(b)**: alignment of the layers (3R stacking) and **(c)**: the two layers mirrored with respect to one another (2H stacking or a twist of $180°$). **(d)**: Sketch of the electrostatics of bilayer MoS_2. The dashed lines indicate the vertical positions of the atoms, and the vectors show the applied field $\mathcal{E}$ and resulting polarization P and internal field $\mathcal{E}_{int}$. **(e)**: Sketch of the charge density of bilayer MoS_2 along the out-of-plane direction, averaged in the in-plane directions.

$$\mathcal{V}_{tot} = \mathcal{V}_{elastic} + \mathcal{V}_{stack} + \mathcal{V}_{elec}$$

$$
\begin{aligned}
\mathcal{V}_{elastic} &= C_{ijkl}\varepsilon_{ij}\varepsilon_{kl} \\
\mathcal{V}_{stack} &= |\mathcal{V}_0(\mathbf{r})| \left[\left(\frac{d_0(\mathbf{r})}{d} \right)^{12} - 2 \left(\frac{d_0(\mathbf{r})}{d} \right)^{6} \right] \\
\mathcal{V}_{elec} &= -\mathcal{E} p_0(\mathbf{r}) - \frac{1}{2}\varepsilon_0 \left(\alpha_0(\mathbf{r}) + \alpha_1(\mathbf{r}) \left(\frac{d}{d_0(\mathbf{r})} - 1 \right) \right) \mathcal{E}^2
\end{aligned}
\qquad (8.2)
$$

In the elastic energy, summation is assumed, C is the linear elasticity tensor and

$$\varepsilon_{ij} = \frac{1}{2} \left(\partial_i U_j(\mathbf{r}) + \partial_j U_i(\mathbf{r}) \right) \qquad (8.3)$$

is the strain tensor, written in terms of a relative in-plane displacement $\mathbf{U}$.

The stacking energy can be included in a number of ways. The simplest is to use the cohesive energy as a function of space, $\mathcal{V}_0(\mathbf{r})$, assuming that at each point in the supercell the layer separation takes the value that minimizes the local stacking energy: $d(\mathbf{r}) = d_0(\mathbf{r})$. Other

studies have allowed the layer separation to vary by performing a harmonic expansion about the equilibrium layer separation [218]. When considering the effect of an applied field, it is necessary to include the full van der Waals potential because some phenomena cannot be captured at the harmonic level, such as the breakdown of the bilayer for stronger fields [237].

The first term in $\mathcal{V}_{\text{elec}}$ is the coupling between the electric field and the out-of-plane spontaneous dipole moment of the bilayer [230]. Bilayer systems without inversion symmetry, such as 3R MoS_2 (Fig. 8.1 (b)), have a local dipole moment throughout the supercell which averages to zero, whereas systems with inversion symmetry, such as 2H MoS_2, have no local dipole moment anywhere in the supercell (Fig. 8.1 (c)). The second term describes the dielectric response of the bilayer to the electric field, where α_0 and α_1 are the first two coefficients in the expansion of the polarizability α about the equilibrium layer separation. A bilayer system cannot simply be treated as a pair of capacitor plates; due to the overlap of electronic states in the vacuum region between the layers, it is more appropriate to treat the system as a single slab with a nonuniform charge density, see Fig. 8.1 (e). Thus, changing the layer separation will affect the polarizability of the system. To capture this physics we perform a Taylor expansion of the polarizability in d about the equilibrium layer separation d_0. In addition, the polarizability will vary throughout the superlattice due to the different local stacking configurations and equilibrium layer separations. A dielectric response occurs in all layered systems, irrespective of symmetry.

Before proceeding to study lattice relaxation under an electric field, we derive and study the three contributions to Eq. (8.2) in detail, both theoretically and using first-principles calculations.

8.1 Physical Model

8.1.1 Twistronics

A twisted bilayer system is composed of two layers with a relative twist angle θ between them, which we call the reference (r) and twisted (t) layers, respectively. For bilayers comprised of hexagonal monolayers, the lattice vectors of the reference layer and the twisted layer are
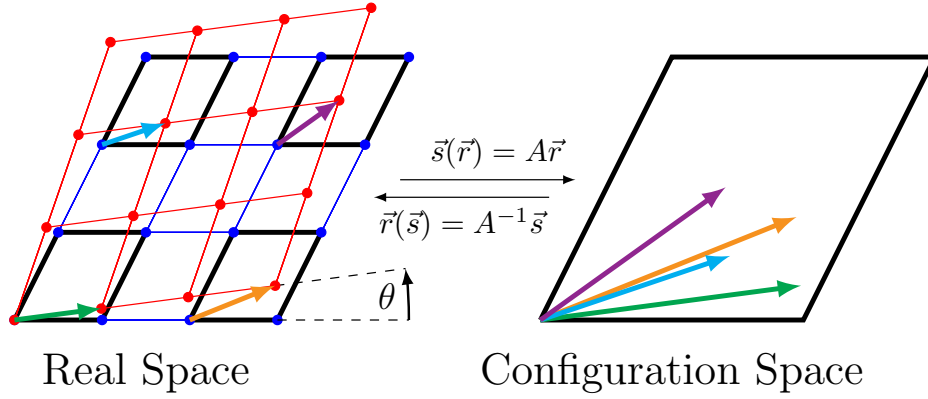
Fig. 8.2 Sketch of the mapping between real space and configuration space. On the left is a 3×3 section of a moiré superlattice with twist angle θ. The positions **r** are mapped into configuration space via the operator $A = (I - R_\theta^{-1})$, modulo a primitive unit cell. The vectors **s** are shown for the four highlighted cells.

$$\mathbf{a}_{\mathrm{r},1} = a \begin{bmatrix} 1 \\ 0 \end{bmatrix}, \qquad \mathbf{a}_{\mathrm{r},2} = \frac{a}{2} \begin{bmatrix} 1 \\ \sqrt{3} \end{bmatrix},$$

$$\mathbf{a}_{\mathrm{t},1} = R_\theta \mathbf{a}_{\mathrm{r},1}, \qquad \mathbf{a}_{\mathrm{t},2} = R_\theta \mathbf{a}_{\mathrm{r},2} \tag{8.4}$$

respectively, where a is the monolayer lattice constant and $R_\theta = \begin{bmatrix} \cos(\theta) & -\sin(\theta) \\ \sin(\theta) & \cos(\theta) \end{bmatrix}$. For a general θ, the two layers are incommensurate, i.e. they form a supercell which is infinitely large. If the two layers form a commensurate supercell we can define supercell lattice vectors $\mathbf{L}_i$ as a linear combinations of the lattice vectors of either layer:

$$\begin{aligned} \mathbf{L}_1 &= n\mathbf{a}_{\mathrm{r},1} + m\mathbf{a}_{\mathrm{r},2} \\ &= p\mathbf{a}_{\mathrm{t},1} + q\mathbf{a}_{\mathrm{t},2} = pR_\theta \mathbf{a}_{\mathrm{r},1} + qR_\theta \mathbf{a}_{\mathrm{r},2} . \\ \mathbf{L}_2 &= R_{\pi/3} \mathbf{L}_1 \end{aligned} \tag{8.5}$$

The second line of Eq. (8.5) leads to a Diophantine equation in the integers n, m, p and q, and the set of angles which result in a commensurate supercell is given by [317–319]

$$\theta(n,m) = \cos^{-1}\left(\frac{n^2 + 4nm + m^2}{2(n^2 + nm + m^2)}\right). \tag{8.6}$$

Consider an atom in the reference layer, with in-plane position $\mathbf{r}_0$. The corresponding atom in the twisted layer has position $\mathbf{r} = R_\theta \mathbf{r}_0$. The displacement due to twisting is $\delta(\mathbf{r}) = \mathbf{r} - \mathbf{r}_0 = \left(I - R_\theta^{-1}\right)\mathbf{r}$. If the layers form a commensurate supercell with lattice vectors $\mathbf{L}_i^{\mathrm{M}}$, say, the atoms will realign when the displacement is equal to a lattice vector, $\delta(\mathbf{L}_i^{\mathrm{M}}) = \mathbf{a}_{\mathrm{r},i}$:

$$\mathbf{L}_i^{\mathrm{M}} = \left(I - R_\theta^{-1}\right)^{-1} \cdot \mathbf{a}_i^1 . \tag{8.7}$$

The cell spanned by $\mathbf{L}_i^{\mathrm{M}}$ is known as a moiré superlattice, and

$$L_M \equiv \left|\mathbf{L}_i^{\mathrm{M}}\right| = \frac{a}{2\sin(\theta/2)} , \tag{8.8}$$

is known as the the moiré period, which is is not necessarily equal to the supercell period:

$$L_{\mathrm{sc}} = \frac{|m - n|\,a}{2\sin(\theta/2)} = |m - n|\,L_M . \tag{8.9}$$

For $m \neq n$, there will be $(m - n)^2$ moiré periods in the supercell.

Having established a geometric description, we can model structural or electronic phenomena in a twisted bilayer using phenomenological or tight-binding models. These models can be parameterized using first-principles calculations. However in practice this is difficult to do in real space because the size of and the number of atoms in the supercell becomes prohibitively large at smaller twist angles. Fortunately, we can take advantage of a useful mapping which allows us to parameterize systems at arbitrary twist angles using just a single cell of a commensurate bilayer.

The set of displacements of every atom in a moiré superlattice can be described by $\delta(\mathbf{r})$. Alternatively, we can describe the displacements by a set of local translations

$$\mathbf{s}(\mathbf{r}) = \left(I - R_\theta^{-1}\right)\mathbf{r} \mod \{\mathbf{a}_{r,1}, \mathbf{a}_{r,2}\}$$
$$\equiv A \cdot \mathbf{r} \tag{8.10}$$

i.e. at $\mathbf{r}$, the system is locally equivalent to an untwisted bilayer, with a relative in-plane slide $\mathbf{s}(\mathbf{r})$ between the layers, see Fig. 8.2. The set of translations $\mathbf{s}(\mathbf{r})$ is contained in a single primitive cell of the reference layer, even in the continuum limit. We call this space of translations configuration space [203, 320, 321, 223]. This space can be traversed by taking an untwisted commensurate bilayer and sliding one layer over the other. Physical properties can be measured in configuration space, and we can use the inverse map,

$$\mathbf{r}(\mathbf{s}) = \left(I - R_\theta^{-1}\right)^{-1}\mathbf{s} = A^{-1}\mathbf{s}, \tag{8.11}$$

to parameterize a moiré superlattice in real space for arbitrary twist angles [223]. Derivatives in real space and configuration space are related by

$$\nabla_r = A^T \nabla_s, \tag{8.12}$$

which is useful for mapping quantities which depend on spatial derivatives, such as strains, to configuration space.

8.1.2 Stacking energy

It is well known layered systems interact via long-range van der Waals forces. For non-polar materials, this is facilitated by induced dipole−induced dipole, or London interactions, where fluctuations in the charge density of one layer lead to a dipolar response in the other layer, and vice versa. This can be described by a van der Waals potential in the layer separation d:

$$\mathcal{V}_{\text{stack}}(d) = \frac{n}{m-n}|\mathcal{V}_0|\left[\left(\frac{d_0}{d}\right)^m - \frac{m}{n}\left(\frac{d_0}{d}\right)^n\right], \tag{8.13}$$

where $\mathcal{V}_0$ is the depth of the potential well or cohesive energy *per unit cell*, d_0 is the equilibrium separation, and the indices (n,m) determine the curvature of the well about the

minimum. Eq. (8.13) can be parameterized using first-principles calculations, which is done in the next section. For two slabs which extend infinitely in area, the energy is expected to behave like d^{-2} at larger separations, since the dipole-dipole interaction is integrated twice over an infinite area [322]. From first-principles calculations we found that this is not the case, and the long-range interactions in bilayer graphene and MoS_2 decay with $n \geq 6$. We suspect that this is because a bilayer is not adequately described as a pair of capacitor plates, but rather a single slab with a non-uniform charge density as in Fig. 8.1 (e). The non-zero overlap of states in the vacuum region may be screening the long-range interactions and could be responsible for larger than expected values of (n,m), although a more detailed study is required to verify this.

8.1.3 Electrostatic energy

The electrostatic energy of a dielectric slab in the presence of a perpendicular electric field $\mathcal{E}$ is

$$\mathcal{V}_{\mathrm{elec}}(P,\mathcal{E},d) = \Omega \left(\frac{1}{2\varepsilon_0 \chi(d)}(P-P_0)^2 - \mathcal{E} \cdot P \right) , \qquad (8.14)$$

where P and P_0 are the total and spontaneous polarization, respectively, Ω is the volume of the bilayer, and $\chi(d)$ is the dielectric susceptibility, which in general depends on the geometry of the system. Eq. (8.14) assumes a linear response to the applied field, $P(\mathcal{E},d) = P_0 + \varepsilon_0 \chi(d)\mathcal{E}$, which inserting into Eq. (8.14) gives:

$$\mathcal{V}_{\mathrm{elec}}(\mathcal{E},d) = -\frac{1}{2}\varepsilon_0 \alpha(d)\mathcal{E}^2 - \mathcal{E}p_0 , \qquad (8.15)$$

where $\alpha = \Omega\chi$ is the polarizability, which describes the linear response of the dipole moment to the applied field, and $p_0 = \Omega P_0$ is the spontaneous dipole moment. When an electric field is applied, the layers are no longer non-polar, and the long-range interactions can no longer be considered to be pure induced dipole−induced dipole interactions. However, we can think of the interactions between the layers as arising due to fluctuations about a finite polarization, rather than zero polarization.

For the polarizability, we perform a Taylor expansion about d_0 to linear order,
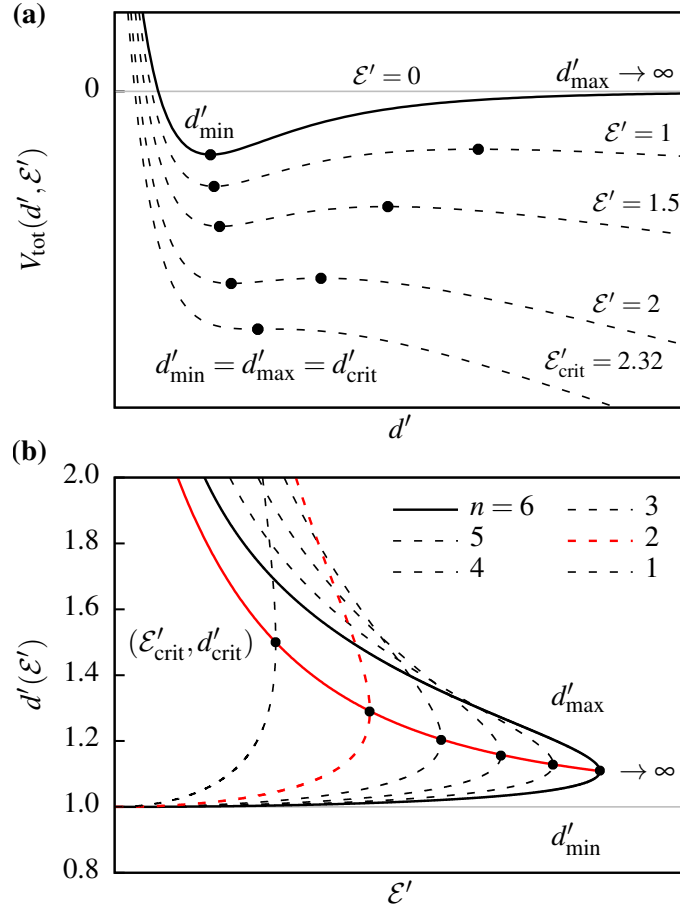
Fig. 8.3 **(a)**: Total energy from Eq. (8.17) as a function of d for increasing values of $\mathcal{E}$. The points show the positions of $d_{\min}$ and $d_{\max}$ on each curve. The lowest curve is for field strength of $\mathcal{E} = \mathcal{E}_{\mathrm{crit}}$, where $d_{\min} = d_{\max} \equiv d_{\mathrm{crit}}$. **(b)**: $d_{\min}$ and $d_{\max}$ as a function of $\mathcal{E}$ for different values of n, increasing from left to right. The solid black curve is $n = 6$, and the dashed red curve is the theoretical value $n = 2$. The solid red curve shows the critical values $(d_{\mathrm{crit}}, \mathcal{E}_{\mathrm{crit}})$ from Eq. (8.18). The critical points on each curve are marked, i.e. when $d = d_{\mathrm{crit}}$ and the bilayer breaks down.

$$\alpha(d) = \alpha_0 + \alpha_1 \left(\frac{d}{d_0} - 1 \right), \tag{8.16}$$

where α_0 and α_1 are both positive and have units of Å^3. In the next section we verify using first-principles calculations that the polarizability is indeed linear about d_0. Taking $(n, m) = (n, 2n)$, we can write the energy, excluding elastic contributions, as

$$
\mathcal{V}_{\text{tot}}(d, \mathcal{E}) = |\mathcal{V}_0| \left[\left(\frac{d_0}{d} \right)^{2n} - 2 \left(\frac{d_0}{d} \right)^{n} \right]
$$
$$
- \mathcal{E} p_0 - \frac{1}{2} \varepsilon_0 \left(\alpha_0 + \alpha_1 \left(\frac{d}{d_0} - 1 \right) \right) \mathcal{E}^2
$$

(8.17)

By plotting contours of the energy as a function of d for fixed values of $\mathcal{E}$, see Fig. 8.3 (a), we can see that the stacking energy is lowered by the electric field, consistent with results the from first-principles calculations. At zero field, $\mathcal{V}_{\text{stack}}$ has a minimum at the equilibrium separation $d_{\min} = d_0$, and a maximum (for $d > d_{\min}$) at $d_{\max} \to \infty$. When a field is applied, $\mathcal{V}_{\text{stack}}$ diverges as $d \to \infty$. This makes physical sense: increasing d will increase the total dipole moment and lower the total energy. For a non-zero field, $d_{\max}$ has a finite value, at the top of the energy barrier which separates $d_{\min}$ and $d \to \infty$. As the field strength increases, $d_{\min}$ and $d_{\max}$ move closer together, eventually meeting at a critical point $(d_{\text{crit}}, \mathcal{E}_{\text{crit}})$ where the energy barrier vanishes, and the bilayer becomes unstable,

$$
d'_{\text{crit}} = \left(\frac{2n+1}{n+1} \right)^{\frac{1}{n}}
$$
$$
\mathcal{E}'_{\text{crit}} = 2n \sqrt{ \frac{(n+1)^{1+\frac{1}{n}}}{(2n+1)^{2+\frac{1}{n}}} }
$$

(8.18)

where $d' \equiv \frac{d}{d_0}$ and $\mathcal{E}' \equiv \sqrt{\frac{\varepsilon_0 \alpha_1 d_0}{|\mathcal{V}_0|}} \mathcal{E}$. In Fig. 8.3 (b) we show $d_{\min}$ and $d_{\max}$ as a function of $\mathcal{E}'$ for several values of n. The solid red line shows Eq. (8.18), which separates $d_{\min}$ and $d_{\max}$. Interestingly, the behavior is highly sensitive to the value of n. For larger values of n, which are predicted from first-principles calculations, $d_{\min}$ does not change by much until $\mathcal{E} \sim \mathcal{E}_{\text{crit}}$, where it increases by about 10% before the bilayer becomes unstable. For smaller values of n, the layers separate more easily because the potential well is shallower, but the breakdown occurs at smaller field strengths.

8.1.4   Elastic energy

The elastic energy in Eq. (8.2) is given as a contraction of the strain tensors with the fourth rank elasticity tensor [223, 323]:

$$
\begin{aligned}
C_{11} &= \begin{bmatrix} B+\mu & 0 \\ 0 & B-\mu \end{bmatrix}, \quad C_{12} = \begin{bmatrix} 0 & \mu \\ \mu & 0 \end{bmatrix}, \\
C_{21} &= \begin{bmatrix} 0 & \mu \\ \mu & 0 \end{bmatrix}, \quad C_{22} = \begin{bmatrix} B-\mu & 0 \\ 0 & B+\mu \end{bmatrix}
\end{aligned}
\tag{8.19}
$$

and is given explicitly as

$$
\begin{aligned}
\mathcal{V}_{\text{elastic}} &= \frac{1}{2}\left[B(\varepsilon_{11}+\varepsilon_{22})^2 + \mu\left((\varepsilon_{11}-\varepsilon_{22})^2 + (\varepsilon_{12}+\varepsilon_{21})^2\right)\right] \\
&= \frac{1}{2}\left[B(\partial_x U_x + \partial_y U_y)^2 + \right. \\
&\qquad \left. + \mu\left((\partial_x U_x - \partial_y U_y)^2 + (\partial_x U_y + \partial_y U_x)^2\right)\right]
\end{aligned}
\tag{8.20}
$$

where B is the bulk modulus and μ is the shear modulus. The strain tensor in configuration space is [223]

$$
\varepsilon_{ij} = \frac{1}{2}\left((\partial_i u_k)A_{kj} + (\partial_j u_k)A_{ki}\right)
\tag{8.21}
$$

which allows us to write down the elastic energy in configuration space:

$$
\begin{aligned}
\mathcal{V}_{\text{elastic}} &= \frac{\theta^2}{2}\left[B\left(\partial_{s_x} u_{s_y} - \partial_{s_y} u_{s_x}\right)^2 + \right. \\
&\qquad \left. + \mu\left(\left(\partial_{s_x} u_{s_y} + \partial_{s_y} u_{s_x}\right)^2 + \left(\partial_{s_x} u_{s_x} - \partial_{s_x} u_{s_x}\right)^2\right)\right]
\end{aligned}
\tag{8.22}
$$

It is convenient to work in terms of the lattice vectors $\mathbf{a}_{r,1}$ and $\mathbf{a}_{r,2}$. Under this transformation, the displacement transforms as $\mathbf{u} \to g\mathbf{u}$ and the strain tensor transforms as $\varepsilon_{ij} \to g_{i\alpha}^{-1} g_{j\beta} \varepsilon_{\alpha\beta}$, where $g = \begin{bmatrix} 1 & 1/2 \\ 0 & \sqrt{3}/2 \end{bmatrix}$. The elastic energy is then

$$
\begin{aligned}
\mathcal{V}_{\text{elastic}} = \frac{\theta^2}{2} \Big[& B \left(\partial_{a_x} u_{a_y} - \partial_{a_y} u_{a_x} \right)^2 + \\
& + \mu \left(\frac{4}{3} \left(\partial_{a_x} u_{a_y} + \partial_{a_y} u_{a_x} \right)^2 + \left(\partial_{a_x} u_{a_x} - \partial_{a_y} u_{a_y} \right)^2 \right) \Big]
\end{aligned}
\tag{8.23}
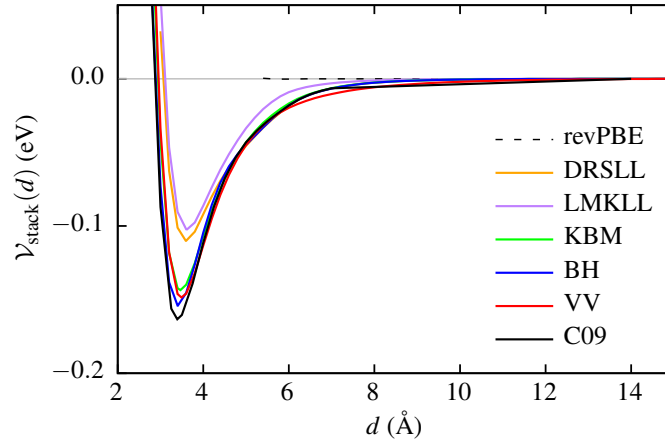$$

8.2 First-principles study of TMD bilayers

Fig. 8.4 Stacking energy as a function of layer separation for bilayer graphene for various VDW-corrected functionals in SIESTA: revPBE [324] (GGA), DRSLL (DF1) [325, 326], LMKLL (DF2) [325, 327], KMB [325, 328], C09 [325, 329], BH [325, 330], VV [331].

First-principles DFT calculations were performed using the SIESTA code [272], as described in the previous chapter. A mesh cutoff of 1200 Ry was used for the real space grid in all calculations. A Monkhorst-Pack k-point grid [288] of $12 \times 12 \times 1$ was used for the initial geometry relaxations, and a mesh of $18 \times 18 \times 1$ was used to calculate polarizabilities. Calculations were converged until the relative changes in the Hamiltonian and density matrix were both less than 10^{-6}. For the geometry relaxations, the atomic positions were fixed in the in-plane directions, and the vertical positions and in-plane stresses were allowed to relax until the force on each atom was less than 0.1 meV/Å. The layer separation d was taken to be the distance between the carbon atoms in bilayer graphene an the distance

between the metals in bilayer MoS_2 (see Fig 8.1 (e)), and the stacking energy is calculated as $\mathcal{V}_{\text{stack}} = \mathcal{V}_{\text{bilayer}} - 2\mathcal{V}_{\text{mono}}$, where $\mathcal{V}_{\text{bilayer}}$ and $\mathcal{V}_{\text{mono}}$ are the total energies of the bilayer and monolayer systems, respectively.

Because GGA functionals tend to underestimate the cohesive energy of van der Waals systems, the different VDW-corrected functionals in SIESTA were tested by measuring the stacking energy of bilayer graphene as a function of layer separation, see Fig. 8.4. The rest of the calculations were performed using the C09 functional, as it was found to give good results for both bilayer graphene and MoS_2.

8.2.1   Parameterizing the stacking energy

We can parameterize the stacking energy by calculating $\mathcal{V}_0$, d_0 and the two indices (n, m). Using suitable values for (n, m), a fit to the stacking energy as a function of layer separation was obtained using Eq. (8.13), which is shown in Fig. 8.5 for bilayer graphene and MoS_2 with 3R stacking. The parameters used to fit Eq. (8.13) to the first-principles calculations are given in Table 8.1.
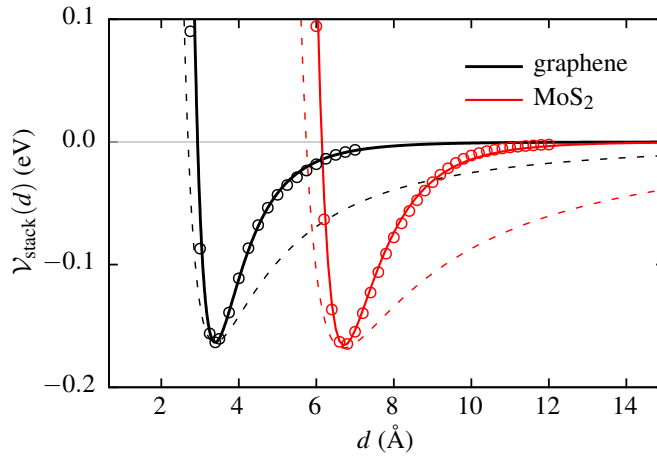

Fig. 8.5 Parameterization of $\mathcal{V}_{\text{stack}}(d)$ for bilayer graphene and MoS_2 (3R stacking). The points show results from DFT calculations, and the solid lines show the parameterization using the values in Table 8.1. The dashed lines show the same parameterization, but with the smaller index changed to 2.

Material	a (Å)	$\mathcal{V}_0$ (eV)	d_0 (Å)	(n, m)
graphene	2.473	-0.163	3.393	$(6, 8)$
MoS$_2$ (3R)	3.164	-0.165	6.716	$(8, 15)$

Table 8.1 Parameterization of $\mathcal{V}_{\mathrm{stack}}(d)$ for bilayer graphene and MoS$_2$ from first-principles calculations.

8.2.2 Parameterizing the electrostatic energy

To parameterize $\mathcal{V}_{\mathrm{elec}}$, an electric field was applied in the out-of-plane direction. A dipole correction [311–314] was used in the vacuum region to remove the fictitious long-range interactions between periodic images. The resulting dipole moment in the out-of-plane direction was then measured.

We first performed geometry relaxations of bilayer MoS$_2$ for electric fields of increasing strength. We found that the layer separation increases only marginally (a very low force tolerance is required to see this, otherwise the layers do not move) until around $\mathcal{E} \sim 2$ V/Å, where the layers begin to separate and the bilayer quickly becomes unstable. In Fig. 8.6 (a) we plot the potential energy curves for bilayer MoS$_2$ as a function of d for different values of applied field in order to clarify this peculiar behavior. We see that the electric field lowers the energy at larger separations, and the bilayer becomes unstable at $\mathcal{E}_{\mathrm{crit}} \approx 2.25$ VÅ, similar to the results obtained in Ref. [237]. By calculating the Mülliken charges on each layer in Fig. 8.6 (b), we find that there is an interlayer charge transfer when an electric field is applied. The charge transfer is linear in $\mathcal{E}$ above $\mathcal{E} \approx 0.27$ V/Å, below which no charge transfer is observed. The charge transfer may be a result of Zener tunneling, facilitated by the electric field, although a more detailed study is required to verify this.

For each value of d, we calculate the dipole moment as a function of electric field, $p(\mathcal{E})$, as shown in Fig. 8.7 (a). We see that, when the field is not strong enough for an interlayer charge transfer to occur, $\mathcal{E} < 0.27$ V/Å, changing the interlayer separation has no effect on the polarizability α. For $\mathcal{E} < 0.27$ V/Å, a charge transfer occurs and $\alpha(d)$ increases linearly with d, see Fig. 8.7 (b).

(a)

(b)
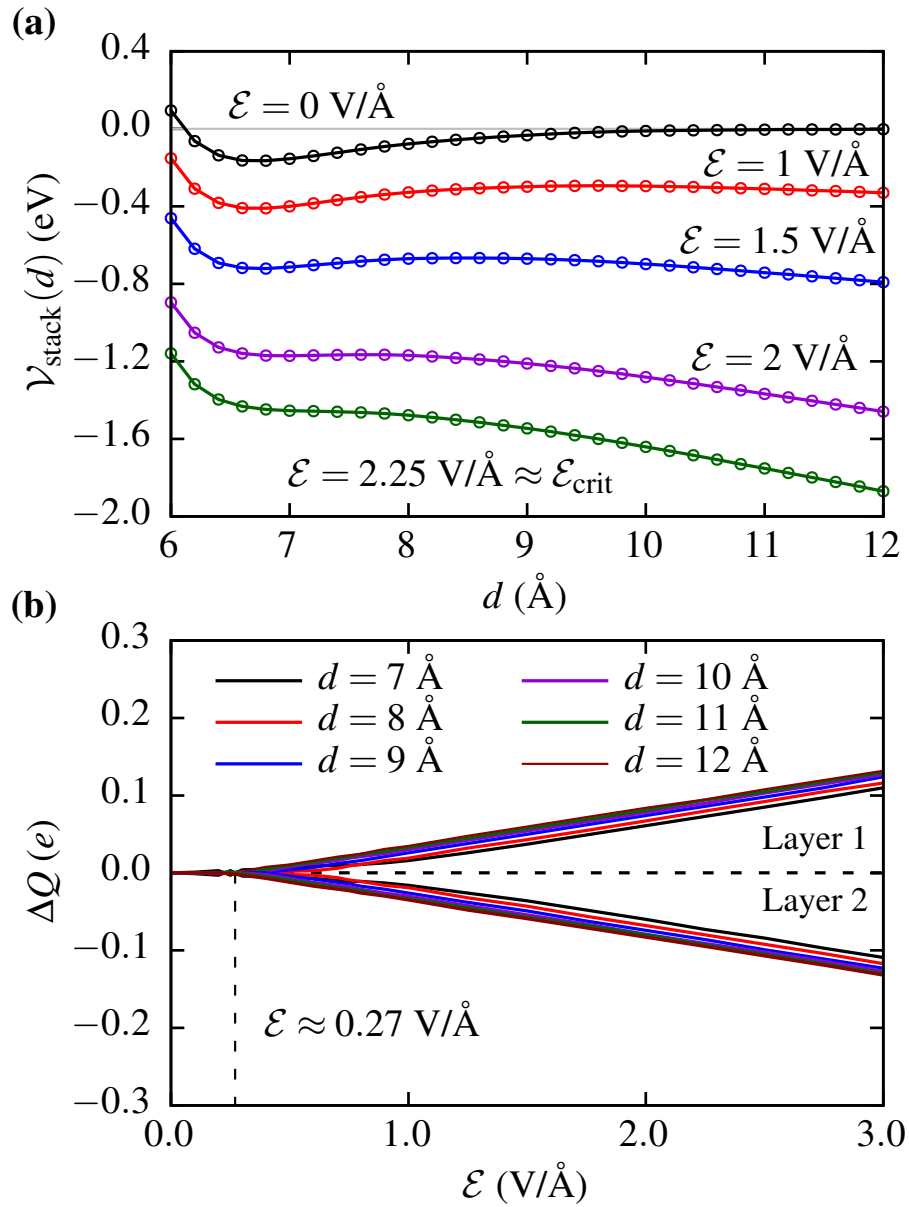
Fig. 8.6 **(a)**: $\mathcal{V}_{\text{stack}}(d)$ for different fixed values of electric field for 3R MoS$_2$. **(b)**: Change in Mülliken charges ΔQ of each layer as a function of electric field. The vertical dashed line indicates the field strength beyond which interlayer charge transfer occurs.
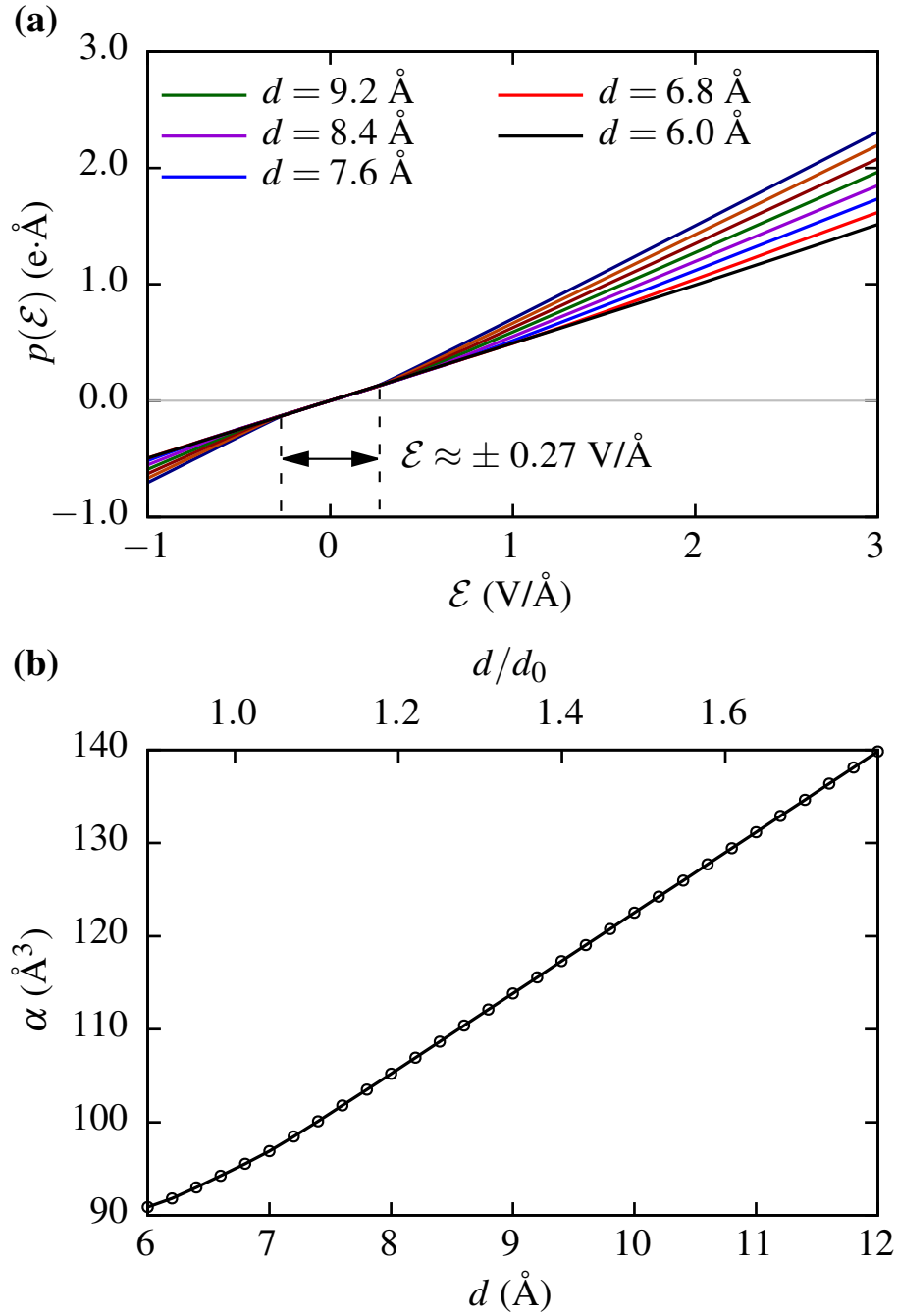
Fig. 8.7 (a): Out-of-plane dipole moment $p(\mathcal{E})$ for various fixed values of d for 3R MoS_2. The vertical dashed lines indicate the field strengths beyond which charge transfer occurs. (b): Polarizability $\alpha(d)$, measured at $\mathcal{E} > 0.27$ V/Å.

8.2.3   Parameterization in configuration space

Calculations were repeated to parameterize $\mathcal{V}_0$, d_0, α_0 and α_1 as a function of $\mathbf{s}$. The high symmetry stacking configurations AA (metal over metal), AB/BA (metal over chalcogen), and the saddle point (SP) all lie along the configuration space diagonal. Thus, it was sufficient to perform a series of calculations along the diagonal, and use a 2D Fourier interpolation to parameterize the model everywhere in configuration space. One layer was fixed, and the other layer was translated by $\mathbf{s} = s(\mathbf{a}_1 + \mathbf{a}_2)$, $s \in [0, 1]$, and the aforementioned quantities were measured on a fine grid of values of s. The interpolation was done following similar approaches in previous studies [220, 221, 214, 223]: each quantity is written as a Fourier expansion. The results from the first-principles calculations at different values of $\mathbf{s}$ are used to fit the Fourier coefficients, and a smooth interpolation of each quantity is obtained everywhere in configuration space. The reciprocal lattice vectors $\mathbf{G}$ of the same length are sorted into shells, and the first few shells are sufficient to obtain good parameterization. The first-principles results and parameterization using the first three shells are shown in Fig. 8.10 for 3R and 2H stacked bilayer MoS_2.

After parameterizing the model, we can examine the effect of an electric field on the system in configuration space. Fig. 8.8 (a) shows the layer separation along the configuration space diagonal at different electric field values for 3R MoS_2. Without lattice relaxation, only the dielectric response affects the layer separation. We can see that the layer separation increases non-uniformly in configuration space, leading to a corresponding reduction in the stacking energy, shown in Fig. 8.8 (b). We plot results only up to $\mathcal{E} = 1.68$ V/Å because that is the smallest critical field at which $d_{\min} \to \infty$ somewhere in configuration space. We examine this in more detail in Fig. 8.8 (c) by showing $d_{\min}$ as a function of electric field at the AA, AB and SP points. We can see that the critical field values for the AB and SP points are considerably larger. We could reach stronger field strengths by including terms proportional to ∇d in the elastic energy from von Karman plate theory [220], but this would make the model considerably more difficult to solve, requiring solutions to fourth order differential equations. However, without including nonlinear terms in the elastic energy, we are limited by the smallest critical field, $\mathcal{E}_{\text{crit}}^{\text{AA}}$.
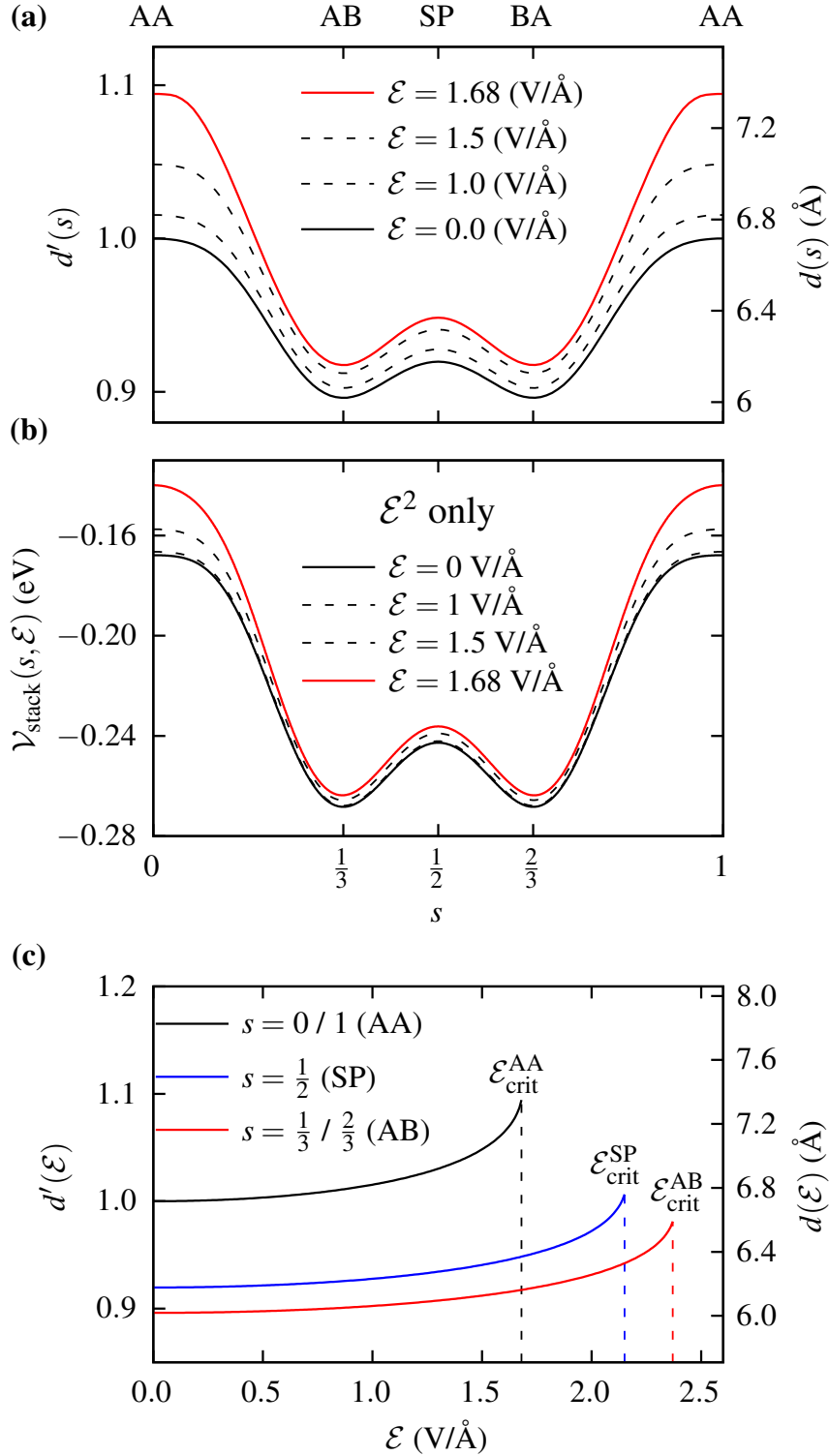
Fig. 8.8 **(a)**: Layer separation along the configuration space diagonal for different values of $\mathcal{E}$ for 3R MoS$_2$. **(b)**: Stacking energy along the configuration space diagonal at different field strengths, including only the quadratic electrostatic term. **(c)**: Layer separation as a function of $\mathcal{E}$ for the AA, SP and AB stacking configurations. The stacking configurations have critical field values $\mathcal{E}_{crit}^{AA} = 1.68$ V/Å, $\mathcal{E}_{crit}^{SP} = 2.15$ V/Å and $\mathcal{E}_{crit}^{AB} = 2.37$ V/Å, respectively.
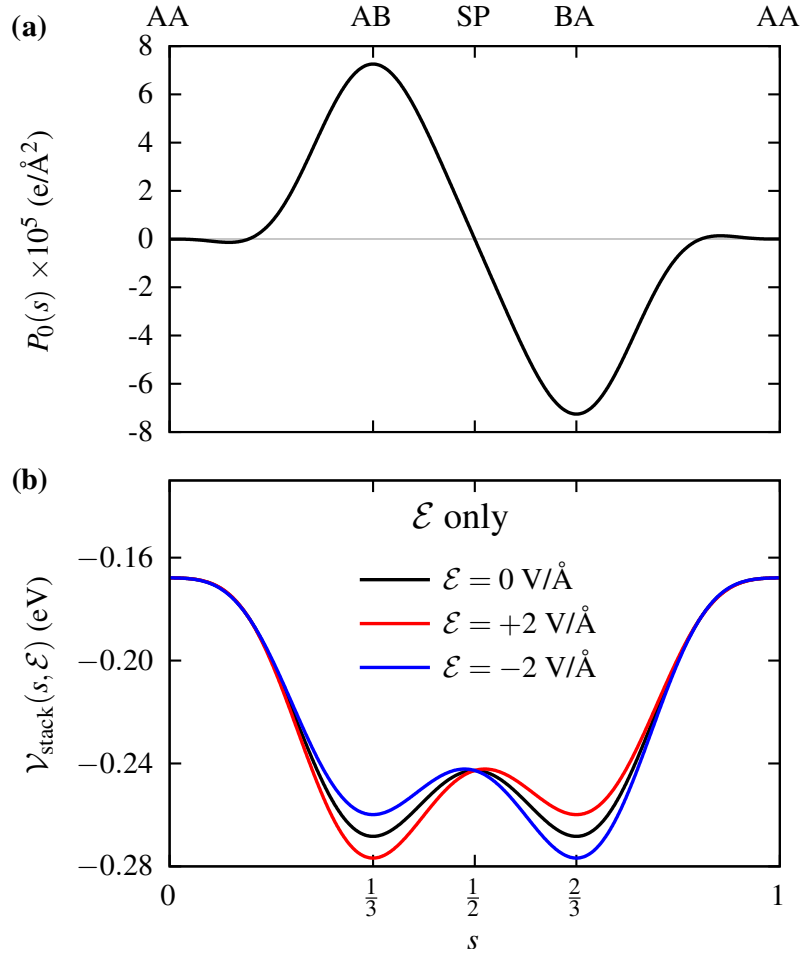
Fig. 8.9 **(a)**: Spontaneous polarization P_0 along the configuration space diagonal for 3R MoS$_2$. **(b)**: Stacking energy along the configuration space diagonal at different field strengths, including only the linear electrostatic term.

In Fig. 8.9 (a) we show the spontaneous polarization $P_0(s)$ along the diagonal in configuration space. The coupling between the polarization and the field leads to an even splitting of the AB and BA wells, increasing one and decreasing the other, which is shown in Fig. 8.9 (b).

In Fig. 8.10 we summarize the parameterizations of 3R and 2H stacked bilayer MoS$_2$ in configuration space. The hollow points show results from first-principles calculations and the solid lines are the Fourier interpolations. The stacking energy and equilibrium layer separation both vary by about 1 Å / 0.1 eV, respectively, which is expected. We also found that both polarizability parameters vary significantly throughout configuration space. Having parameterized Eq. (8.2), we can now proceed to study the effect of an applied field on lattice relaxation.
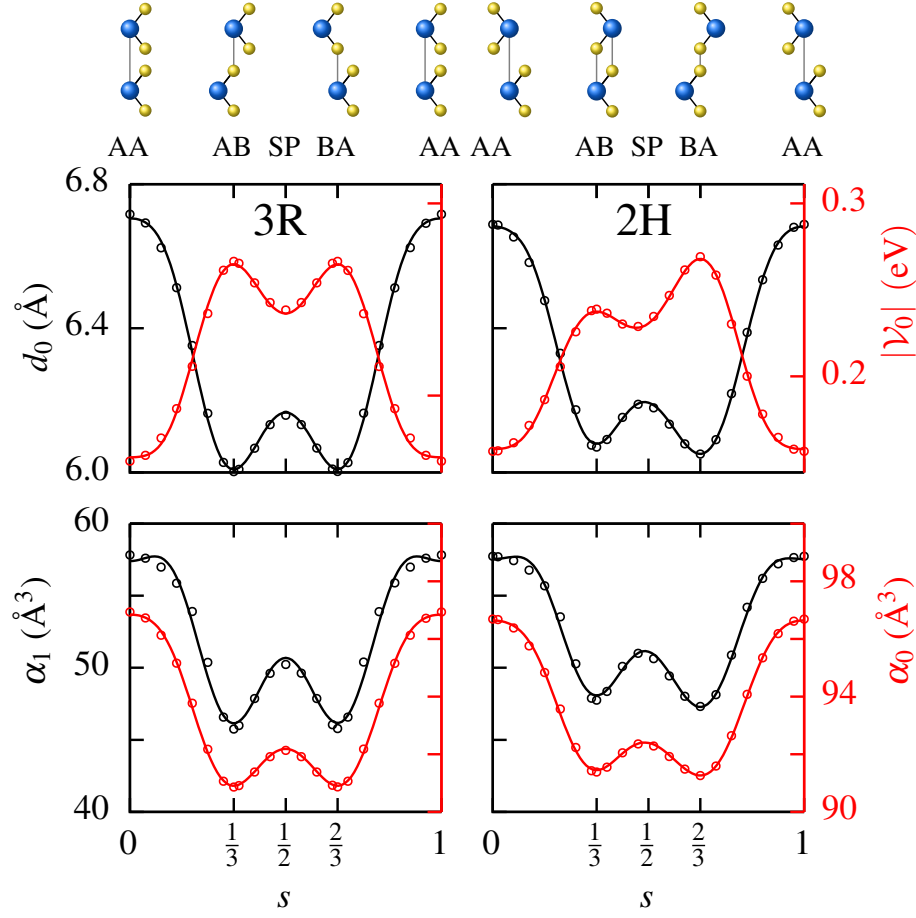
Fig. 8.10 Parameterization of Eq. (8.2) along the configuration space diagonal for 3R (left) and 2H (right) stackings of bilayer MoS_2. The hollow points are results from first-principles calculations, and the solid lines show the corresponding Fourier interpolations. The configurations AA $(s = 0, 1)$, AB $\left(s = \frac{1}{3}\right)$ SP $\left(s = \frac{1}{2}\right)$ and BA $\left(s = \frac{2}{3}\right)$ are marked and sketched above the plots.

8.3 Lattice Relaxation

The lattice relaxations at finite electric fields were performed in configuration space by including an additional in-plane displacement $\mathbf{u}(\mathbf{s})$ in the stacking and electrostatic energies, and minimizing the total energy numerically. The two terms in $\mathcal{V}_{\text{elec}}$ were included separately in order to illustrate their individual effects. The quadratic term arising from the dielectric response of the bilayer to the field does not break any symmetries. Thus, we can study its effect on the domain structures by mapping the moiré superlattice to a 1D Frenkel-Kontorova (FK) model [332, 333, 224]. We discuss this in detail in the next section. The linear term describing the coupling to the spontaneous local polarization breaks the $\mathcal{C}_6$ rotation symmetry

of the 3R moiré superlattice, leading to a breaking of the degeneracy of the AB and BA domains, which cannot be captured by a 1D FK model.

Eq. (8.1) can be minimized by using variational methods and solving the resulting differential equations. This can be relatively demanding in 2D. Instead, we minimized the total energy using numerical optimization methods. Eq. (8.1) is a functional of the in-plane displacement $\mathbf{u}$ in configuration space. If we perform a plane-wave expansion, $\mathbf{u}(\mathbf{s}) = \sum_{\mathbf{G}} \mathbf{u_G} e^{i\mathbf{G}\cdot\mathbf{s}}$, where $\mathbf{G}$ are the reciprocal lattice vectors of the commensurate bilayer, then the total energy becomes a function of $\{\mathbf{u_G}\}$: $V_{\text{tot}}[\mathbf{u}] \to V_{\text{tot}}(\{\mathbf{u_G}\})$, and can be minimized numerically with respect to the coefficients: $\nabla_{\mathbf{u_G}} V_{\text{tot}} = 0$. The gradient with respect to the Fourier components is

$$\nabla_{\mathbf{u_G}} V_{\text{tot}} = \frac{1}{A_{\text{s}}} \int_{A_{\text{s}}} \frac{\delta \mathcal{V}_{\text{tot}}}{\delta \mathbf{u}} \nabla_{\mathbf{u_G}} \mathbf{u} \, d\mathbf{s} \,, \tag{8.24}$$

where each component of $\nabla_{\mathbf{u_G}} \mathbf{u}$ picks out the basis function for the Fourier component $\mathbf{u_G}$. If we also write the functional derivative as an expansion over the reciprocal lattice vectors,

$$\frac{\delta \mathcal{V}_{\text{tot}}}{\delta \mathbf{u}} \equiv \mathcal{L} = \sum_{\mathbf{G}} \mathcal{L}_{\mathbf{G}} e^{i\mathbf{G}\cdot\mathbf{s}} \,, \tag{8.25}$$

then each component of the right-hand side of Eq. (8.24) projects out the Fourier coefficient corresponding to the vector $\mathbf{G}$:

$$\nabla_{\mathbf{u_G}} V = \begin{bmatrix} \mathcal{L}_{\mathbf{G}_1} \\ \vdots \\ \mathcal{L}_{\mathbf{G}_N} \end{bmatrix} \,, \tag{8.26}$$

which must be truncated at some suitable choice of N. For a given $\{\mathbf{u_G}\}$, we can calculate $\{\mathcal{L}_{\mathbf{G}}\}$ numerically, and thus we can solve $\nabla_{\mathbf{u_G}} V_{\text{tot}} = 0$ using root finding methods. Although we have an analytic expression for the gradient, we cannot obtain an analytic expression for the Hessian, so we cannot use Newton's method. Instead, we must resort to a quasi-Newton method, such as the limited memory BFGS algorithm (L-BFGS) [334]. This was done in JULIA, using the OPTIM package. The total energy was optimized until the gradient was below 1×10^{-5} eV.

We can take advantage of the $\mathcal{C}_3$ symmetry of our model to greatly reduce the number of independent **G** vectors:

$$
\mathbf{u(s)} = \sum_{n=1}^{3} \sum_{\mathbf{G}} \mathcal{C}_3^{n-1} \Big[(\mathbf{u_G} + \mathbf{u_{-G}}) \cos \left(\mathcal{C}_3^{n-1} \mathbf{G \cdot s} \right) \\
+ i (\mathbf{u_G} - \mathbf{u_{-G}}) \sin \left(\mathcal{C}_3^{n-1} \mathbf{G \cdot s} \right) \Big] .
\tag{8.27}
$$

When there is a $\mathcal{C}_6$ symmetry, i.e. for 3R MoS$_2$ at zero field, we have $\mathbf{u_{-G}} = -\mathbf{u_G}$, and the cosine terms vanish. The optimization was done using the independent **G** in the first five shells (10 vectors) for $\theta \geq 0.5°$, six shells (21 vectors) for $0.5° > \theta \geq 0.3°$ and and seven shells (28 vectors) for $0.3° > \theta \geq 0.1°$.
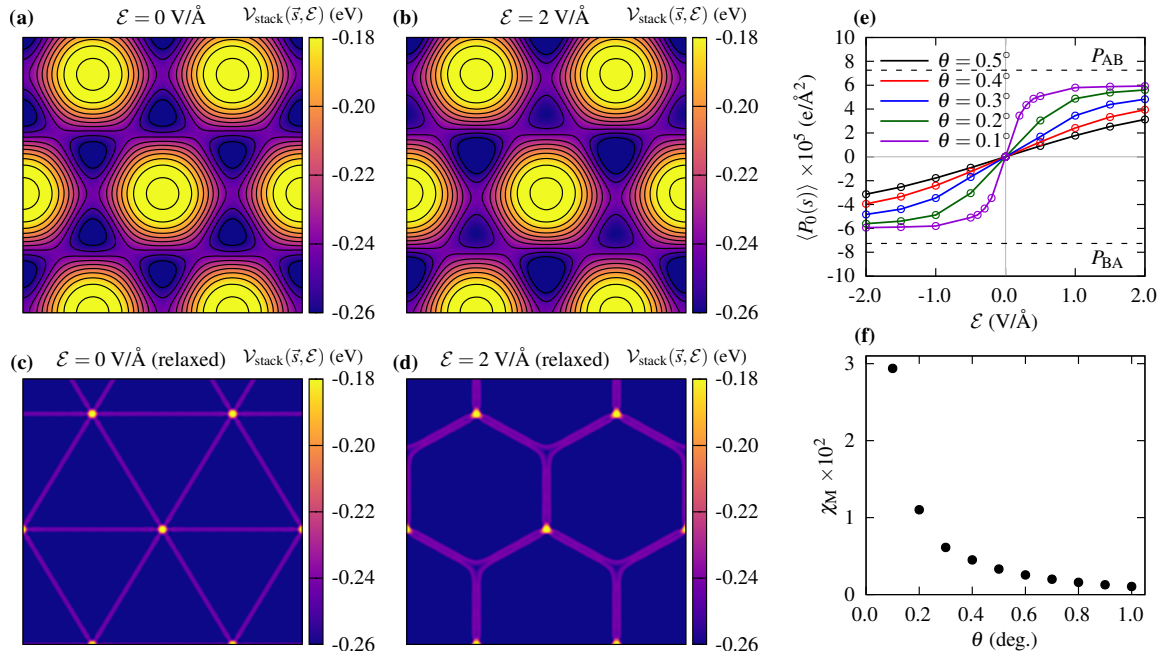
Fig. 8.11 **(a)-(d)**: Lattice relaxation in configuration space for 3R MoS$_2$ including the linear electrostatic term. The top panels show the stacking energy before lattice relaxation at electric field strengths of **(a)**: 0 V/Å and **(b)**: 2 V/Å. **(c)** and **(d)** show the corresponding stacking energies after lattice relaxation at a twist angle of $\theta = 0.1°$. The AA regions (yellow) shrink and the AB/BA regions (purple) expand. When an electric field is applied, the AB and BA regions relax unevenly, one increasing in area and the other decreasing. **(e)**: average polarization as a function of electric field for several twist angles. **(f)**: Susceptibility of the moiré superlattice χ_M as a function of twist angle, obtained from the slopes from **(e)** about $\mathcal{E} = 0$.

The 2D relaxation including only the coupling between the electric field and spontaneous polarization was performed for a range of twist angles $0.1° \leq \theta \leq 1.0°$ and field strengths $0 \leq \mathcal{E} \leq 2$ V/Å, and the results are summarized in Fig. 8.11. In Figs 8.11 (a) and (b) we show the stacking energy in 3R MoS$_2$ in configuration space obtained from first-principles calculations, at electric field strengths of 0 and 2 V/Å, respectively. The electric field increases the depth of the well at AB and decreases the depth of the well in BA by the same amount, breaking the $\mathcal{C}_6$ rotation symmetry. The panels below, Figs 8.11 (c) and (d), show the corresponding stacking energies after lattice relaxation for a twist angle of $\theta = 0.1°$. At zero field, the relaxation reduces the area of the AA regions and increases the area of the AB/BA regions, leading to a triangular domain structure with sharp domain walls. When an electric field is applied, the AB and BA regions relax unevenly, leading to larger AB regions and smaller BA regions reducing the rotation symmetry to $\mathcal{C}_3$. When the AB and BA domains are no longer equal in area, the polarization no longer averages to zero. In Fig. 8.11 (e) we show the average spontaneous polarization $\langle P_0(s) \rangle$ in configuration space as a function of field for different twist angles. We can see that the response to the field is very sensitive to the twist angle. In Fig. 8.11 (f) we show the susceptibility of the moiré superlattice χ_M as a function of twist angle, which was obtained by taking the slope of the polarization about zero field. We can see that the susceptibility increases dramatically as the twist angle decreases. In Figs. 8.12–8.15 we show the stacking energy in configuration space after lattice relaxation for $0.1° \leq \theta \leq 0.4°$ and 0 V/Å $\leq \mathcal{E} \leq 2$ V/Å.

Fig. 8.12 Lattice relaxation for 3R stacked bilayer MoS$_2$ at a twist angle of $\theta = 0.4°$ for several electric field values.

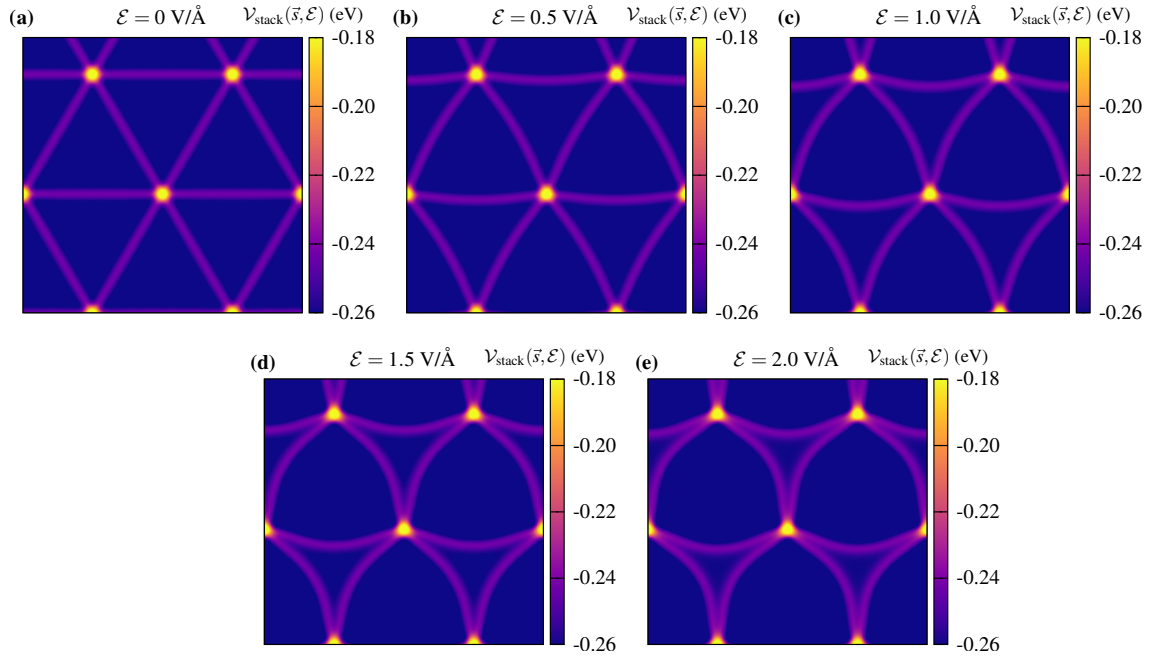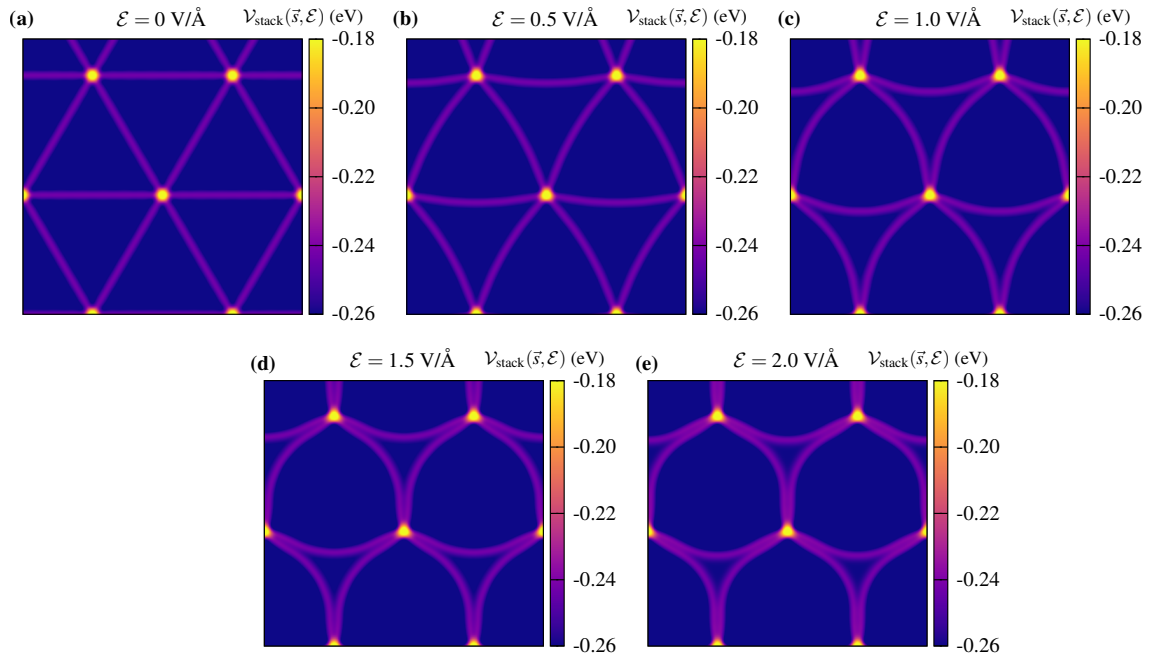
Fig. 8.13 Lattice relaxation for 3R stacked bilayer MoS$_2$ at a twist angle of $\theta = 0.3°$ for several electric field values.
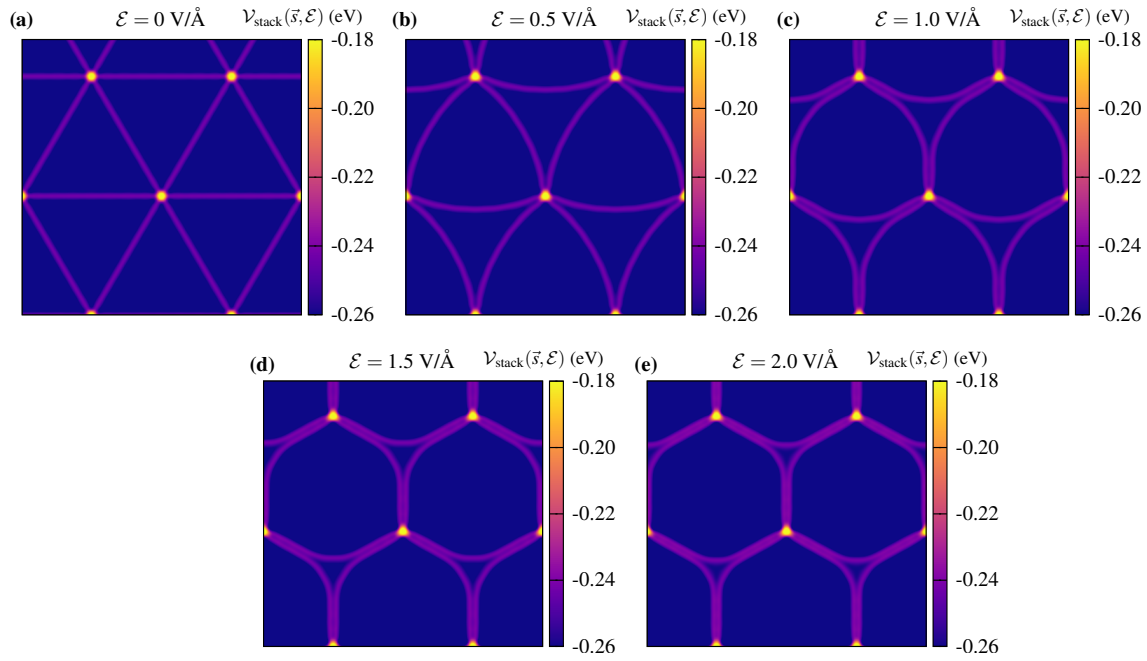
Fig. 8.14 Lattice relaxation for 3R stacked bilayer MoS_2 at a twist angle of $\theta = 0.2°$ for several electric field values.
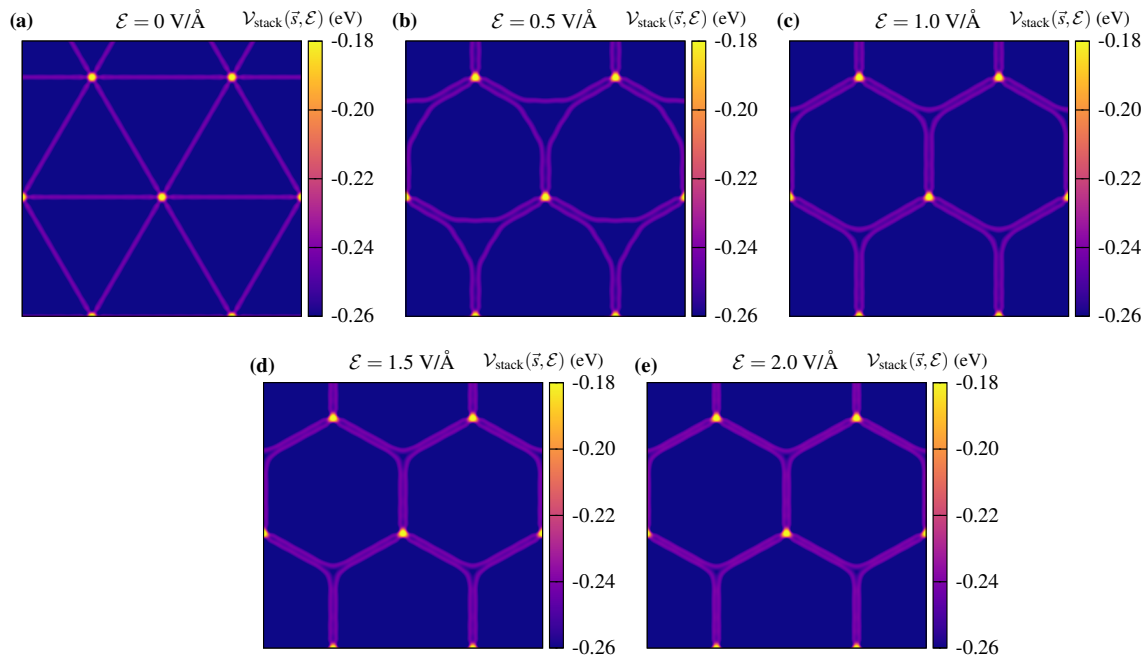
Fig. 8.15 Lattice relaxation for 3R stacked bilayer MoS_2 at a twist angle of $\theta = 0.1°$ for several electric field values.

8.4 Frenkel-Kontorova model
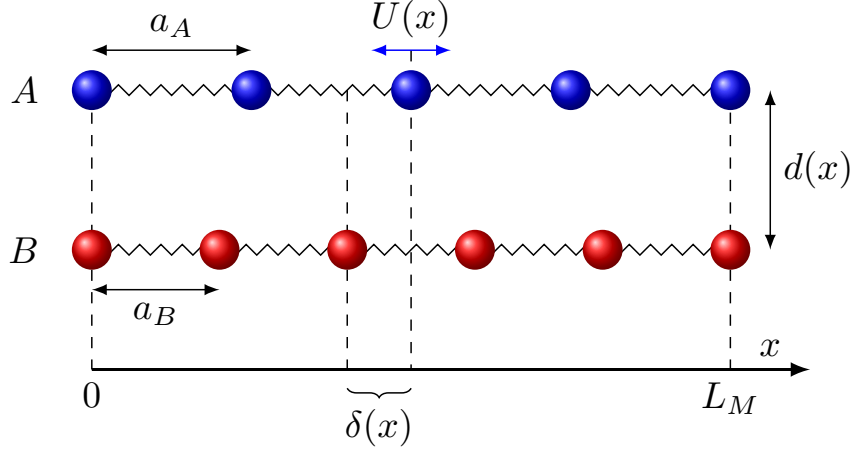
Fig. 8.16 Sketch of a 1D FK model. The layers are represented by chains of atoms A and B, connected by springs. The supercell period of the chains L_M is shown along the x-axis. The lattice mismatch between the chains plays the role of the twist angle.

The Frenkel-Kontorova (FK) model was first introduced in the 1930s and is widely used in condensed matter physics [335, 336]. It is a discrete model where a chain of atoms is subject to a rigid periodic potential, from a substrate for example [335, 337–339]. The FK model has been used as a 1D representation of twisted bilayer systems [332, 221, 320], replacing the rigid substrate with a second chain of atoms which can also deform, see Fig. 8.16, and has successfully been used to describe commensurate-incommensurate phase transitions [332, 333], lattice relaxation and domain structures [221, 223, 225].

Because the dielectric response does not break any symmetries, we can study its effect on the domain walls using a 1D FK model. For 3R MoS_2, the domain walls are along the path $AB \rightarrow SP \rightarrow BA$, so we use those points to parameterize the stacking energy [332, 333, 224] in a one dimensional version of configuration space,

$$\mathcal{V}_0^{\mathrm{FK}}(s) = \mathcal{V}_0^+ + \mathcal{V}_0^- \cos(2\pi s)$$
$$\mathcal{V}_0^\pm = \frac{1}{2}\left(\mathcal{V}_0\left(\tfrac{1}{2}\right) \pm \mathcal{V}_0\left(\tfrac{1}{3}\right)\right) \tag{8.28}$$

described by a single variable s, the relative displacement between the atoms in the two chains, and similarly for d_0, α_0 and α_1.
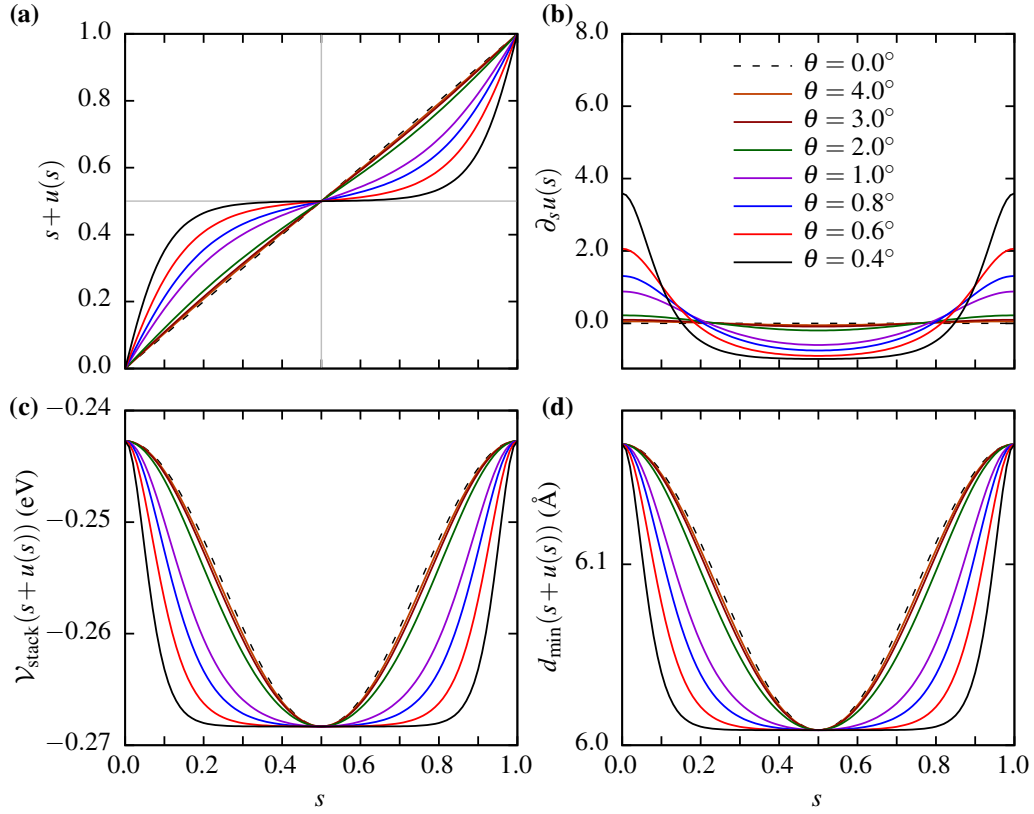
Fig. 8.17 Solutions to Eq. (8.30) at zero field for various twist angles: **(a)**: total displacement in configuration space $s + u(s)$, **(b)**: change in displacement $\partial_s u(s)$, equivalent to the strain tensor in 1D, **(c)**: stacking energy as a function of total displacement $\mathcal{V}_{\text{stack}}(s + u(s))$ and **(d)**: equilibrium layer separation as a function of total displacement $d_{\min}(s + u(s))$.

The total energy in configuration space is

$$
V_{\text{tot}}^{\text{FK}} = \frac{1}{A_s} \int_{A_s} \left[\frac{1}{2} B \theta^2 \left(\partial_s u \right)^2 + \mathcal{V}_{\text{stack}}^{\text{FK}}(s + u(s), d) \right.
$$
$$
\left. + \mathcal{V}_{\text{elec}}^{\text{FK}}(s + u(s), d, \mathcal{E}) \right] ds \tag{8.29}
$$

where θ is the lattice mismatch, B is the bulk modulus [223] and $\mathcal{V}_{\text{stack}}$ and $\mathcal{V}_{\text{elec}}$ include the displacement $u(s)$ to allow for relaxations. Eq. 8.29 can be also be minimized using optimization techniques, but in 1D the differential equations are easy enough to solve. Minimizing with respect to both u and d, we obtain
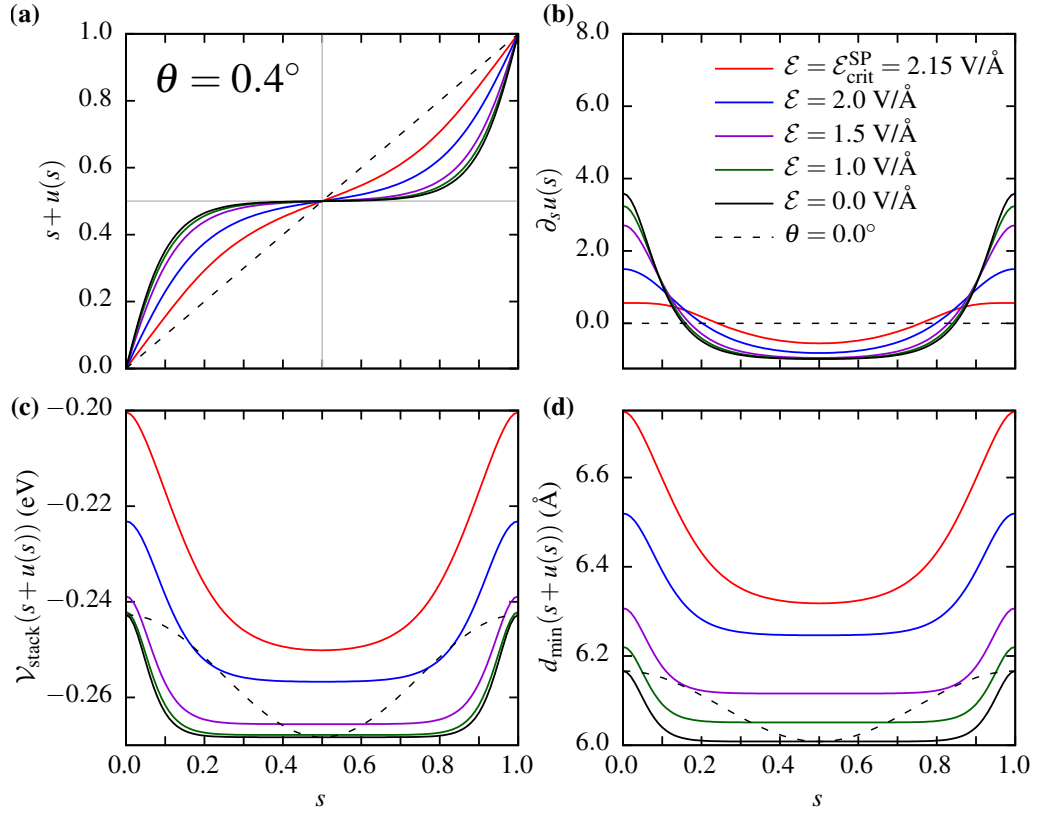
Fig. 8.18 Lattice relaxation from the 1D FK model, including the quadratic electrostatic term. **(a)**: total displacement in configuration space $s+u(s)$, **(b)**: gradient of displacement $\partial_s u(s)$, **(c)**: stacking energy as a function of total displacement $\mathcal{V}_{\text{stack}}(s+u(s))$ and **(d)**: equilibrium layer separation as a function of total displacement $d_{\min}(s+u(s))$.

$$\partial_u \left[\mathcal{V}_{\text{stack}}^{\text{FK}}(s+u(s),d) + \mathcal{V}_{\text{elec}}^{\text{FK}}(s+u(s),d,\mathcal{E}) \right] - B\theta^2 \partial_s^2 u(s) = 0$$
$$\partial_d \left[\mathcal{V}_{\text{stack}}^{\text{FK}}(s+u(s),d) + V_{\text{elec}}^{\text{FK}}(s+u(s),d,\mathcal{E}) \right] = 0 \qquad (8.30)$$

The second equation can be solved independently to obtain $d_{\min}(s,\mathcal{E})$. This is inserted into the first equation, which can be solved numerically.

In Fig. (8.17) we show results for MoS$_2$ for various values of θ at zero field. For larger θ, the atoms do not move much from their initial stacking configuration. As θ decreases, the elastic energy is reduced, and the atoms are able to relax more. We see from Fig. (8.17) (a), the total displacement $s+u(s)$, that the atoms move to maximize the area around $s=\frac{1}{2}$, the

stacking configuration with lowest energy. Figs. (8.17) (c) and (d) show the effect of the lattice relaxation on the stacking energy and layer separation. We can see that a domain structure forms, with wide AB/BA regions and narrow SP regions. The two are separated by a domain wall, the width of which is proportional to θ. Fig. (8.17) (b) shows the change in displacement $\partial_s u(s)$, which is equivalent to the strain tensor in 1D, from which we see that there is a large strain gradient across the domain wall.

In Fig. 8.18 we show results for finite electric fields at $\theta = 0.4°$. Fig. 8.18 (a) shows that, as the field strength increases, the atoms move back towards their initial stacking configuration. This can be understood from Figs. 8.18 (c) and (d): when a field is applied, the equilibrium separation increases everywhere in configuration space, which reduces the stacking energy. This reduces the atoms' ability to relax, leading to a softer domain structure.

At $s = 0$, we have the analytic approximation [332]:

$$u(s) = \frac{2}{\pi} \tan^{-1} \left(e^{2\pi \sqrt{\frac{V_0^- - \frac{1}{2}\varepsilon_0 \mathcal{E}^2 \alpha_0^-}{B\theta^2}} s} \right) - \frac{1}{2} \, , \tag{8.31}$$

which is shown alongside the numerical solutions to Eq. (8.30) in Fig. 8.19 (a). We can approximate the width of the domain wall as

$$w \sim \frac{1}{2} \sqrt{\frac{B\theta^2}{\left(V_0^- - \frac{1}{2}\varepsilon_0 \mathcal{E}^2 \alpha_0^-\right)}} \, , \tag{8.32}$$

illustrating the dependence on both twist angle and electric field. In Fig. 8.19 (b) we plot $w(\mathcal{E})$ for several values of θ. w diverges at a critical field $\mathcal{E}_{\text{crit}}^w = \sqrt{\frac{2V_0^-}{\varepsilon_0 \alpha_0^-}}$ which is independent of the lattice mismatch. For MoS_2, we have $\mathcal{E}_{\text{crit}}^w \approx 2.47$ V/Å which is larger than the largest critical field $\mathcal{E}_{\text{crit}}^{\text{AB}} = 2.37$ V/Å.
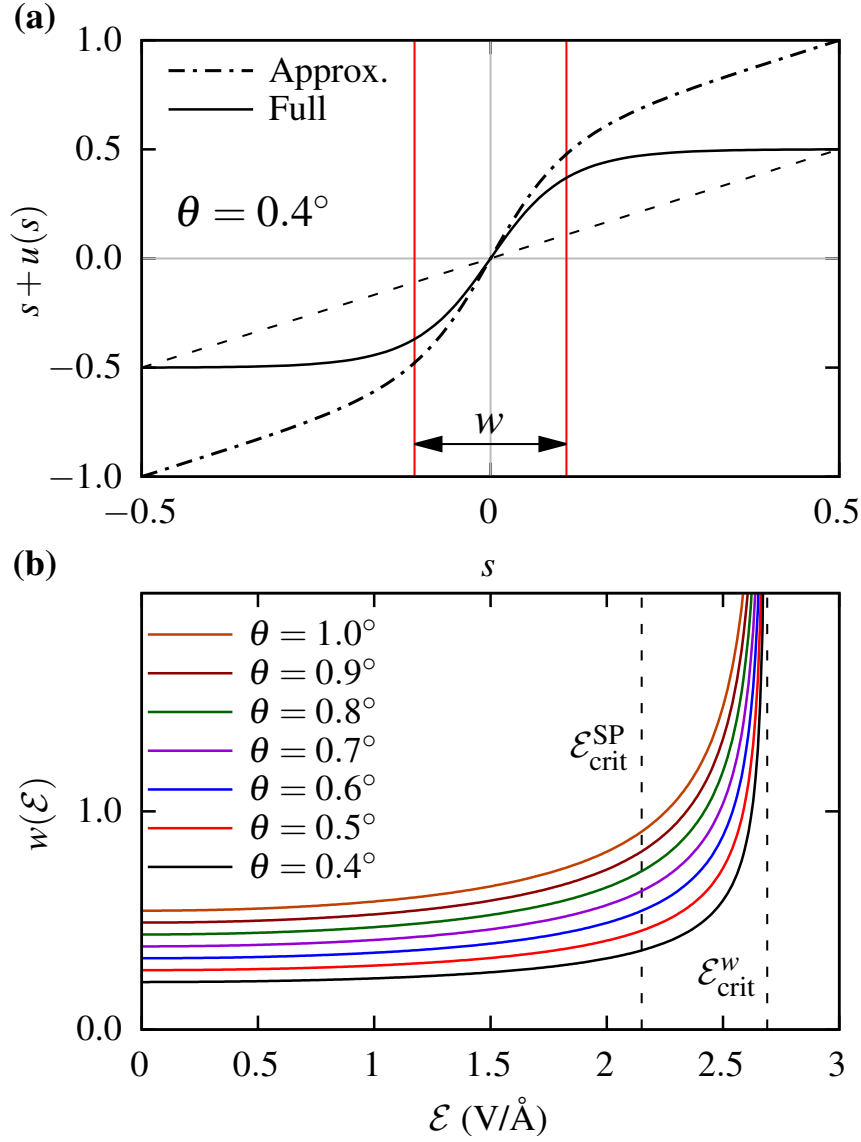
Fig. 8.19 (a): Displacement $u(s)$ obtained by solving Eq. (8.30) numerically and from the analytic approximation Eq. (8.31) about $s = 0$. The domain width Eq. (8.32) is indicated by the vertical red lines. (b): $w(\mathcal{E})$ for various lattice mismatches from Eq. (8.32). The dashed lines indicate the minimum critical field in the FK model, $\mathcal{E}_{\mathrm{crit}}^{\mathrm{SP}} = 2.15$ V/Å and the critical field at which the domain width diverges, $\mathcal{E}_{\mathrm{crit}}^{w} \approx 2.47$ V/Å.

Chapter 9

Conclusions and outlook

9.1   Polar-nonpolar perovskite interfaces

In Chapter 3, we introduced a phenomenological theory which considers the influence of homogeneous tilts on the appearance of carriers at polar-nonpolar perovskite interfaces. We show that, upon coupling, four new types of transitions of tilts and carriers with film thickness or applied field are possible, depending only on the energetics of the tilts, the polar discontinuity, and the biquadratic coupling between the tilts and the polar mode. These include the simultaneous appearance of tilts and carriers at a reduced thickness compared to the uncoupled theory, which can be either continuous or discontinuous, and separate transitions, with carriers appearing first and then tilts, the second transition being either continuous or discontinuous.

First-principles calculations of bulk LAO were performed to predict the character of the transitions at the LAO/STO interface. For various exchange-correlation functionals, all of the calculations predicted that at zero temperature, LAO/STO lies in region II of Fig. 3.4, i.e. a single continuous transition of both tilts and carriers. We also investigated the possibility of tuning the character of the transition via biaxial strain by changing the in-plane lattice constant by up to $\pm 1\%$ and repeating the calculations. We found that the position of the point in Fig. 3.4 can be changed by adjusting the strain, but not by enough to change the character of the transitions. However, in general, if a system were closer to a boundary between regions, it may be possible to change the regions using biaxial strain. Additionally, if compressive strain is applied to a_{LAO}, the tilt pattern changes to $a^0a^0c^-$ [277], which would change the

competition with the polar mode. This could be achieved by using a nonpolar perovskite with a smaller lattice constant than LAO as the substrate material.

In addition to changing the strain and the tilt pattern as mentioned above, changing the materials which form the polar-nonpolar interface can also change the chemistry at the interface, and hence the polar discontinuity. Different interfaces have been investigated experimentally [78, 340–342], computationally [343–345], and high throughput searches for new interfaces have been done [346]. Carrier transitions have also been observed at spinel-perovskite interfaces [347–349]. Thus, it may be possible to observe a wide variety of behavior in the carrier transitions at different polar-nonpolar perovskite interfaces for different combinations of materials. More specifically, by estimating where different systems would lie on Fig. 3.4, it may be possible to establish an atlas of transitions across different possible polar-nonpolar perovskite interfaces.

We also showed how the appearance of carriers can be tuned via temperature through the temperature dependence of the tilts. At a finite temperature, the curvature of the tilt double well is $X_\phi^{-1}(T) = X_\phi^{-1}\left(1 - \frac{T}{T_C}\right)$, so increasing the temperature would move any point on the diagram in Fig. 3.4 to the left. We would expect the dependence of the biquadratic coupling term $A(T)$ on temperature to be similar but weaker. Thus, it may be possible to move a system from one point in the diagram to another if the initial point is sufficiently close to a boundary. In Ref. [278], when grown on a substrate of cubic STO, LAO was found to undergo a transition from untilted to tilted below $695°$C for a thickness of 24 unit cells and $540°$C for a thickness of 9 unit cells, where both samples were under the same strain conditions. Because both films were supercritical there was no carrier transition associated with the tilt transitions, but their observations are in agreement with our prediction of a second transition temperature, T_C'', which is sensitive to the ratio $\frac{d}{d_c}$. Assuming that the films were sufficiently thick so that the effect of gradients are negligible, this may provide evidence for the additional transition temperature arising from the coupling between tilts and carriers.

In Chapter 4 we investigated the influence of the inhomogeneity of the tilts on the coupling between tilts and carriers. Upon coupling to homogeneous tilts, the diagram in Fig. 3.4 becomes five dimensional, with additional axes for the correlation length of the tilts in the polar film, and extrapolation lengths for the interface and the free surface of the film. Practically, it would be very demanding to explore this five dimensional space numerically, and to our knowledge, it can't be done analytically. However, since the biqaudratic coupling between tilts and carriers only depends on the mean of the tilt squared throughout the film, we

can examine the influence of inhomogeneous tilts by examining the effect of the correlation length on transitions in each region in Fig. 3.4, with the rest of the parameters fixed. We found that, for the regions corresponding to the separate appearances of tilts and then carriers, the order of the transitions is unaffected by the correlation length, except for the value of the second transition shifting slightly. For the regions corresponding to simultaneous transitions, we found that a finite correlation length can actually change the character of the transition, and can lead to two new types of transitions which are not possible for homogeneous tilts, where the tilts appear before carriers, either continuously or discontinuously.

We also considered the influence of direct coupling between oxygen vacancies and tilts at the surface of the polar thin film. We found that, if the coupling between oxygen vacancies and tilts at the surface is cooperative, then the appearance of carriers will always result in a small tilt at the surface of the thin film, which decays into the film and possibly the substrate. If the coupling is strong enough, the appearance of both carriers and the surface tilts becomes completely discontinuous. We found that the inclusion of the direct coupling leads to very different results in thinner films, but is negligible in thicker films. For a 3 unit cell thick film of LAO, the tilted phase is unstable when only considering the biquadratic coupling of the tilts and the polar mode. However, when the direct coupling between oxygen vacancies and tilts at the surface was included, we found that a small tilt appeared at the surface, which decayed towards the interface. This rationalizes results obtained from first-principles calculations of the LAO/STO interface, and experimental measurements of tilts in the same system [89].

Due to the large number of system parameters required, many of which cannot be directly measured, it remains difficult to conclusively determine the order of the carrier transition at polar-nonpolar perovskite interfaces. However, we have shown that, even using a phenomenological description, an extremely rich variety of behavior is possible for the appearance of carriers at polar-nonpolar perovskite interfaces. This includes first-order transitions, which have been observed experimentally [22], and have been claimed to occur in other theoretical studies [79], but without a detailed explanation.

One important caveat with this work is the distinction between the onset of carriers and the onset of conduction. In the original discovery, the electron-doped interface was found to be conducting while the hole-doped interface was found to be insulating [22]. It may be possible that carriers can appear but are not conducting. This is supported by experimental evidence: a density of trapped Ti 3d-like states has been observed in LAO/STO at just 2 unit

cells of LAO, i.e. before the observation of the 2DEG [296–299]. For carriers generated via oxygen vacancies, the charge carriers are trapped below the surface defects which generated them, and thus will be localized in the plane of the interface [88]. As the thickness of the film increases, more surface defects will be created and the associated carriers will become more delocalized, and conductivity will occur at a thickness later than the thickness at which carriers first appear. We have presented a phenomenological theory which describes the appearance of carriers, using the carrier concentration σ as the order parameter. Without a microscopic model to describe the delocalization of the carriers at the interface, it is difficult to make any conclusions about the difference between the onset of carriers and conductivity. Qualitatively however, if the carriers become delocalized in the plane of the interface at a thickness which is less than the smaller of d_c and d_ϕ in our model, then the transitions which occur at d_c and d_ϕ would truly be insulator–metal transitions, since the carriers would be conducting as soon as they appear.

9.2 Ferroelectric Thin Films and Superlattices

9.2.1 Electrostatics

In Chapter 5 we extended the continuum electrostatic description of an isolated ferroelectric thin film within Kittel's model to thin films surrounded by dielectric media and FE/PE superlattices. While some of the generalizations have previously appeared in the literature, a detailed comparison had not been done before. In doing so, we have understood how the surrounding dielectric materials influence the domain structure in the ferroelectric materials, both in the Kittel limit and beyond.

In the Kittel limit, the square root behavior is only affected in scale, the domain width increasing with dielectric permittivity, κ_s. This provides a useful correction to measurements of domain width with film thickness, as Kittel's law for an isolated film typically underestimates domain widths. Beyond Kittel's regime, we found that increasing κ_s decreases d_m, the thickness for which the domain width is minimal.

For FE/PE superlattices, we found that κ_s can either decrease or increase d_m, depending on the ratio of thicknesses, $\alpha = d_{PE}/d_{FE}$. We relate this behavior to the different coupling regimes between the ferroelectric layers, as discussed in Ref. [104] for example. When α is

large, the ferroelectric layers are weakly coupled, and the minimum thickness decreases with κ_s. When α is small, the ferroelectric layers are strongly coupled, and d_m increases with κ_s. Remarkably, when $\alpha = \alpha_c \equiv \chi = \sqrt{\kappa_a/\kappa_c}$, the dielectric anisotropy of the ferroelectric layers, d_m/l_k is unaffected by κ_s. In reality d_m does change, since the Kittel length depends on κ_s, but the scaling is different above/below α_c. The critical ratio α_c serves as a clear boundary between the strong and weak coupling regimes from an electrostatic viewpoint.

One important approximation in the Kittel-like model used is the description of the polarization in the ferroelectric material, assuming a dielectric linear-response modification of the spontaneous polarization P_s (or using Eq. (5.3) instead of Eq. (5.2) as the free energy term related to the polarization). Within this approximation, the system approaches a monodomain phase in a thin-limit regime in which the more complete treatment may predict $P = 0$. We investigate this possibility by considering a theory with Eq. (5.2) for the polarization, and Eq. (5.20) as the model electrostatic energy. We find that the polarization is zero for small thicknesses until

$$d_c = 27(\kappa_c\beta)^2 l_k , \tag{9.1}$$

at which the polarization jumps to $P_s/\sqrt{3}$ and quickly saturates to P_s [133]. Or, coming from $d > d_c$, the polarization decreases and the domain width increases, until d_c, where the ferroelectric material becomes paraelectric.

If $d_c < d_\infty$ the theory is unaffected, and the polydomain to monodomain transition would occur before the ferroelectric to paraelectric transition. Otherwise, the ferroelectric film becomes paraelectric without a polydomain to monodomain transition. For an isolated thin film of PTO, $d_m \sim 0.2l_k$ and $d_c \sim 0.8l_k$, meaning a ferroelectric to paraelectric transition takes place before the polydomain to monodomain transition. However, d_c is also very sensitive to the environment of the film. For a sandwich system with a thin film of PTO between two regions of STO, again $d_c \gg d_m$. For strongly-coupled FE/PE superlattices (small α), however, d_m increases with κ_s, and we would have $d_m \gg d_c$, and therefore the thin-limit behavior presented above should be observable before the films becoming paraelectric.

The model described in Chapter 5 makes use of a number of significant approximations. Domains are typically not straight or of infinite length, and the domain structure may not be an equilibrium one ($A \neq 0, \pm 1$). In addition, the polarization gradients expected close to surface, interfaces and domain walls are better described within a Ginzburg-Landau

theory, which will give significantly different predictions for ultrathin films, where complex structures such as polar vortices and skyrmions have been observed [350, 351].

However, the comparative study gives the expected behavior of ferroelectric/dielectric heterostructures within the simplest Kittel continuum model (continuum electrostatics for a given spontaneous polarization and dielectric response, plus ideal domain wall formation). While the domain width outside of Kittel regime may not be a realistic description for some materials, the values of d_m predicted by this theory provide an estimate for when Kittel's law breaks down. In particular, we have seen how the break down of Kittel's law can be changed by the material parameters of the ferroelectric, as well as the surrounding environment. The described behaviors are already quite rich, and represent a paradigmatic reference as basis for the understanding of more complex effects. In particular for superlattices, the strong to weak coupling regime separation based on this simplest model should be a useful guiding concept.

9.2.2 2DEG formation in polydomain ferroelectrics

In Chapter 6, we introduced a model which allows for 2DEG formation in the presence of ferroelectric domains, building on the previous competition-based study [133]. We found that, after allowing for the simultaneous screening of the polar discontinuity via both carriers and domains, the discontinuous transition between polydomain and monodomain (sustained by a 2DEG) phases was replaced by an intermediate region in which carriers and domains coexist. The onset and range of the coexistence region is very sensitive to the material parameters, and requires a finite density of states. At smaller thicknesses, there are no carriers, and the domain wall width follows Kittel's law. At a first critical thickness d_1, the carriers switch on continuously causing the domain width to deviate from Kittel's law and grow more rapidly with thickness. At a second critical thickness d_2, the carriers saturate, having fully screened the polar discontinuity, and the domain width diverges.

Using the theoretical parameters for PTO and STO, we were able to estimate the values of d_1 and d_2 for carriers generated via oxygen vacancies and electronic reconstruction. We saw that for carriers generated via oxygen vacancies, d_1 was of the order of a few nanometers, whereas it was of the order of hundreds of nanometers for carriers generated via electronic reconstruction. For both scenarios, d_2 was of the order of hundreds of nanometers, indicating that it is more likely to observe carriers in coexistence with ferroelectric domains, even in thicker films. This is a very different to the result obtained when considering the polydomain

and monodomain phases in isolation, where it was predicted that a discontinuous transition to a monodomain phase sustained by a 2DEG would occur at only a few nanometers [133].

Using the generalized electrostatics detailed in Chapter 5 we showed that the surrounding environment has a large influence not only on the domain structure, but also on the coexistence with the 2DEG, through its modification of the depolarizing field. The presence of a dielectric leads to additional screening of the depolarizing field, partially reducing the need for carriers and domains. As a result the domain width increases, as was seen in Chapter 5, but the onset of carriers with thickness also increased.

The aim of the work presented in this chapter was to understand the physics of coexistence between domains and carriers in ferroelectric systems, motivated by experimental observations [134–136]. We propose that our model could be used to identify 2DEG formation in experiments from measurements of domain width with ferroelectric film thickness: if a deviation from the Kittel law is observed, it may indicate that carriers have formed at the interface and are contributing to the screening of the depolarizing field. The Kittel length and the onset of coexistence, d_1, could be estimated from the square root curve and the thickness at which deviation from the square root curve occurs. By measuring these quantities, it may be possible to infer the mechanism by which a 2DEG has formed, i.e via oxygen vacancies or electronic reconstruction. The measurements of d_1 in Table 6.1 indicate that for carriers to form in relatively thin films, a few nanometers in thickness, they would need to be generated by oxygen vacancies.

9.3 Polarization in 2D materials

9.3.1 Flexoelectric polarization of single-walled nanotubes

In Chapter 7 we used first-principles DFT calculations to illustrate that a radial polarization is present in the walls of all NTs, even when they are only a single atom thick. We saw that the electronic polarization diverges in CNTs below $C(n,m)/a \sim 10$ by calculating the drop in the electrostatic potential across the walls of the NTs. A similar effect was observed in TMD NTs, however they displayed a finite polarization even when $C(n,m)/a > 10$. We found that polarization of the TMD NTs reaches a maximum around $C(n,m)/a \sim 15$ and decreases below before eventually diverging like the polarization of the CNTs. This behavior

was observed in all TMD NTs and is interesting and unexpected, but its origin is unclear. Plots of the radial strain on the bonds in the TMD NTs did not reveal an explanation for this maximum, but did reveal that the polarization in the walls is mainly caused by a larger compression on the outer bonds than the inner bonds.

The aim of the work presented in this chapter was not to provide a theory of flexoelectricity in NTs, but it does show that the flexoelectric response of the walls of NTs is interesting. In fact, it is debatable whether or not the polarization observed here should be called flexoelectric polarization. Typically one thinks of flexoelectric polarization as the response to an applied strain gradient such as bending, whereas the strain gradient here is intrinsic to the geometry of the NTs, and there is no reference state for a given NT with zero strain gradient. One could think of the order parameter that controls the strain as the inverse radius, $1/R$, such that the reference state is a flat 2D monolayer with $P_R = 0$, obtained when $R \to \infty$, i.e. when $1/R \to 0$. However, each radius corresponds to a different NT. Thus, the polarization is not a parameter that is directly tunable in experiment, since it is fixed for a given nanotube.

In any case, the behavior of the polarization of the walls with the size of the NTs is unexpected. The total dipole moment of the NTs is still zero, but the *local* polarization is non-zero. Because of this, there will be no induced dipole-dipole interactions between NTs, which is known from theory and other first-principles calculations. However, in situations where local polarization can have an effect, such as the interactions between NTs and liquids, this may be significant. It has already been seen that liquid crystals can have their flexoelectric coefficients enhanced via doping with CNTs [352]. Thus, this polarization could influence the behavior of water and other liquids or biomolecules inside or in the vicinity of the NTs. Knowledge of this effect and its influence on liquids and biomaterials could lead to advances in technology on the nanoscale, such as nanofiltration or screening of impurities in liquids, for example [353, 354].

9.3.2   Ferroelectricity in twisted bilayer systems

In Chapter 8 we introduced a model which illustrates the effect of an applied electric field on lattice relaxation in moiré superlattices. The model contains two electrostatic contributions. The first is a linear coupling between the field and the local spontaneous polarization in bilayers without centrosymmetry, which breaks the degeneracy between the AB and BA stacking domains. Under an electric field, the AB and BA regions will relax unevenly

with one growing and the other shrinking with respect to the relaxed structure at zero field. This leads to a nonzero average out-of-plane polarization in the superlattice. The second contribution is the dielectric response to the field, which occurs in all bilayers. This term leads to a nonuniform increase the layer separation, which reduces stacking energy, leading to softer domains structures under lattice relaxation.

Finally, we provide some thoughts on the recent experimental observations of ferroelectricity in the context of our theoretical model. For a system to be considered ferroelectric, it must (i): exhibit a spontaneous polarization at zero field which (ii): must be switchable with an electric field. The stacking domains indeed have a local spontaneous polarization at zero field, and while the average polarization of a domain can change via lattice relaxation under an electric field, the sign of the polarization in each domain cannot be switched. Therefore, the stacking domains in moiré superlattices are in general not ferroelectric. Conversely, the moiré superlattice itself exhibits an average polarization, the direction of which can be changed by the field, but has zero average polarization at zero field. Therefore, under ideal conditions, moiré superlattices are also not ferroelectric. This may not be true in experimental situations, where samples are not ideal, and defects, mislocations or strain induced by the finite size of samples may lead to uneven domains at zero field. Also, the direct couplings between strain and polarization, piezoelectricity and flexoelectricity, have not been considered, which may make it energetically favorable for the domains to relax unevenly and the superlattice to have a nonzero average polarization at zero field. We leave the consideration of these effects for future work. To summarize, for an ideal system, when considering the spontaneous local polarization and lattice relaxation under an electric field, *neither the moiré superlattice nor the stacking domains are ferroelectric*, since the former does not have a spontaneous polarization at zero field and the latter does not have a switchable polarization.

There have also been reports of a switching of the polarization in a single stacking domain by a sliding of the atoms by half a monolayer lattice constant when a local field was applied to the domain using a biased atomic force microscopy (AFM) tip [217]. This sliding changed the stacking configuration from AB $\leftrightarrow$ BA, resulting in a first order switching of the polarization. This is a separate mechanism to the one mediated by lattice relaxation, which results in a second order change in the polarization. We can understand this sliding in the context of our model. When a field is applied to the domain, the linear coupling between the field and polarization will lower the energy if the two are aligned and result in a large energy penalty if they are anti-aligned. In either case, the dielectric response will reduce the stacking energy by the same amount, making it easier for one layer to slide with respect to the other. When

the field and polarization are anti-aligned, the energy can be lowered considerably via a sliding by half a monolayer unit cell, flipping the polarization so that it becomes aligned with the field. However, the field is applied to the domain locally via an AFM tip, and it is not clear whether the sliding occurs locally under the tip, or throughout the entire domain. It is also not clear whether or not the domain will remain flipped once the field is removed, or relax back to its original orientation. Thus, it is not clear whether or not this mechanism for a first order switching of polarization in a stacking domain is truly ferroelectric either.

The model introduced in this chapter illustrates, clearly and intuitively, the effect an electric field can have on lattice relaxation in moiré superlattices. We propose an electric field as a third quantity with which the domain structures in moiré superlattices can be tuned. Unlike the twist angle and lattice mismatch which are fixed for a given sample, an electric field can be applied dynamically to tune a sample in-situ. Thus, it may serve as a more practical approach to achieve control in moiré superlattices. We have also discussed how our theoretical model can be used to understand the recent observations of ferroelectricity in moiré superlattices. We believe it is inaccurate to consider moiré materials to be truly ferroelectric via lattice relaxation or sliding under an electric field. However, this motivates further study into polar phenomena in moiré materials.

References

[1] A. K. Geim and K. S. Novoselov, "The rise of graphene," in *Nanoscience and technology: a collection of reviews from nature journals*, pp. 11–19, World Scientific, 2010.

[2] J. N. Coleman, M. Lotya, A. O'Neill, S. D. Bergin, P. J. King, U. Khan, K. Young, A. Gaucher, S. De, R. J. Smith, *et al.*, "Two-dimensional nanosheets produced by liquid exfoliation of layered materials," *Science*, vol. 331, no. 6017, pp. 568–571, 2011.

[3] Q. H. Wang, K. Kalantar-Zadeh, A. Kis, J. N. Coleman, and M. S. Strano, "Electronics and optoelectronics of two-dimensional transition metal dichalcogenides," *Nature nanotechnology*, vol. 7, no. 11, pp. 699–712, 2012.

[4] D. B. Chrisey and G. K. Hubler, "Pulsed laser deposition of thin films," *Pulsed Laser Deposition of Thin Films*, p. 648, 2003.

[5] N.-G. Park, "Perovskite solar cells: an emerging photovoltaic technology," *Materials today*, vol. 18, no. 2, pp. 65–72, 2015.

[6] R. Migoni, H. Bilz, and D. Bäuerle, "Origin of raman scattering and ferroelectricity in oxidic perovskites," *Physical Review Letters*, vol. 37, no. 17, p. 1155, 1976.

[7] R. E. Cohen, "Origin of ferroelectricity in perovskite oxides," *Nature*, vol. 358, no. 6382, pp. 136–138, 1992.

[8] J. Wang, J. Neaton, H. Zheng, V. Nagarajan, S. Ogale, B. Liu, D. Viehland, V. Vaithyanathan, D. Schlom, U. Waghmare, *et al.*, "Epitaxial $BiFeO_3$ multiferroic thin film heterostructures," *science*, vol. 299, no. 5613, pp. 1719–1722, 2003.

[9] K. A. Müller and H. Burkard, "$SrTiO_3$: An intrinsic quantum paraelectric below 4K," *Physical Review B*, vol. 19, no. 7, p. 3593, 1979.

[10] S. Rowley, L. Spalek, R. Smith, M. Dean, M. Itoh, J. Scott, G. Lonzarich, and S. Saxena, "Ferroelectric quantum criticality," *Nature Physics*, vol. 10, no. 5, pp. 367–372, 2014.

[11] K. G. Wilson and J. Kogut, "The renormalization group and the ε expansion," *Physics reports*, vol. 12, no. 2, pp. 75–199, 1974.

[12] K. G. Wilson, "The renormalization group: Critical phenomena and the kondo problem," *Reviews of modern physics*, vol. 47, no. 4, p. 773, 1975.

[13] N. F. Mott, "Metal-insulator transition," *Reviews of Modern Physics*, vol. 40, no. 4, p. 677, 1968.

[14] M. Imada, A. Fujimori, and Y. Tokura, "Metal-insulator transitions," *Reviews of modern physics*, vol. 70, no. 4, p. 1039, 1998.

[15] F. Morin, "Oxides which show a metal-to-insulator transition at the neel temperature," *Physical review letters*, vol. 3, no. 1, p. 34, 1959.

[16] D. Adler, "Mechanisms for metal-nonmental transitions in transition-metal oxides and sulfides," *Reviews of Modern Physics*, vol. 40, no. 4, p. 714, 1968.

[17] A. Raychaudhuri, "Metal-insulator transition in perovskite oxides: a low-temperature perspective," *Advances in Physics*, vol. 44, no. 1, pp. 21–46, 1995.

[18] Z. Yang, C. Ko, and S. Ramanathan, "Oxide electronics utilizing ultrafast metal-insulator transitions," *Annual Review of Materials Research*, vol. 41, pp. 337–367, 2011.

[19] S. Kravchenko and M. Sarachik, "Metal–insulator transition in two-dimensional electron systems," *Reports on Progress in Physics*, vol. 67, no. 1, p. 1, 2003.

[20] S. Kravchenko, W. E. Mason, G. Bowker, J. Furneaux, V. Pudalov, and M. D'iorio, "Scaling of an anomalous metal-insulator transition in a two-dimensional system in silicon at $b = 0$," *Physical Review B*, vol. 51, no. 11, p. 7038, 1995.

[21] A. Ohtomo, D. Muller, J. Grazul, and H. Y. Hwang, "Artificial charge-modulation in atomic-scale perovskite titanate superlattices," *Nature*, vol. 419, no. 6905, p. 378, 2002.

[22] A. Ohtomo and H. Hwang, "A high-mobility electron gas at the $LaAlO_3/SrTiO_3$ heterointerface," *Nature*, vol. 427, no. 6973, p. 423, 2004.

[23] L. D. Landau, "On the theory of phase transitions. i.," *Zh. Eksp. Teor. Fiz.*, vol. 11, p. 19, 1937.

[24] L. Landau and E. Lifshitz, "Statistical physics, part 1: Volume 5 (course of theoretical physics, volume 5)," *Publisher: Butterworth-Heinemann*, vol. 3, 1980.

[25] P.-G. De Gennes, *Superconductivity of metals and alloys*. CRC Press, 2018.

[26] T. Lubensky and M. H. Rubin, "Critical phenomena in semi-infinite systems. ii. mean-field theory," *Physical Review B*, vol. 12, no. 9, p. 3885, 1975.

[27] R. Kretschmer and K. Binder, "Surface effects on phase transitions in ferroelectrics and dipolar magnets," *Physical Review B*, vol. 20, no. 3, p. 1065, 1979.

[28] P. Chandra and P. B. Littlewood, "A Landau primer for ferroelectrics," *Physics of ferroelectrics*, pp. 69–116, 2007.

[29] I. A. Luk'yanchuk, L. Lahoche, and A. Sené, "Universal properties of ferroelectric domains," *Phys. Rev. Lett.*, vol. 102, p. 147601, Apr 2009.

[30] A. K. Tagantsev, L. E. Cross, and J. Fousek, *Domains in Ferroic Crystals and Thin Films*. Springer, 2010.

[31] A. Kopal, T. Bahnik, and J. Fousek, "Domain formation in thin ferroelectric films: The role of depolarization energy," *Ferroelectrics*, vol. 202, pp. 267–274, oct 1997.

[32] C. Kittel, "Physical theory of ferromagnetic domains," *Review of Modern Physics*, vol. 21, no. 4, pp. 541–583, 1948.

[33] T. Mitsui and J. Furuichi, "Domain structure of Rochelle salt and KH_2PO_4," *Physical Review*, vol. 90, no. 2, p. 193, 1953.

[34] N. A. Benedek and C. J. Fennie, "Why are there so few perovskite ferroelectrics?," *The Journal of Physical Chemistry C*, vol. 117, no. 26, pp. 13339–13349, 2013.

[35] W. Zhong and D. Vanderbilt, "Competing structural instabilities in cubic perovskites," *Physical review letters*, vol. 74, no. 13, p. 2587, 1995.

[36] N. W. Thomas and A. Beitollahi, "Inter-relationship of octahedral geometry, poly-hedral volume ratio and ferroelectric properties in rhombohedral perovskites," *Acta Crystallographica Section B: Structural Science*, vol. 50, no. 5, pp. 549–560, 1994.

[37] E. K. Salje, "Application of Landau theory for the analysis of phase transitions in minerals," *Physics reports*, vol. 215, no. 2, pp. 49–99, 1992.

[38] A. Glazer, "The classification of tilted octahedra in perovskites," *Acta Crystallographica Section B: Structural Crystallography and Crystal Chemistry*, vol. 28, no. 11, pp. 3384–3392, 1972.

[39] V. M. Goldschmidt, "Die gesetze der krystallochemie," *Naturwissenschaften*, vol. 14, no. 21, pp. 477–485, 1926.

[40] E. Salje, "Phase transitions in ferroelastic and co-elastic crystals," *Ferroelectrics*, vol. 104, no. 1, pp. 111–120, 1990.

[41] L. Li, C. Richter, S. Paetel, T. Kopp, J. Mannhart, and R. Ashoori, "Very large capacitance enhancement in a two-dimensional electron system," *Science*, vol. 332, no. 6031, pp. 825–828, 2011.

[42] N. Reyren, S. Thiel, A. Caviglia, L. F. Kourkoutis, G. Hammerl, C. Richter, C. Schnei-der, T. Kopp, A.-S. Rüetschi, D. Jaccard, *et al.*, "Superconducting interfaces between insulating oxides," *Science*, vol. 317, no. 5842, pp. 1196–1199, 2007.

[43] A. Brinkman, M. Huijben, M. Van Zalk, J. Huijben, U. Zeitler, J. Maan, W. G. van der Wiel, G. Rijnders, D. H. Blank, and H. Hilgenkamp, "Magnetic effects at the interface between non-magnetic oxides," *Nature materials*, vol. 6, no. 7, pp. 493–496, 2007.

[44] L. Li, C. Richter, J. Mannhart, and R. C. Ashoori, "Coexistence of magnetic order and two-dimensional superconductivity at $LaAlO_3$/$SrTiO_3$ interfaces," *Nature Physics*, vol. 7, pp. 762–766, oct 2011.

[45] J. A. Bert, B. Kalisky, C. Bell, M. Kim, Y. Hikita, H. Y. Hwang, and K. A. Moler, "Direct imaging of the coexistence of ferromagnetism and superconductivity at the LaAlO$_3$/SrTiO$_3$ interface," *Nature Physics*, vol. 7, pp. 767–771, oct 2011.

[46] S. Thiel, G. Hammerl, A. Schmehl, C. Schneider, and J. Mannhart, "Tunable quasi-two-dimensional electron gases in oxide heterostructures," *Science*, vol. 313, no. 5795, pp. 1942–1945, 2006.

[47] C. Cen, S. Thiel, G. Hammerl, C. W. Schneider, K. Andersen, C. Hellberg, J. Mannhart, and J. Levy, "Nanoscale control of an interfacial metal-insulator transition at room temperature," *Nature materials*, vol. 7, no. 4, pp. 298–302, 2008.

[48] B. Förg, C. Richter, and J. Mannhart, "Field-effect devices utilizing LaAlO$_3$-SrTiO$_3$ interfaces," *Applied Physics Letters*, vol. 100, no. 5, p. 053506, 2012.

[49] Y. Xie, Y. Hikita, C. Bell, and H. Y. Hwang, "Control of electronic conduction at an oxide heterointerface using surface polar adsorbates," *Nature communications*, vol. 2, no. 1, pp. 1–5, 2011.

[50] P. Irvin, Y. Ma, D. F. Bogorin, C. Cen, C. W. Bark, C. M. Folkman, C.-B. Eom, and J. Levy, "Rewritable nanoscale oxide photodetector," *Nature Photonics*, vol. 4, no. 12, p. 849, 2010.

[51] I. Pallecchi, M. Codda, E. G. d'Agliano, D. Marré, A. Caviglia, N. Reyren, S. Gariglio, and J.-M. Triscone, "Seebeck effect in the conducting LaAlO$_3$/SrTiO$_3$ interface," *Physical Review B*, vol. 81, no. 8, p. 085414, 2010.

[52] A. Filippetti, P. Delugas, M. Verstraete, I. Pallecchi, A. Gadaleta, D. Marré, D. Li, S. Gariglio, and V. Fiorentini, "Thermopower in oxide heterostructures: The importance of being multiple-band conductors," *Physical Review B*, vol. 86, no. 19, p. 195301, 2012.

[53] E. Assmann, P. Blaha, R. Laskowski, K. Held, S. Okamoto, and G. Sangiovanni, "Oxide heterostructures for efficient solar cells," *Physical review letters*, vol. 110, no. 7, p. 078701, 2013.

[54] H. Liang, L. Cheng, X. Zhai, N. Pan, H. Guo, J. Zhao, H. Zhang, L. Li, X. Zhang, X. Wang, *et al.*, "Giant photovoltaic effects driven by residual polar field within unit-cell-scale LaAlO$_3$ films on SrTiO$_3$," *Scientific reports*, vol. 3, no. 1, pp. 1–7, 2013.

[55] H. Y. Hwang, "Tuning interface states," *Science*, vol. 313, no. 5795, pp. 1895–1896, 2006.

[56] S. Pauli and P. Willmott, "Conducting interfaces between polar and non-polar insulating perovskites," *Journal of Physics: Condensed Matter*, vol. 20, no. 26, p. 264012, 2008.

[57] M. Huijben, A. Brinkman, G. Koster, G. Rijnders, H. Hilgenkamp, and D. H. Blank, "Structure-property relation of SrTiO$_3$/LaAlO$_3$ interfaces," *Advanced Materials*, vol. 21, no. 17, pp. 1665–1677, 2009.

[58] J. Mannhart and D. Schlom, "Oxide interfaces—an opportunity for electronics," *Science*, vol. 327, no. 5973, pp. 1607–1611, 2010.

[59] R. Pentcheva and W. E. Pickett, "Electronic phenomena at complex oxide interfaces: Insights from first principles," *Journal of Physics: Condensed Matter*, vol. 22, no. 4, p. 043001, 2010.

[60] H. Chen, A. M. Kolpak, and S. Ismail-Beigi, "Electronic and magnetic properties of $SrTiO_3$/$LaAlO_3$ interfaces from first principles," *Advanced Materials*, vol. 22, no. 26-27, pp. 2881–2899, 2010.

[61] M. Warusawithana, C. Richter, J. A. Mundy, P. Roy, J. Ludwig, S. Paetel, T. Heeg, A. Pawlicki, L. F. Kourkoutis, M. Zheng, *et al.*, "$LaAlO_3$ stoichiometry is key to electron liquid formation at $LaAlO_3$/$SrTiO_3$ interfaces," *Nature communications*, vol. 4, no. 1, pp. 1–9, 2013.

[62] S. A. Chambers, "Understanding the mechanism of conductivity at the $LaAlO_3$/$SrTiO_3$ (001) interface," *Surface Science*, vol. 605, no. 13-14, pp. 1133–1140, 2011.

[63] R. Pentcheva, R. Arras, K. Otte, V. G. Ruiz, and W. E. Pickett, "Termination control of electronic phases in oxide thin films and interfaces: $LaAlO_3$/$SrTiO_3$ (001)," *Philosophical Transactions of the Royal Society A: Mathematical, Physical and Engineering Sciences*, vol. 370, no. 1977, pp. 4904–4926, 2012.

[64] M. Gabay, S. Gariglio, J.-M. Triscone, and A. Santander-Syro, "2-dimensional oxide electronic gases: Interfaces and surfaces," *The European Physical Journal Special Topics*, vol. 222, no. 5, pp. 1177–1183, 2013.

[65] S. Stemmer and S. James Allen, "Two-dimensional electron gases at complex oxide interfaces," *Annual Review of Materials Research*, vol. 44, pp. 151–171, 2014.

[66] N. Bristowe, P. Ghosez, P. B. Littlewood, and E. Artacho, "The origin of two-dimensional electron gases at oxide interfaces: Insights from theory," *Journal of Physics: Condensed Matter*, vol. 26, no. 14, p. 143201, 2014.

[67] N. Nakagawa, H. Y. Hwang, and D. A. Muller, "Why some interfaces cannot be sharp," *Nature materials*, vol. 5, no. 3, pp. 204–209, 2006.

[68] Z. S. Popović, S. Satpathy, and R. M. Martin, "Origin of the two-dimensional electron gas carrier density at the $LaAlO_3$ on $SrTiO_3$ interface," *Physical review letters*, vol. 101, no. 25, p. 256801, 2008.

[69] R. Pentcheva and W. E. Pickett, "Avoiding the polarization catastrophe in $LaAlO_3$ overlayers on $SrTiO_3$ (001) through polar distortion," *Physical review letters*, vol. 102, no. 10, p. 107602, 2009.

[70] A. Kalabukhov, R. Gunnarsson, J. Börjesson, E. Olsson, T. Claeson, and D. Winkler, "Effect of oxygen vacancies in the $SrTiO_3$ substrate on the electrical properties of the $LaAlO_3$/$SrTiO_3$ interface," *Physical Review B*, vol. 75, no. 12, p. 121404, 2007.

[71] W. Siemons, G. Koster, H. Yamamoto, W. A. Harrison, G. Lucovsky, T. H. Geballe, D. H. Blank, and M. R. Beasley, "Origin of charge density at LaAlO$_3$ on SrTiO$_3$ heterointerfaces: Possibility of intrinsic doping," *Physical review letters*, vol. 98, no. 19, p. 196802, 2007.

[72] G. Herranz, M. Basletić, M. Bibes, C. Carrétéro, E. Tafra, E. Jacquet, K. Bouzehouane, C. Deranlot, A. Hamzić, J.-M. Broto, *et al.*, "High mobility in LaAlO$_3$/SrTiO$_3$ heterostructures: origin, dimensionality, and perspectives," *Physical review letters*, vol. 98, no. 21, p. 216803, 2007.

[73] J. N. Eckstein, "Watch out for the lack of oxygen," *Nature Materials*, vol. 6, no. 7, pp. 473–474, 2007.

[74] K. Shibuya, T. Ohnishi, M. Lippmaa, and M. Oshima, "Metallic conductivity at the CaHfO$_3$/SrTiO$_3$ interface," *Applied Physics Letters*, vol. 91, no. 23, p. 232106, 2007.

[75] Y. Chen, N. Pryds, J. E. Kleibeuker, G. Koster, J. Sun, E. Stamate, B. Shen, G. Rijnders, and S. Linderoth, "Metallic and insulating interfaces of amorphous SrTiO$_3$-based oxide heterostructures," *Nano letters*, vol. 11, no. 9, pp. 3774–3778, 2011.

[76] S. W. Lee, Y. Liu, J. Heo, and R. G. Gordon, "Creation and control of two-dimensional electron gas using Al-based amorphous oxides/SrTiO$_3$ heterostructures grown by atomic layer deposition," *Nano letters*, vol. 12, no. 9, pp. 4775–4783, 2012.

[77] Z. Liu, C. Li, W. Lü, X. Huang, Z. Huang, S. Zeng, X. Qiu, L. Huang, A. Annadi, J. Chen, *et al.*, "Origin of the two-dimensional electron gas at LaAlO$_3$/SrTiO$_3$ interfaces: the role of oxygen vacancies and electronic reconstruction," *Physical Review X*, vol. 3, no. 2, p. 021010, 2013.

[78] C. Li, Z. Liu, W. Lü, X. R. Wang, A. Annadi, Z. Huang, S. Zeng, T. Venkatesan, *et al.*, "Tailoring the two dimensional electron gas at polar ABO$_3$/SrTiO$_3$ interfaces for oxide electronics," *Scientific reports*, vol. 5, no. 1, pp. 1–7, 2015.

[79] L. Yu and A. Zunger, "A polarity-induced defect mechanism for conductivity and magnetism at polar-nonpolar oxide interfaces," *Nature communications*, vol. 5, p. 5118, 2014.

[80] Z. Chen, H. Yuan, Y. Xie, D. Lu, H. Inoue, Y. Hikita, C. Bell, and H. Y. Hwang, "Dual-gate modulation of carrier density and disorder in an oxide two-dimensional electron system," *Nano letters*, vol. 16, no. 10, pp. 6130–6136, 2016.

[81] S. K. Kim, S.-I. Kim, H. Lim, D. S. Jeong, B. Kwon, S.-H. Baek, and J.-S. Kim, "Electric-field-induced shift in the threshold voltage in LaAlO$_3$/SrTiO$_3$ heterostructures," *Scientific reports*, vol. 5, p. 8023, 2015.

[82] M. Hosoda, Y. Hikita, H. Y. Hwang, and C. Bell, "Transistor operation and mobility enhancement in top-gated LaAlO$_3$/SrTiO$_3$ heterostructures," *Applied Physics Letters*, vol. 103, no. 10, p. 103507, 2013.

[83] J. A. Bert, K. C. Nowack, B. Kalisky, H. Noad, J. R. Kirtley, C. Bell, H. K. Sato, M. Hosoda, Y. Hikita, H. Y. Hwang, *et al.*, "Gate-tuned superfluid density at the superconducting $LaAlO_3/SrTiO_3$ interface," *Physical Review B*, vol. 86, no. 6, p. 060503, 2012.

[84] P. Eerkes, W. G. van der Wiel, and H. Hilgenkamp, "Modulation of conductance and superconductivity by top-gating in $LaAlO_3/SrTiO_3$ 2-dimensional electron systems," *Applied physics letters*, vol. 103, no. 20, p. 201603, 2013.

[85] S. Davis, Z. Huang, K. Han, T. Venkatesan, V. Chandrasekhar, *et al.*, "Anisotropic superconductivity and frozen electronic states at the (111) $LaAlO_3/SrTiO_3$ interface," *Physical Review B*, vol. 98, no. 2, p. 024504, 2018.

[86] W. Liu, S. Gariglio, A. Fête, D. Li, M. Boselli, D. Stornaiuolo, and J.-M. Triscone, "Magneto-transport study of top-and back-gated $LaAlO_3/SrTiO_3$ heterostructures," *APL materials*, vol. 3, no. 6, p. 062805, 2015.

[87] Y. Lei, Y. Li, Y. Chen, Y. Xie, Y. Chen, S. Wang, J. Wang, B. Shen, N. Pryds, H. Hwang, *et al.*, "Visible-light-enhanced gating effect at the $LaAlO_3/SrTiO_3$ interface," *Nature communications*, vol. 5, no. 1, pp. 1–7, 2014.

[88] N. Bristowe, P. Littlewood, and E. Artacho, "Surface defects and conduction in polar oxide heterostructures," *Physical Review B*, vol. 83, no. 20, p. 205405, 2011.

[89] J. Gazquez, M. Stengel, R. Mishra, M. Scigaj, M. Varela, M. Roldan, J. Fontcuberta, F. Sánchez, and G. Herranz, "Competition between polar and nonpolar lattice distortions in oxide quantum wells: New critical thickness at polar interfaces," *Physical review letters*, vol. 119, no. 10, p. 106102, 2017.

[90] L. Landau and E. Lifshitz, "On the theory of the dispersion of magnetic permeability in ferromagnetic bodies," in *Perspectives in Theoretical Physics*, pp. 51–65, Elsevier, 1992.

[91] L. D. Landau, J. Bell, M. Kearsley, L. Pitaevskii, E. Lifshitz, and J. Sykes, *Electrodynamics of continuous media*, vol. 8. elsevier, 2013.

[92] A. Hubert and R. Schäfer, *Magnetic domains: the analysis of magnetic microstructures*. Springer Science & Business Media, 2008.

[93] C. Kittel, "Theory of the structure of ferromagnetic domains in films and small particles," *Physical Review*, vol. 70, no. 11-12, p. 965, 1946.

[94] Z. Málek and V. Kamberskỳ, "On the theory of the domain structure of thin films of magnetically uni-axial materials," *Cechoslovackij fiziceskij zurnal*, vol. 8, no. 4, pp. 416–421, 1958.

[95] S. Middelhoek, "Domain walls in thin Ni–Fe films," *Journal of Applied Physics*, vol. 34, no. 4, pp. 1054–1059, 1963.

[96] W. F. Brown Jr and A. E. LaBonte, "Structure and energy of one-dimensional domain walls in ferromagnetic thin films," *Journal of Applied Physics*, vol. 36, no. 4, pp. 1380–1386, 1965.

[97] J. Kwo, E. Gyorgy, D. McWhan, M. Hong, F. DiSalvo, C. Vettier, and J. Bower, "Magnetic and structural properties of single-crystal rare-earth Gd–Y superlattices," *Physical Review Letters*, vol. 55, no. 13, p. 1402, 1985.

[98] K. Iijima, T. Terashima, Y. Bando, K. Kamigaki, and H. Terauchi, "Atomic layer growth of oxide thin films with perovskite-type structure by reactive evaporation," *Journal of Applied Physics*, vol. 72, no. 7, pp. 2840–2845, 1992.

[99] T. Tsurumi, T. Suzuki, M. Yamane, and M. Daimon, "Fabrication of barium titanate / strontium titanate artificial superlattice by atomic layer epitaxy," *Japanese Journal of Applied Physics*, vol. 33, no. 9S, p. 5192, 1994.

[100] S. J. Callori, J. Gabel, D. Su, J. Sinsheimer, M. V. Fernandez-Serra, and M. Dawber, "Ferroelectric $PbTiO_3/SrRuO_3$ superlattices with broken inversion symmetry," *Physical Review Letters*, vol. 109, p. 067601, aug 2012.

[101] Q. Zhang, E. Dufresne, P. Chen, J. Park, M. Cosgriff, M. Yusuf, Y. Dong, D. Fong, H. Zhou, Z. Cai, R. Harder, S. Callori, M. Dawber, P. Evans, and A. Sandy, "Thermal fluctuations of ferroelectric nanodomains in a ferroelectric-dielectric $PbTiO_3/SrTiO_3$ superlattice," *Physical Review Letters*, vol. 118, p. 097601, feb 2017.

[102] M. Dawber, "Balancing polar vortices and stripes," *Nature Materials*, vol. 16, pp. 971–972, oct 2017.

[103] J. Park, J. Mangeri, Q. Zhang, M. H. Yusuf, A. Pateras, M. Dawber, M. V. Holt, O. G. Heinonen, S. Nakhmanson, and P. G. Evans, "Domain alignment within ferroelectric/dielectric $PbTiO_3/SrTiO_3$ superlattice nanostructures," *Nanoscale*, vol. 10, pp. 3262–3271, feb 2018.

[104] V. Stephanovich, I. Luk'yanchuk, and M. Karkut, "Domain-enhanced interlayer coupling in ferroelectric/paraelectric superlattices," *Physical Review Letters*, vol. 94, no. 4, p. 047601, 2005.

[105] F. De Guerville, I. Luk'yanchuk, L. Lahoche, and M. El Marssi, "Modeling of ferroelectric domains in thin films and superlattices," *Materials Science and Engineering: B*, vol. 120, no. 1-3, pp. 16–20, 2005.

[106] P. Zubko, N. Jecklin, A. Torres-Pardo, P. Aguado-Puente, A. Gloter, C. Lichtensteiger, J. Junquera, O. Stéphan, and J.-M. Triscone, "Electrostatic coupling and local structural distortions at interfaces in ferroelectric/paraelectric superlattices," *Nano Letters*, vol. 12, no. 6, pp. 2846–2851, 2012.

[107] S. K. Streiffer, J. A. Eastman, D. D. Fong, C. Thompson, A. Munkholm, M. V. Ramana Murty, O. Auciello, G. R. Bai, and G. B. Stephenson, "Observation of nanoscale 180° stripe domains in ferroelectric $PbTiO_3$ thin films," *Physical Review Letters*, vol. 89, p. 067601, jul 2002.

[108] A. M. Bratkovsky and A. P. Levanyuk, "Abrupt appearance of the domain pattern and fatigue of thin ferroelectric films," *Physical Review Letters*, vol. 84, pp. 3177–3180, apr 2000.

[109] A. Bratkovsky and A. Levanyuk, "Very large dielectric response of thin ferroelectric films with the dead layers," *Physical Review B*, vol. 63, no. 13, p. 132103, 2001.

[110] J. L. Bjorkstam and R. E. Oettel, "180° domain formation in ferroelectrics with shorted electrodes," *Physical Review*, vol. 159, no. 2, p. 427, 1967.

[111] A. Kopal, P. Mokrỳ, J. Fousek, and T. Bahnik, "Displacements of 180° domain walls in electroded ferroelectric single crystals: The effect of surface layers on restoring force," *Ferroelectrics*, vol. 223, no. 1, pp. 127–134, 1999.

[112] Y. Watanabe, "Theoretical stability of the polarization in a thin semiconducting ferroelectric," *Physical Review B*, vol. 57, no. 2, p. 789, 1998.

[113] Y. Watanabe, "Theoretical stability of the polarization in insulating ferroelectric/semiconductor structures," *Journal of Applied Physics*, vol. 83, no. 4, pp. 2179–2193, 1998.

[114] A. Schilling, T. Adams, R. Bowman, J. Gregg, G. Catalan, and J. Scott, "Scaling of domain periodicity with thickness measured in $BaTiO_3$ single crystal lamellae and comparison with other ferroics," *Physical Review B*, vol. 74, no. 2, p. 024115, 2006.

[115] J. Y. Son, S. Song, J.-H. Lee, and H. M. Jang, "Anomalous domain periodicity observed in ferroelectric $PbTiO_3$ nanodots having 180° stripe domains," *Scientific Reports*, vol. 6, p. 26644, jul 2016.

[116] B. Yin, P. Aguado-Puente, S. Qu, and E. Artacho, "Two-dimensional electron gas at the $PbTiO_3/SrTiO_3$ interface: An ab initio study," *Physical Review B*, vol. 92, no. 11, p. 115406, 2015.

[117] J. Junquera and P. Ghosez, "Critical thickness for ferroelectricity in perovskite ultrathin films," *Nature*, vol. 422, no. 6931, p. 506, 2003.

[118] P. Aguado-Puente and J. Junquera, "Ferromagneticlike closure domains in ferroelectric ultrathin films: First-principles simulations," *Physical Review Letters*, vol. 100, no. 17, p. 177601, 2008.

[119] I. A. Kornev, H. Fu, and L. Bellaiche, "Properties of ferroelectric ultrathin films from first principles," *Journal of materials science*, vol. 41, no. 1, pp. 137–145, 2006.

[120] K. Rabe and P. Ghosez, "Ferroelectricity in $PbTiO_3$ thin films: a first principles approach," *Journal of Electroceramics*, vol. 4, no. 2-3, pp. 379–383, 2000.

[121] J. Junquera and P. Ghosez, "First-principles study of ferroelectric oxide epitaxial thin films and superlattices: role of the mechanical and electrical boundary conditions," *Journal of Computational and theoretical nanoscience*, vol. 5, no. 11, pp. 2071–2088, 2008.

[122] J. Íniguez and D. Vanderbilt, "First-principles study of the temperature-pressure phase diagram of $BaTiO_3$," *Physical Review Letters*, vol. 89, no. 11, p. 115503, 2002.

[123] W. Zhong, D. Vanderbilt, and K. M. Rabe, "Phase transitions in $BaTiO_3$ from first principles," *Phys. Rev. Lett.*, vol. 73, pp. 1861–1864, Sep 1994.

[124] O. Diéguez, S. Tinte, A. Antons, C. Bungaro, J. Neaton, K. M. Rabe, and D. Vanderbilt, "Ab initio study of the phase diagram of epitaxial BaTiO$_3$," *Physical Review B*, vol. 69, no. 21, p. 212101, 2004.

[125] K. M. Rabe and J. D. Joannopoulos, "Ab initio determination of a structural phase transition temperature," *Phys. Rev. Lett.*, vol. 59, pp. 570–573, Aug 1987.

[126] J. C. Wojdeł, P. Hermet, M. P. Ljungberg, P. Ghosez, and J. Íñiguez, "First-principles model potentials for lattice-dynamical studies: General methodology and example of application to ferroic perovskite oxides," *Journal of Physics: Condensed Matter*, vol. 25, no. 30, p. 305401, 2013.

[127] P. García-Fernández, J. C. Wojdeł, J. Íñiguez, and J. Junquera, "Second-principles method for materials simulations including electron and lattice degrees of freedom," *Phys. Rev. B*, vol. 93, p. 195137, May 2016.

[128] L. Bellaiche, A. García, and D. Vanderbilt, "Finite-temperature properties of Pb(Zr$_{1-x}$Ti$_x$)O$_3$ alloys from first principles," *Phys. Rev. Lett.*, vol. 84, pp. 5427–5430, Jun 2000.

[129] D. Wang, J. Weerasinghe, and L. Bellaiche, "Atomistic molecular dynamic simulations of multiferroics," *Phys. Rev. Lett.*, vol. 109, p. 067203, Aug 2012.

[130] I. A. Kornev, S. Lisenkov, R. Haumont, B. Dkhil, and L. Bellaiche, "Finite-temperature properties of multiferroic BiFeO$_3$," *Phys. Rev. Lett.*, vol. 99, p. 227602, Nov 2007.

[131] P. Zubko, J. C. Wojdeł, M. Hadjimichael, S. Fernandez-Pena, A. Sené, I. Luk'yanchuk, J.-M. Triscone, and J. Íñiguez, "Negative capacitance in multidomain ferroelectric superlattices," *Nature*, vol. 534, no. 7608, p. 524, 2016.

[132] S. Das, Y. Tang, Z. Hong, M. Gonçalves, M. McCarter, C. Klewe, K. Nguyen, F. Gómez-Ortiz, P. Shafer, E. Arenholz, *et al.*, "Observation of room-temperature polar skyrmions," *Nature*, vol. 568, no. 7752, p. 368, 2019.

[133] P. Aguado-Puente, N. Bristowe, B. Yin, R. Shirasawa, P. Ghosez, P. B. Littlewood, and E. Artacho, "Model of two-dimensional electron gas formation at ferroelectric interfaces," *Physical Review B*, vol. 92, no. 3, p. 035438, 2015.

[134] Y. Zhang, H. Lu, L. Xie, X. Yan, T. R. Paudel, J. Kim, X. Cheng, H. Wang, C. Heikes, L. Li, *et al.*, "Anisotropic polarization-induced conductance at a ferroelectric-insulator interface," *Nature Nanotechnology*, vol. 13, no. 12, p. 1132, 2018.

[135] O. Pacherova, D. Chvostova, T. Kocourek, M. Jelinek, A. Dejneka, E. Eliseev, A. Morozovska, and M. Tyunina, "Thermooptical evidence of carrier-stabilized ferroelectricity in ultrathin electrodeless films," *Scientific Reports*, vol. 8, p. 8497, dec 2018.

[136] Y. Zhang, L. Xie, J. Kim, A. Stern, H. Wang, K. Zhang, X. Yan, L. Li, H. Liu, G. Zhao, *et al.*, "Discovery of a magnetic conductive interface in PbZr$_{0.2}$Ti$_{0.8}$O$_3$/SrTiO$_3$ heterostructures," *Nature Communications*, vol. 9, no. 1, pp. 1–9, 2018.

[137] V. Mashkevich and K. Tolpygo, "Electrical, optical and elastic properties of diamond type crystals," *Sov. Phys. JETP*, vol. 5, no. 3, pp. 435–439, 1957.

[138] K. Tolpygo, "Investigation of long-wavelength vibrations of diamond-type crystals with an allowance for long-range forces," *Sov. Phys.—Solid States*, vol. 4, no. 7, pp. 1765–1777, 1962.

[139] S. M. Kogan, "Piezoelectric effect during inhomogeneous deformation and acoustic scattering of carriers in crystals," *Soviet Physics-Solid State*, vol. 5, no. 10, pp. 2069–2070, 1964.

[140] A. Tagantsev, "Theory of flexoelectric effect in crystals," *Zhurnal Eksperimental'noi i Teoreticheskoi Fiziki*, vol. 88, no. 6, pp. 2108–22, 1985.

[141] A. Tagantsev, "Piezoelectricity and flexoelectricity in crystalline dielectrics," *Physical Review B*, vol. 34, no. 8, p. 5883, 1986.

[142] A. K. Tagantsev, "Electric polarization in crystals and its response to thermal and elastic perturbations," *Phase Transitions: A Multinational Journal*, vol. 35, no. 3-4, pp. 119–203, 1991.

[143] R. Maranganti and P. Sharma, "Atomistic determination of flexoelectric properties of crystalline dielectrics," *Phys. Rev. B*, vol. 80, p. 054109, Aug 2009.

[144] R. Resta, "Towards a bulk theory of flexoelectricity," *Phys. Rev. Lett.*, vol. 105, p. 127601, Sep 2010.

[145] J. Hong and D. Vanderbilt, "First-principles theory of frozen-ion flexoelectricity," *Phys. Rev. B*, vol. 84, p. 180101, Nov 2011.

[146] J. Hong and D. Vanderbilt, "First-principles theory and calculation of flexoelectricity," *Phys. Rev. B*, vol. 88, p. 174107, Nov 2013.

[147] M. Stengel, "Flexoelectricity from density-functional perturbation theory," *Phys. Rev. B*, vol. 88, p. 174106, Nov 2013.

[148] M. Stengel, "Microscopic response to inhomogeneous deformations in curvilinear coordinates," *Nature communications*, vol. 4, no. 1, pp. 1–8, 2013.

[149] C. E. Dreyer, M. Stengel, and D. Vanderbilt, "Current-density implementation for calculating flexoelectric coefficients," *Physical Review B*, vol. 98, no. 7, p. 075153, 2018.

[150] A. Schiaffino, C. E. Dreyer, D. Vanderbilt, and M. Stengel, "Metric wave approach to flexoelectricity within density functional perturbation theory," *Phys. Rev. B*, vol. 99, p. 085107, Feb 2019.

[151] M. Royo and M. Stengel, "First-principles theory of spatial dispersion: Dynamical quadrupoles and flexoelectricity," *Phys. Rev. X*, vol. 9, p. 021050, Jun 2019.

[152] J. Hong, G. Catalan, J. Scott, and E. Artacho, "The flexoelectricity of barium and strontium titanates from first principles," *Journal of Physics: Condensed Matter*, vol. 22, no. 11, p. 112201, 2010.

[153] I. Ponomareva, A. Tagantsev, and L. Bellaiche, "Finite-temperature flexoelectricity in ferroelectric thin films from first principles," *Physical Review B*, vol. 85, no. 10, p. 104101, 2012.

[154] M. Stengel, "Surface control of flexoelectricity," *Phys. Rev. B*, vol. 90, p. 201112, Nov 2014.

[155] P. Zubko, G. Catalan, A. Buckley, P. Welche, and J. Scott, "Strain-gradient-induced polarization in SrTiO$_3$ single crystals," *Physical Review Letters*, vol. 99, no. 16, p. 167601, 2007.

[156] R. Maranganti, N. Sharma, and P. Sharma, "Electromechanical coupling in nonpiezoelectric materials due to nanoscale nonlocal size effects: Green's function solutions and embedded inclusions," *Physical Review B*, vol. 74, no. 1, p. 014110, 2006.

[157] M. Majdoub, P. Sharma, and T. Cagin, "Enhanced size-dependent piezoelectricity and elasticity in nanostructures due to the flexoelectric effect," *Physical Review B*, vol. 77, no. 12, p. 125424, 2008.

[158] Z. Zhang and L. Jiang, "Size effects on electromechanical coupling fields of a bending piezoelectric nanoplate due to surface effects and flexoelectricity," *Journal of Applied Physics*, vol. 116, no. 13, p. 134308, 2014.

[159] W. Ma and L. E. Cross, "Flexoelectric polarization of barium strontium titanate in the paraelectric state," *Applied Physics Letters*, vol. 81, no. 18, pp. 3440–3442, 2002.

[160] L. E. Cross, "Flexoelectric effects: Charge separation in insulating solids subjected to elastic strain gradients," *Journal of materials science*, vol. 41, no. 1, pp. 53–63, 2006.

[161] W. Ma and L. E. Cross, "Flexoelectricity of barium titanate," *Applied Physics Letters*, vol. 88, no. 23, p. 232902, 2006.

[162] G. Catalan, L. Sinnamon, and J. Gregg, "The effect of flexoelectricity on the dielectric properties of inhomogeneously strained ferroelectric thin films," *Journal of Physics: Condensed Matter*, vol. 16, no. 13, p. 2253, 2004.

[163] W. Ma, "A study of flexoelectric coupling associated internal electric field and stress in thin film ferroelectrics," *Physica status Solidi (b)*, vol. 245, no. 4, pp. 761–768, 2008.

[164] U. K. Bhaskar, N. Banerjee, A. Abdollahi, Z. Wang, D. G. Schlom, G. Rijnders, and G. Catalan, "A flexoelectric microelectromechanical system on silicon," *Nature nanotechnology*, vol. 11, no. 3, pp. 263–266, 2016.

[165] G. Catalan, A. Lubk, A. Vlooswijk, E. Snoeck, C. Magen, A. Janssens, G. Rispens, G. Rijnders, D. H. Blank, and B. Noheda, "Flexoelectric rotation of polarization in ferroelectric thin films," *Nature materials*, vol. 10, no. 12, pp. 963–967, 2011.

[166] H. Lu, C.-W. Bark, D. E. De Los Ojos, J. Alcala, C.-B. Eom, G. Catalan, and A. Gruverman, "Mechanical writing of ferroelectric polarization," *Science*, vol. 336, no. 6077, pp. 59–61, 2012.

[167] J. Narvaez, F. Vasquez-Sancho, and G. Catalan, "Enhanced flexoelectric-like response in oxide semiconductors," *Nature*, vol. 538, no. 7624, pp. 219–221, 2016.

[168] Z. Yan and L. Y. Jiang, "Flexoelectric effect on the electroelastic responses of bending piezoelectric nanobeams," *Journal of Applied Physics*, vol. 113, no. 19, p. 194102, 2013.

[169] Z. Yan and L. Jiang, "Size-dependent bending and vibration behaviour of piezoelectric nanobeams due to flexoelectricity," *Journal of Physics D: Applied Physics*, vol. 46, p. 355502, aug 2013.

[170] F. Ahmadpoor and P. Sharma, "Flexoelectricity in two-dimensional crystalline and biological membranes," *Nanoscale*, vol. 7, no. 40, pp. 16555–16570, 2015.

[171] Q. Deng, L. Liu, and P. Sharma, "Flexoelectricity in soft materials and biological membranes," *Journal of the Mechanics and Physics of Solids*, vol. 62, pp. 209–227, 2014.

[172] A. Petrov, M. Spassova, and J. Fendler, "Flexoelectricity and photoflexoelectricity in model and biomembranes," *Thin Solid Films*, vol. 284-285, pp. 845 – 848, 1996. Seventh International Conference on Organized Molecular Films.

[173] A. G. Petrov, "Mechanosensitivity of cell membranes: role of liquid crystalline lipid matrix," in *Liquid Crystals: Chemistry and Structure* (M. Tykarska, R. S. Dabrowski, and J. Zielinski, eds.), vol. 3319, pp. 306 – 318, International Society for Optics and Photonics, SPIE, 1998.

[174] W. Kuczyński and J. Hoffmann, "Determination of piezoelectric and flexoelectric polarization in ferroelectric liquid crystals," *Phys. Rev. E*, vol. 72, p. 041701, Oct 2005.

[175] J. Harden, M. Chambers, R. Verduzco, P. Luchette, J. T. Gleeson, S. Sprunt, and A. Jákli, "Giant flexoelectricity in bent-core nematic liquid crystal elastomers," *Applied Physics Letters*, vol. 96, no. 10, p. 102907, 2010.

[176] S. Jewell, "Living systems and liquid crystals," *Liquid Crystals*, vol. 38, no. 11-12, pp. 1699–1714, 2011.

[177] P. Zubko, G. Catalan, and A. K. Tagantsev, "Flexoelectric effect in solids," *Annual Review of Materials Research*, vol. 43, 2013.

[178] P. Yudin and A. Tagantsev, "Fundamentals of flexoelectricity in solids," *Nanotechnology*, vol. 24, no. 43, p. 432001, 2013.

[179] T. D. Nguyen, S. Mao, Y.-W. Yeh, P. K. Purohit, and M. C. McAlpine, "Nanoscale flexoelectricity," *Advanced Materials*, vol. 25, no. 7, pp. 946–974, 2013.

[180] A. K. Tagantsev, P. V. Yudin, and A. K. Tagantsev, *Flexoelectricity in solids: from theory to applications.* World Scientific Publishing Company, 2016.

[181] L. Shu, R. Liang, Z. Rao, L. Fei, S. Ke, and Y. Wang, "Flexoelectric materials and their related applications: A focused review," *Journal of Advanced Ceramics*, pp. 1–21, 2019.

[182] L. Liu, "An energy formulation of continuum magneto-electro-elasticity with applications," *Journal of the Mechanics and Physics of Solids*, vol. 63, pp. 451–480, 2014.

[183] A. D. Rey, "Liquid crystal model of membrane flexoelectricity," *Physical Review E*, vol. 74, no. 1, p. 011710, 2006.

[184] L.-T. Gao, X.-Q. Feng, Y.-J. Yin, and H. Gao, "An electromechanical liquid crystal model of vesicles," *Journal of the Mechanics and Physics of Solids*, vol. 56, no. 9, pp. 2844–2862, 2008.

[185] P. Mohammadi, L. Liu, and P. Sharma, "A theory of flexoelectric membranes and effective properties of heterogeneous membranes," *Journal of Applied Mechanics*, vol. 81, no. 1, 2014.

[186] I. Naumov, A. M. Bratkovsky, and V. Ranjan, "Unusual flexoelectric effect in two-dimensional noncentrosymmetric sp^2-bonded crystals," *Phys. Rev. Lett.*, vol. 102, p. 217601, May 2009.

[187] T. Dumitrică, C. M. Landis, and B. I. Yakobson, "Curvature-induced polarization in carbon nanoshells," *Chemical Physics Letters*, vol. 360, no. 1, pp. 182 – 188, 2002.

[188] S. V. Kalinin and V. Meunier, "Electronic flexoelectricity in low-dimensional systems," *Phys. Rev. B*, vol. 77, p. 033403, Jan 2008.

[189] J. Zhang, K. P. Ong, and P. Wu, "The influence of out-of-plane deformation on the band gap of graphene nanoribbons," *The Journal of Physical Chemistry C*, vol. 114, no. 29, pp. 12749–12753, 2010.

[190] A. G. Kvashnin, P. B. Sorokin, and B. I. Yakobson, "Flexoelectricity in carbon nanostructures: nanotubes, fullerenes, and nanocones," *The journal of physical chemistry letters*, vol. 6, no. 14, pp. 2740–2744, 2015.

[191] S. Chandratre and P. Sharma, "Coaxing graphene to be piezoelectric," *Applied Physics Letters*, vol. 100, no. 2, p. 023114, 2012.

[192] W. Shi, Y. Guo, Z. Zhang, and W. Guo, "Flexoelectricity in monolayer transition metal dichalcogenides," *The journal of physical chemistry letters*, vol. 9, no. 23, pp. 6841–6846, 2018.

[193] J. K. Han, S. Kim, S. Jang, Y. R. Lim, S.-W. Kim, H. Chang, W. Song, S. S. Lee, J. Lim, K.-S. An, *et al.*, "Tunable piezoelectric nanogenerators using flexoelectricity of well-ordered hollow 2D MoS$_2$ shells arrays for energy harvesting," *Nano Energy*, vol. 61, pp. 471–477, 2019.

[194] B. Javvaji, B. He, X. Zhuang, and H. S. Park, "High flexoelectric constants in janus transition-metal dichalcogenides," *Phys. Rev. Materials*, vol. 3, p. 125402, Dec 2019.

[195] X. Zhuang, B. He, B. Javvaji, and H. S. Park, "Intrinsic bending flexoelectric constants in two-dimensional materials," *Phys. Rev. B*, vol. 99, p. 054105, Feb 2019.

[196] R. Tenne, L. Margulis, M. e. Genut, and G. Hodes, "Polyhedral and cylindrical structures of tungsten disulphide," *Nature*, vol. 360, no. 6403, pp. 444–446, 1992.

[197] L. Margulis, G. Salitra, R. Tenne, and M. Talianker, "Nested fullerene-like structures," *Nature*, vol. 365, no. 6442, pp. 113–114, 1993.

[198] G. Seifert, H. Terrones, M. Terrones, G. Jungnickel, and T. Frauenheim, "Structure and electronic properties of MoS_2 nanotubes," *Physical Review Letters*, vol. 85, no. 1, p. 146, 2000.

[199] I. Milošević, B. Nikolić, E. Dobardžić, M. Damnjanović, I. Popov, and G. Seifert, "Electronic properties and optical spectra of MoS_2 and WS_2 nanotubes," *Physical Review B*, vol. 76, no. 23, p. 233414, 2007.

[200] R. Tenne and M. Redlich, "Recent progress in the research of inorganic fullerene-like nanoparticles and inorganic nanotubes," *Chemical Society Reviews*, vol. 39, no. 5, pp. 1423–1434, 2010.

[201] N. Zibouche, A. Kuc, and T. Heine, "From layers to nanotubes: Transition metal disulfides TMS_2," *The European Physical Journal B*, vol. 85, no. 1, p. 49, 2012.

[202] V. I. Artyukhov, S. Gupta, A. Kutana, and B. I. Yakobson, "Flexoelectricity and charge separation in carbon nanotubes," *Nano letters*, vol. 20, no. 5, pp. 3240–3246, 2020.

[203] S. Carr, D. Massatt, S. Fang, P. Cazeaux, M. Luskin, and E. Kaxiras, "Twistronics: Manipulating the electronic properties of two-dimensional layered structures through their twist angle," *Physical Review B*, vol. 95, no. 7, p. 075420, 2017.

[204] E. S. Morell, J. Correa, P. Vargas, M. Pacheco, and Z. Barticevic, "Flat bands in slightly twisted bilayer graphene: Tight-binding calculations," *Physical Review B*, vol. 82, no. 12, p. 121407, 2010.

[205] R. Bistritzer and A. H. MacDonald, "Moiré bands in twisted double-layer graphene," *Proceedings of the National Academy of Sciences*, vol. 108, no. 30, pp. 12233–12237, 2011.

[206] Y. Cao, V. Fatemi, S. Fang, K. Watanabe, T. Taniguchi, E. Kaxiras, and P. Jarillo-Herrero, "Unconventional superconductivity in magic-angle graphene superlattices," *Nature*, vol. 556, no. 7699, pp. 43–50, 2018.

[207] M. Yankowitz, S. Chen, H. Polshyn, Y. Zhang, K. Watanabe, T. Taniguchi, D. Graf, A. F. Young, and C. R. Dean, "Tuning superconductivity in twisted bilayer graphene," *Science*, vol. 363, no. 6431, pp. 1059–1064, 2019.

[208] Y. Cao, V. Fatemi, A. Demir, S. Fang, S. L. Tomarken, J. Y. Luo, J. D. Sanchez-Yamagishi, K. Watanabe, T. Taniguchi, E. Kaxiras, *et al.*, "Correlated insulator behaviour at half-filling in magic-angle graphene superlattices," *Nature*, vol. 556, no. 7699, pp. 80–84, 2018.

[209] A. L. Sharpe, E. J. Fox, A. W. Barnard, J. Finney, K. Watanabe, T. Taniguchi, M. Kastner, and D. Goldhaber-Gordon, "Emergent ferromagnetism near three-quarters filling in twisted bilayer graphene," *Science*, vol. 365, no. 6453, pp. 605–608, 2019.

[210] L.-J. Yin, H. Jiang, J.-B. Qiao, and L. He, "Direct imaging of topological edge states at a bilayer graphene domain wall," *Nature communications*, vol. 7, no. 1, pp. 1–6, 2016.

[211] P. Rickhaus, J. Wallbank, S. Slizovskiy, R. Pisoni, H. Overweg, Y. Lee, M. Eich, M.-H. Liu, K. Watanabe, T. Taniguchi, *et al.*, "Transport through a network of topological channels in twisted bilayer graphene," *Nano letters*, vol. 18, no. 11, pp. 6725–6730, 2018.

[212] S. Huang, K. Kim, D. K. Efimkin, T. Lovorn, T. Taniguchi, K. Watanabe, A. H. MacDonald, E. Tutuc, and B. J. LeRoy, "Topologically protected helical states in minimally twisted bilayer graphene," *Physical review letters*, vol. 121, no. 3, p. 037702, 2018.

[213] S. Sunku, G. Ni, B.-Y. Jiang, H. Yoo, A. Sternbach, A. McLeod, T. Stauber, L. Xiong, T. Taniguchi, K. Watanabe, *et al.*, "Photonic crystals for nano-light in moiré graphene superlattices," *Science*, vol. 362, no. 6419, pp. 1153–1156, 2018.

[214] H. Yu, G.-B. Liu, J. Tang, X. Xu, and W. Yao, "Moiré excitons: From programmable quantum emitter arrays to spin-orbit–coupled artificial lattices," *Science advances*, vol. 3, no. 11, p. e1701696, 2017.

[215] K. L. Seyler, P. Rivera, H. Yu, N. P. Wilson, E. L. Ray, D. G. Mandrus, J. Yan, W. Yao, and X. Xu, "Signatures of moiré-trapped valley excitons in $MoSe_2$/WSe_2 heterobilayers," *Nature*, vol. 567, no. 7746, pp. 66–70, 2019.

[216] Z. Zheng, Q. Ma, Z. Bi, S. de la Barrera, M.-H. Liu, N. Mao, Y. Zhang, N. Kiper, K. Watanabe, T. Taniguchi, *et al.*, "Unconventional ferroelectricity in moiré heterostructures," *Nature*, vol. 588, no. 7836, pp. 71–76, 2020.

[217] M. V. Stern, Y. Waschitz, W. Cao, I. Nevo, K. Watanabe, T. Taniguchi, E. Sela, M. Urbakh, O. Hod, and M. B. Shalom, "Interfacial ferroelectricity by van der Waals sliding," *Science*, 2021.

[218] F. Guinea, B. Horovitz, and P. Le Doussal, "Gauge field induced by ripples in graphene," *Physical Review B*, vol. 77, no. 20, p. 205421, 2008.

[219] P. San-Jose, A. Gutiérrez-Rubio, M. Sturla, and F. Guinea, "Spontaneous strains and gap in graphene on boron nitride," *Physical Review B*, vol. 90, no. 7, p. 075428, 2014.

[220] J. Jung, A. M. DaSilva, A. H. MacDonald, and S. Adam, "Origin of band gaps in graphene on hexagonal boron nitride," *Nature communications*, vol. 6, no. 1, pp. 1–11, 2015.

[221] N. N. Nam and M. Koshino, "Lattice relaxation and energy band modulation in twisted bilayer graphene," *Physical Review B*, vol. 96, no. 7, p. 075311, 2017.

[222] K. Zhang and E. B. Tadmor, "Structural and electron diffraction scaling of twisted graphene bilayers," *Journal of the Mechanics and Physics of Solids*, vol. 112, pp. 225–238, 2018.

[223] S. Carr, D. Massatt, S. B. Torrisi, P. Cazeaux, M. Luskin, and E. Kaxiras, "Relaxation and domain formation in incommensurate two-dimensional heterostructures," *Physical Review B*, vol. 98, no. 22, p. 224102, 2018.

[224] I. V. Lebedeva and A. M. Popov, "Commensurate-incommensurate phase transition and a network of domain walls in bilayer graphene with a biaxially stretched layer," *Physical Review B*, vol. 99, no. 19, p. 195448, 2019.

[225] I. V. Lebedeva and A. M. Popov, "Energetics and structure of domain wall networks in minimally twisted bilayer graphene under strain," *The Journal of Physical Chemistry C*, vol. 124, no. 3, pp. 2120–2130, 2019.

[226] I. V. Lebedeva and A. M. Popov, "Two phases with different domain wall networks and a reentrant phase transition in bilayer graphene under strain," *Physical review letters*, vol. 124, no. 11, p. 116101, 2020.

[227] J. S. Alden, A. W. Tsen, P. Y. Huang, R. Hovden, L. Brown, J. Park, D. A. Muller, and P. L. McEuen, "Strain solitons and topological defects in bilayer graphene," *Proceedings of the National Academy of Sciences*, vol. 110, no. 28, pp. 11256–11260, 2013.

[228] C. Woods, L. Britnell, A. Eckmann, R. Ma, J. Lu, H. Guo, X. Lin, G. Yu, Y. Cao, R. V. Gorbachev, *et al.*, "Commensurate–incommensurate transition in graphene on hexagonal boron nitride," *Nature physics*, vol. 10, no. 6, pp. 451–456, 2014.

[229] M. Yankowitz, K. Watanabe, T. Taniguchi, P. San-Jose, and B. J. LeRoy, "Pressure-induced commensurate stacking of graphene on boron nitride," *Nature communications*, vol. 7, no. 1, pp. 1–8, 2016.

[230] L. Li and M. Wu, "Binary compound bilayer and multilayer with vertical polarizations: two-dimensional ferroelectrics, multiferroics, and nanogenerators," *ACS nano*, vol. 11, no. 6, pp. 6382–6388, 2017.

[231] L. J. McGilly, A. Kerelsky, N. R. Finney, K. Shapovalov, E.-M. Shih, A. Ghiotto, Y. Zeng, S. L. Moore, W. Wu, Y. Bai, *et al.*, "Visualization of moiré superlattices," *Nature Nanotechnology*, vol. 15, no. 7, pp. 580–584, 2020.

[232] V. Enaldiev, F. Ferreira, S. Magorrian, and V. I. Fal'ko, "Piezoelectric networks and ferroelectric domains in twistronic superlattices in WS_2/MoS_2 and $WSe_2/MoSe_2$ bilayers," *2D Materials*, vol. 8, no. 2, p. 025030, 2021.

[233] F. Ferreira, V. Enaldiev, V. Fal'ko, and S. Magorrian, "Weak ferroelectric charge transfer in layer-asymmetric bilayers of 2D semiconductors," *arXiv preprint arXiv:2103.06093*, 2021.

[234] D. Bennett, "Flexoelectric-like radial polarization of single-walled nanotubes from first-principles," *Electronic Structure*, vol. 3, no. 1, p. 015001, 2021.

[235] A. Vaezi, Y. Liang, D. H. Ngai, L. Yang, and E.-A. Kim, "Topological edge states at a tilt boundary in gated multilayer graphene," *Physical Review X*, vol. 3, no. 2, p. 021018, 2013.

[236] D. K. Efimkin and A. H. MacDonald, "Helical network model for twisted bilayer graphene," *Physical Review B*, vol. 98, no. 3, p. 035404, 2018.

[237] E. J. Santos and E. Kaxiras, "Electrically driven tuning of the dielectric constant in MoS_2 layers," *ACS nano*, vol. 7, no. 12, pp. 10741–10746, 2013.

[238] L. H. Li, T. Tian, Q. Cai, C.-J. Shih, and E. J. Santos, "Asymmetric electric field screening in van der Waals heterostructures," *Nature communications*, vol. 9, no. 1, pp. 1–11, 2018.

[239] P. Hohenberg and W. Kohn, "Inhomogeneous electron gas," *Physical review*, vol. 136, no. 3B, p. B864, 1964.

[240] W. Kohn and L. J. Sham, "Self-consistent equations including exchange and correlation effects," *Physical review*, vol. 140, no. 4A, p. A1133, 1965.

[241] J. Ihm, A. Zunger, and M. L. Cohen, "Momentum-space formalism for the total energy of solids," *Journal of Physics C: Solid State Physics*, vol. 12, no. 21, p. 4409, 1979.

[242] P. Denteneer and W. Van Haeringen, "The pseudopotential-density-functional method in momentum space: details and test cases," *Journal of Physics C: Solid State Physics*, vol. 18, no. 21, p. 4127, 1985.

[243] R. O. Jones and O. Gunnarsson, "The density functional formalism, its applications and prospects," *Reviews of Modern Physics*, vol. 61, no. 3, p. 689, 1989.

[244] M. C. Payne, M. P. Teter, D. C. Allan, T. Arias, and a. J. Joannopoulos, "Iterative minimization techniques for ab initio total-energy calculations: molecular dynamics and conjugate gradients," *Reviews of modern physics*, vol. 64, no. 4, p. 1045, 1992.

[245] J. Oppenheimer and M. Born, "On the quantum theory of molecules," *Ann. Physik*, vol. 84, p. 458, 1927.

[246] M. Levy, "Universal variational functionals of electron densities, first-order density matrices, and natural spin-orbitals and solution of the v-representability problem," *Proceedings of the National Academy of Sciences*, vol. 76, no. 12, pp. 6062–6065, 1979.

[247] D. M. Ceperley and B. J. Alder, "Ground state of the electron gas by a stochastic method," *Physical review letters*, vol. 45, no. 7, p. 566, 1980.

[248] E. Wigner, "Effects of the electron interaction on the energy levels of electrons in metals," *Transactions of the Faraday Society*, vol. 34, pp. 678–685, 1938.

[249] L. Hedin and B. I. Lundqvist, "Explicit local exchange-correlation potentials," *Journal of Physics C: Solid state physics*, vol. 4, no. 14, p. 2064, 1971.

[250] S. H. Vosko, L. Wilk, and M. Nusair, "Accurate spin-dependent electron liquid correlation energies for local spin density calculations: a critical analysis," *Canadian Journal of physics*, vol. 58, no. 8, pp. 1200–1211, 1980.

[251] J. P. Perdew and A. Zunger, "Self-interaction correction to density-functional approximations for many-electron systems," *Physical Review B*, vol. 23, no. 10, p. 5048, 1981.

[252] W. E. Pickett, "Pseudopotential methods in condensed matter applications," *Computer Physics Reports*, vol. 9, no. 3, pp. 115–197, 1989.

[253] A. Dal Corso, S. Baroni, R. Resta, and S. de Gironcoli, "Ab initio calculation of phonon dispersions in II-VI semiconductors," *Physical Review B*, vol. 47, no. 7, p. 3588, 1993.

[254] A. Khein, D. J. Singh, and C. J. Umrigar, "All-electron study of gradient corrections to the local-density functional in metallic systems," *Physical Review B*, vol. 51, no. 7, p. 4105, 1995.

[255] A. Dal Corso, S. Baroni, and R. Resta, "Density-functional theory of the dielectric constant: Gradient-corrected calculation for silicon," *Physical Review B*, vol. 49, no. 8, p. 5323, 1994.

[256] J. Goniakowski, J. Holender, L. Kantorovich, M. Gillan, and J. White, "Influence of gradient corrections on the bulk and surface properties of TiO_2 and SnO_2," *Physical Review B*, vol. 53, no. 3, p. 957, 1996.

[257] J. C. Phillips, "Energy-band interpolation scheme based on a pseudopotential," *Physical Review*, vol. 112, no. 3, p. 685, 1958.

[258] V. Heine, "The pseudopotential concept," *Solid state physics*, vol. 24, pp. 1–36, 1970.

[259] M. L. Cohen and V. Heine, "The fitting of pseudopotentials to experimental data and their subsequent application," in *Solid state physics*, vol. 24, pp. 37–248, Elsevier, 1970.

[260] G. B. Bachelet, D. R. Hamann, and M. Schlüter, "Pseudopotentials that work: From H to Pu," *Physical Review B*, vol. 26, no. 8, p. 4199, 1982.

[261] D. Hamann, M. Schlüter, and C. Chiang, "Norm-conserving pseudopotentials," *Physical Review Letters*, vol. 43, no. 20, p. 1494, 1979.

[262] M. Segall, P. J. Lindan, M. a. Probert, C. J. Pickard, P. J. Hasnip, S. Clark, and M. Payne, "First-principles simulation: ideas, illustrations and the CASTEP code," *Journal of physics: condensed matter*, vol. 14, no. 11, p. 2717, 2002.

[263] S. J. Clark, M. D. Segall, C. J. Pickard, P. J. Hasnip, M. I. Probert, K. Refson, and M. C. Payne, "First principles methods using CASTEP," *Zeitschrift für Kristallographie-Crystalline Materials*, vol. 220, no. 5-6, pp. 567–570, 2005.

[264] X. Gonze, J.-M. Beuken, R. Caracas, F. Detraux, M. Fuchs, G.-M. Rignanese, L. Sindic, M. Verstraete, G. Zerah, F. Jollet, *et al.*, "First-principles computation of material properties: the ABINIT software project," *Computational Materials Science*, vol. 25, no. 3, pp. 478–492, 2002.

[265] X. Gonze, "A brief introduction to the ABINIT software package," *Zeitschrift für Kristallographie-Crystalline Materials*, vol. 220, no. 5/6, pp. 558–562, 2005.

[266] X. Gonze, B. Amadon, P.-M. Anglade, J.-M. Beuken, F. Bottin, P. Boulanger, F. Bruneval, D. Caliste, R. Caracas, M. Côté, *et al.*, "ABINIT: First-principles approach to material and nanosystem properties," *Computer Physics Communications*, vol. 180, no. 12, pp. 2582–2615, 2009.

[267] X. Gonze, F. Jollet, F. A. Araujo, D. Adams, B. Amadon, T. Applencourt, C. Audouze, J.-M. Beuken, J. Bieder, A. Bokhanchuk, *et al.*, "Recent developments in the ABINIT software package," *Computer Physics Communications*, vol. 205, pp. 106–131, 2016.

[268] X. Gonze, B. Amadon, G. Antonius, F. Arnardi, L. Baguet, J.-M. Beuken, J. Bieder, F. Bottin, J. Bouchet, E. Bousquet, *et al.*, "The abinit project: Impact, environment and recent developments," *Computer Physics Communications*, vol. 248, p. 107042, 2020.

[269] E. Artacho, D. Sánchez-Portal, P. Ordejón, A. Garcia, and J. M. Soler, "Linear-scaling ab-initio calculations for large and complex systems," *physica status solidi (b)*, vol. 215, no. 1, pp. 809–817, 1999.

[270] J. Junquera, Ó. Paz, D. Sánchez-Portal, and E. Artacho, "Numerical atomic orbitals for linear-scaling calculations," *Physical Review B*, vol. 64, no. 23, p. 235111, 2001.

[271] E. Anglada, J. M. Soler, J. Junquera, and E. Artacho, "Systematic generation of finite-range atomic basis sets for linear-scaling calculations," *Physical Review B*, vol. 66, no. 20, p. 205101, 2002.

[272] J. M. Soler, E. Artacho, J. D. Gale, A. García, J. Junquera, P. Ordejón, and D. Sánchez-Portal, "The SIESTA method for ab initio order-*n* materials simulation," *Journal of Physics: Condensed Matter*, vol. 14, no. 11, p. 2745, 2002.

[273] E. Artacho and D. D. O'Regan, "Quantum mechanics in an evolving Hilbert space," *Physical Review B*, vol. 95, no. 11, p. 115155, 2017.

[274] A. Caviglia, S. Gariglio, N. Reyren, D. Jaccard, T. Schneider, M. Gabay, S. Thiel, G. Hammerl, J. Mannhart, and J.-M. Triscone, "Electric field control of the laalo 3/srtio 3 interface ground state," *Nature*, vol. 456, no. 7222, pp. 624–627, 2008.

[275] M. Stengel, N. A. Spaldin, and D. Vanderbilt, "Electric displacement as the fundamental variable in electronic-structure calculations," *Nature Physics*, vol. 5, no. 4, pp. 304–308, 2009.

[276] H. Lehnert, H. Boysen, J. Schneider, F. Frey, D. Hohlwein, P. Radaelli, and H. Ehrenberg, "A powder diffraction study of the phase transition in LaAlO$_3$," *Zeitschrift für Kristallographie-Crystalline Materials*, vol. 215, no. 9, pp. 536–541, 2000.

[277] A. J. Hatt and N. A. Spaldin, "Structural phases of strained LaAlO$_3$ driven by octahedral tilt instabilities," *Physical Review B - Condensed Matter and Materials Physics*, vol. 82, no. 19, pp. 1–5, 2010.

[278] T. Fister, H. Zhou, Z. Luo, S. S. A. Seo, S. Hruszkewycz, D. Proffit, J. Eastman, P. Fuoss, P. Baldo, H. N. Lee, *et al.*, "Octahedral rotations in strained LaAlO$_3$/SrTiO$_3$ (001) heterostructures," *APL Materials*, vol. 2, no. 2, p. 021102, 2014.

[279] J. P. Perdew, K. Burke, and M. Ernzerhof, "Generalized gradient approximation made simple," *Phys. Rev. Lett.*, vol. 77, pp. 3865–3868, Oct 1996.

[280] J. P. Perdew, A. Ruzsinszky, G. I. Csonka, O. A. Vydrov, G. E. Scuseria, L. A. Constantin, X. Zhou, and K. Burke, "Restoring the density-gradient expansion for exchange in solids and surfaces," *Physical review letters*, vol. 100, no. 13, p. 136406, 2008.

[281] M. A. Marques, M. J. Oliveira, and T. Burnus, "Libxc: A library of exchange and correlation functionals for density functional theory," *Computer physics communications*, vol. 183, no. 10, pp. 2272–2281, 2012.

[282] A. García, M. J. Verstraete, Y. Pouillon, and J. Junquera, "The PSML format and library for norm-conserving pseudopotential data curation and interoperability," *Computer Physics Communications*, vol. 227, pp. 51–71, 2018.

[283] D. Hamann, "Optimized norm-conserving Vanderbilt pseudopotentials," *Physical Review B*, vol. 88, no. 8, p. 085117, 2013.

[284] M. Van Setten, M. Giantomassi, E. Bousquet, M. J. Verstraete, D. R. Hamann, X. Gonze, and G.-M. Rignanese, "The PseudoDojo: Training and grading a 85 element optimized norm-conserving pseudopotential table," *Computer Physics Communications*, vol. 226, pp. 39–54, 2018.

[285] J. P. Perdew and Y. Wang, "Accurate and simple analytic representation of the electron-gas correlation energy," *Phys. Rev. B*, vol. 45, pp. 13244–13249, Jun 1992.

[286] P. E. Blöchl, "Projector augmented-wave method," *Physical review B*, vol. 50, no. 24, p. 17953, 1994.

[287] M. Torrent, F. Jollet, F. Bottin, G. Zérah, and X. Gonze, "Implementation of the projector augmented-wave method in the ABINIT code: Application to the study of iron under pressure," *Computational Materials Science*, vol. 42, no. 2, pp. 337–351, 2008.

[288] H. J. Monkhorst and J. D. Pack, "Special points for Brillouin-zone integrations," *Physical Review B*, vol. 13, no. 12, p. 5188, 1976.

[289] R. W. Nunes and D. Vanderbilt, "Real-space approach to calculation of electric polarization and dielectric constants," *Phys. Rev. Lett.*, vol. 73, pp. 712–715, Aug 1994.

[290] R. W. Nunes and X. Gonze, "Berry-phase treatment of the homogeneous electric field perturbation in insulators," *Phys. Rev. B*, vol. 63, p. 155107, Mar 2001.

[291] I. Souza, J. Íñiguez, and D. Vanderbilt, "First-principles approach to insulators in finite electric fields," *Phys. Rev. Lett.*, vol. 89, p. 117602, Aug 2002.

[292] P. Umari and A. Pasquarello, "Ab initio molecular dynamics in a finite homogeneous electric field," *Phys. Rev. Lett.*, vol. 89, p. 157602, Sep 2002.

[293] O. Diéguez and D. Vanderbilt, "First-principles calculations for insulators at constant polarization," *Phys. Rev. Lett.*, vol. 96, p. 056401, Feb 2006.

[294] M. V. Berry, "Quantal phase factors accompanying adiabatic changes," *Proceedings of the Royal Society of London. A. Mathematical and Physical Sciences*, vol. 392, no. 1802, pp. 45–57, 1984.

[295] R. King-Smith and D. Vanderbilt, "Theory of polarization of crystalline solids," *Physical Review B*, vol. 47, no. 3, p. 1651, 1993.

[296] M. Sing, G. Berner, K. Goß, A. Müller, A. Ruff, A. Wetscherek, S. Thiel, J. Mannhart, S. Pauli, C. W. Schneider, *et al.*, "Profiling the interface electron gas of $LaAlO_3/SrTiO_3$ heterostructures with hard X-ray photoelectron spectroscopy," *Physical Review Letters*, vol. 102, no. 17, p. 176805, 2009.

[297] G. Berner, S. Glawion, J. Walde, F. Pfaff, H. Hollmark, L.-C. Duda, S. Paetel, C. Richter, J. Mannhart, M. Sing, *et al.*, "$LaAlO_3/SrTiO_3$ oxide heterostructures studied by resonant inelastic X-ray scattering," *Physical Review B*, vol. 82, no. 24, p. 241405, 2010.

[298] M. Takizawa, S. Tsuda, T. Susaki, H. Hwang, and A. Fujimori, "Electronic charges and electric potential at $LaAlO_3/SrTiO_3$ interfaces studied by core-level photoemission spectroscopy," *Physical Review B*, vol. 84, no. 24, p. 245124, 2011.

[299] E. Slooten, Z. Zhong, H. Molegraaf, P. Eerkes, S. De Jong, F. Massee, E. Van Heumen, M. Kruize, S. Wenderich, J. Kleibeuker, *et al.*, "Hard x-ray photoemission and density functional theory study of the internal electric field in $SrTiO_3/LaAlO_3$ oxide heterostructures," *Physical Review B*, vol. 87, no. 8, p. 085128, 2013.

[300] S. Dudarev, G. Botton, S. Savrasov, C. Humphreys, and A. Sutton, "Electron-energy-loss spectra and the structural stability of nickel oxide: An LSDA+U study," *Physical Review B*, vol. 57, no. 3, p. 1505, 1998.

[301] R. Pentcheva and W. E. Pickett, "Correlation-driven charge order at the interface between a Mott and a band insulator," *Physical review letters*, vol. 99, no. 1, p. 016802, 2007.

[302] J. Lee and A. A. Demkov, "Charge origin and localization at the n-type $SrTiO_3/LaAlO_3$ interface," *Physical Review B*, vol. 78, no. 19, p. 193104, 2008.

[303] M. Stengel, "First-principles modeling of electrostatically doped perovskite systems," *Physical review letters*, vol. 106, no. 13, p. 136803, 2011.

[304] M. Stengel and D. Vanderbilt, "Berry-phase theory of polar discontinuities at oxide-oxide interfaces," *Physical Review B*, vol. 80, no. 24, p. 241103, 2009.

[305] L. Bellaiche and D. Vanderbilt, "Virtual crystal approximation revisited: Application to dielectric and piezoelectric properties of perovskites," *Physical Review B*, vol. 61, no. 12, p. 7877, 2000.

[306] P. Aguado-Puente and J. Junquera, "Structural and energetic properties of domains in PbTiO$_3$/SrTiO$_3$ superlattices from first principles," *Physical Review B*, vol. 85, p. 184105, may 2012.

[307] J. Junquera, M. Zimmer, P. Ordejón, and P. Ghosez, "First-principles calculation of the band offset at BaO/BaTiO$_3$ and SrO/SrTiO$_3$ interfaces," *Physical Review B*, vol. 67, no. 15, p. 155327, 2003.

[308] J. Junquera, M. H. Cohen, and K. M. Rabe, "Nanoscale smoothing and the analysis of interfacial charge and dipolar densities," *Journal of Physics: Condensed Matter*, vol. 19, no. 21, p. 213203, 2007.

[309] M. Stengel, P. Aguado-Puente, N. A. Spaldin, and J. Junquera, "Band alignment at metal/ferroelectric interfaces: Insights and artifacts from first principles," *Physical Review B*, vol. 83, no. 23, p. 235112, 2011.

[310] F. Corsetti, M.-V. Fernández-Serra, J. M. Soler, and E. Artacho, "Optimal finite-range atomic basis sets for liquid water and ice," *Journal of Physics: Condensed Matter*, vol. 25, p. 435504, oct 2013.

[311] J. Neugebauer and M. Scheffler, "Adsorbate-substrate and adsorbate-adsorbate interactions of Na and K adlayers on Al(111)," *Phys. Rev. B*, vol. 46, pp. 16067–16080, Dec 1992.

[312] L. Bengtsson, "Dipole correction for surface supercell calculations," *Phys. Rev. B*, vol. 59, pp. 12301–12304, May 1999.

[313] L. N. Kantorovich, "Elimination of the long-range dipole interaction in calculations with periodic boundary conditions," *Phys. Rev. B*, vol. 60, pp. 15476–15479, Dec 1999.

[314] B. Meyer and D. Vanderbilt, "Ab initio study of BaTiO$_3$ and PbTiO$_3$ surfaces in external electric fields," *Physical Review B*, vol. 63, no. 20, p. 205426, 2001.

[315] F. A. Rasmussen and K. S. Thygesen, "Computational 2D materials database: electronic structure of transition-metal dichalcogenides and oxides," *The Journal of Physical Chemistry C*, vol. 119, no. 23, pp. 13169–13183, 2015.

[316] M. J. Rutter, "C2x: A tool for visualisation and input preparation for Castep and other electronic structure codes," *Computer Physics Communications*, vol. 225, pp. 174–179, 2018.

[317] S. Shallcross, S. Sharma, E. Kandelaki, and O. Pankratov, "Electronic structure of turbostratic graphene," *Physical Review B*, vol. 81, no. 16, p. 165105, 2010.

[318] E. J. Mele, "Commensuration and interlayer coherence in twisted bilayer graphene," *Physical Review B*, vol. 81, no. 16, p. 161405, 2010.

[319] K. Hermann, "Periodic overlayers and moiré patterns: theoretical studies of geometric properties," *Journal of Physics: Condensed Matter*, vol. 24, no. 31, p. 314210, 2012.

[320] P. Cazeaux, M. Luskin, and E. B. Tadmor, "Analysis of rippling in incommensurate one-dimensional coupled chains," *Multiscale Modeling & Simulation*, vol. 15, no. 1, pp. 56–73, 2017.

[321] D. Massatt, M. Luskin, and C. Ortner, "Electronic density of states for incommensurate layers," *Multiscale Modeling & Simulation*, vol. 15, no. 1, pp. 476–499, 2017.

[322] R. Tadmor, "The London-van der Waals interaction energy between objects of various geometries," *Journal of physics: Condensed matter*, vol. 13, no. 9, p. L195, 2001.

[323] Z. Zhu, S. Carr, D. Massatt, M. Luskin, and E. Kaxiras, "Twisted trilayer graphene: a precisely tunable platform for correlated electrons," *Physical review letters*, vol. 125, no. 11, p. 116404, 2020.

[324] Y. Zhang and W. Yang, "Comment on "generalized gradient approximation made simple"," *Physical Review Letters*, vol. 80, no. 4, p. 890, 1998.

[325] M. Dion, H. Rydberg, E. Schröder, D. Langreth, and B. Lundqvist, "Erratum: van der Waals density functional for general geometries [Phys. Rev. Lett. 92, 246401 (2004)]," *Physical Review Letters*, vol. 95, no. 10, p. 109902, 2005.

[326] G. Román-Pérez and J. M. Soler, "Efficient implementation of a van der Waals density functional: application to double-wall carbon nanotubes," *Physical review letters*, vol. 103, no. 9, p. 096102, 2009.

[327] K. Lee, É. D. Murray, L. Kong, B. I. Lundqvist, and D. C. Langreth, "Higher-accuracy van der Waals density functional," *Physical Review B*, vol. 82, no. 8, p. 081101, 2010.

[328] J. Klimeš, D. R. Bowler, and A. Michaelides, "Chemical accuracy for the van der Waals density functional," *Journal of Physics: Condensed Matter*, vol. 22, no. 2, p. 022201, 2009.

[329] V. R. Cooper, "Van der Waals density functional: An appropriate exchange functional," *Physical Review B*, vol. 81, no. 16, p. 161104, 2010.

[330] K. Berland and P. Hyldgaard, "Exchange functional that tests the robustness of the plasmon description of the van der Waals density functional," *Physical Review B*, vol. 89, no. 3, p. 035412, 2014.

[331] O. A. Vydrov and T. Van Voorhis, "Nonlocal van der Waals density functional: The simpler the better," *The Journal of chemical physics*, vol. 133, no. 24, p. 244103, 2010.

[332] A. M. Popov, I. V. Lebedeva, A. A. Knizhnik, Y. E. Lozovik, and B. V. Potapkin, "Commensurate-incommensurate phase transition in bilayer graphene," *Physical Review B*, vol. 84, no. 4, p. 045404, 2011.

[333] I. V. Lebedeva, A. V. Lebedev, A. M. Popov, and A. A. Knizhnik, "Dislocations in stacking and commensurate-incommensurate phase transition in bilayer graphene and hexagonal boron nitride," *Physical Review B*, vol. 93, no. 23, p. 235414, 2016.

[334] D. C. Liu and J. Nocedal, "On the limited memory BFGS method for large scale optimization," *Mathematical programming*, vol. 45, no. 1, pp. 503–528, 1989.

[335] Y. Frenkel, "The Frenkel-Kontorova model: Concepts, methods, and applications," *Phys Z Sowietunion*, vol. 13, p. 1, 1938.

[336] O. M. Braun and Y. S. Kivshar, "Nonlinear dynamics of the Frenkel–Kontorova model," *Physics Reports*, vol. 306, no. 1-2, pp. 1–108, 1998.

[337] W. L. McMillan, "Theory of discommensurations and the commensurate-incommensurate charge-density-wave phase transition," *Physical Review B*, vol. 14, no. 4, p. 1496, 1976.

[338] L. Bulaevski and D. Khomski, "Commensurability effects and collective excitations in systems with charge-density waves," *Zh. Eksp. Teor. Fiz*, vol. 74, pp. 1863–1871, 1978.

[339] V. Pokrovskiĭ and A. Talapov, "Phase transitions and vibrational spectra of almost commensurate structures," *Soviet Journal of Experimental and Theoretical Physics*, vol. 48, p. 579, 1978.

[340] S. Kumar, J. Kaswan, B. Satpati, A. Shukla, B. Gahtori, J. Pulikkotil, and A. Dogra, "$LaScO_3/SrTiO_3$: A conducting polar heterointerface of two 3d band insulating perovskites," *Applied Physics Letters*, vol. 116, no. 5, p. 051603, 2020.

[341] Y. Wang, W. Tang, J. Cheng, M. Behtash, and K. Yang, "Creating two-dimensional electron gas in polar/polar perovskite oxide heterostructures: first-principles characterization of $LaAlO_3/A^+B_5^+O_3$," *ACS applied materials & interfaces*, vol. 8, no. 21, pp. 13659–13668, 2016.

[342] P. Moetakef, T. A. Cain, D. G. Ouellette, J. Y. Zhang, D. O. Klenov, A. Janotti, C. G. Van de Walle, S. Rajan, S. J. Allen, and S. Stemmer, "Electrostatic carrier doping of $GdTiO_3/SrTiO_3$ interfaces," *Applied Physics Letters*, vol. 99, no. 23, p. 232116, 2011.

[343] X. Fan, W. Zheng, X. Chen, and D. J. Singh, "2degs at perovskite interfaces between $KTaO_3$ or $KNbO_3$ and stannates," *PLOS ONE*, vol. 9, pp. 1–10, 03 2014.

[344] I. V. Maznichenko, S. Ostanin, A. Ernst, J. Henk, and I. Mertig, "Formation and tuning of 2D electron gas in perovskite heterostructures," *physica status solidi (b)*, p. 1900540, 2019.

[345] Y. Kim, Y. M. Kim, J. Shin, and K. Char, "$LaInO_3/BaSnO_3$ polar interface on MgO substrates," *APL Materials*, vol. 6, no. 9, p. 096104, 2018.

[346] K. Yang, S. Nazir, M. Behtash, and J. Cheng, "High-throughput design of two-dimensional electron gas systems based on polar/nonpolar perovskite oxide heterostructures," *Scientific reports*, vol. 6, p. 34667, 2016.

[347] Y. Chen, N. Bovet, F. Trier, D. Christensen, F. Qu, N. H. Andersen, T. Kasama, W. Zhang, R. Giraud, J. Dufouleur, *et al.*, "A high-mobility two-dimensional electron gas at the spinel/perovskite interface of γ-$Al_2O_3/SrTiO_3$," *Nature communications*, vol. 4, no. 1, pp. 1–6, 2013.

[348] W. Niu, Y. Zhang, Y. Gan, D. V. Christensen, M. V. Soosten, E. J. Garcia-Suarez, A. Riisager, X. Wang, Y. Xu, R. Zhang, *et al.*, "Giant tunability of the two-dimensional electron gas at the interface of γ-Al$_2$O$_3$/SrTiO$_3$," *Nano letters*, vol. 17, no. 11, pp. 6878–6885, 2017.

[349] X. Yang, H. Su, and G. Wu, "Orbital-adapted electronic structure and anisotropic transport in γ-Al$_2$O$_3$/SrTiO$_3$ heterostructure," *Physical Review Materials*, vol. 4, no. 1, p. 016001, 2020.

[350] A. Yadav, C. Nelson, S. Hsu, Z. Hong, J. Clarkson, C. Schlepütz, A. Damodaran, P. Shafer, E. Arenholz, L. Dedon, *et al.*, "Observation of polar vortices in oxide superlattices," *Nature*, vol. 530, no. 7589, pp. 198–201, 2016.

[351] S. Das, Y. Tang, Z. Hong, M. Gonçalves, M. McCarter, C. Klewe, K. Nguyen, F. Gómez-Ortiz, P. Shafer, E. Arenholz, *et al.*, "Observation of room-temperature polar skyrmions," *Nature*, vol. 568, no. 7752, pp. 368–372, 2019.

[352] F. Moghadas, J. Poursamad, M. Sahrai, and M. Emdadi, "Flexoelectric coefficients enhancement via doping carbon nanotubes in nematic liquid crystal host," *The European Physical Journal E*, vol. 42, no. 8, p. 103, 2019.

[353] D. Lu, Y. Li, S. V. Rotkin, U. Ravaioli, and K. Schulten, "Finite-size effect and wall polarization in a carbon nanotube channel," *Nano Letters*, vol. 4, no. 12, pp. 2383–2387, 2004.

[354] Y. Li, D. Lu, K. Schulten, U. Ravaioli, and S. V. Rotkin, "Screening of water dipoles inside finite-length armchair carbon nanotubes," *Journal of computational electronics*, vol. 4, no. 1-2, pp. 161–165, 2005.